Characterization of the multi-detector GABRIELA and decay spectroscopy of ^{2} Rf and ^{2} ^{1}No

Rikel Chakma

Rikel Chakma. Characterization of the multi-detector GABRIELA and decay spectroscopy of ^{2} Rf and ^{2} ^{1}No. Nuclear Experiment [nucl-ex]. Université Paris-Saclay, 2020. English. NNT : 2020UPASP066 . tel-03137409

HAL Id: tel-03137409
https://tel.archives-ouvertes.fr/tel-03137409
Submitted on 10 Feb 2021

Characterization of the multi-detector GABRIELA and decay spectroscopy of ^{255}Rf and ^{251}No

Thèse de doctorat de l'Université Paris-Saclay

École doctorale n° 576, Particules, Hadrons, Énergie, Noyau, Instrumentation, Imagerie, Cosmos et Simulation (PHENIICS)
Spécialité de doctorat: Structure nucléaire
Unité de recherche: Université Paris-Saclay, CNRS, IJCLab, 91405, Orsay, France
Référent: : Faculté des sciences d'Orsay

Thèse présentée et soutenue à Orsay, le 27 novembre 2020, par

Rikel CHAKMA

Composition du jury:

Christophe Theisen Directeur de recherche, CEA Saclay (DPhN)	Président
Rolf-Dietmar Herzberg Professeur, University of Liverpool	Rapporteur
Olivier Stezowski Directeur de recherche, Université Claude Bernard de Lyon (IP2I)	Rapporteur
Christophe Theisen Directeur de recherche, CEA Saclay (DPhN)	Examinateur
Stéphane Grévy Directeur de recherche,Université de Bordeaux (CENBG)	Examinateur
Araceli Lopez-Martens Directrice de recherche, Université Paris-Saclay (IJCLab)	Directrice
Karl Hauschild Chargé de recherche, Université Paris-Saclay (IJCLab)	Coencadrant

Thèse de doctorat

NNT: 2020UPASP066

To my grandfather Ven. Prajnananda Mahathera

Acknowledgements

First of all, I would like to pay my special regards and express my sincere appreciation to my supervisor, Araceli Lopez-Martens, who has patiently guided me throughout this project and encouraged me to be professional. Without her constant support, the goal of this project would not have been realized. I also wish to express my deepest gratitude to my co-supervisor Karl Hauschild for his assistance and providing me GABRIELA's Geant4 geometry code which was indispensable for characterizing the detectors and interpreting the experimental results using simulations. I am indebted to my colleagues Alexander Yeremin, Oleg Malyshev, Yuriy Popov, Alexander Svirikhin, Victor Chepigin, Merei Tezekhbaeva and other collaborators from Joint Institute for Nuclear Research, Dubna, Russia, and Olivier Dorvaux, Benoit Gall, and Kieran Kessaci from Institut Pluridisciplinaire Hubert Curien, Strasbourg for their wonderful collaboration. I would also like to thank my tutor Carole Gaulard for her guidance throughout my studies.

I also wish to show my gratitude to Christophe Theisen, Olivier Stezowski, Rolf-Dietmar Herzberg, and Stéphane Grévy for agreeing to be members of the Ph.D. jury. I thank Olivier Stezowski and Rolf-Dietmar Herzberg, who are also the rapporteurs of my thesis, for their valuable suggestions to improve the text.

Finally, I wish to acknowledge the support and great love of my parents and my grandfather Ven. Prajnananda Mahathera who kept me going on and this work would not have been possible without their moral support. I would also like to thank all my friends for their support, especially Christopher Nahed, who assisted me considerably and always encouraged me to stay strong and do the right thing even when the road got rough. I had many interesting discussions with him on various subjects during our stay together in Orsay.

Résumé de la thèse

0.1 Introduction

Une question sans réponse qui se trouve au carrefour de la physique et de la chimie est: quelle est la limite du tableau périodique. Les théories nucléaires suggèrent l'existence de ce qu'on appelle un “îlot de stabilité” (voir figure 1), habité par des éléments à longue durée de vie.

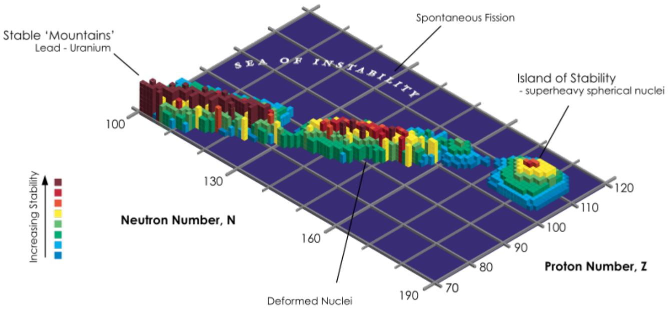

Figure 1: Stabilité (en terme de durée de vie) des noyaux lourds. L'îlot de stabilité est ici prédit pour des noyaux ayant un nombre de neutrons et protons voisins de 184 et 114 respectivement [1].

Ces éléments, comme tous les élément à partir du Rf (104 protons) et qu'on appelle « superlourd », ne doivent leur existence qu'à d'importants effets quantiques et forment un laboratoire unique pour l'étude de la structure et de la dynamique nucléaires sous l'influence d'une très forte répulsion Coulombienne entre les nombreux protons du noyau. Cependant, un défi théorique réside dans la prédiction de la position exacte de cet îlot, car différents modèles prédisent la position au nombre de protons Z=114,120 ou 126, et au nombre de neutrons N=172 ou 184 de façon plutôt inharmonieuse [12]. Pour mieux comprendre le comportement de la matière nucléaire dans des conditions extrêmes du nombre de protons et de neutrons et contraindre les modèles nucléaires, il est donc nécessaire d'étudier la nature et la séquence d'états nucléaires dans des noyaux superlourds plus légers dont les taux de production en laboratoire permettent des études spectroscopiques détaillées.

0.2 Méthodes expérimentales

Dans ce travail, des états de ^{255}Rf ont été peuplés par la réaction de fusion-évaporation ^{50}Ti(^{207}Pb, 2n)^{255}Rf en utilisant un faisceau intense de ^{50}Ti [138] fourni par le cyclotron U400 du FLNR à Dubna. Les résidus d'évaporation ont été séparés du faisceau et du fond d'autres produits de réaction à l'aide du séparateur de noyaux de recul SHELS [38] et implantés dans le détecteur d'implantation du dispositif GABRIELA [37] (voir figure 2). Le multidétecteur GABRIELA permet d'effectuer des corrélations en temps et en position

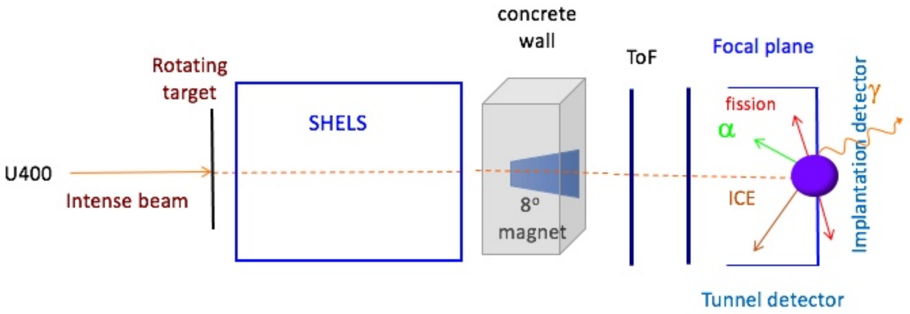

Figure 2: Schéma du dispositif expérimental où apparaissent le filtre des produits de réaction SHELS et le multidétecteur GABRIELA installé au plan focal de SHELS.

entre les noyaux implantés et leurs désintégrations ultérieures et est sensible à l'émission de rayonnements gamma, d'électrons de conversion interne, de particules alpha et de produits de fission.

0.3 Caractérisation de GABRIELA à l'aide de GEANT4

Afin d'interpréter les spectres de désintégration expérimentaux, le multidétecteur GABRIELA a été caractérisé à l'aide de simulations GEANT4 [159]. Ce progiciel n'est cependant pas adapté aux décroissances radioactives de noyaux ayant un numéro atomique supérieur à 100. Il a donc fallu adapter GEANT4 jusqu'au Rf (Z=104), en générant les fichiers de données des processus de relaxation atomique nécessaires et en modifiant certaines parties du code source. Les simulations ont été validées avec des données d'étalonnage (voir figure 3).

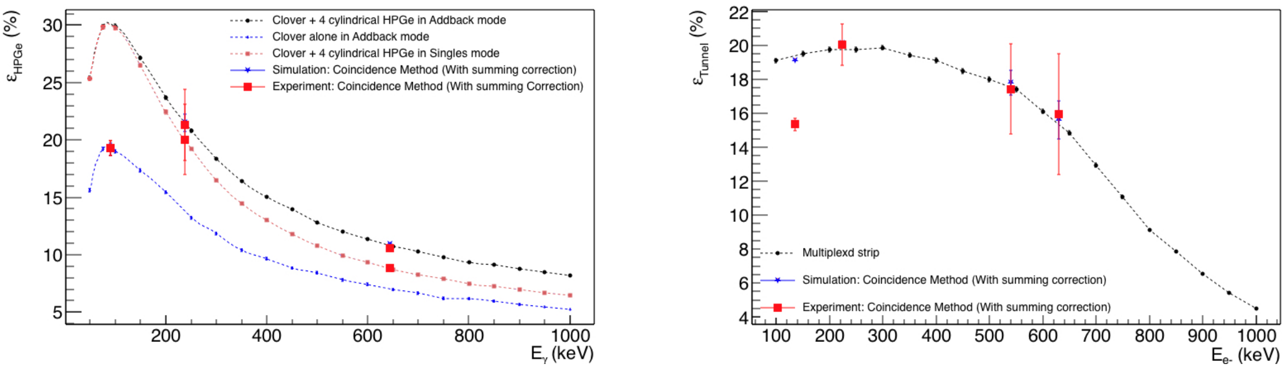

(a) (b)

Figure 3: Efficacités de détection (en %) a) des rayons gamma et b) des électrons de conversion interne en fonction de leur énergie en keV. Les courbes représentent les efficacités simulées et les symboles représentent les efficacités extraites à partir de données d'étalonnage simulées (étoiles bleues) et expérimentales (carrés rouges) après correction d'effets de sommation (voir texte pour plus de détails).

L'impact des effets de sommation dans les détecteurs sur l'efficacité de détection des rayons gamma et des électrons de conversion a été analysé en détail dans la réf. [2] et il a été démontré que les simulations sont essentielles pour interpréter les spectres des multiples particules détectées dans des dispositifs compactes et efficaces comme GABRIELA. Une nouvelle méthode pour estimer le profil de profondeur d'implantation des résidus d'évaporation a été mise au point, ce qui est essentiel notamment pour la spectroscopie des électrons de conversion interne, comme illustré sur la figure 4.

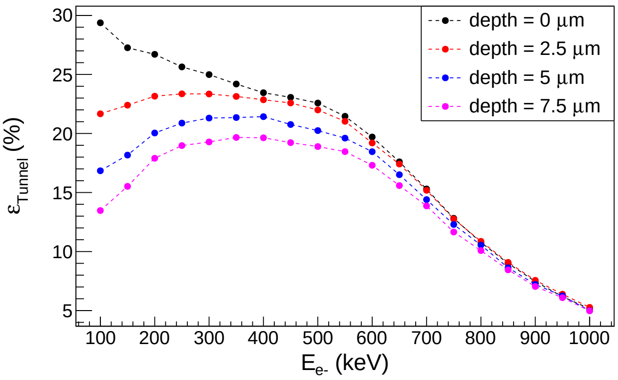

Figure 4: Effets de la profondeur d'implantation des noyaux lourds d'intérêt sur l'efficacité de détecter des électrons de conversion interne dans les détecteurs dits « tunnels » de GABRIELA.

0.4 Résultats expérimentaux

Grâce à l'étude des corrélations spatio-temporelles entre les résidus d'évaporation et leur décroissance radioactive ultérieure, le temps de vie de l'état fondamental du ^{255}Rf a pu être mesuré de 2 manières : via la distribution en temps de son émission alpha caractéristique et celle de sa fission spontanée. Les demi- vie $T_{1/2,\alpha} = 1,67(5)$ s, $T_{1/2,fission} = 1,69(3)$ s et les rapports d'embranchement $Br_{\alpha} = 49,1(1.3)\%$, $Br_{fission} = 50,9(1,1)\%$ mesurés sont en bon accord avec les valeurs données dans la littérature. Dans un premier temps, la structure fine de décroissance alpha du ^{255}Rf a été étudiée. Le schéma de décroissance vers des états excités du noyau fils ^{251}No établi par le groupe de GSI [185] a ainsi pu être confirmé. Notre étude a également permis de déterminer les coefficients de conversion interne des 2 transitions

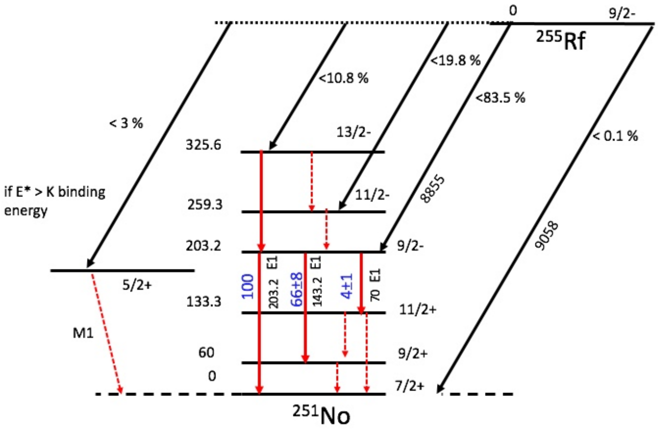

Figure 5: Schéma de niveaux peuplés par l'émission de particules alpha du ^{255}Rf. Les limites supérieures des rapports d'embranchement sont indiqués en % pour l'émission alpha. Pour la désexcitation électromagnétique de l'état $9/2^-$, les rapports d'embranchement sont donnés en relatif par rapport à la transition $9/2^- \rightarrow 7/2^+$.

les plus intenses et confirmer leur caractère dipolaire électrique. Elle a également permis d'identifier de nouveaux états. Enfin les rapports d'embranchements de la décroissance alpha et de la désexcitation électromagnétique ont pu être extraits grâce à une technique de comparaison en χ^2 avec de nombreuses réalisations de simulations GEANT4. Le schéma de décroissance obtenu est illustré dans la figure 5.

Notre étude s'est alors portée vers les états excités du ^{255}Rf. Trois états métastables ont pu être mis en évidence grâce à une analyse assistée par simulation GEANT4 des corrélations génétiques observées dans les détecteurs de GABRIELA. Le premier état est interprété comme un isomère de spin $5/2^+$, dont l'existence avait été déjà suggérée par le GSI [186] d'après la systématique des états de basse énergie des isotones N = 151. Les 2 autres états sont interprétés comme des états à 3 quasi-particules impliquant un neutron célibataire et des excitations de 2 quasi-protons attribuées à des états isomériques dans les noyaux pair-pair voisins ^{254}No [13, 130] et ^{256}Rf [132–134] (voir figure 6).

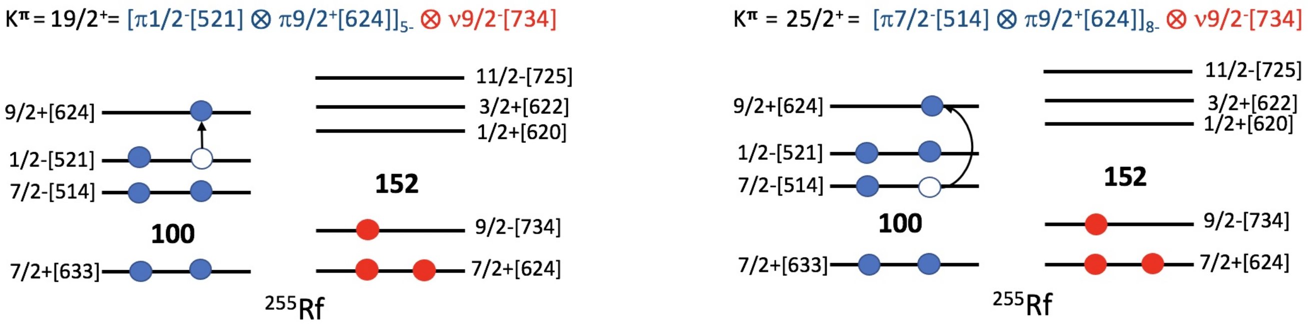

Figure 6: Spectres schématiques des orbitales neutrons et protons et nombres de Nilsson asymptotiques correspondants. Pour les 2 isomères de haute énergie identifies dans le noyau ^{255}Rf, les excitations de protons proposées et les spins et parités (K^π) resultants sont illustrés.

L'existence de ces 2 isomères avait également été mise en avant dans un article récent [188], mais notre étude a permis de séparer les différentes contributions des isomères peuplés dans la réaction et d'établir un schéma de désexcitation complet.

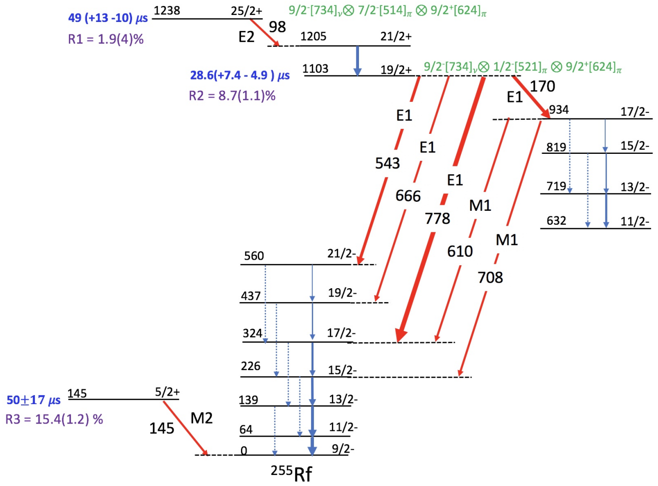

Figure 7: Schéma de niveaux partiel proposé pour le noyau ^{255}Rf avec les demi-vies des 3 états isomériques, leurs configurations probables en terme d'excitations nucléaire et leur population dans la réaction de fusion-évaporation.

La figure 7 résume le schéma de désexcitation de l'isomère de spin et celui proposé pour les 2 isomères dit de haut « K », qui implique une structure intermédiaire bâtie sur un état correspondant à une excitation du neutron célibataire sur l'orbitale de Nilsson $11/2^{-}[725]$. Les propriétés électromagnétiques des états nucléaires de ce schéma permettent de reproduire l'ensemble des observables experimentales, notamment la forme et l'intensité des spectres des différents détecteurs de GABRIELA, comme l'illustre la figure 8.

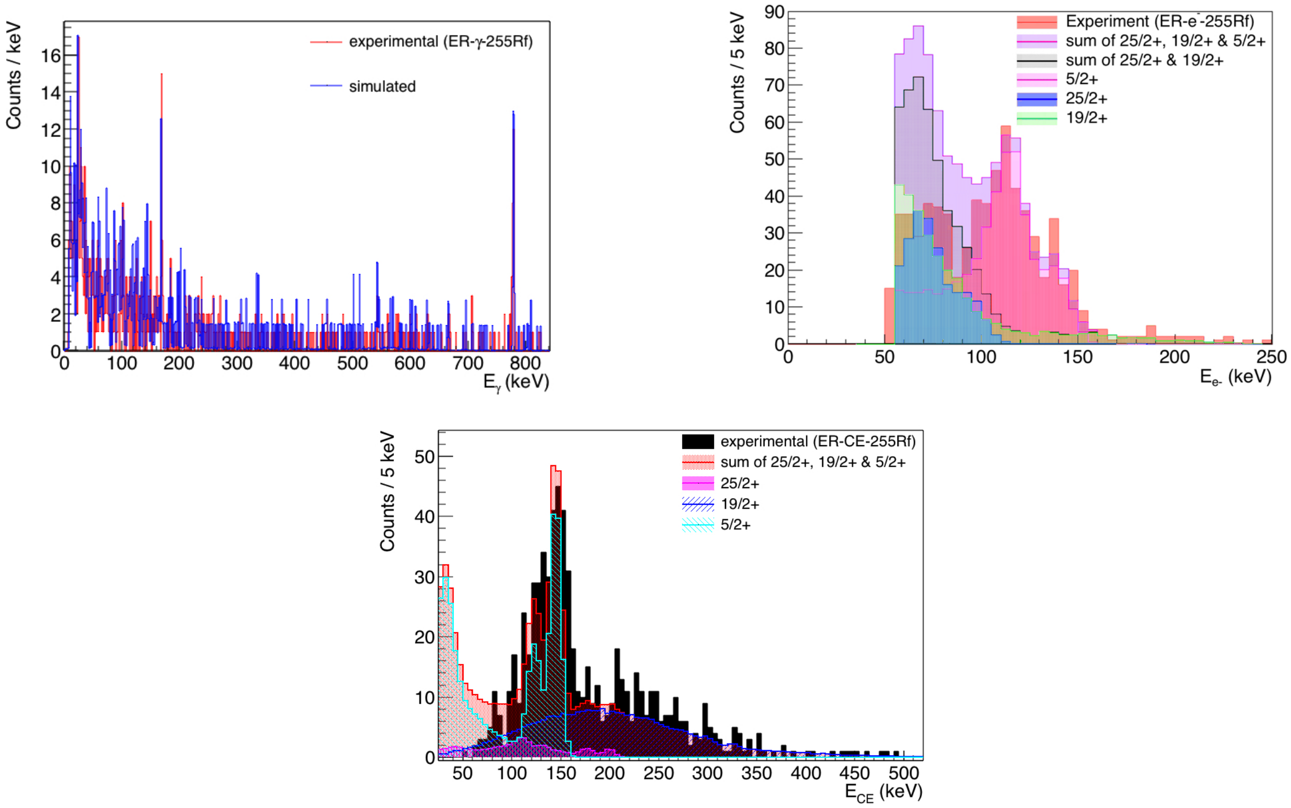

Figure 8: Comparaison des spectres expérimentaux a) des photons b) des électrons de conversion interne et c) des signaux de basse énergie détectés dans le détecteur d'implantation avec les spectres simulés suivant le schéma de désexcitations de la figure 5. Dans les figures b) et c), la contribution de chaque isomère est également indiquée.

0.5 Conclusions & Perspectives

Durant cette thèse, un important travail de modifications de GEANT4 et de simulations de processus radioactifs de noyaux superlourds a été effectué. L'efficacité de détection de photons et d'électrons de conversion interne du multidétecteur GABRIELA a été simulée et les résultats ont été validés par des données expérimentales. Des nouvelles techniques d'analyse de données assistée par simulation ont été développées et ont permis d'interpréter les spectres d'émission des noyaux ^{255}Rf et ^{251}No et d'établir un schéma de niveaux partiel dans chaque cas, qui est consistant avec ce qui est connu dans les isotones plus légers et les propriétés d'isomères dans les noyaux pairs-pairs voisins. Ces résultats devront être confirmés par spectroscopie prompte à la cible de production et par des études de radioactivités en utilisant une électronique digitale car les temps de vie mesurés sont extrêmement courts et les mesures réalisées dans ce travail ont souffert d'un important temps mort électronique. La suite logique de cette étude serait de réaliser une expérience visant à produire le prochain isotone : ^{257}Sg, pour lequel rien n'est connu et dont l'existence même est incertaine, car il se situe aux limites de la charte des noyaux en terme de stabilité face à la fission spontanée. Enfin, en ce qui concerne les simulations, il serait utile d'étendre le travail de modification de GEANT4 aux noyaux au delà de Rf, d'inclure les effets temporels (temps de vie et temps mort) et de rendre l'outil disponible à la communauté.

Contents

0.1 Introduction . . . iii
0.2 Méthodes expérimentales . . . iii
0.3 Caractérisation de GABRIELA à l'aide de GEANT4 . . . iv
0.4 Résultats expérimentaux . . . v
0.5 Conclusions & Perspectives . . . vii

1 Introduction **13**

2 Theoretical Overview **19**
2.1 Macroscopic models . . . 19
  2.1.1 The Liquid Drop Model (LDM) . . . 20
  2.1.2 The Collective model . . . 21
  2.1.3 Rotations and Vibrations . . . 22
2.2 Microscopic models . . . 25
  2.2.1 Mean-Field approach . . . 26
  2.2.2 The Spherical Shell Model . . . 27
  2.2.3 The Deformed Shell Model . . . 29
  2.2.4 Cranked Shell Model . . . 32
  2.2.5 Pairing Correlations . . . 34
2.3 Unified Model . . . 37
  2.3.1 Shell model correction to LDM (Microscopic-Macroscopic model) . . . 39

3 Radioactive decays **41**
3.1 Alpha decay . . . 42
  3.1.1 Hindrance factor . . . 45
3.2 Spontaneous Fission . . . 48
3.3 β decay . . . 50
3.4 Electromagnetic decay . . . 51
  3.4.1 Electromagnetic transition rates . . . 51
  3.4.2 Electromagnetic transitions in deformed systems . . . 54
  3.4.3 Internal conversion process . . . 57
3.5 Isomers . . . 59
  3.5.1 Quasiparticle states in neighboring nuclei . . . 61

4 Experimental Techniques **65**
4.1 Production: Fusion evaporation reactions . . . 66
4.2 Separation: SHELS . . . 69
4.3 Detection Setup: GABRIELA . . . 70

4.3.1 Time of Flight detector 71
4.3.2 Implantation detector 71
4.3.3 Silicon detector array for *ICE*-spectroscopy 72
4.3.4 Germanium detector array for gamma-spectroscopy 72
4.3.5 Basic working principles of the semiconductor detectors 73
4.4 Instrumentation 75
4.5 Data Format 78
4.5.1 Data Analysis Methodology 78
4.6 GEANT4 87
4.7 Efficiency Characterization 92
4.7.1 Method to estimate the implantation depth of evaporation residues 94
4.7.2 Electron detection efficiency of the Tunnel Detectors 97
4.7.3 Gamma-ray detection efficiency 99
4.8 Effects of distributions 101
4.9 Validation 102

5 Decay Spectroscopy of ^{255}Rf and ^{251}No 113
5.1 Discovery of Rf 113
5.2 Discovery of No 113
5.3 What is known in ^{255}Rf 114
5.4 Ground state decay properties of ^{255}Rf 118
5.5 Alpha decay of ^{255}Rf 120
5.6 Determination of relative γ-ray branching ratios 120
5.7 Determination of alpha-decay branching ratios 127
5.7.1 Decay to $9/2^-$ state band 127
5.7.2 Decay to ground state band 130
5.7.3 Decay to $5/2^+$ state 131
5.8 Hindrance Factors 132
5.9 Investigation of isomeric states in ^{255}Rf 134
5.9.1 Isomer spectroscopy of ^{255}Rf 134
5.9.2 Discussion 143

6 Conclusions and Perspectives 153

A Lifetime measurement method 155

B Brief explanation of the GEANT4 data formats 157
B.1 Fluorescence and Auger 157
B.2 Radioactive decay 158

C GEANT4 EM Physics lists after the modifications in the source code 161

Bibliography 176

List of Figures

1 Stabilité (en terme de durée de vie) des noyaux lourds. L'îlot de stabilité est ici prédit pour des noyaux ayant un nombre de neutrons et protons voisins de 184 et 114 respectivement [1]. iii

2 Schéma du dispositif expérimental où apparaissent le filtre des produits de réaction SHELS et le multidétecteur GABRIELA installé au plan focal de SHELS. iv

3 Efficacités de détection (en %) a) des rayons gamma et b) des électrons de conversion interne en fonction de leur énergie en keV. Les courbes représentent les efficacités simulées et les symboles représentent les efficacités extraites à partir de données d'étalonnage simulées (étoiles bleues) et expérimentales (carrés rouges) après correction d'effets de sommation (voir texte pour plus de détails). iv

4 Effets de la profondeur d'implantation des noyaux lourds d'intérêt sur l'efficacité de détecter des électrons de conversion interne dans les détecteurs dits « tunnels » de GABRIELA. v

5 Schéma de niveaux peuplés par l'émission de particules alpha du ^{255}Rf. Les limites supérieures des rapports d'embranchement sont indiqués en % pour l'émission alpha. Pour la désexcitation électromagnétique de l'état $9/2^-$, les rapports d'embranchement sont donnés en relatif par rapport à la transition $9/2^- \rightarrow 7/2^+$. v

6 Spectres schématiques des orbitales neutrons et protons et nombres de Nilsson asymptotiques correspondants. Pour les 2 isomères de haute énergie identifies dans le noyau ^{255}Rf, les excitations de protons proposées et les spins et parités (K^π) resultants sont illustrés. . . vi

7 Schéma de niveaux partiel proposé pour le noyau ^{255}Rf avec les demi-vies des 3 états isomériques, leurs configurations probables en terme d'excitations nucléaire et leur population dans la réaction de fusion-évaporation. vi

8 Comparaison des spectres expérimentaux a) des photons b) des électrons de conversion interne et c) des signaux de basse énergie détectés dans le détecteur d'implantation avec les spectres simulés suivant le schéma de désexcitations de la figure 5. Dans les figures b) et c), la contribution de chaque isomère est également indiquée. vii

1.1 a) The spontaneous fission half-lives for even-even nuclei are compared between experimental data (circles) and LDM predictions (dashed line) as a function of the fissility parameter. Starting with rutherfordium the LDM prediction falls below the minimum lifetime for the formation of a chemical element [7, 8]. b) The top figure shows the shapes of the LDM potential energies of heavy (green) and superheavy (red) nuclei and the bottom figure shows the effects of shell correction on their potential energies as a function of deformation [9]. 14

1.2 Schematic illustration of the spherical single-proton orbitals in the region of superheavy elements showing different gap openings depending on the strength of the spin-orbit interaction. With large spin–orbit coupling (left), the gap appears at 114 and with reduced spin–orbit coupling (right) the gap is at 120 [13]. 15

1.3 The upper end chart of the presently known nuclei. The decay modes of each isotopes are represented with different color codes: α-decay (yellow), β^+- or electron-capture decay (red), β^--decay (blue), spontaneous fission (green), and γ-decaying isomers (white) [14]. The deformed magic numbers are seen at Z = 108 and N = 162 and the next spherical magic number at Z = 114, 120 (uncertain) and N = 184. One can also see how far are these known elements from the predicted island of stability. 16
1.4 3-D rendering of the island of stability [1]. 17
1.5 a) Available experimental information for nuclei from Cm to Hs [7]. b) Single particle proton and neutron energies calculated by phenomenological models with Woods Saxon (WS) or Folded Yukawa (FY) potentials or by self-consistent mean field models using Skyrme (SLy4), Gogny (DS1) or relativistic interactions (NL1) [32]. 18

2.1 Nuclear colour-coded chart showing calculated values of the quadrupole deformation. The blue areas correspond to the regions of prolate shapes [44]. 19
2.2 a) Binding energy per nucleon calculated using a mass formula (curve) over the experimental values for β-stable odd-A nuclei (○) [48]. b) LDM limits of stability drawn on the nuclear chart. The proton and neutron drip lines are indicated by green lines. The vanishing fission barrier and spontaneous fission half-life of 10^{-14} s are indicated by blue lines. The red line corresponds to the beta-stability line [12]. 21
2.3 A schematic of the lowest order vibration modes [53]. 23
2.4 Schematic of flow patterns for rotation of an ellipsoidal body [54]. 24
2.5 An illustration of the projection K of the angular momentum J on the symmetry axis in the intrinsic frame (1,2,3 axes) [54]. 25
2.6 Most common phenomenological shell model potentials: square well, harmonic oscillator and Woods-Saxon. 27
2.7 Single particle energy levels for the modified oscillator potential. The “magic numbers” indicated with red color are obtained after adding l^2 and spin-orbit terms to the potential [53]. 28
2.8 A schematic of splitting of levels as a function of deformation [59]. 30
2.9 Proton and neutron single-particle levels obtained from momentum dependent Woods-Saxon potential with universal parameters as a function of quadrupole deformation, ν_2 [60]. The orbitals around ^{254}No (Z = 102, N = 152) relevant to this work are highlighted with red squares. 31
2.10 a) Deformation energy (in MeV) defined as a difference between the ground-state energy and the energy at the spherical shape. b) Predicted ground-state mass quadrupole deformation β and corresponding nuclear shapes: prolate shapes are coloured red–orange, oblate shapes are blue–green, and spherical shapes are light yellow [61, 62]. 32
2.11 A schematic representation of smearing of the Fermi surface because of pairing interaction [53]. 36
2.12 A schematic representation of angular-momentum coupling in a deformed nucleus; the K quantum number is built from the projections of the angular momentum of the 2 valence particles onto the symmetry axis [75]. 38
2.13 Schematic representation of the level density in an infinite three dimensional potential [48]. 39
2.14 Ground-state microscopic corrections [44]. 40

3.1 Nuclear landscape (Sergè Chart) by the type of decay [78]. 41
3.2 Modification of the potential energy in a decay due to the centrifugal potential (adapted from [59]). 43

3.3 A schematic diagram of alpha decay. In an e-e nucleus the last bound pairs can easily form the alpha particle whereas in an e-o system, the alpha particle can be formed by breaking a pair or by the first pairs from the alpha particle leaving the daughter nucleus in an excited state [7]. 45
3.4 The leading order Feynman diagram of a) β^- decay b) β^+ decay and c) EC decay. 50
3.5 Schematic representations of quadrupole deformations [59]. 55
3.6 A schematic illustration of the processes to fill a vacancy in L1 subshell: a) X-ray fluorescence b) Auger process and b) Coster-Kronig process [117]. 58
3.7 Secondary minima in the potential energy of a nucleus as a function of various nuclear variables lead to differentiate kinds of isomers [124]. 59
3.8 Trends of the hindrance factor F_W from the systematics of Lobner [125] for electromagnetic transitions of different multipolarities as functions of ΔK [126]. 60
3.9 a) Decay scheme of the 8^- isomer in ^{252}No [129]. b) Decay scheme of the 8^- isomer in ^{254}No [13]. 62
3.10 a) Suggested (highlighted with red square) two and four quasiparticle configurations for the isomers observed in ^{254}Rf [131]. b) Decay scheme of the lowest isomer observed in ^{256}Rf [134]. 62
3.11 Tentative level scheme of ^{253}No [42]. 63

4.1 6 ^{207}Pb target foils mounted on the rotating target wheel. 65
4.2 A schematic of the experimental setup. 66
4.3 A schematic representation of (a) different reaction modes [136] (b) fusion evaporation reaction [137] (see the text for details). 67
4.4 Energy distribution of 253 MeV ^{50}Ti ions after Ti backing and half lead target in SRIM [139] calculation. The red-curve is a Gaussian fit. 68
4.5 Calculated excitation functions of the reaction ^{207}Pb(^{50}Ti, xn)$^{257-xn*}$Rf [138]. 69
4.6 Measured cross sections for a) cold and b) hot fusion reactions [142]. 69
4.7 Ion optical scheme of SHELS [38]. 70
4.8 Photographs showing the components of the GABRIELA setup:(a) Implantation detector and tunnel DSSDs (b) Ge array and (c) Inside of the vacuum chamber showing 4 of the 5 inserts. 71
4.9 Variation of the relative dominance of the three types of gamma-ray interactions at different gamma-ray energies $h\nu$ for different absorber of atomic number Z [150]. 74
4.10 (a) Schematic diagram of an pn junction, (b) diagram of electron energy levels showing the creation of a contact potential V_0, (e) associated charge density, and (d) the electric field intensity [151] 75
4.11 A schematic drawing of GABRIELA's instrumentation as it was in 2016 [152]. The only difference with the setup used in this work is that the Clover detector has also a BGO shield. 76
4.12 A schematic of data acquisition system [152]. 77
4.13 A schematic of the data format. 79
4.14 Figures showing the components of the fits used for gamma-ray and electron peaks. 80
4.15 Calibrated spectra after the calibration procedure for (a) DSSD high gain (b) DSSD low gain (c) tunnel detectors (d) Ge detectors. 81

4.16 The energy spectra of the electrons emitted from a ^{133}Ba source detected in all the strips of (a) the implantation detector and (c) the tunnel detectors. (b) Spectrum of alpha-particle energies emitted by the nuclei produced in the reaction ^{170}Er(^{50}Ti, xn yp) (d) Energy spectrum of the Compton suppressed gamma rays detected within 24 µs from the implantation of ^{210}Ra nuclei. The insets in the figures show the corresponding fits (red curves) of the peaks, from which the resolutions of table 4.3 have been extracted. The histograms of insets a) and (c) have been scaled up by 100 to show their differences. The inset of figure (d) shows the fit on the 1332.5 keV peak of ^{60}Co since gamma-ray resolutions are often quoted at this energy. 82
4.17 Spectrum of low energy signals (CE) observed in the implantation DSSD in the decay of the 117 µs isomer in ^{209}Ra (a) before and (b) after pole-zero software correction. 83
4.18 Punch-through signals in the Clover detector appearing $\sim$ 30 µs after a decay signal in the implantation DSSD. 83
4.19 Measured FWHM for the Ge array. 84
4.20 ToF in ADC channel number as a function of Recoil Energy (E_R) in the reaction ^{207}Pb(^{50}Ti,xn)$^{(257-xn)*}$Rf 85
4.21 Schematic of the sequence of implantation and decay signals observed in the implantation detector and an entry of the correlation tree based on these decay chains. 86
4.22 By selecting a) ^{251}No alpha-peak and fission events in the correlation tree b) ^{255}Rf mother decay events can be obtained. Similarly, by selecting mother c) ^{255}Rf alpha-peak events d) daughter ^{251}No events can be obtained. 88
4.23 3D rendering of the various elements of GABRIELA, as described in GEANT4 (courtesy of K. Hauschild). 89
4.24 Fluorescence transition (a) probability and (b) energy as a function of atomic number for a K vacancy. 90
4.25 The difference between the extrapolated Energy in (a) Fluorescence and (b) Auger transitions and the corresponding calculated value given in ToI for K shell vacancy in ^{255}Rf. . . . 91
4.26 (a) Comparison of extrapolated and Fluorescence emission probabilities with calculated values given in ToI for K shell vacancy in ^{255}Rf after correcting the transition energies. (b) shows the relative differences with $\Delta P = Extrapolated - ToI$. 91
4.27 Cuts applied to select ^{209}Ra ions implanted in an isomeric state. 93
4.28 position distribution comparison between ^{209}Ra isomers and ^{255}Rf nuclei. 94
4.29 Effect of implantation depth on peak shape and intensity in the tunnel detector. 94
4.30 Absolute efficiency to detect (a) gamma rays in the Ge array and (b) electrons in the tunnel detectors that are emitted from a point source at (0, 0, depth) various implantation depths in the implantation detector. 95
4.31 (a) Estimated true recoil E distribution: SRIM input energy for 238U projectiles. (b) Depth profile of ^{238}U beam in Si from SRIM calculation. The incident energy of the beam was the recoil energy detected for ^{255}Rf ERs after PHD correction (see fig. 4.31a). 96
4.32 (a) Plot showing the χ^2 difference (see equation 4.13) between the experimental and simulated energy spectra of ^{255}Rf alpha particles that escape the DSSD as a function of the mean and the standard deviation of a Gaussian implantation depth distribution. (b) Experimentally observed and simulated spectra of ^{255}Rf alpha particles at minimum χ^2 value. The inset shows the comparison of the alpha peaks in the spectra. In the simulation, the decay scheme of ^{255}Rf was taken from ref. [185] with alpha decay to additional levels (see chapter 5 section 5.7). 97
4.33 Energy loss by an electron in the DSSD as a function of its energy 97

4.34 Comparison between the scaled-down and original efficiency curves 98

4.35 Electron detection efficiency as a function of energy for various ways of treating the signals from the tunnel detector. 99

4.36 (a) Absolute gamma-ray detection efficiency of the components of the Ge array and (b) the corresponding peak to total ratio. 99

4.37 (a) The contribution of the clover detector to the total efficiency with its (b) addback factor as a function of gamma-ray energy. 100

4.38 (a) Effect of missing 1 ring detector in the Ge array on the gamma-ray detection efficiency. (b) Relative loss of efficiency due to the absence of 1 ring detector. 101

4.39 Absolute efficiency curves as a function of energy for different XY-distributions in the implantation detector with the same implantation depth profile, which minimizes the χ^2 test on the ^{255}Rf escaped alpha-particle energy spectra. (a) Ge-array Compton-suppressed efficiencies for a point source in addback mode ★ and in singles mode ✚, for the ^{209}Ra distribution in addback mode ● and in singles mode ■, and for the ^{255}Rf distribution in addback mode ○ and in singles mode □; (b) Tunnel detector efficiencies in the case of a point source ★, for the ^{209}Ra ● and ^{255}Rf ○ distributions. 101

4.40 Partial level schemes of (a) ^{209}Ra [164] and (b) ^{207}Rn [167] showing the low-lying 13/2+ isomer, whose decay has been used to validate the Geant4 simulations. 102

4.41 (a) Experimental and (b) simulated spectrum of gamma rays emitted in the isomeric decay of ^{209}Ra. 103

4.42 (a) Experimental and (b) simulated spectrum of ICE emitted in the isomeric decay of ^{209}Ra. 103

4.43 Selected region of the simulated gamma-ray and ICE coincidence matrix measured in the isomeric decay of ^{209}Ra, showing the effect of summing. 105

4.44 An illustration of inverse transform sampling method. 108

4.45 Summing of Ke^- of 238.4 keV transtions with KX rays and KAuger electrons in the tunnel detectors. 109

4.46 Absolute efficiency curves for the (a) Ge and (b) Tunnel detectors. (a) ■, ● and ★ denote the simulated efficiencies in singles and add back mode for the whole Ge array and the clover detector alone. (b) ● represent the simulated electron efficiency for the 113 active strips during the ^{209}Ra calibration run. ✚ and ✖ correspond to the simulated efficiencies extracted from simulated ^{209}Ra isomeric data using the singles and coincidence methods. ■ correspond to the measured gamma-ray or electron efficiencies. 109

4.47 P/T measurement on the 644 keV peak. 111

4.48 Using the decay scheme established by Rissanen et al. [168], the spectrum of isomeric gamma rays observed in Dubna could be reproduced with the GABRIELA Geant4 program. The excess L X ray intensity is due to the contribution of a second isomer which was also observed in the data [K. Hauschild et al. to be published]. 111

5.1 Decay scheme proposed for ^{255}Rf. The numbers denote the Q values [184]. 115

5.2 a)^{251}Fm α-decay scheme [189] b) ^{253}No α-decay scheme [190]. 116

5.3 Systematics of low-lying states in N= 151 isotones. 116

5.4 (a) Suggested alpha decay scheme of ^{259}Sg. (b) Energy spectrum and the lifetime fit (inset) of the isomeric conversion electrons following the alpha decay of ^{259}Sg [186]. 117

5.5 a) CE energies as a function of the time difference between the implantation of an ER and the detection of a CE. Red dots, electrons not in coincidence with gamma rays; blue dots, electrons in coincidence with gamma rays. b) Energy spectrum of coincident gamma rays [188]. 118
5.6 Proposed decay scheme of K isomers in ^{255}Rf (left) along with the alpha decay scheme of ^{259}Sg (right). Adapted from ref. [188]. 118
5.7 Log$_2$ of the time difference between a recoil implant and subsequent decay vs energy of the decay observed in the reaction ^{207}Pb(^{50}Ti,xn)$^{257-\mathrm{xn}}$Rf. 119
5.8 Lifetime fit of the ^{255}Rf (a) the alpha peak and (b) the fission events of fig. 5.7. 119
5.9 Experimental a) $\alpha - \gamma$ and b) $\alpha - e^-$ coincidence matrices. 120
5.10 Spectra of the a) γ rays and b) electrons in coincidence with $^{255}Rf - \alpha$ peak. 121
5.11 Simple ground state decay scheme of ^{255}Rf. 121
5.12 Energy spectra of a) gamma rays and b) electrons coincident with ^{255}Rf alpha-peak events. c) The full energy peak of the alphas in coincident with gamma rays. Note that in the γ-ray spectrum the apparent mismatch between the experimental and simulated peak intensities of 203 keV and 143 keV lines is a visual rendering. 124
5.13 Simulated energy spectra of alpha particles coincident with ICE. The simulations of 143 keV and 203 keV were carried out individually. 125
5.14 Comparison of a) γ and b) e^-energy spectra gated by α peak. 125
5.15 Relative gamma branching ratios from 9/2$^-$ state. 126
5.16 Energy spectra of a) gamma rays b) electrons coincident with ^{255}Rf alpha peak and c) alpha particles coincident with gamma rays. 126
5.17 additional levels of the 9/2$^-$ band. 128
5.18 Simulated alpha particle energies when 100 % branching is given to each level. For each case, the simulated peaks are normalized to the experimental peak. 129
5.19 χ^2 value: a) 11/2$^-$ vs 13/2$^-$ b) 9/2$^-$ vs 11/2$^-$ c) 9/2$^-$ vs 13/2$^-$. The dark area is the limit beyond which $\chi^2 > \chi^2_{critical}$ d) Comparison of experimental and simulated alpha peak shapes at the minimum χ^2 value. The contribution due to each decay branch is shown separately. The experimental and simulated peak integrals are 937 and 931 respectively. 131
5.20 Proposed decay scheme of ^{255}Rf where the given alpha branching ratios are the maximum limits and the energies correspond to Q values. 133
5.21 a) Energy and time distribution plot, and b) the fit on the lifetimes of the CEs in the decay chains ER*-[CE]-^{255}Rf. 134
5.22 (a) 103 gamma rays and (b) 69 electrons(tunnel) observed in coincidence with CEs in the decay chains ER-[CE]-^{255}Rf. 135
5.23 CE time with respect to recoil implant vs the total energy E_{max} obtained by summing all the energies detected in coincidence on an event-by-event basis. 136
5.24 (a) Spectrum of gamma rays (b) zoomed at low energy and (c) spectrum of tunnel electrons observed in the chains ER-$\gamma/e-$- ^{255}Rf. 137
5.25 Measured lifetime of prominent gamma-ray lines for ER- γ correlations with or without CEs (i.e low-energy signals in the implantation DSSD) followed by the ground-state decay of ^{255}Rf. 138
5.26 a) 65 $\gamma - e^-$ coincidences and b) 66 $\gamma - \gamma$ coincidences observed in the decay chains ER-$\gamma/e-$ - ^{255}Rf decay. 138
5.27 Comparison of E_{max} and lifetime of the isomer detected in two different correlations. . . . 139

5.28 a) Energy and b) time distribution comparisons between the CE observed in the 27 decay chains ER-CE-CE-^{255}Rf. 139

5.29 a) 6 gamma rays and b) 8 electrons(tunnel) observed in coincidence with 2nd CEs in the chains ER-CE-[CE]-^{255}Rf. 140

5.30 (a) E_{max} obtained by summing the energy of the (a) 2nd CE and the coincident gamma rays and electron. (b) + CE1 on event-by-event basis. 141

5.31 Energy and time distributions of the a) gamma rays and b) electron seen before the detection of the CE in the decay chains ER-$\gamma/e-$-CE-^{255}Rf. 141

5.32 a) Energy and time distributions of the CEs in the decay chains ER-$\gamma/e-$-CE-^{255}Rf. Their lifetimes have been compared with the lifetime of iso2 mocking the non detection of iso1 in the ER*-CE-[CE]-^{255}Rf decay chains. b)Energy step of the 2nd isomer (CE) in the decay chain ER-$\gamma/e-$*-[CE]-^{255}Rf. 142

5.33 Lifetime and E_{max} compared for the a) 1st isomer and b) the 2nd isomer. 143

5.34 Experimental half-lives of the prominent gamma transitions listed in table 5.17 for ER-γ - ^{255}Rf decay compared with Weisskof estimates including a K-hindrance a) $\nu = 3 - L$ and b) $\nu = 4 - L$. The Weisskof estimates have been corrected for the internal conversion coefficients. For each transitions in the figures, the band corresponds to $f_\nu = 30 - 300$ with a line corresponding to $f_\nu = 100$. The upper and lower limits on the half-life of iso1 and iso 2 are from table 5.19 and 5.21. A band has been drawn to highlight its half-life in the visible range. 144

5.35 Same as for fig. 5.34 for $\nu = 5 - L$. 145

5.36 Scenario 1: a) Decay scheme b) simulated γ ray spectrum where experimental background has been added. 145

5.37 Scenario 2: a) Decay scheme b) simulated γ ray spectrum with added experimental background. 146

5.38 Revised partial decay scheme of ^{253}No. 147

5.39 Scenario 3: a) Decay scheme (bottom) and a zoomed part of experimental γ-ray spectrum (top) b) simulated γ ray spectrum with added experimental background. 148

5.40 Scenario 4: a) Decay scheme (bottom) and a zoomed part of experimental γ-ray spectrum (top) b) simulated γ-ray spectrum with added experimental background. 148

5.41 a) E_max of the in the decay from 19/2$^+$ isomer b) Comparison of e- spectra, where the contribution from each of the isomeric decays are shown. 149

5.42 Simulated tunnel spectrum a) of iso1 + iso2 when scaled by 4, b) after including 5/2$^+$ isomeric decay. c) γ-ray spectrum after adding 5/2$^+$ isomer's contribution. Note that the missing LX rays in fig. 5.41b are recovered. 150

5.43 Comparison of the experimental CE spectrum with simulations showing the contributions of all 3 isomers for a) 60 keV and b) 100 keV thresholds. 152

5.44 Proposed partial level scheme for ^{255}Rf. 152

B.1 (a) Fluorescence and (b) Auger data formats in GEANT4 for Z =100. 158

B.2 Radioactive decay in GEANT4 160

C.1 Energy loss by 5.48 MeV α particles in Si as simulated in GEANT4 using modified Penelope Physics list. 163

List of Tables

3.1 Average hindrance factors [86]. . . . 44
3.2 Most significant (a) Electric and (b) Magnetic transition probabilities of multipolarity λ. The transition energies are given in [MeV]. . . . 54
3.3 Relevant single-particle g_K values (Woods-Saxon). . . . 56

4.1 Ranges of ionizing particles in Si. . . . 79
4.2 List of Missing strips or detectors in the two experiments. . . . 83
4.3 The resolutions and the typical thresholds of the GABRIELA detectors. The fits at these energies are shown in the insets of fig. 4.16. . . . 84
4.4 Fit parameters of the gamma efficiency curves in addback mode. . . . 102
4.5 Internal conversion coefficients and electron energies of the isomeric transitions obtained from BRICC [116]. . . . 104
4.6 The absolute detection efficiency of tunnel detector for X rays emitted from each subshell of L having intensity weighted energy. The fluorescence yield, ω is taken from ToI [163]. . . 107
4.7 Intensity-weighted conversion coefficients used in this work (see text for details). . . . 109
4.8 The measured gamma-ray and electron efficiency values obtained from singles and coincidence methods: ε corresponds to efficiency from a ^{209}Ra distributed source emitting either a single gamma or an electron isotropically with the given energy. ε_0 and ε^* indicate values extracted without or with summing corrections (see the text) for ^{209}Ra isomeric decay. . . . 110

5.1 α fine structure observed in the study of ref. [185]. . . . 115
5.2 Details of the 2 experiments: duration, average beam energy, total beam dose, number of ^{255}Rf ions detected and corresponding production cross section (assuming a 22$^+$ charge state for the Ti ions and a transmission and detection efficiency of SHELS of 40%). . . . 118
5.3 Calculated excitation energies and branching ratios of the first three rotational states in the the ground-state band. . . . 122
5.4 Conversion coefficients and electron energies from BRICC. The Ece_{N+} are weighted by the conversion coefficients and indicated by *. . . . 123
5.5 gamma in coincident with ^{255}Rf alpha peak. . . . 123
5.6 electron in coincident with ^{255}Rf alpha 8.6-8.85 MeV. . . . 124
5.7 Measured LMN+e intensities. . . . 124
5.8 Measured conversion coefficients. Since the K conversion electrons of the 203 keV transition have energy below the thresholds of the tunnel detectors, $\alpha_K(203)$ was scaled using the same factor as for the $\alpha_{LMN+}(203)$. . . . 125
5.9 Calculated excitation energies, branching ratios (br in %) and mixing ratios (δ) of the first three rotational states in the 9/2$^-$ band. . . . 128

5.10 Energy of the conversion electrons for the three in band transitions of the 9/2$^-$ band. * values are the weighted values. 128
5.11 Relative alpha decay rates k_l as a function of angular momentum carried away by the alpha particle. 130
5.12 Table showing the branching ratios extracted from the χ^2 comparison test for the alpha decay to the 9/2$^-$ band. The branchings are given at the minimum χ^2 value and for the χ^2 values at the limits of acceptance. 130
5.13 Table showing how the intensity of the simulated alpha peak between 8850 and 9000 keV varies according to the relative branching to the 7/2$^+$ ground state. 132
5.14 Table showing how the intensity of the X rays and electrons vary with branching to the 5/2$^+$ state. A maximum of 3 % branching can be accommodated. 132
5.15 HF calculated using Preston's Method. + and - indicate maximum and minimum values as discussed in the text. The alpha particle energies have been corrected for mass dependence of the contribution of the recoil daughter to the detected energy. 133
5.16 Half-lives (in µs) of conversion electrons for the chain ER*- [CE]-^{255}Rf in different conditions. Here 'w' and 'wo' refer to with and without coincidence respectively. Since CE events suffer from deadtime, the $T_{1/2}$ values should be considered as upper limits. 135
5.17 Half-lives (in µs) of prominent gamma lines observed (see fig. 5.24a) before the ground-sate decay of ^{255}Rf. [CEs] indicates that gamma rays in coincident with the CEs in the implantation detector were also included. 136
5.18 Energy ranges and associated half-lives (in µs) of electrons detected in the tunnel detectors (see fig. 5.24c) before the ground-sate decay of ^{255}Rf (see text for details on the last 3 columns of the table). 138
5.19 Half-lives (in µs) of the CEs measured in different conditions. 140
5.20 Half-life (in µs) of conversion electrons for the chain ER-CE*- [CE]-^{255}Rf in different conditions. 141
5.21 Half-lives (in µs) of gamma rays and electrons in the tunnel and in the DSSD of fig. 5.31 and 5.32a. 142
5.22 Half-lives (in µs) of CEs for the chain ER- $\gamma/e-$*-[CE]-^{255}Rf in different conditions. . . . 143
5.23 Calculated transition energies, B(M1)/B(E2) ratios in $(\mu_n/eb)^2$, mixing ratios δ, relative gamma emission branching ratios and internal conversion coefficients for the M1 and E2 Intra band transitions from states (Spin I) having excitation energies (E* in keV). In the cases where δ is not given α_{mixed} is the internal conversion coefficient of M1 transition α_{M1}. 149
5.24 Table of inter band transitions of multipole character σ with relative gamma emission branching ratios br_γ and internal conversion coefficients α. 150
5.25 Fractions of isomers that would not be detected (dead), detected (alive) because of the dead-time associated with the ADCs of the implantation DSSD. The fractions of the CE spectra below (<) and above (>) the 60 keV and 100 keV thresholds were obtained from simulations. 151

B.1 ENDL Atomic subshell designators 159

C.1 Built-in EM physics lists that can (c1) and cannot (c2) be used. 161
C.2 Models that that can (c1) and cannot (c2) be used for $Z > 100$. The models indicated by '*' do not exist in the GEANT4 version used for this work. 162
C.3 Changes in the stepFunction Limit for ionization process made in the Penelope Physics list. 162

Chapter 1

Introduction

It has been more than a century since E. Rutherford discovered the nucleus at the center of an atom [3,4]. An atomic nucleus is a dense clump of protons and neutrons held together by the strong force and gives most of the mass to the atom. The number of protons in the nucleus determines whether the atom is gold or silver. Together with the number of neutrons, they decide the stability of the nucleus, hence the fate of the atom. Protons and neutrons (together known as nucleons) are not fundamental structureless particles. They are made of three quarks bound together by the strong force mediated by gluons. The strong force is mostly confined within the nucleons, only a tiny fraction of it acts outside the nucleons. This "residual" strong force (or the nuclear force) holds the atomic nuclei together against the disruptive electromagnetic force between the positively charged protons. The residual strong force is very much similar to the van der Waals force that originates from the Coulomb force [6]. The exact nature of the nuclear interaction is still not well understood and remains one of the unsolved problems in physics. No one knows for sure how nucleons behave inside a nucleus. In 1982, physicists at the European Organization for Nuclear Research (CERN) have discovered the EMC effect (named after European Muon Collaboration) that is nucleons appear much larger inside a nucleus than when they are free (not bound). Nuclei being quantum many-body systems, are complicated to deal with and certainly hiding a lot of mysteries within them.

Clues exist in the patterns that prevail from the simplest to the complex nuclides. Pattern seeking is an old human habit for explaining the order in nature. In the same light, it took over two centuries to organize the known elements into the periodic table, depending on their chemical properties. The periodic table became a road-map of building blocks of matter for the chemists. Scientists have been adding new elements to the periodic table ever since. With the advent of the particle accelerator, many new man-made elements have been added to the periodic table, starting with the first synthetic element technetium in 1937 [5]. But when will the end of the periodic table be reached remains one of the most persistent mysteries in Chemistry. Richard Feynman predicted the end of the periodic table at element 137 based on relativistic calculations where he presumed the atomic nucleus to be pointlike. His calculations showed that electron orbitals would break down beyond this point. Recent calculations showed that this limit can be pushed to 173 if the size of the nucleus is taken into account [10, 11]. But, relativity is not the only factor that determines the existence of an atom. Positively charged protons inside a nucleus repel each other making it less and less stable with more addition of protons. Uranium, with an atomic number of 92, is the last relatively stable element to occur naturally on Earth. Every element beyond uranium disintegrates quickly.

A macroscopic model known as the Liquid Drop Model (LDM), treats a nucleus as a charged droplet of incompressible quantum liquid of constant density with the strong nuclear force holding the drop together against the Coulomb repulsion between the protons that upsets its stability. Although the LDM succeeded in describing the overall mode of nuclear stability across the known nuclides, nevertheless, large deviations were observed for nuclei containing specific numbers of protons and neutrons. These numbers, 2,8,20,28,50 and 82 for protons and neutrons in the elements lighter than uranium and another number 126 for neutrons, later became known as magic numbers attributing extra stability to the associated nuclides. The nuclear shell model is particularly successful in explaining the origin of these magic numbers. In this model, the protons and neutrons inside a nucleus fill up energy levels of increasing energy. Inhomogeneity in the distribution of the levels causes levels to cluster together forming shells with relatively large energy gaps between them. Magic numbers correspond to the number of particles required to fill up energy shells completely. It requires a large jump in energy for one nucleon to cross the gap to the next shell. Thus, nuclei with closed shells are unusually stable, resembling the unreactive nature of the noble gases which have the right number of electrons to fill the electronic shells. Complete filling of both proton and neutron shells imparts double stability to the nuclei. The shell model not only explains the stability trend across the nuclear chart it also explains the existence of the super-heavy nuclei (SHN). These SHN should not exist based on LDM because the Coulomb repulsion would simply overpower the nuclear force splitting the nucleus instantly. In fig. 1.1a the spontaneous fission half-lives have been drawn as a function of the fissility parameter (see chapter 3 section 3.2 eq. 3.33): at Rf, the lifetime becomes less than the lifetime (10^{-14} s [8]) required to form an atom. However, it is clear that the LDM underestimates the fission half-lives of the elements lighter than and heavier than Rf, and in fact, elements up to 118 have already been synthesized in laboratories. These elements owe their existence to quantum shell effects which creates a minimum in the potential energy surface of the nucleus at some deformation as shown in fig. 1.1b.

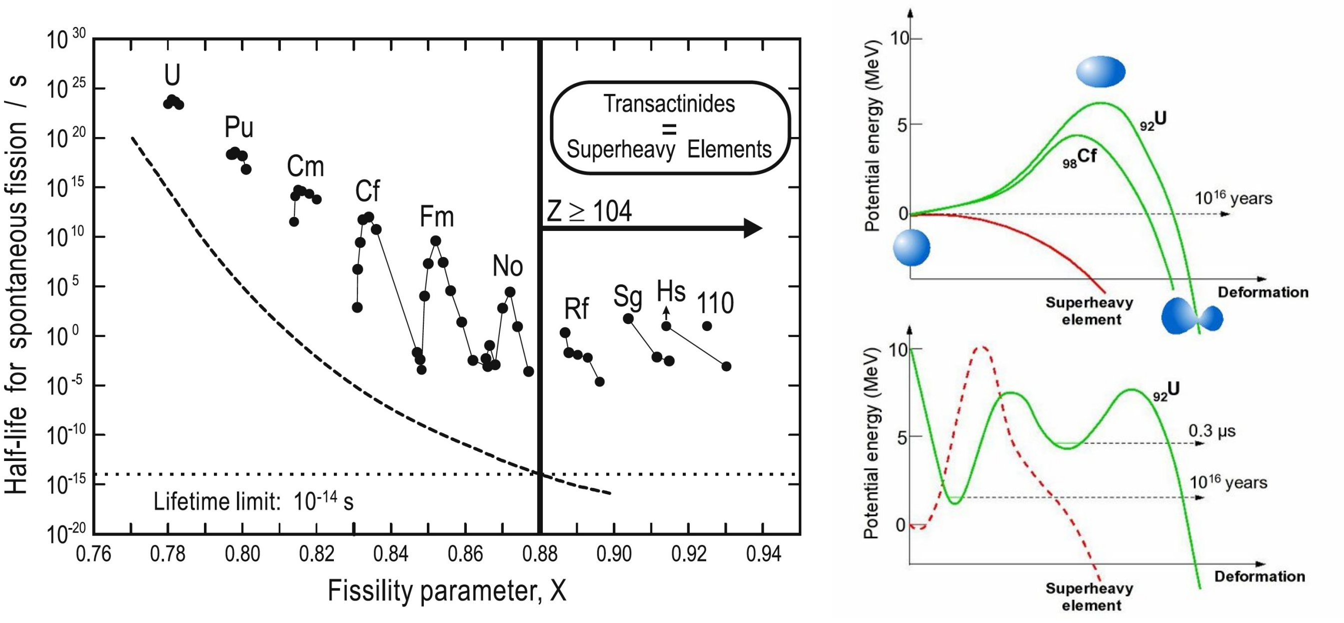

(a)

(b)

Figure 1.1: a) The spontaneous fission half-lives for even-even nuclei are compared between experimental data (circles) and LDM predictions (dashed line) as a function of the fissility parameter. Starting with rutherfordium the LDM prediction falls below the minimum lifetime for the formation of a chemical element [7, 8]. b) The top figure shows the shapes of the LDM potential energies of heavy (green) and superheavy (red) nuclei and the bottom figure shows the effects of shell correction on their potential energies as a function of deformation [9].

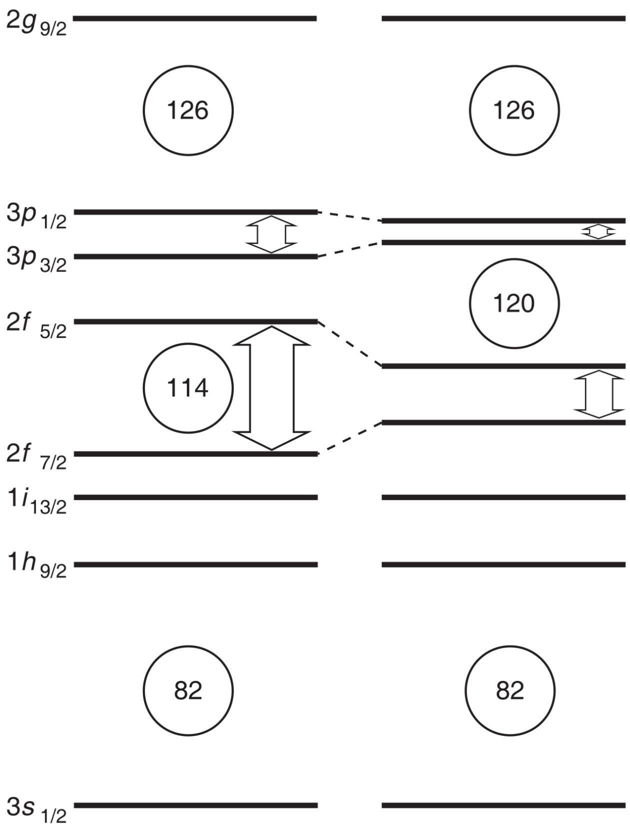

Figure 1.2: Schematic illustration of the spherical single-proton orbitals in the region of superheavy elements showing different gap openings depending on the strength of the spin-orbit interaction. With large spin–orbit coupling (left), the gap appears at 114 and with reduced spin–orbit coupling (right) the gap is at 120 [13].

Since shells define the stability, it is natural to seek the next proton and neutron spherical shell closures. Unfortunately, there is no consensus across different theoretical models in the prediction of the next spherical magic numbers beyond ^{208}Pb (Z = 82, N = 126). Phenomenological models predict them to be Z = 114, N = 184 while density functional theories based on Skyrme or Gogny interaction predict Z= 126, N =184 and those based on relativistic mean-field interaction predict Z = 120, N = 172 [12]. One factor that gives rise to such differences is the strength of the spin-orbit interaction. For instance, in a nucleus with 114 protons that fill all the orbitals up to $2f_{7/2}$ orbital, the strength of the spin-orbit interaction between the proton $2f_{7/2}$-$2f_{5/2}$ spin-orbit partners opens the proton shell gap either at 114 with large spin-orbit coupling or at 120 with small spin-orbit coupling [13] (see fig. 1.2). Owing solely to the stability resulting from the nucleonic shell effects, there lies a possibility of a real "island of stability" occupied by the "superheavy elements" well beyond the limits of known elements. It was A. Sobiczewski, F.A. Gareev, and B. N. Kalinkin from Dubna, Russia who first predicted the possible existence of superheavy stable nuclei centered at Z = 114 and N = 184 [15]. Nuclear theories have predicted that the half-lives of these elements can range from minutes to many years, even possibly spanning the age of the earth [7], hence, experimentally accessible. The region then came to be known as the "island of stability", a term first coined by W. D. Myers and W. J. Swiatecki [16]. Immediately after the conception of this island of stability, attempts were made to find them in nature [17–19] and to synthesize them in a laboratory. The earliest claim of discovering super-heavy elements in nature came in 1976 by a group of nuclear physi-

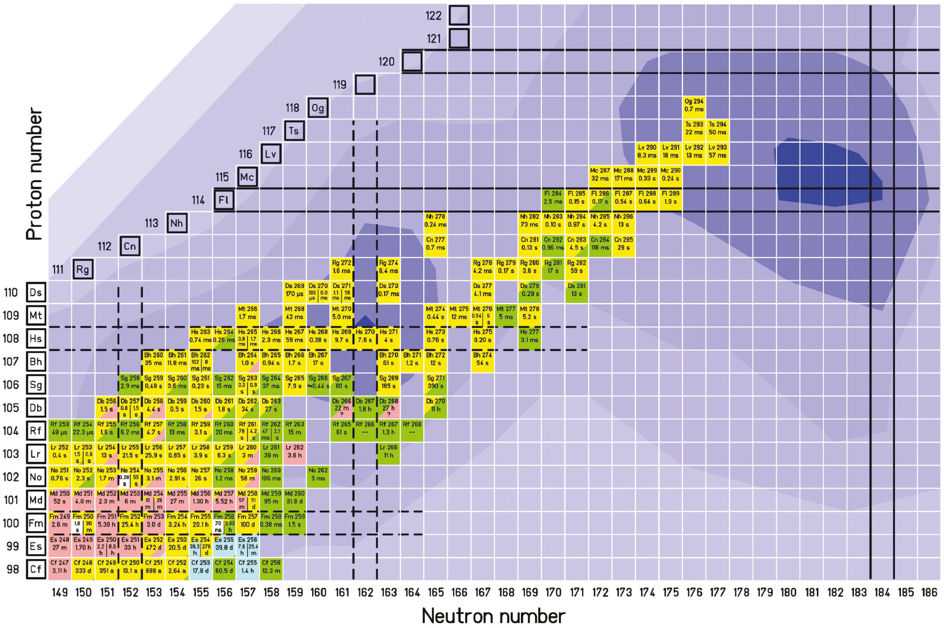

Figure 1.3: The upper end chart of the presently known nuclei. The decay modes of each isotopes are represented with different color codes: α-decay (yellow), β^+- or electron-capture decay (red), β^--decay (blue), spontaneous fission (green), and γ-decaying isomers (white) [14]. The deformed magic numbers are seen at Z = 108 and N = 162 and the next spherical magic number at Z = 114, 120 (uncertain) and N = 184. One can also see how far are these known elements from the predicted island of stability.

cists from the US, who claimed to have detected elements 116, 124, and 126 in the mineral monazite from Madagascar [20, 21]. However, later searches for superheavy elements in monazite from Madagascar [22–25] and India [26, 27] were unsuccessful casting a doubt on the previous claim. The quest for superheavy elements has culminated in the synthesis of the heaviest man-made element Z = 118. These recently discovered heavy elements survive just fractions of a second suggesting that perhaps we reached the shores of the island of stability (see fig. 1.3). Despite some indication in the measured lifetimes of the heaviest synthesized nuclei (see the review [28]), the fabled island of stability awaits discovery. Fig. 1.4 illustrates the stability of nuclides as a function of the proton and neutron number. Theory predicts about 6000 nuclei lie in the limit of existence, out of which nearly 3300 nuclei have been observed so far, and only 252 are known to be stable, and the rest are unstable. The degree of instability grows as we go further away from the line of stability and the stable nuclei move towards stability through radioactivity. The last heavy non-radioactive stable isotope is doubly magic ^{208}Pb with 82 protons and 126 neutrons, and the neighboring single magic isotope ^{209}Bi is fairly stable with an extremely long half-life. All elements with an atomic number greater than 82 are unstable, and their half-lives decrease with increasing atomic numbers. The half-life raises again to some high values between thorium and plutonium. This region is the island of relative stability, with peaks at the non-magical ^{232}Th and ^{238}U whose lifetimes are comparable with the age of the earth. Earlier it was postulated that the island containing spherical nuclei would require a leap across the sea of instability. However, more recent studies [29, 30] suggest that the superheavies are deformed and more resilient to spontaneous fission. New magic numbers Z = 108 and N = 162 appear as a consequence of deformed shell structure. This converted the lone faraway island of stability into a peninsula with an isthmus of relatively stable deformed nuclei linking it to the region of stable nuclei [7] (see fig. 1.4).

Elements heavier than uranium called transuranium elements are so unstable that they are not usu-

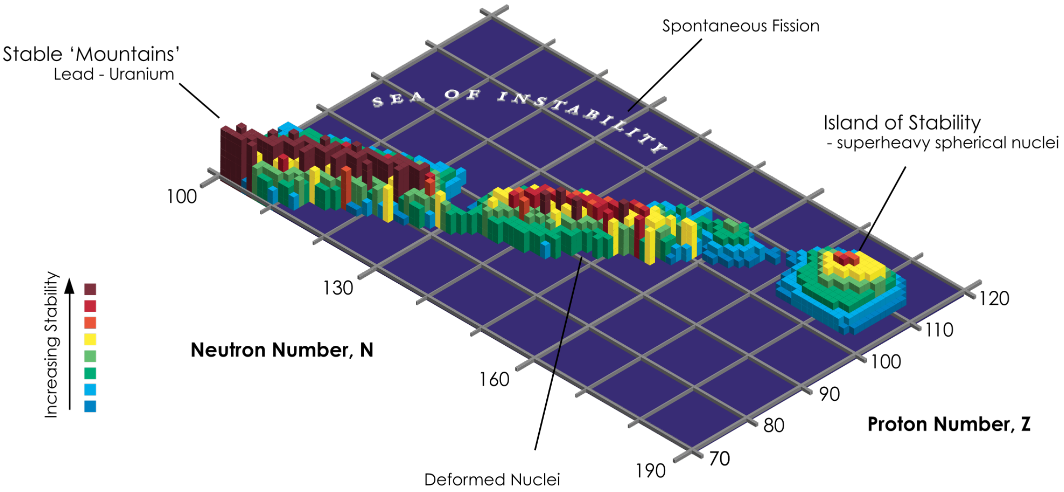

Figure 1.4: 3-D rendering of the island of stability [1].

ally found in nature. Physicists synthesize the transuranium elements using accelerated beams of nuclei that impinge on the heaviest possible target nuclei. As the half-life of elements decreases with increasing atomic number, synthesis of elements with an atomic number beyond that of uranium becomes challenging. The elements residing in the island of stability are neutron-rich, and the targets and projectiles available currently for fusion experiments are not neutron-rich enough to reach the island. With such technological challenges, there is a growing fear that the island might never come to sight.

To confirm the position of the island of stability and constrain the nuclear models, it is pertinent to study the nature, sequence, and spacing of the states of the lighter heavy nuclei. With the current state of technology, they are relatively easier to produce than their heavier counterparts. One customary way to study the nuclear structure is through decay spectroscopic studies. Hitherto the spectroscopic data in the transfermium region remains sparse (see fig. 1.5a). Constant efforts are underway in major experimental facilities around the globe. Recent developments in nuclear spectroscopy techniques and instrumentation have allowed the identification of single-particle and collective states in many heavy systems and the results reveal discrepancies [32] (see fig. 1.5b) in the sophisticated theoretical models. To study the structure in detail, two techniques are currently employed: the first one is prompt spectroscopy at the target [33], generally performed using the recoil decay tagging method (RDT) [34,35]. The other complementary technique is decay spectroscopy either at the focal plane of a recoil separator or at a decay station coupled to a gas-jet transport system [36] where alpha, gamma, and internal conversion electron (ICE) spectroscopy of superheavy nuclei and their daughter products is performed. Gamma spectroscopy has been carried out for a few transfermium nuclei. However, in heavy nuclei, the emission of ICEs is a competitive de-excitation mode. Thus, ICE spectroscopy is a necessary supplementary technique to gamma spectroscopy, in studying the structure of heavy nuclei. The GABRIELA [37] setup at the focal plane of SHELS [38] in Dubna, Russia is aimed at performing detailed alpha, gamma, and ICE spectroscopy in the transfermium region. Since the beginning of the project in 2003, the decay properties of several nuclei have been studied (see refs. [39–43]) or are being investigated (for example, ^{256,257}Rf, ^{250}No, ^{255,256}No). The detection setup is gradually being modernized and upgraded.

This study attempts to investigate the nuclear structures of ^{255}Rf produced in the reaction ^{207}Pb(^{50}Ti, 2n)^{255}Rf and its daughter ^{251}No. First, an overview of the relevant theoretical models is presented in chapter 2. Then in chapter 3, different decay modes heavy nuclei can undergo are discussed briefly. The details

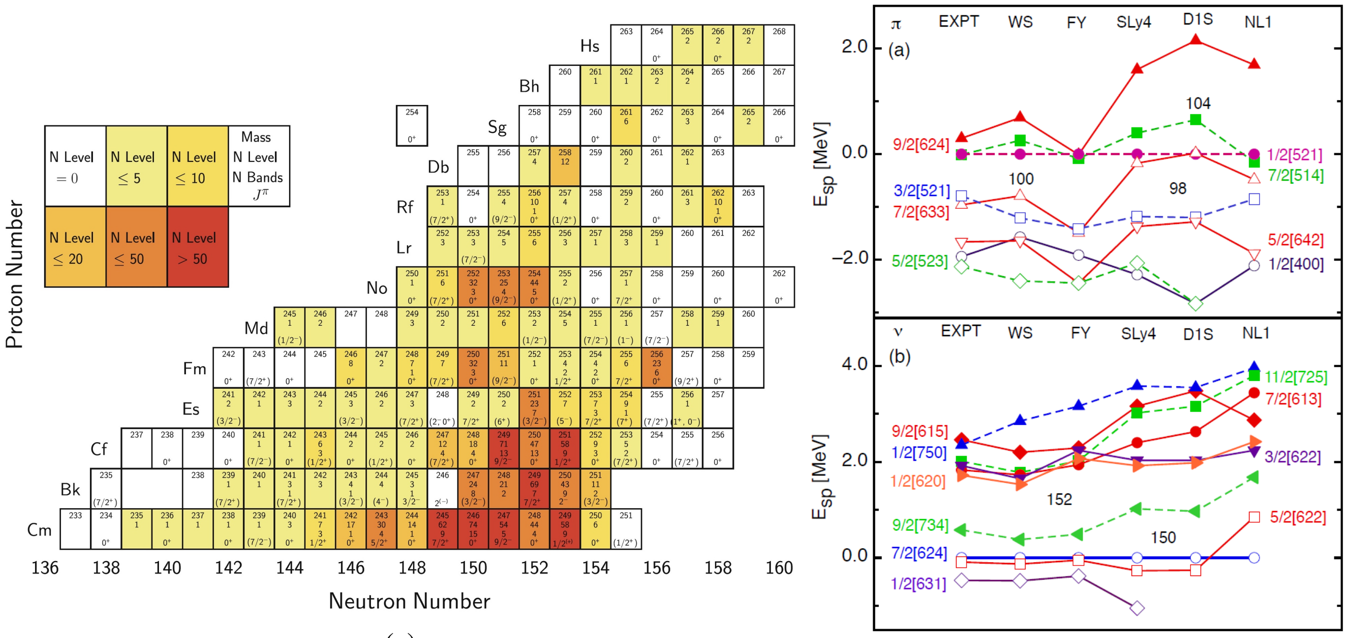

(a)

(b)

Figure 1.5: a) Available experimental information for nuclei from Cm to Hs [7]. b) Single particle proton and neutron energies calculated by phenomenological models with Woods Saxon (WS) or Folded Yukawa (FY) potentials or by self-consistent mean field models using Skyrme (SLy4), Gogny (DS1) or relativistic interactions (NL1) [32].

of the experiment, the setup, and its characteristics determined using the GEANT4 Monte Carlo simulation toolkit are presented in chapter 4. Afterward, in chapter 5, first, brief historical accounts of ^{255}Rf and ^{251}No isotopes are presented. Then the ground-state alpha decay populating excited states in ^{251}No is explored. The techniques followed to obtain the observables such as alpha decay and gamma branching ratios, internal conversion coefficients are also discussed. After that, the experimental findings related to the isomeric states observed in ^{255}Rf are presented with possible interpretations and the methodology followed to support our claims. Finally, the study is concluded in chapter 6.

Chapter 2

Theoretical Overview

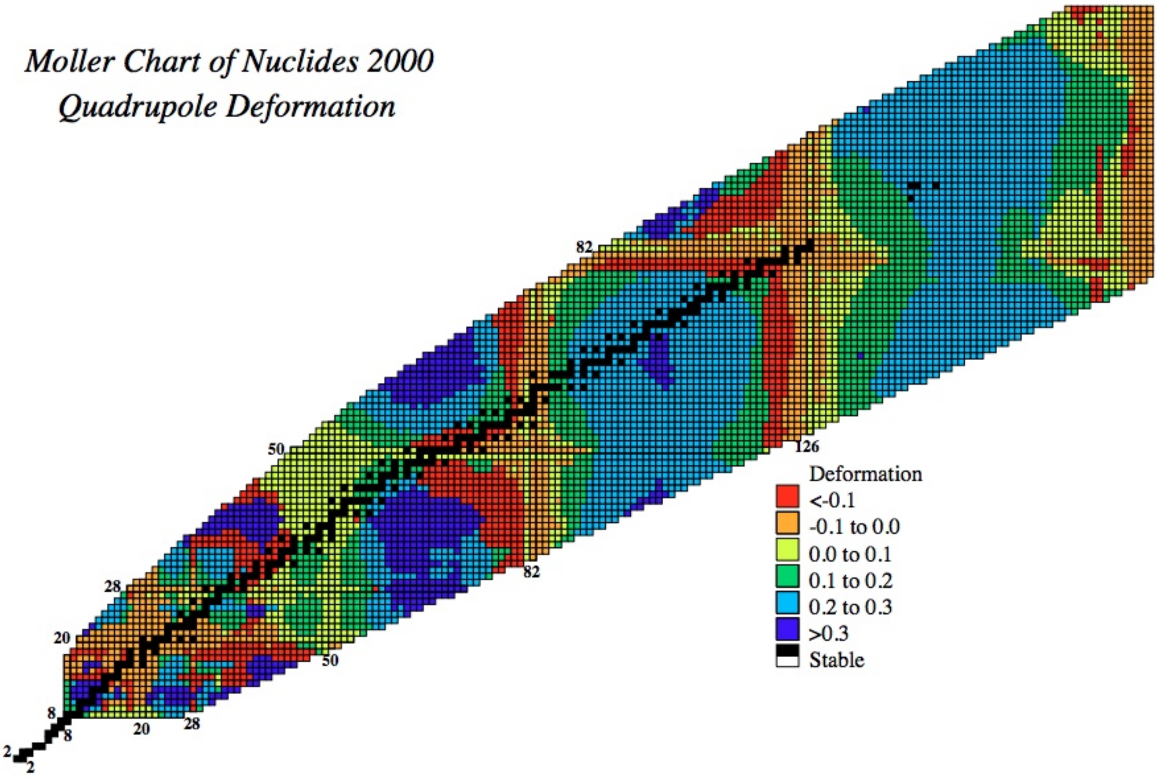

Figure 2.1: Nuclear colour-coded chart showing calculated values of the quadrupole deformation. The blue areas correspond to the regions of prolate shapes [44].

2.1 Macroscopic models

Macroscopic properties such as binding energy, shape, and nuclear stability are emergent properties of the complex nuclear systems. Emergent properties are seen everywhere from ripples in water to cosmic structures. An individual entity never show these aspects on its own. These properties only appear when the parts interact with one another in the whole ensemble. Hence the emergent behaviors are collective behaviors. The correlated motions of many nucleons in different orbitals in the microscopic theories can manifest dynamic properties such as surface vibrations, rotations, or a combination of both. Some form of order appears in the seeming chaotic motions of many particles. Many interesting nuclear emergent properties are expected as we go higher in mass numbers. From a simple hypothesis, one can say that the number of collective behavior is proportional to the number of interactions between the system's components. In the nuclear landscape, the properties that are observed in one mass region may not be evident in the other parts of the chart. Fig. 2.1 shows one such example where quadrupole deformations of nuclei are plotted across the whole nuclear landscape. In the following sections, the macroscopic models which treat nuclei as a whole are briefly described.

2.1.1 The Liquid Drop Model (LDM)

Historically, LDM is the first model to describe different nuclear properties and was conceived based on few observational facts: the saturation property of the nuclear forces and evidence of low compressibility and a well-defined surface by a nucleus. In this model, a nucleus is viewed as an incompressible drop of nuclear fluid resembling an ordinary liquid drop, with nucleons behaving like molecules in a liquid. Interestingly, before the discovery of the neutron in 1932 by J. Chadwick [45], G. Gamow in 1929 proposed the LDM [46], hypothesizing that nuclei are composed of alpha particles. Later, based on this model C. F. v. Weizsaecker in 1935, first introduced the semi-empirical mass formula [47]. It was followed by numerous similar attempts to explain the binding energies, and many semi-empirical mass formulae had emerged. The most commonly used one is that of Bethe and Weizsaecker given by the following equation [48]:

$$B(N,Z) = a_V A + a_S A^{2/3} + a_C \frac{Z^2}{A^{1/3}} + a_{sym} \frac{(N-Z)^2}{A} - a_P A^{-3/4} \quad [MeV] \tag{2.1}$$

where, the coefficients are determined empirically from a fit to experimental data: $a_V = -15.68$, $a_S = 18.56$, $a_C = 0.717$, $a_{sym} = 28.1$ and

$$a_P = \begin{cases} 34 & \textit{for e-e nuclei.} \\ 0 & \textit{for e-o nuclei.} \\ -34 & \textit{for o-o nuclei.} \end{cases}$$

Each term in the equation have different theoretical justifications and named as such. The volume term reflects the characteristics of strong nuclear force such as short-range and charge independence. The surface term introduces a correction to the volume term as the nucleons close to the surface contribute less to the binding energy. The Coulomb term includes the decrease in the binding energy due to the repulsion of the protons. The symmetry energy or Pauli term comes from the imbalance between the neutron and proton numbers, causing the system energy to be higher than what would be for N = Z. Finally, the pairing energy term is because of the spin-coupling of like particles. The system would have lower energy if an equal number of spin up and spin down of each kind of nucleons are there.

The binding energy appears from the mass difference between the mass a nucleus and the total mass of its constituents. The average binding energy per nucleon (see fig. 2.2a) increases with mass number, reaching a maximum about 8.8 MeV at mass number $A \sim 60$. It trends downwards gently beyond this point with increasing mass and atomic numbers as the Coulomb repulsion compete with the attractive

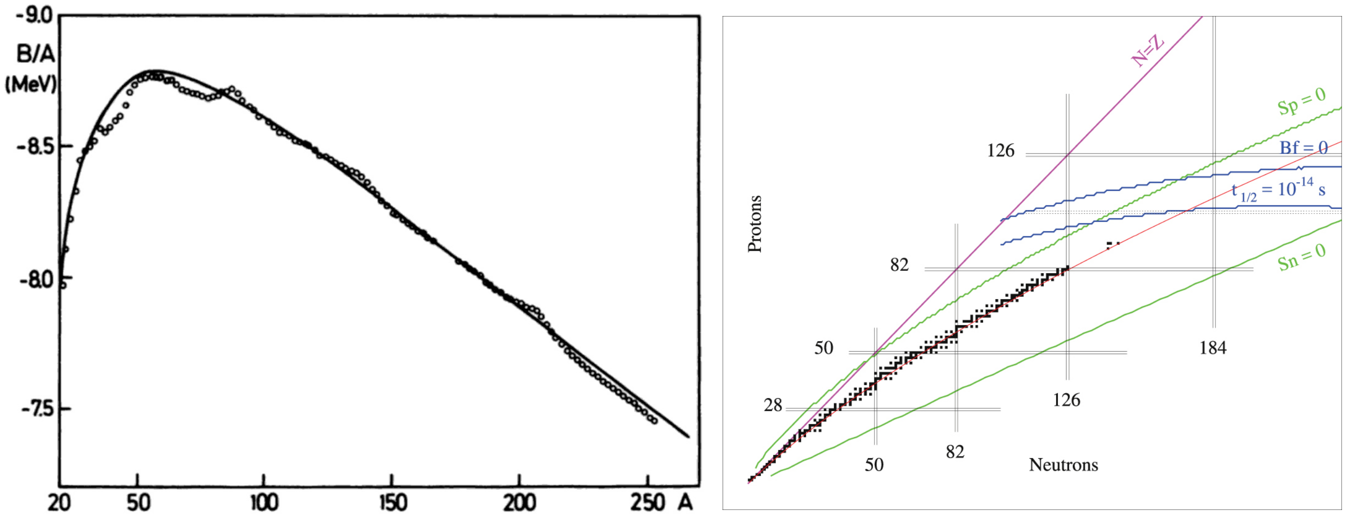

(a)

(b)

Figure 2.2: a) Binding energy per nucleon calculated using a mass formula (curve) over the experimental values for β-stable odd-A nuclei (○) [48]. b) LDM limits of stability drawn on the nuclear chart. The proton and neutron drip lines are indicated by green lines. The vanishing fission barrier and spontaneous fission half-life of 10^{-14} s are indicated by blue lines. The red line corresponds to the beta-stability line [12].

nuclear force. The approximate constant nature of the curve is a clear indication of the saturation property of the nuclear force. In the vicinity of proton and/or neutron magic numbers and also in very deformed nuclei, large deviations of the overall fit on the binding energy as a function of A are noticeable. These local inconsistencies are attributed to the nuclear shell effects [48].

Using the semi-empirical mass formula the limiting contours on the nuclear chart can be drawn that define the existence of nuclei (see fig. 2.2b). The proton and neutron separation energies defined as

$$S_p = B(A, Z) - B(A-1, Z-1)$$

$$S_n = B(A, Z) - B(A-1, Z)$$

set limits on the stability at the proton and neutron drip lines, where $S_p = 0$ and $S_n = 0$ respectively. The drip lines denote the proton and neutron numbers at which the strong force fails to keep the nuclei bounded ending nuclear existence. The nuclear landscape is also bounded at the top (heavy mass region) because of the strong Coulomb repulsion among the protons that tend to deform nuclear drops making them unstable against fission. This upper limit on Z against the spontaneous fission occur when the fission barrier vanishes $B_f = 0$ (see section 3.2).

2.1.2 The Collective model

In a dynamical LDM, the oscillations on the surface of a spherical drop are usually parametrized by

$$R(\theta, \phi, t) = R_0 \left(1 + \sum_{l=0}^{\infty} \sum_{m=-l}^{l} a_{lm}(t) Y_{lm}(\theta, \phi) \right) \tag{2.2}$$

where, $R(\theta, \phi, t)$ is the distance between the center of the nucleus to the surface at angles (θ, ϕ) at time t, R_0 is radius of the nucleus if it was a sphere, $R_0 = r_0 A^{1/3}$ with $r_0 = 1.2$ fm, $Y_{lm}(\theta, \phi)$ are the spherical harmonic functions of degree l and order m, and a_{lm} are the expansion coefficients. The monopole term a_{00} corresponds to a change in the nuclear volume [49], and the dipole terms $l = 1$ correspond to a translation of the whole system. Hence, they are excluded from equation 2.2 when small deformations are considered. The quadrupole term $l = 2$ was found to play a dominant role in nuclear spectroscopy. In this case, nuclei have either a prolate or an oblate deformation. A prolate spheroid has one major- and two minor-axes and an oblate spheroid has two major- and one minor-axis. The $l = 3$ terms are responsible for pear shapes and octupole collectivity in nuclei. For a pure quadrupole deformed system at a given time t, eq. 2.2 becomes

$$R(\theta,\phi) = R_0\left(1 + \sum_{m=-2}^{2} a_{2m}Y_{2m}(\theta,\phi)\right) \tag{2.3}$$

In a rotational transformation from a laboratory frame to the body fixed frame, the five parameters for quadrupole deformations a_{2m}, $-2 \le m \le 2$ are reduced to two, a_{20} and $a_{22} = a_{2-2}$ ($a_{21} = a_{2-1} = 0$) (related to the intrinsic shape), which together with three Euler angles (corresponding to its instantaneous orientation in space) describe the whole system [48,49]. Using the Hill-Wheeler polar coordinates [50] β ($\equiv$ deformation magnitude) and γ ($\equiv$ shape parameter) that are related to the quadrupole deformation parameters by (first introduced by A. Bohr)

$$a_{20} = \beta cos(\gamma)$$
$$a_{22} = \frac{1}{\sqrt{2}}\beta sin(\gamma)$$

the increments of the three semi axes in the body fixed frame are given by:

$$\delta_{R_i} = R_0\sqrt{\frac{5}{4\pi}}\beta cos(\gamma - \frac{2\pi}{3}i) \quad i = 1,2,3. \tag{2.4}$$

The nucleus has a prolate shape if $\gamma = 0°, 120°, 240°$ with the 3, 2 and 1 axes as the symmetry axes and has corresponding oblate shapes if $\gamma = 180°, 300°, 60°$ [48]. In the axially symmetric case, β can be derived from the above equation

$$\beta = \frac{4}{3}\sqrt{\frac{\pi}{5}}\frac{\delta R}{R_0} \tag{2.5}$$

where δR is the difference between the major axis and the axis of the spheroid. It follows from this equation that, $\beta = 0$, $\beta > 0$ and $\beta < 0$ for no, prolate and oblate deformation respectively. Typically for a normal deformation $\beta \approx 0.2 - 0.3$ and nuclei with $\beta \approx 0.4 - 0.6$ are called superdeformed nuclei. Another deformation parameter ϵ is common in literature which is related to the β parameter by

$$\epsilon = \frac{\delta R}{R_0} = 0.946\beta \tag{2.6}$$

In the cases when the γ parameter has intermediate values, the nuclei have triaxial deformation.

2.1.3 Rotations and Vibrations

Vibration

The low lying excitations produce small oscillations around the spherical shape ($a_{lm} = 0$). The Collective Hamiltonian of the form of a harmonic oscillator is expressed as [48,51,52]

$$H_{coll} = T + V = \frac{1}{2}\sum_{l\geq 2}\sum_{m}(B_l|\frac{da_{lm}}{dt}|^2 + C_l|a_{lm}|^2)$$

where, B_l and C_l are the mass and stiffness parameters with $\omega_l = \sqrt{C_l/B_l}$. These parameters are calculated from the classical hydrodynamical model with an assumption that the nuclear matter has an irrotational flow and uniform charge distribution inside the nucleus. They are expressed as

$$B_l = \frac{3}{4\pi l} A m R_0^2 \tag{2.7}$$

$$C_l = (l-1)(l+2)R_0^2\sigma - \frac{3(l-1)}{2\pi(2l+1)}\frac{(Ze)^2}{R_0} \tag{2.8}$$

where, m is the nucleon mass, and σ, the surface tension per unit area which is related to the coefficient a_S in eq. 2.1 by $\sigma = \frac{a_S}{4\pi r_0^2}$.

The quantized form of this collective Hamiltonian is given by

$$\mathbf{H_{coll}} = \frac{1}{2}\sum_{l\geq 2}\sum_{m} \hbar\omega_l(\mathbf{b^\dagger_{lm}}\mathbf{b_{lm}} + \frac{1}{2}) \tag{2.9}$$

where, $\mathbf{b^\dagger_{lm}}$ and $\mathbf{b_{lm}}$ creates and destroys phonons of multipole l and obey Bose commutation rule

$$[b_{l'm'}, b^\dagger_{lm}] = \delta_{ll'}\delta_{mm'}.$$

A multiphonon state is achieved by acting $b^\dagger$ onto the ground state which has no phonon $b_{lm}|0>= 0$. Using angular momentum coupling rules the vibration spectrum is obtained. In the case of quadrupole vibration, $l = 2$, we have two types of vibrations . The β-vibrations are the shape oscillations along the symmetry axis which preserve the axial symmetry. In the γ-vibrations, the axial symmetry is no longer preserved (see fig. 2.3).

Rotation

Nuclei having stable ground state deformation can exhibit collective rotations, which can be described by time-dependent parameters $a_{lm}(t)$ in the laboratory frame. Excitations of the system are the rotations and small oscillations around this ground-state equilibrium deformation. Restricting to quadrupole deformation only and transforming to the body-fixed frame which shall be denoted by 123 axes, the Hamiltonian is

$$H(\beta,\gamma) = T(\beta,\gamma) + V(\beta,\gamma) \tag{2.10}$$

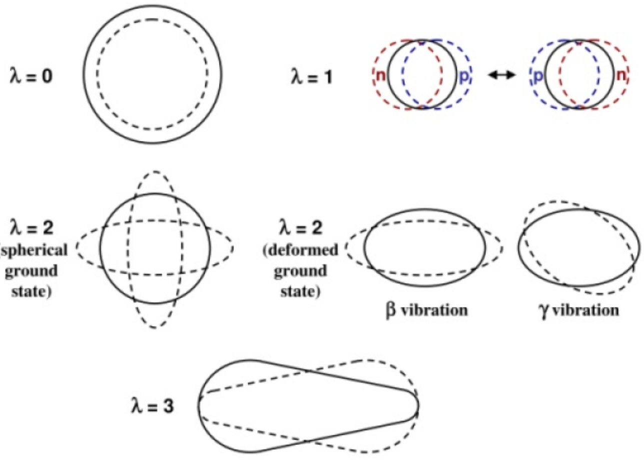

Figure 2.3: A schematic of the lowest order vibration modes [53].

with potential energy expanded around the equilibrium position ($a^{\circ}_{20}, a^{\circ}_{22} = a^{\circ}_{2-2}$)

$$V(\beta,\gamma) = \frac{1}{2}C_{20}[a_{20}(\beta,\gamma) - a^{\circ}_{20}]^2 + C_{22}[a_{22}(\beta,\gamma) - a^{\circ}_{22}]^2 \tag{2.11}$$

and the kinetic energy of the system

$$T(\beta,\gamma) = T_{rot}(\beta,\gamma) + T_{vib}(\beta,\gamma) \tag{2.12}$$

with

$$T_{rot}(\beta,\gamma) = \frac{1}{2}\sum_{i=1}^{3}\mathcal{J}_i\omega_i^2 \tag{2.13}$$

where i represents an axis in the body-fixed frame, ω_i is the angular velocity around the axis i and $\mathcal{J}_i$ is the moment of inertia

$$\mathcal{J}_i = 4B_2\beta^2 sin^2(\gamma - \frac{2\pi}{3}i) \quad i = 1,2,3. \tag{2.14}$$

Using eq. 2.7, it becomes

$$\mathcal{J}_i^{irr} = \frac{3}{2\pi}mAR_0^2\beta^2 sin^2(\gamma - \frac{2\pi}{3}i) \quad i = 1,2,3. \tag{2.15}$$

which is different from the moment of inertia of a rigid body with same deformation (see fig. 2.4 for an illustration)

$$\mathcal{J}_i^{rig} = \frac{2}{5}mAR_0^2(1 - \sqrt{\frac{5}{4\pi}}\beta cos(\gamma - \frac{2\pi}{3}i)) \quad i = 1,2,3 \tag{2.16}$$

and experimental value [48]

$$\mathcal{J}^{exp} \approx \frac{\beta^2A^{7/3}}{400} \quad [MeV^{-1}] \tag{2.17}$$

measured from the first 2^+ state of a rotational band. In well deformed nuclei ($\beta \sim 0.2 - 0.4$), it is found that the flow within the nuclei is neither irrotational nor of a rigid rotor.

$$\mathcal{J}^{irr} < \mathcal{J}^{exp} < \mathcal{J}^{rig}$$

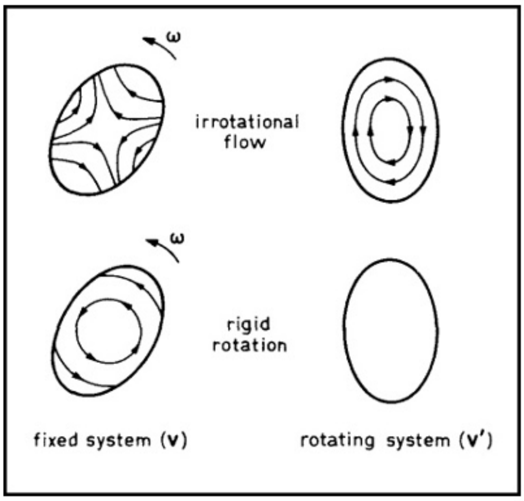

Figure 2.4: Schematic of flow patterns for rotation of an ellipsoidal body [54].

Since, the components of the total angular momentum I along the intrinsic axes are $I_i = \mathcal{J}_i\omega_i$, the rotational kinetic part can be expressed as

$$T_{rot} = \sum_{i}^{3}\frac{I_i^2}{2\mathcal{J}_i} \tag{2.18}$$

The vibrational part is given by

$$T_{vib} = \frac{1}{2}B_2(\dot{\beta}^2 + \beta^2\dot{\gamma}^2) \tag{2.19}$$

The quantized form of the collective quadrupole Hamiltonian in the formalism of A. Bohr is given by

$$H = \sum_{i=1,2,3}\frac{I_i^2}{2\mathcal{J}_i} - \frac{\hbar^2}{2B_2}[\frac{1}{\beta^4}\frac{\partial}{\partial\beta}\beta^4\frac{\partial}{\partial\beta} + \frac{1}{\beta^2}\frac{1}{sin3\gamma}\frac{\partial}{\partial\gamma}sin3\gamma\frac{\partial}{\partial\gamma}] + V(\beta,\gamma) \tag{2.20}$$

with volume element $d\tau = \beta^4|sin3\gamma|d\beta d\gamma d\Omega$.

In a symmetric rigid rotor with the 3-axis being the symmetry axis, we assume that the potential energy surface has a deep deformed axially symmetric minimum at $(\beta_0, 0)$. The Hamiltonian is approximated using $\mathcal{J}_1(\beta_0, 0) = \mathcal{J}_2(\beta_0, 0) = \mathcal{J}_0$ taking only the 0th order expansion term. The higher-order terms couple rotations and vibrations and can be neglected in an attempt to decouple the rotational motions from vibrations. The only remaining rotation vibration coupling term in the Hamiltonian is $\frac{I_3}{2\mathcal{J}_3}$ that cannot be expanded. The approximated rotational energy is

$$T'_{rot} = \frac{I^2 - I_3^2}{2\mathcal{J}_0} \tag{2.21}$$

The energy spectrum is obtained by solving the eigenvalue problem

$$(H_{rot} + H_{vib})|\psi(\beta, \gamma) > \quad = E|\psi(\beta, \gamma) > \tag{2.22}$$

where, the rotational band is seen to be superimposed on each vibrational state (n_β, n_γ).

$$E(I) = E(0) + \frac{\hbar^2}{2\mathcal{J}_0}(I(I+1) - K^2) \tag{2.23}$$

with,

$$E(0) = \hbar\omega_\beta(n_\beta + 1/2) + \hbar\omega_\gamma(2n_\gamma + 3/2 + 1/2(|K| - 1))$$

where, $\omega_\beta = \sqrt{C_{20}/B_2}$ is the frequency and n_β is the number of phonons of β-vibration, similarly, $\omega_\gamma = \sqrt{C_{22}/B_2}$ is the frequency and n_γ is the number of phonons of γ-vibration and $K \leq I$ is the projection of the angular momentum on the symmetry axis (see fig. 2.5). Only even values of K are allowed from rotational symmetry around 1 and 2-axes by 180° (see ref. [48, 49]) and the spin sequence for $K \neq 0$, is $I = |K|, |K| + 1, |K| + 2, ...$ and when $K = 0$, it is $I = 0, 2, 4, ...$

2.2 Microscopic models

Nuclei are strongly interacting many-body fermionic systems. It is the interactions between the bodies and the intricate motions of the particles that make the n-body problem extraordinarily complex or even

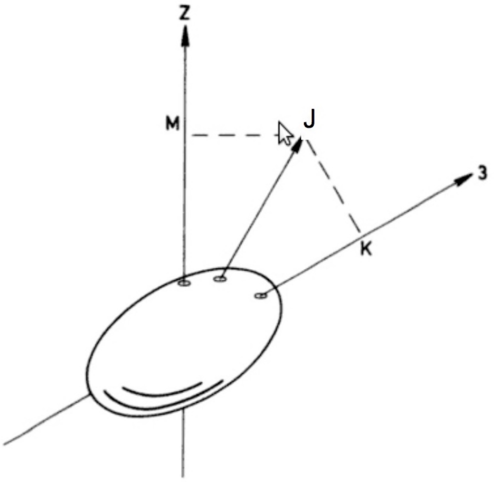

Figure 2.5: An illustration of the projection K of the angular momentum J on the symmetry axis in the intrinsic frame (1,2,3 axes) [54].

unsolvable exactly. The general many-body nuclear Hamiltonian that describes the nucleus in terms of nucleonic degrees of freedom and their interactions is given by

$$\hat{H} = \sum_{i=1}^{A} T_i + \sum_{i<j} \hat{V}(i, j) + \sum_{i<j<k} \hat{V}(i, j, k) + ... \tag{2.24}$$

where T_i is the kinetic energy term, $V(ij)$ and $V(ijk)$ are the 2, 3 body forces, and i represents all the coordinates (position, spin, isospin) of the i^{th} nucleon besides being the particle index number.

2.2.1 Mean-Field approach

Restricting to 2-body interactions and neglecting relativistic effects the nuclear many-body Hamiltonian is

$$\hat{H} = \sum_{i=1}^{A} \frac{\hat{p}_i^2}{2m} + \sum_{i=1}^{A} \sum_{j>i}^{A} \hat{V}(i, j) \tag{2.25}$$

In the mean-field approach, the A-body system of strongly interacting particles is approximated into weakly interacting quasiparticles with perturbative residual interactions between them. The residual interactions are often ignored, and the particles are treated as non-interacting independent particles moving in an average potential well $\hat{U}$ created by the other nucleons. In this approximation

$$\hat{H} = \sum_{i=1}^{A} \left(\frac{\hat{p}_i^2}{2m} + \hat{U}(i) \right) + \sum_{i=1}^{A} \sum_{j>i}^{A} \left(\hat{V}_{ij} - \hat{U}(i) \right) = \hat{H}_{mf} + \hat{H}_{res} \tag{2.26}$$

where $\hat{U}(i)$ is the mean field felt by the ith nucleon created by the rest of the nucleons, $\hat{H}_{mf}$ is the mean-field Hamiltonian, which can be written as $\hat{H}_{mf} = \sum_{i=1}^{A} \hat{h}_i$ the sum of the Hamiltonian of individual particles, describing the motion of A nucleons independent of each other in the same average field and $\hat{H}_{res} = \hat{V}_{res}$, the remaining residual interactions that generate correlations in the nucleus. The states in the phase space are obtained by solving the Schrodinger equation

$$\hat{H}_{mf} \Psi(1, 2, ..., A) = E \Psi(1, 2, ..., A) \tag{2.27}$$

which can be decomposed into

$$\sum_{i=1}^{A} \hat{h}_i \psi_{k_i}(i) = \sum_{i=1}^{A} \epsilon_{k_i} \psi_{k_i}(i) \tag{2.28}$$

Using the Hartree product, the A-body wave function is written as $\Psi(1, 2, ..., A) = \prod_i^A \psi_{k_i}(i)$ with corresponding energy eigenvalue $E = \sum_{i=1}^{A} \epsilon_{k_i}$. To fulfill the Pauli principle for identical nucleons, fully antisymmetrized wave functions called Slater determinants are used as defined in equation 2.29.

$$\Psi(1, 2, ..., A) = \frac{1}{A!} \begin{vmatrix} \psi_{k1}(1) & ... & \psi_{k1}(A) \\ ... & ... & ... \\ \psi_{kA}(1) & ... & \psi_{kA}(A) \end{vmatrix} \tag{2.29}$$

In the occupation number representation, the creation $a^\dagger$ and the annihilation a operators are responsible for creating and destroying a particle with wavefunction ψ_k in the level k. These operators obey Fermi's commutation laws. When the system is excited, the transfer of nucleons occurs from levels below the Fermi level to the levels above it. They are represented by particle-hole ph state (particles above the

Fermi level and holes below it) $|\Psi_{mi}>= a^{\dagger}_{m}a_i|\Psi_0>$ with an excitation energy $\epsilon_{mi} = \epsilon_m - \epsilon_i$, where m correspond to a level above the Fermi level and i to a level below it and $|\Psi_0>$, the ground state. In the quasiparticle picture (see section 2.2.5), the ground state represents the vacuum $\alpha_k|\Psi_0>= 0$, and ph states are two-quasiparticle states.

In the mean-field approximation, the complicated many-nucleon problem is transformed into a simpler one-body problem, perhaps solvable exactly depending on the form of the mean potential. The mean-field potential is chosen in such a way that it minimizes the residual interaction between the quasiparticles. The residual interaction can then be either neglected or treated as a perturbation. Sometimes, the residual interaction is not so residual after all, whose effects are manifested as pairing correlations, collective oscillations of the mean-field, etc. Realistic (best) average potentials can be determined from variational techniques such as the Hartree Fock method using an effective interaction, for example, Skyrme force, Gogny force, relativistic mean-field, etc. One can also use phenomenological potentials to a good approximation. In the following subsections, such phenomenological mean field models will be discussed.

2.2.2 The Spherical Shell Model

The shell model was motivated by the experimentally known magic numbers of nucleons 2, 8, 20, 28, 50, 82, 126 at which the nuclei are more stable than other nuclei analogous to atomic inert gas configurations. The shell model treats every nucleon to be independent of one another held together by an average spherically symmetric potential created by themselves. The most commonly used ad hoc potential is the Woods-Saxon potential [55].

$$V(r) = -V_0\left[1 + \exp\left(\frac{r - R_0}{a}\right)\right]^{-1} \tag{2.30}$$

with $R_0 = 1.2A^{1/3}$ fm is the nuclear radius, $V_0 \approx 50\,\text{MeV}$ depth of the potential and $a \simeq 0.5\,\text{fm}$ the diffuseness parameter of the nuclear surface. The eigenfunctions of this realistic potential cannot be determined analytically. Hence, the infinite square well and harmonic oscillator potential well are used as approximations (see fig. 2.6 for the shapes of these potentials), which serve as the limits for the realistic potential (as pointed out by M. Goeppert-Mayer and J. Hans D. Jensen in 1950). The energy levels are obtained by solving the one-body Schrodinger equation for each case and the realistic single-particle energy levels are determined from interpolation between the two limiting cases for each level. The simple harmonic potential (SHO) is given by

$$V(r) = -V_0 + \frac{1}{2}m\omega^2 r^2$$

with $\omega = \sqrt{2V_0/mR^2}$ and the infinite square well is

$$V(r) = \begin{cases} -V_0 & \text{for } r \leq R_0 \\ +\infty & \text{for } r > R_0 \end{cases}$$

Solving the Schrodinger equation for SHO potential

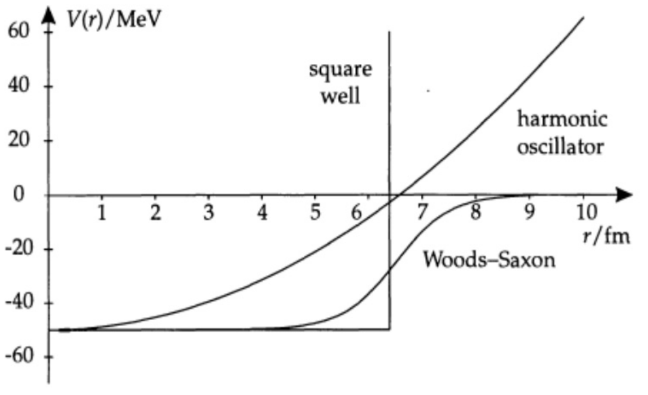

Figure 2.6: Most common phenomenological shell model potentials: square well, harmonic oscillator and Woods-Saxon.

$$\left[-\frac{\hbar^2}{2m}\Delta + V(r)\right]\phi_i(r) = \epsilon_i\phi_i(r)$$

we obtain

$$E_N = \hbar\omega(N + \frac{3}{2}); \quad N = 2n + l; \quad N = 0, 1, 2, ...; \quad l = N, N-2, ...1 \text{ or } 0; \text{ and } n = (N-l)/2 \qquad (2.31)$$

where, N is the principal quantum number which gives the number of oscillator quanta, n, the radial quantum number corresponds to the number of nodes in the radial part of the wavefunction, l is the orbital quantum number. The degeneracy for each N is $(N+1)(N+2) = \sum_l 2(2l+1)$, where, for each l there are $(2l+1)$ projections of m_l (because of spherical symmetry m_l values are not identifiable hence they are degenerate) and the factor 2 is due to 2 spin states. The relation $l = N - 2n$ allows l values to be either even or odd for a given quantum number N, consequently the parity $\pi = (-1)^l = (-1)^N$. The harmonic oscillator states are labeled by the (nlj) quantum numbers with spectroscopic notation s, p, d, f, g, h,... for l = 0, 1, 2, 3, 4, 5,...

Both these potentials fail to explain the magic number sequence beyond 20. This was solved by adding to the Hamiltonian a phenomenological attractive potential associated with the coupling of the intrinsic spin s and the orbital momentum l of a nucleon, having the form $U(r)(\hat{l}.\hat{s})$, where $U(r) = \lambda\frac{1}{r}\frac{dV}{dr}$ with $\lambda \simeq -0.5\,\text{fm}^2$. The term l.s can be written as

$$\hat{l}.\hat{s} = \frac{1}{2}(\hat{j}^2 - \hat{l}^2 - \hat{s}^2), \quad \text{where} \quad \hat{j} = \hat{l} + \hat{s} \qquad (2.32)$$

This potential breaks the degeneracy by $j = l \pm \frac{1}{2}$, pushing $l + 1/2$ levels energetically below the $l - 1/2$ levels with a separation gap proportional to $(2l+1)$ in a given oscillator shell. For $l > 3$, the energy splitting between the $l + 1/2$ and $l - 1/2$ can be large enough to lower the $l + 1/2$ state from one oscillator shell (N) to the shell below (N-1). Such states are known as intruder states which have parity opposite to the states of the shell they occupy (see fig. 2.7).

Instead of the interpolation method, a more practical method to achieve the desirable effect was introduced by S.G. Nilsson i.e. to add another attractive potential $\propto l^2$ to the SHO potential. The final mean

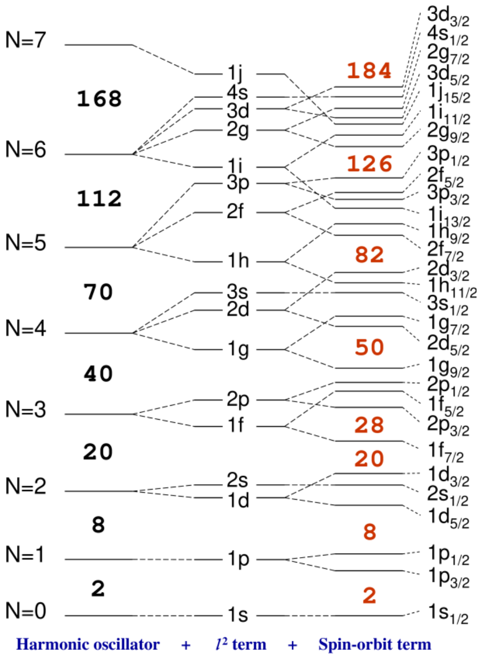

Figure 2.7: Single particle energy levels for the modified oscillator potential. The “magic numbers” indicated with red color are obtained after adding l^2 and spin-orbit terms to the potential [53].

field potential has then the form:

$$V(r) = \frac{1}{2}m\omega^2 r^2 + C\hat{l}.\hat{s} + D\hat{l}^2 \tag{2.33}$$

The shell model describes the single-particle orbits of every nucleon in a nucleus. The nucleons occupy the energy states in ascending order starting from the lowest level while obeying the Pauli exclusion principle. With an assumption that due to pairing of nucleons, only the unpaired nucleon would describe the total state of the nucleus that one observes experimentally. This is because of the short-range residual interaction that couple two nucleons in the orbits $|jm>$ and $|j{-}m>$ (which have biggest overlap in the wave functions hence large interaction energy) to $I^+ = 0$. Besides its success in reproducing the magic numbers, the model manages to predict the ground-state and excited-state spin and parities in many nuclei accurately. The model also describes magnetic moments, isomeric states, beta decay systematic. Although the shell model is quite successful in describing the light, spherical and near-spherical nuclei (in which the number of nucleons outside closed-shell is small), it fails to describe nuclei if the number of valence nucleons is large because the residual interactions between them can make their motions collective. In some cases, the nuclei can become permanently deformed if these collective effects are large enough to lower the systems' energy in deformed shapes than in their corresponding spherical shapes. Hence, the shell model cannot explain the origin of rotational and vibrational spectra observed in heavy nuclei because it assumes that the nucleons move in a spherically symmetric potential. And, quantum-mechanically a sphere cannot have collective rotation. For this reason, A. Bohr, B. Mottelson, and S. G. Nilsson constructed nuclear models with a deformed potential. In fact, the first failure of the shell model was identified in quadrupole moments of heavy nuclei (in 1949) which the shell model predicts to be much smaller than the measured value [56]. This led J. Rainwater (in 1950) to suggest that the nuclear shape, in this case, is not spherical but spheroidal [57].

2.2.3 The Deformed Shell Model

The detailed microscopic properties of the quantum system determine the equilibrium shape of the nucleus. In a deformed nucleus, the potential in which the nucleons move breaks the spherical symmetry. Nilsson assumed the potential to be that of an anisotropic harmonic oscillator (ellipsoidal shape). Hamiltonian of a nucleon in the body-fixed coordinate system is expressed as [58]:

$$\hat{H}_O = -\frac{\hbar^2}{2m}\Delta + \frac{m}{2}(\omega_x^2 x^2 + \omega_y^2 y^2 + \omega_z^2 z^2) \tag{2.34}$$

For an ellipsoidal potential ($\gamma = 0°$ and $R = R_0(1 + \beta Y_{20})$), with 3-axis as the symmetry axis and a deformation parameter δ, the angular frequencies are given by

$$\omega_x^2 = \omega_y^2 = \omega_0^2(\delta)(1 + \frac{2}{3}\delta) \tag{2.35}$$

$$\omega_z^2 = \omega_0^2(\delta)(1 - \frac{4}{3}\delta) \tag{2.36}$$

where,

$$\omega_0(\delta) = \mathring{\omega}_0(1 - \frac{4}{3}\delta^2 - \frac{16}{27}\delta^3)^{-1/6}, \quad \mathring{\omega}_0 = \omega_0(\delta = 0) \tag{2.37}$$

which comes from volume conservation

$$\omega_x \omega_y \omega_z = \mathring{\omega}_0^3 \tag{2.38}$$

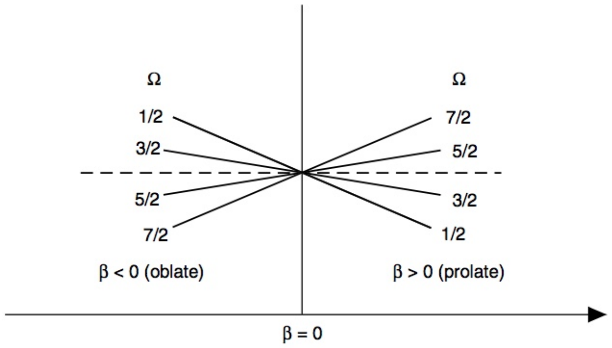

Figure 2.8: A schematic of splitting of levels as a function of deformation [59].

the deformation parameter δ is the ϵ of equation 2.6. The oscillator Hamiltonian is separated into a spherically symmetric term and particle deformation coupling term by introducing a dimensionless parameter:

$$r = \sqrt{\frac{m\omega_0}{\hbar}}r'$$

$$\hat{H}_O\phi = (\frac{1}{2}\hbar\omega_0(-\Delta + r^2) - \delta\hbar\omega_0\frac{4}{3}\sqrt{\frac{\pi}{5}}r^2Y_{20})\phi = (\mathring{H}_O + H_\delta)\phi = \epsilon_0\phi \tag{2.39}$$

The energy eigenvalues in cylindrical coordinates are given by

$$\epsilon_0 \simeq \hbar\mathring{\omega}_0\left((N + \frac{3}{2}) + \delta(\frac{N}{3} - n_z)\right), \quad N = n_x + n_y + n_z = 2n_\rho + n_z + \Lambda, \quad n = 0, 1, 2, 3, ...$$

N being the total number of oscillator quanta. The deformed eigenstates are characterized by $\Omega^\pi[Nn_z\Lambda]$ where $\Omega = \Lambda + \Sigma$, $\Sigma = \pm 1/2$ and Λ are the projections of intrinsic spin and orbital angular momentum l on the symmetry axis and the parity of the orbit $\pi = (-1)^l = (-1)^N$.

By introducing new parameters $\kappa = -\frac{C}{2\hbar\mathring{\omega}_0}$ and $\mu = \frac{2D}{C}$, the Nilsson Hamiltonian is expressed as:

$$\hat{H}_{Nilsson} = \hat{H}_O + \hat{H}_\delta - 2\hbar\mathring{\omega}_0\kappa(\hat{l}.\hat{s} + \mu(\hat{l}^2 - < \hat{l}^2 >_N)) \tag{2.40}$$

$$= \hat{H}_O + C\hat{l}.\hat{s} + D(\hat{l}^2 - < \hat{l}^2 > N) \tag{2.41}$$

where κ and μ are adjusted such that the sequence of levels are reproduced for $\delta = 0$ and $< \hat{l}^2 >= \frac{1}{2}N(N+3)$ is the expectation value of $\hat{l}^2$ in a major shell N. Because of deformation the $(2j + 1)$ degeneracy of each level for zero deformation is broken into two-fold degenerate states $\pm\Omega$ i.e. a j state split into $(j + 1/2)$ levels (see fig. 2.8). Also, only parity and eigenvalue Ω remain good quantum number. No two levels with the same quantum numbers Ω and π can cross because they repel each other, only levels with different Ω or π can cross. The ground state spin and parity of an odd nucleus can then be determined by the unpaired nucleon likewise in the spherical shell model. From the fig. 2.8, it can be seen that a prolate shape is favored in the lower or mid-level single neutron and single proton energies of their respective shells, whereas in the upper portions, an oblate shape is preferred. But interestingly, more prolate than oblate nuclei are observed. The fundamental origin of the preference of prolate shape over oblate is still an open question. There are several explanations available: 1) the strength of the spin-orbit potential plays a crucial role in determining this predominance [63] 2) the collective effect of the surface and Coulomb terms in eq. 2 cause a significant number of nuclei to acquire energetically-favored prolate shapes [64].

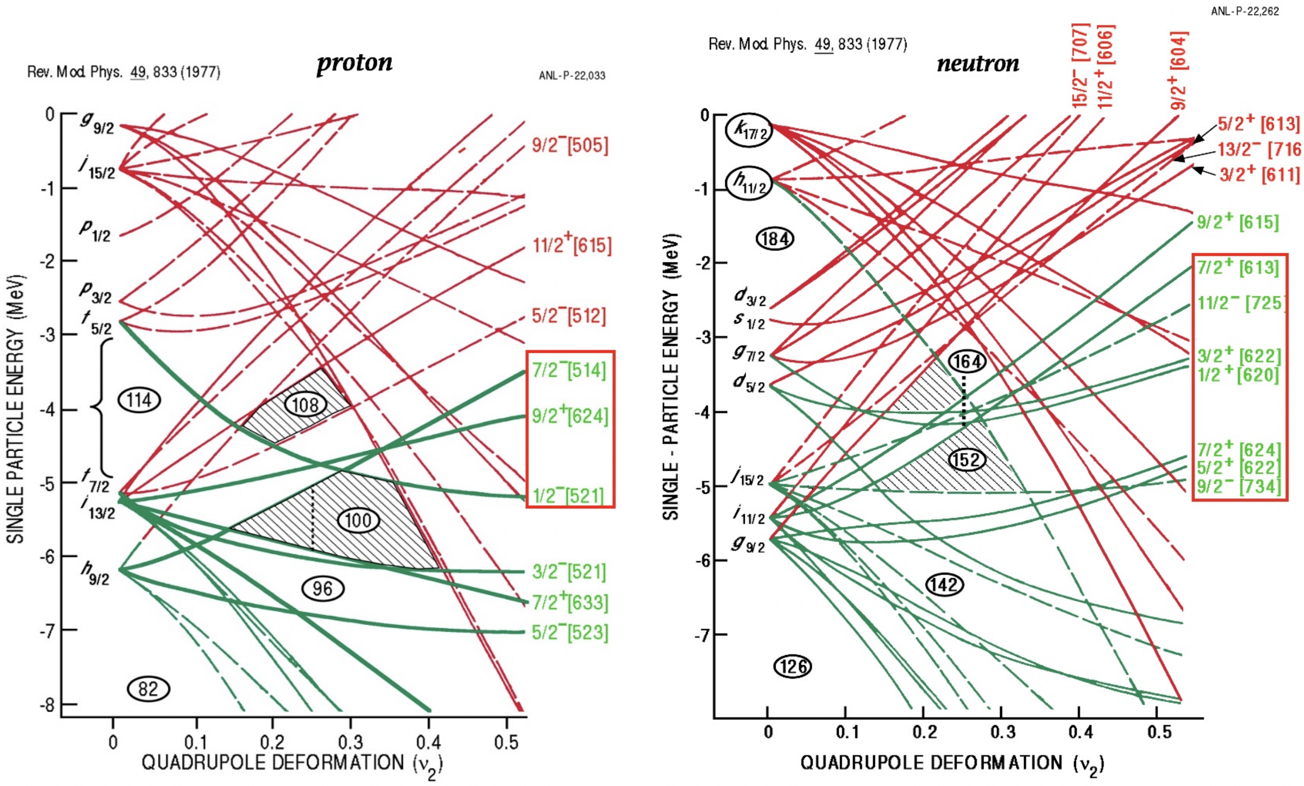

Figure 2.9: Proton and neutron single-particle levels obtained from momentum dependent Woods-Saxon potential with universal parameters as a function of quadrupole deformation, ν_2 [60]. The orbitals around ^{254}No (Z = 102, N = 152) relevant to this work are highlighted with red squares.

Fig. 2.9 shows calculated proton and neutron single-particle states for actinides as a function of quadrupole deformation $\nu_2 = \beta$ in a momentum dependent Woods-Saxon potential [60]. The relevant single-particle orbitals for this study are highlighted around Z = 102, and N = 152. The observation of rotational bands in nuclei around ^{254}No is a proof that these heavy nuclei are permanently deformed. For ^{255}Rf the predicted quadrupole deformation parameter is $\beta = 0.252$ and for ^{251}No it is $\beta = 0.25$. In fig. 2.9, around quadrupole deformation $\nu_2 \approx 0.25$, there are shell gaps of approximately 1 MeV at Z = 100 and N = 152. Such quadrupole deformations are also calculated with energy self-consistent density functional approaches using realistic interactions like SLy4 interaction (see fig. 2.10 [61]). Fig. 2.10 shows the calculated ground-state deformation energies and quadrupole deformations for even-even heavy and superheavy nuclei. It is clear from fig. 2.10b that the nuclei in the region of our interest are well deformed (prolate shaped) and in fact, the largest ground-state shape elongations are predicted around ^{254}No. It is because these nuclei gain in energy from deformation (see fig. 2.10a where the difference between the energies of the spherical and the deformed configurations for even-even nuclei above uranium are displayed) and become relatively stable as a result. From fig. 2.9, by virtue of paring the ground state of ^{255}Rf is defined by the last unpaired neutron and is predicted to have spin 9/2 and negative parity. This spin was confirmed experimentally through laser spectroscopy in the case of the isotone ^{253}No [65]. Similarly, the ground-state of ^{251}No (Z = 102, N = 149) is predicted to be 7/2^{+} which agrees well with the ground-state of N = 149 isotones derived from α-spectroscopy (see refs. [66, 189, 190]).

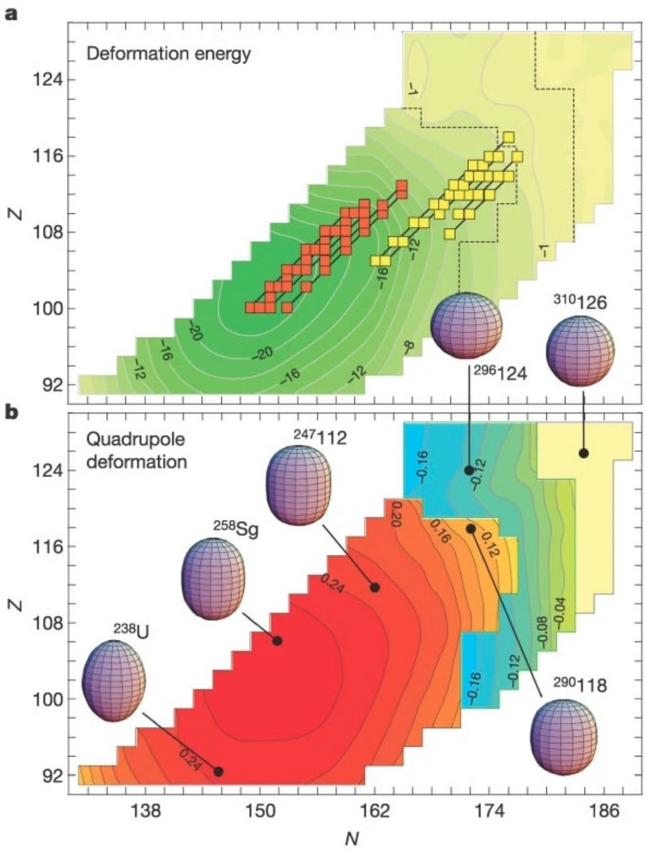

Figure 2.10: a) Deformation energy (in MeV) defined as a difference between the ground-state energy and the energy at the spherical shape. b) Predicted ground-state mass quadrupole deformation β and corresponding nuclear shapes: prolate shapes are coloured red–orange, oblate shapes are blue–green, and spherical shapes are light yellow [61, 62].

2.2.4 Cranked Shell Model

A nucleus rotating with a non-zero quadrupole moment can have rotational excitations, and because the potential is not symmetric, the angular momentum J is no longer a good quantum number. However, a Lagrange multiplier $-\omega.J$ can be added to the Hamiltonian. D. R. Inglis in 1954, introduced the microscopic theory of a rotating nucleus based on the semiclassical cranking model [67]. In this model, the nucleons move independently in an average unsymmetrical potential well that rotates with constant angular velocity ω around a fixed axis in space. The rotational axis is chosen to be along x-axis perpendicular to the symmetry axis (z-axis) with no collective rotation. The Hamiltonian in the rotating frame (known as cranking Hamiltonian or Routhian) is expressed as

$$H_\omega = H - \hbar\omega J_x = \sum_{i=1}^{A} h^i_\omega = \sum_{i=1}^{A} (h^i - \hbar\omega j^i_x) \tag{2.42}$$

where H is the sum of deformed single-particle Hamiltonians (in the laboratory frame) and the collective angular momentum J is taken as the sum of single-particle angular momenta with $J_x = \sum_{i=1}^{A} j^i_x$, the projection of total angular momentum on the rotational axis of the system in which $\vec{j} = \vec{l} + \vec{s}$ operators generate rotations. The cranking term $-\hbar\omega J_x$ corresponds to centrifugal and Coriolis forces appearing in the rotating frame. To get the energy in the laboratory frame one solves the eigenvalue problem

$$E(\omega) =< \Psi_\omega|H|\Psi_\omega >=< \Psi_\omega|H_\omega|\Psi_\omega > +\hbar\omega < \Psi_\omega|J_x|\Psi_\omega >= E(0) + \frac{1}{2}\mathcal{J}_1\omega^2 + ... \tag{2.43}$$

where $|\Psi_\omega >$ is the ground-state Slater determinant and ... refers to higher order expansion terms. As a function of the nuclear spin, it is expressed as

$$E(I) = E(0) + \frac{\hbar^2 I(I+1)}{2\mathcal{J}_1} \tag{2.44}$$

by including the zero point oscillations with the condition that $J(\omega) =< \Psi_\omega|J_x|\Psi_\omega >= \hbar\sqrt{I(I+1)} \approx \mathcal{J}_1\omega$.

The two-fold degeneracy ($\pm\Omega$) with respect to time reversal symmetry of Nilsson levels at $\omega = 0$ is broken by the Coriolis term $-\omega J_x$ for $\omega \neq 0$ as the Coriolis force has opposite signs based on whether the nucleons are moving in the same or opposite direction to the rotation of the nucleus. Both the levels correspond to eigenstates of the rotation operator $R_x = e^{i\pi j_x}$ with eigenvalues $r_x = \pm i$ known as the signature of the level. The total wavefunction remains unchanged for a system with even number of fermions and changes sign for an odd number of fermions A, which can be expressed as $R_x^2 = (-1)^A$. The signature quantum number α is defined as $r = exp(-i\pi\alpha)$. In terms of total nuclear spin I its value is $r = (-1)^I$ (Bohr and Mottelson 1975). Thus for system with even number of nucleons

$$r = +1 \quad (\alpha = 0) \quad I = 0, 2, 4, ...$$
$$r = -1 \quad (\alpha = 1) \quad I = 1, 3, 5, ...$$

while for an odd system:

$$r = -i \quad (\alpha = +1/2) \quad I = 1/2, 5/2, 9/2, ...$$
$$r = +i \quad (\alpha = -1/2) \quad I = 3/2, 7/2, 11/2, ...$$

where α is related to the total spin by $I = \alpha\, mod\, 2$ and to the particle number by $A = 2\alpha\, mod\, 2$. The only symmetry that H_ω conserve is the parity, hence the Routhian levels are often designated by (α, π).

The Coriolis and centrifugal forces affect the intrinsic structure of a rotating nucleus akin to the effect of the earth's rotation on the ocean currents and the weather patterns. Their effects are very strong for the configurations with high j and small Ω values causing Ω- mixing and alignment along the rotational axis. This can bring high lying orbits down in energy, possibly modifying the ground state structure band and may even open new shell closures at high angular momenta. This effect is frustrated in even nuclei by pairing forces that try to keep the particles in pairwise coupled orbits. The impact of the pairing force can be seen in the lower value of the experimentally derived moment of inertia $\mathcal{J}_{exp}$ than the calculated value $\mathcal{J}_{Inglis}$ [67] which is close to the rigid body value $\mathcal{J}_{rigid}$. The rotational motion tends to reduce the effective pairing force from the non-rotation value *i.e.*, an increase in the angular velocity ω would result in less pairing and consequently a larger moment of inertia [68]. By including higher-order perturbation terms in $H' = -\omega J_x$ than in the usual case where only up to second order is taken, the energy spectrum and the moment of inertia can be improved. Taking up to fourth-order term, the energy in the laboratory system can be written as

$$E(\omega) = E(0) + \frac{1}{2}\mathcal{J}(\omega)\omega^2 \tag{2.45}$$

with $\mathcal{J}(\omega) = \mathcal{J}_0 + 3C\omega^2$ and the expectation value of the angular momentum

$$< \Psi_\omega|J_x|\Psi_\omega >= \omega J(\omega) = \omega\left(\mathcal{J}_0 + 2C\omega^2\right) \tag{2.46}$$

The parameters $\mathcal{J}_0$ and C are called Harris parameters [69].

We notice that the rotational motion of a nucleus is not as simple as for a rigid body. For a perfect rotor, the rotational energy at spin I is $E = \frac{\hbar^2 I^2}{2\mathcal{J}}$. The variations in the moment of inertia due to changes in the internal structure of the nucleus are quantified using two types of moments of inertia called kinematic and dynamical moments of inertia. The kinematic moment of inertia is related to the overall motion of the nucleus, and expressed as the first derivative of the rotational energy to the spin.

$$\mathcal{J}^{(1)} = I_x \hbar^2 \left(\frac{dE(\omega)}{dI} \right)^{-1} = \hbar \frac{I_x}{\omega} \tag{2.47}$$

The dynamic moment of inertia is expressed as the second derivative

$$\mathcal{J}^{(2)} = \hbar^2 \left(\frac{d^2E(\omega)}{dI^2} \right)^{-1} = \hbar \frac{dI_x}{d\omega} \tag{2.48}$$

which is related to the torque and represents the rate of change of spin with frequency.

$$\mathcal{J}^{(2)} = \mathcal{J}^{(1)} + \omega \frac{d\mathcal{J}^{(1)}}{d\omega} \tag{2.49}$$

And the rotational frequency is derived from the relation

$$\hbar\omega = \frac{dE(I)}{dI_x} \tag{2.50}$$

For a rigid rotor,$\mathcal{J}^{(2)} = \mathcal{J}^{(1)}$ reflecting that there is no change in the internal structure due to rotation.

2.2.5 Pairing Correlations

The evidence of pairing was found in the odd-even staggering of nuclear masses in the early days of nuclear physics. M. Goeppert-Mayer in 1950 provided the theoretical explanation that the short-range part of the nucleon-nucleon interactions energetically favors ($J^+ = 0^+$) coupled pairs in a given shell j [70,71]. The most efficient way two neutrons (or two protons) moving in the nucleus can minimize their energy is by time-reversed motion in the same orbit having a maximal spatial overlap of their wavefunctions. The Pauli exclusion principle is violated if both nucleons in the same sense of motion have identical quantum numbers as oppose to the case in time-reversed motion, in which the magnetic quantum numbers, m, of the two nucleons have opposite signs. As a result, the net intrinsic angular momentum imparted to the nucleus is zero, and the nucleons are said to be paired. The pairing correlations become important if the energy gap between the major oscillator shells $\hbar\omega_0$ becomes equivalent or smaller than the residual interaction $< H_{res} >$. In light nuclei, $\hbar\omega_0 >> < H_{res} >$ hence, the Hartree Fock ground state remains stable and the excited states are well defined as independent particle-hole excitations [72]. However, for non-closed shell nuclei, the nucleon distribution in the ground state can lead to smaller gaps. The spatial localization of large j and m orbitals distorts the nuclear matter distribution away from spherical symmetry. As seen previously, the loss of spherical symmetry decreases degeneracy and modifies level spacing. If the level spacing becomes sufficiently small, then there is a probability to scatter the time-reversed particle pairs from one level to another. Depending on the density of states and the strength of the pairing interactions, the scattering of the nucleon pairs from occupied states into empty states will smear the Fermi surface by affecting the occupation probabilities of the single-particle states. The first theoretical description of this phenomenon was proposed by Bohr, Mottelson, and Pines in 1958 analogous to the BCS pairing in superconductors. The pairing correlations are reduced if the nucleus rotates because the Coriolis force tend to break the pairs apart and align the individual angular momenta onto the rotational axis. In the BCS formalism, the general pairing Hamiltonian is written as

$$H_p = \sum_{k>0} \epsilon_k (a_k^\dagger a_k + a_{-k}^\dagger a_{-k}) + \sum_{kk'>0} < k_2 - k_2 | V_{pair} | k_1 - k_1 > a_k^\dagger a_{-k}^\dagger a_{-k'} a_{k'} \tag{2.51}$$

$$= \sum_{k>0} \epsilon_k (a_k^\dagger a_k + a_{-k}^\dagger a_{-k}) - |G| \sum_{kk'>0} a_k^\dagger a_{-k}^\dagger a_{-k} a_{k'} \tag{2.52}$$

where ϵ_k is the single-particle energy in state i obtained from a phenomenological or a self-consistent mean field model, $< j_2 m_2 j_2 - m_2 | V_{pair} | j_1 m_1 j_1 - m_1 >=< k_2 - k_2 | V_{pair} | k_1 - k_1 >= -|G|$, is the pairing interaction strength of scattering a pair in time-reversed orbits (k,-k).

It is supposed that the ground state of the nucleus is constructed from pure pair configurations on the vacuum sate of real particle $a_k|0>= 0$.

$$|BCS >= \prod_{k>0}^{\infty} (u_k + v_k a_k^\dagger a_{-k}^\dagger)|0 >$$

where u_k and v_k are the variation parameters represent the non-occupation and occupation probabilities in a given state k respectively and satisfy the relation

$$u_k^2 + v_k^2 = 1$$

As the $|BCS >$ is not an eigenstate of the particle number operator $\hat{N}$, the particle conservation is established by determining the variational parameters u_k and v_k in such a way that the expectation value of $\hat{N}$ is the number of particles.

$$< BCS | \hat{N} | BCS >\equiv \langle \hat{N} \rangle = 2 \sum_{k>0} v_k^2 = N \tag{2.53}$$

This is achieved by adding the term $-\lambda \hat{N}$ to the pairing Hamiltonian

$$\hat{H}' = \hat{H}_p - \lambda \hat{N} \tag{2.54}$$

where λ is a Lagrange multiplier and it is related to the particle number conservation condition, which is given by

$$\lambda = \frac{d < BCS | H | BCS >}{dN = \frac{dE}{dN}}$$

λ is also known as the Fermi energy and the chemical potential since the total energy of the system is increased by λ after adding 1 particle. The parameters v_k and u_k are varied to minimize the Hamiltonian H' on the BCS ground-state.

$$\delta < BCS | H' | BCS >= 0$$

The auxiliary Hamiltonian H' has the same form as in eq. 2.51 except that the single-particle energies are modified by the chemical potential

$$\tilde{\epsilon}_k = \epsilon_k - \lambda \tag{2.55}$$

The expectation value of the BCS ground state is given by

$$< BCS | H' | BCS >= 2 \sum_{k>0} \tilde{\epsilon}_k v_k^2 - G \sum_{k>0} [u_k v_k]^2 \tag{2.56}$$

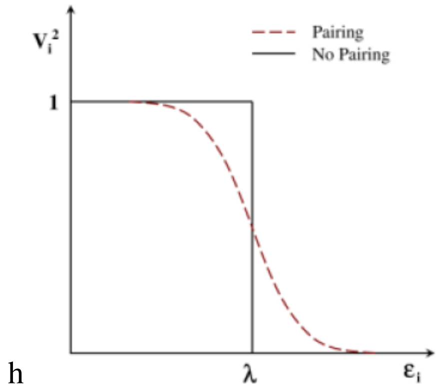

Figure 2.11: A schematic representation of smearing of the Fermi surface because of pairing interaction [53].

And, the probability of occupying the state i by a hole is thus given by

$$u_k^2 = \frac{1}{2}\left[1 + \frac{\tilde{\epsilon}_k}{\sqrt{\tilde{\epsilon}_k^2 + \Delta^2}}\right] \tag{2.57}$$

and the occupation probability by a particle is

$$v_k^2 = \frac{1}{2}\left[1 - \frac{\tilde{\epsilon}_k}{\sqrt{\tilde{\epsilon}_k^2 + \Delta^2}}\right] \tag{2.58}$$

where, Δ is called the gap parameter defined as

$$\Delta = G\sum_{k>0} u_k v_k \tag{2.59}$$

In these expressions, it is noticeable that if the single-particle energies lie far below the Fermi surface ($\epsilon_i \ll \lambda$), $v_i^2 = 1$ and if far above the Fermi surface ($\epsilon_i \gg \lambda$), $u_i^2 = 1$ and close to the Fermi surface the occupations probabilities are mixed (see fig. 2.11).

From eq.[2.57 - 2.59], the so called gap equation can be obtained

$$1 = \frac{1}{2}\sum_{k>0}(\tilde{\epsilon}_k^2 + \Delta^2)^{-\frac{1}{2}} \tag{2.60}$$

Eq. 2.53,2.57,2.58 and 2.59 are known as the BCS equations.

The Bogolyubov transformation to quasiparticles is an alternative method to formulate the BCS model. In this approach, the creation and annihilation operators for the quasiparticles are defined as

$$\alpha_k = u_k a_k - v_k a_{-k}^\dagger \tag{2.61}$$

$$\alpha_k^\dagger = u_k a_k^\dagger - v_k a_{-k} \tag{2.62}$$

which obey the commutation relations

$$[\alpha_k, \alpha_{k'}^\dagger] = \delta_{kk'}; \quad [\alpha_k, \alpha_{k'}] = [\alpha_k^\dagger, \alpha_{k'}^\dagger] = 0. \tag{2.63}$$

The quasiparticles can be thought as nucleons whose energies and wavefunctions are modified by pairing correlations.

$$E_i = \sqrt{(\epsilon_i - \lambda)^2 + \Delta^2} \tag{2.64}$$

In odd nuclei, the singly occupied quasiparticle orbitals block the scattering of pairs. This is called the blocking effect. In odd-odd nuclei, the attractive proton-neutron potential between the valence particles can play a important role.

2.3 Unified Model

The unified model is a fusion of the shell model and LDM. It assumes the motions of the nucleons are coupled strongly to the variations of the nuclear potential that represent collective oscillations. If the variations in the potential are sufficiently slow, the motions of the nucleons ($\approx$ in a fixed field) can be separated approximately from the collective motions (vibrations and rotations). But in many cases, they are strongly coupled, requiring a unified treatment of both the single-particle and collective motions. In 1952, Bohr described the interaction between the collective motions of the core and the motions of valence particles moving in the potential created by the core [73, 74]. Depending on the shape and the single-particle orbits, the coupling can be weak for nearly spherical nuclei with small surface vibration or strong for nuclei with permanent deformation. The nuclear Hamiltonian is described by

$$H = H_{sp} + H_{coll} + H_{int} \tag{2.65}$$

where, the particle Hamiltonian is

$$H_{sp} = \sum_i T_i + V(r_i, \hat{l}_i, \hat{s}_i) \tag{2.66}$$

with T_i kinetic energy and V_i the shell model or Nilsson potential of the valence particle i and the collective Hamiltonian is

$$H_{coll} = T_{vib} + T_{rot} + V(\beta, \gamma) \tag{2.67}$$

and the coupling term

$$H_{int} = \sum_i f(r_i) \sum_{\lambda\mu} a_{\lambda\mu} Y_{\lambda\mu}(\theta_i, \phi_i) \tag{2.68}$$

Collective vibrations are characterized by quantum numbers n_β and n_γ and the nuclear rotation characterized by total angular momentum I. The rotational energies depend on the deformation and become smaller than the vibrational energies in strongly deformed nuclei. Restricting to the coupled system of particles and a rigid top (rotational model), the collective Hamiltonian is given by

$$H_{coll} = \sum_{i=1}^{3} \frac{R_i^2}{2\mathcal{J}_i} \tag{2.69}$$

where, R_i are the components of the collective angular momentum of the inert core in the body-fixed frame. If there are valence particles the total angular momentum I of the system is $I = R + J = R + \sum_k j$, j are the angular momenta of the valence particles (see fig. 2.12 for angular momentum coupling). The collective Hamiltonian can be separated into

$$H_{coll} = \sum_{i=1}^{3} \frac{I_i^2 + J_i^2 - 2I_iJ_i}{2\mathcal{J}_i} = H_{rot} + H_{rec} + H_{cor} \tag{2.70}$$

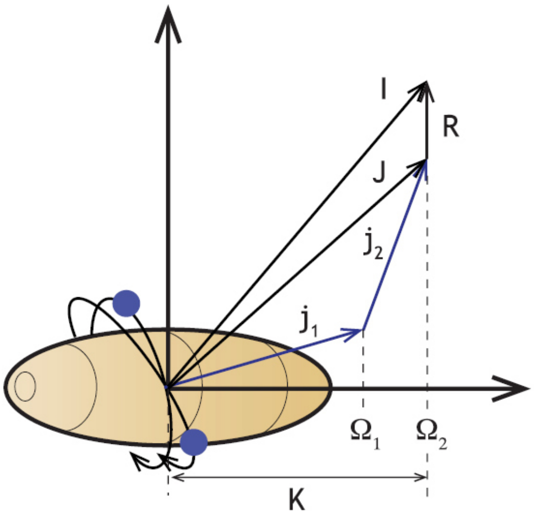

Figure 2.12: A schematic representation of angular-momentum coupling in a deformed nucleus; the K quantum number is built from the projections of the angular momentum of the 2 valence particles onto the symmetry axis [75].

where, H_{rot} represents the pure rotation, H_{rec} represents a recoil energy of the rotor and H_{cor}, the Coriolis interaction between the valence particles and the rotor.

For axially symmetric nuclei, there is no collective rotation around the symmetry axis $R_3 = 0$, hence K, 3-component of I on the symmetry axis is $K = \Omega$, the 3-component of J. In the strong coupling (deformation aligned) limit K is a good quantum number. The angular momentum J of the valence particles precesses around the symmetry axis. Neglecting the Coriolis term, the excitation energy of a quantum mechanical rotor is given by

$$E_K(I) = E_K(I_0) + \frac{1}{2\mathcal{J}}(I(I+1) - K^2) \tag{2.71}$$

where, $E_K(I_0)$ is the excitation energy due to the intrinsic nuclear excitation called the bandhead energy. The form of the energy spectrum remains valid even with the inclusion of the coupling term except when $K = 1/2$ in which case it is given by

$$E_K(I) = E_K(I_0) + \frac{1}{2\mathcal{J}}(I(I+1) - K^2 + a(I+1/2)(-1)^{I+1/2}) \tag{2.72}$$

where, a is the decoupling factor whose value depends on the intrinsic motion of the odd nucleon and is expressed as

$$a = \sum_j (-1)^{j-1/2}(j+1/2)|c_j^2| \tag{2.73}$$

where c_j are Clebsch-Gordon coefficients.

A rotational band associated with each nuclear configuration is the distinctive characteristic of collective rotation. The energy spectrum of collective rotation shows regularity as opposed to the level scheme of the shell model, which is very irregular. In even-even nuclei, for ground-state band $I = K = 0$, there is no intrinsic excitation energy, and the spin of the level sequence is $I = 0, 2, 4, ...$ having even parities. In odd A, odd-odd, and excited states in even-even nuclei where $K \neq 0$, the spin sequence is $I = I_0, I_0+1, I_0+2, ...$ with same parity as that of the intrinsic state on which the rotational band is built. This particular spin sequence comes from the symmetry properties of the nuclear wavefunction. The coupling scheme of an axially symmetric deformed nucleus is shown in fig. 2.12 and we have $I = K + R$ with $\Omega = K$ which results in $I \geq K$.

In general, the rotational energy can be improved by expanding in powers of $I(I+1)$ to include Coriolis coupling and other spin dependent effects

$$E_{rot}(I(I+1)) = E_0 + AI(I+1) - K^2 + BI^2((I+1) - K^2)^2 + CI^3((I+1) - K^2)^3 + ... \tag{2.74}$$

where, $A = \frac{\hbar^2}{2\mathcal{J}}$ and B,C,.. are the corresponding higher order parameters. However, the leading order correction terms for $K > 1/2$ are found to be small [76].

2.3.1 Shell model correction to LDM (Microscopic-Macroscopic model)

The Nilsson model had proven to be successful in describing many microscopic aspects of the nucleus, for instance, the ground state, the excited state properties of many deformed nuclei, and also predicts their existence in stable deformation. However, this phenomenological shell model fails to reproduce the bulk properties of the nuclei namely the masses and the total binding energies. The LDM gives an overall prediction of these behaviors. The LDM assumes a uniform distribution of the nucleons in phase space and gives a smooth behavior of the nuclear binding energies as a function of A. The deviation from the actual values in the neighborhood of shell closures (magic numbers) indicates rather in-homogeneous distribution. To account for the oscillatory behavior of the binding energies V. M. Strutinski [77] introduced corrections based entirely on quantum mechanical effects. The binding energy E is divided into a smoothly varying LDM part and an oscillatory part:

$$E = E_{LDM} + E_{osc} \tag{2.75}$$

where, the E_{osc} part is derived from shell model by subtracting the smoothly varying part $\tilde{E}_{shell}$ from the sum of single particle energies.

$$E_{osc} = E_{shell} - \tilde{E}_{shell} = \sum_{i=1}^{A} \epsilon_i - \tilde{E}_{shell} \tag{2.76}$$

Shells occur from the clustering of levels, and their inhomogeneity is reflected in the level density $g(\epsilon)$ function (see fig. 2.13) that satisfies the particle number condition

$$A = \int_{-\infty}^{\lambda} g(\epsilon) d\epsilon \tag{2.77}$$

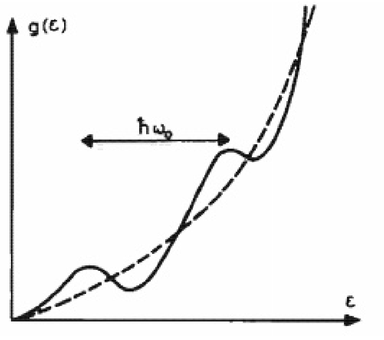

Figure 2.13: Schematic representation of the level density in an infinite three dimensional potential [48].

E_{shell} can be found by integrating up to the properly chosen Fermi level λ.

$$E_{shell} = \int_{-\infty}^{\lambda} \epsilon g(\epsilon) d\epsilon \tag{2.78}$$

The smooth average energy part $\tilde{E}_{shell}$ is derived by integrating on a uniform level density $g\tilde{(\epsilon)}$ function that has a mean functional behavior of $g(\epsilon)$ upto the corresponding mean Fermi level $\tilde{\lambda}$, calculated from particle conservation

$$A = \int_{-\infty}^{\tilde{\lambda}} \tilde{g}(\epsilon) d\epsilon \tag{2.79}$$

$$\tilde{E}_{shell} = \int_{-\infty}^{\tilde{\lambda}} \epsilon g\tilde{(\epsilon)} d\epsilon \tag{2.80}$$

The average density function is determined by transforming $g(\epsilon)$ using a smoothing function f over an average energy separation γ between two shells

$$\tilde{g}(\epsilon) = \frac{1}{\gamma} \int_{-\infty}^{+\infty} g(\epsilon') f\left(\frac{\epsilon' - \epsilon}{\gamma}\right) d\epsilon' \tag{2.81}$$

where $\gamma \simeq \hbar\omega_0$, the shell interval. Pairing correlations also affect the density of states and after including pairing correction term, the total energy is given by

$$E = E_{LDM} + E_{shell} - \tilde{E}_{shell} + P_{BCS} - \tilde{P}_{BCS} \tag{2.82}$$

For nuclei with magic or near a magic number of proton or neutron, the ground state masses are lowered because of the shell correction. This effect is also seen for mid-shell nuclei at some finite deformation i.e., permanent deformations in nuclei stem from their intrinsic nuclear configurations. Fig. 2.14 shows the shell corrections across the whole nuclear chart. Without shell effects, the heaviest nuclei would fission spontaneously on a scale much shorter than what is observed. The fission isomers that LDM fails to explain are also accounted naturally by the double-humped fission barrier predicted from the Strutinski's model.

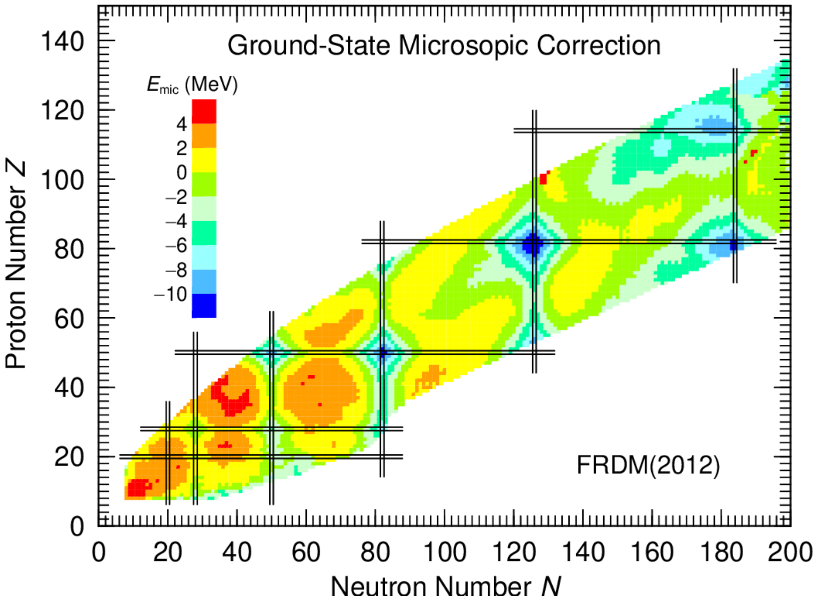

Figure 2.14: Ground-state microscopic corrections [44].

Chapter 3

Radioactive decays

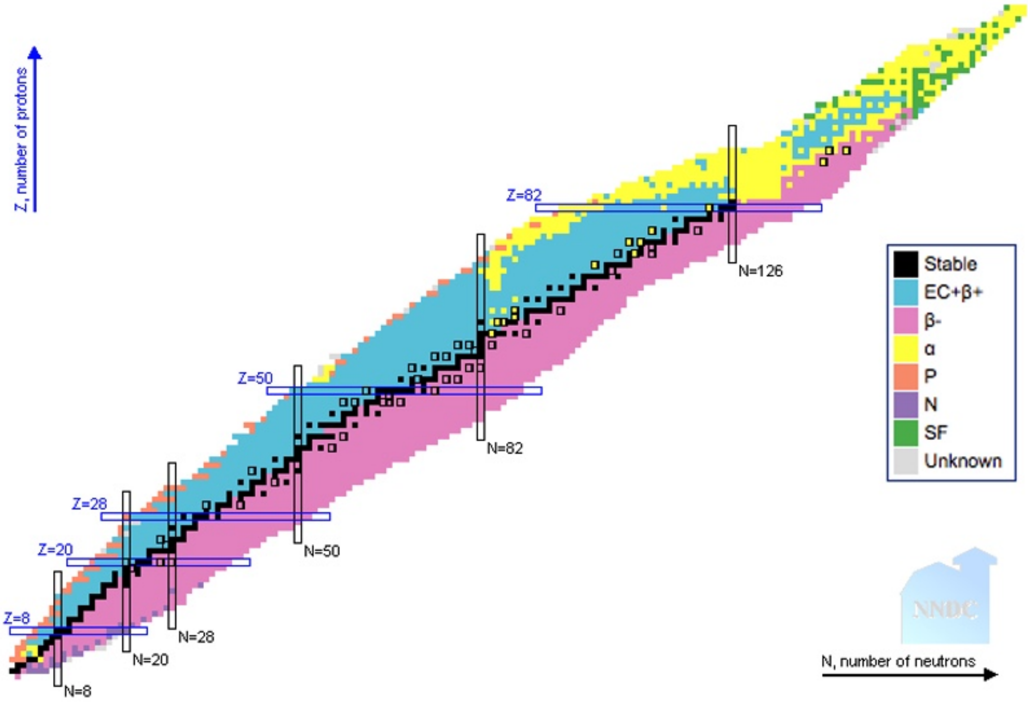

Figure 3.1: Nuclear landscape (Sergè Chart) by the type of decay [78].

Radioactivity was accidentally discovered by Henri Becquerel in Uranium in 1896 [79, 80]. Subsequently, G. Carl Schmidt and then Marie and Pierre Curie observed emission of radiation in thorium. It was Marie Curie who first coined the term radioactivity (see ref. [81]). Radioactivity is an irreversible statistical process, in which the unstable nuclei disintegrate into more stable nuclide, which may also be radioactive. The number of nuclei in a radioactive sample follows the exponential decay law

$$N(t) = N_{t=0} e^{-\lambda t} \tag{3.1}$$

where N_0, is the number of nuclei present at time $t = 0$. The half-life is related to the mean lifetime τ of a nucleus and its decay probability per unit time λ by:

$$T_{1/2} = \ln(2)\tau = \frac{\ln(2)}{\lambda} \tag{3.2}$$

Some nucleides decay via more than one mode (described briefly in the following subsections). Then the total decay constant λ is

$$\lambda = \sum_{i=1}^{N} \lambda_i \tag{3.3}$$

and the total half-life $T_{1/2}$

$$\frac{1}{T_{1/2}} = \sum_{i=1}^{N} \frac{1}{T^i_{1/2}} \tag{3.4}$$

where i represents the ith mode of decay with the branching ratio $br_i = \lambda_i/\lambda$ and $T^i_{\frac{1}{2}}$ are the partial half-lives (see appendix A for details about the lifetime measurement method).

Fig. 3.1 gives the nuclear landscape based on the radioactive decay modes, only the decay types that are relevant to super heavy nuclei are briefly discussed in the following sections.

3.1 Alpha decay

Alpha decay is a type of radiative disintegration in which an unstable nucleus dissipates excess energy by ejecting an alpha particle (a $^4He^{2+}$ ion) spontaneously. This decay process is represented by:

$$^{A}_{Z}X_N \rightarrow ^{A-4}_{Z-2} Y_{N-2} + \alpha$$

where the parent nucleus X transmutes into Y with the emission of an α particle. This disintegration occurs due to the disruptive Coulomb repulsive force, that grows at a faster rate proportional to Z^2 than the nuclear binding force $\propto A$. Because the alpha particle is a stable and highly bound system (28.3 MeV binding energy), it is the most energetically favored decay particle for many nuclei to release the largest possible kinetic energy. This spontaneous kinetic energy appears from a decrease in the mass of the system and quantitatively known as the Q-value of α decay.

$$Q_\alpha = T_Y + T_\alpha = (M_X - M_Y - M_\alpha)c^2 \tag{3.5}$$

where T_Y and T_α are the kinetic energies of the daughter nucleus and the α particle respectively and M_X, M_Y and M_α are the masses of the mother, daughter and the α particles. Definitely, Q must be greater than 0 for this spontaneous decay to occur. In a ground state to ground state (g.s. → g.s.) alpha transition, the kinetic energy of the α particle is given by

$$T_\alpha = Q_\alpha \frac{A-4}{A} \tag{3.6}$$

assuming the original nucleus X to be at rest. The recoil energy of the daughter nucleus can be calculated from the relation $T_Y = Q_\alpha - T_\alpha$. Although, the α particle carries away most of the Q_α value energy, the recoil energy of the heavier fragment cannot be ignored while calibrating detectors (see chapter 4).

Although the alpha radioactivity was first discovered by E. Rutherford in 1899 [82], which he later identified in 1907 as a $^4He^{2+}$ ion [83], only in 1928, G. Gamow [84] and independently R. W. Gurney and E. U. Condon [85] provided the first theoretical description of the decay process after the advent of quantum mechanics. In this view, a preformed alpha particle inside the parent nucleus bombards the Coulomb barrier repeatedly and finally tunnels through the barrier. For this reason, the alpha preformation probability $\omega(\alpha)$ inside the parent nucleus must not be equal to 0 and $Q_\alpha > 0$, i.e., kinetic energy is available to the alpha particle for tunneling through the Coulomb barrier $V_C = \frac{2Ze^2}{4\pi\varepsilon_0 r}$ with Z the atomic

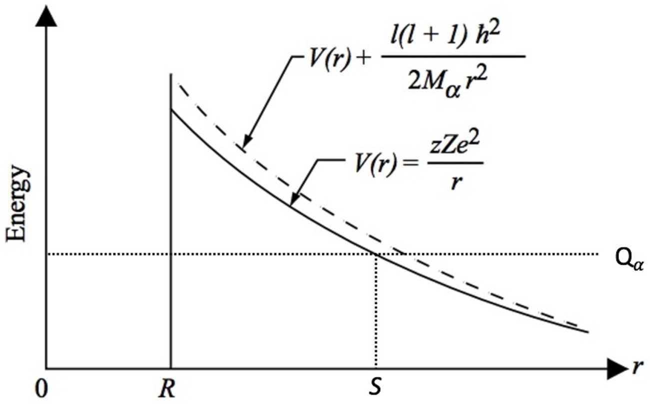

Figure 3.2: Modification of the potential energy in a decay due to the centrifugal potential (adapted from [59]).

number of the daughter and r the distance of the α particle from the center of the system (see fig. 3.2). The decay constant is then given by

$$\lambda = fT\omega(\alpha) \tag{3.7}$$

where f is the frequency with which the alpha bombards the barrier and T, the tunneling probability.

In an α particle, the nucleons are in 1s state and coupled pairwise to 0 hence, the spin and parity of an α particle is 0^+. Therefore, when an alpha transition occur from an initial state I_i to a final state I_f, the orbital angular momentum l the α particle can carry away is restricted in the range ($|I_i - I_f| \leq l \leq I_i + I_f$) and the parity change associated with the process is $(-1)^l$. In the case of $l \neq 0$, the alpha particle must tunnel through an additional centrifugal barrier $V_l = \frac{l(l+1)\hbar^2}{2M_\alpha r^2}$ (as illustrated in fig. 3.2). The alpha decay rate $\lambda_{l\neq0}$ for this instance is related to the rate in the absence of such centrifugal barrier by [59]

$$\lambda_{l\neq0} \approx \lambda_{l=0} e^{-(2.027(l(l+1))Z^{-1/2}A^{-1/6})} \tag{3.8}$$

Parity is conserved in strong interactions, hence another selection rule applies to an alpha decay process

$$\pi_i = \pi_f(-1)^l. \tag{3.9}$$

This means that in an alpha transition if the initial and final states have the same parity, the alpha particle must have only even l-values, but if there is a parity change $\Delta\pi = -1$ then only odd l-values are permitted. This selection rule forbids a g.s. → g.s. alpha decay if there is parity change and the transition proceeds instead to an excited state of the daughter nucleus. However, decay to an excited state lowers the Q_α-value by

$$Q_\alpha^* = Q_\alpha^{\text{g.s.}} - E_Y^* \tag{3.10}$$

where $Q_\alpha^{\text{g.s.}}$ is the Q_α-value for the g.s. → g.s. transition and E_Y^* is the excitation energy of the nuclear state of the daughter nucleus Y populated in the transition. Lowering of the Q_α-value means decreasing of the probability T to penetrate the complete barrier.

$$T = e^{-2G} \tag{3.11}$$

where G is known as the Gamow factor given by the expression:

$$G = \sqrt{\frac{2\mu}{\hbar^2}} \int_R^S [V(r) - Q_\alpha]^{1/2} \tag{3.12}$$

where μ is the reduced mass of the alpha particle and R and S are the classical turning points shown in fig. 3.2. Hence, the decay rates to the excited states decrease with an increase in excitation energy.

Often the predictions of alpha decay half-lives is a theoretical challenge, therefore the use of empirical relations is quite prevalent. Interestingly, the empirical rule (see eq. 3.13) proposed by Geiger-Nuttall surfaced before the theoretical explanation of the trend given by Gamow [84]:

$$log(T_{1/2}) = a + bQ_{\alpha}^{-1/2} \tag{3.13}$$

where $T_{1/2}(\alpha)$ is given in s, Q in MeV, a, and b are constants and determined from fitting experimental data.

Following later theoretical developments many multi-parameter empirical relations have also been developed. Most notable is the Viola-Seaborg formula [86] that incorporates the hindrance factor *logF* for odd nuclei (see section 3.1.1)

$$logT_{1/2} = a(Z)Q_{eff}^{-1/2} + b(Z) + logF \tag{3.14}$$

where Q_{eff} is the effective alpha decay energy [MeV] inside the parent nucleus computed by adding the recoil energy T_Y of the daughter nucleus and the orbital electron screening correction ΔE_{sc} to the measured alpha energy E_α

$$Q_{eff} = E_\alpha + T_Y + \Delta E_{sc}. \tag{3.15}$$

The orbital electron screening correction ΔE_{sc} is a measure of the loss of the kinetic energy because of the attraction of the orbital electrons and the alpha particle and is estimated from the relation:

$$\Delta E_{sc}(Z) = 65.3 \times Z^{\frac{7}{5}} - 80 \times Z^{\frac{2}{5}} \quad \text{[eV]} \tag{3.16}$$

where Z is the atomic number of the parent nucleus. The parameters in the expression 3.14

$$a(Z) = 2.11329 \times Z - 48.9879$$

and

$$b(Z) = -0.39004 \times Z - 16.9543$$

are determined from experimental data fitting (see refs. [86, 87]).

Z	N	$\log F$
Even	Odd	1.066
Odd	Even	0.772
Odd	Odd	1.114

Table 3.1: Average hindrance factors [86].

The Viola-Seaborg formula does not take into account the l dependence of the decay rate. The following improved empirical relations of G. Royer [88] include the effect of the centrifugal barrier on the decay rate.

$$\log T_{1/2} = -a - bA^{1/6}\sqrt{Z} + \frac{cZ}{\sqrt{Q}} \quad \Delta l = 0 \tag{3.17}$$

$$\log T_{1/2} = -a - bA^{1/6}\sqrt{Z} + \frac{cZ}{\sqrt{Q}} + \frac{dANZ[l(l+1)]^{1/4}}{Q} + eA[1-(-1)^l] \quad \Delta l \neq 0 \tag{3.18}$$

In these equations, the Q-value is obtained from the Atomic Mass Evaluation and the parameters are obtained from the experimental data fits. It is worth mentioning that there are several other empirical relations (see ref. [89–91]) that exist in the literature.

3.1.1 Hindrance factor

The one-body theory (where the alpha particle is treated as point like particle moving in the potential created by the daughter nucleus) is only applicable to even-even alpha emitters. Odd A nuclei decay at a slower rate than suggested by the one body theory. There are a couple of factors that influence this decay rate. Firstly, the alpha preformation factor is affected by the presence of an unpaired nucleon (see fig. 3.3). Secondly, there is a higher barrier resulting from non-zero angular momentum. Thirdly, the spin change involved in a transition can deter an alpha decay. Such hindrances to the alpha decay process are grossly quantified through a dimensionless quantity called the hindrance factor (HF). It is defined as the ratio of measured partial half-life for a given alpha transition to the half-life calculated from the one-body theory applied to ground state to excited state (g.s. → ex.s.) in neighboring e-e nuclei.

$$HF = \frac{T_{1/2}^{partial}(measured)}{T_{1/2}^{e-e}(calculated,\ \mathrm{g.s.} \rightarrow \mathrm{g.s.})} = \frac{\lambda_{claculated}}{\lambda_{measured}} \tag{3.19}$$

It gives a measure of a departure (a slower rate) of a given alpha-decay than what would be from systematics based on g.s. → g.s. transition rates of the nearest e-e neighbors [92]. There can be hindrances to alpha decay even in e-e nuclei if a transition occurs to an excited state in the daughter nucleus. The HF in e-e nuclei can be defined similarly as the ratio of the measured partial half-life of a g.s. → ex.s. transition to the measured partial half-life of g.s. → g.s. transition.

$$HF_{e-e} = \frac{T_{1/2}^{partial}(\mathrm{g.s.} \rightarrow \mathrm{ex.s.})}{T_{1/2}^{partial}(\mathrm{g.s.} \rightarrow \mathrm{g.s.})} \tag{3.20}$$

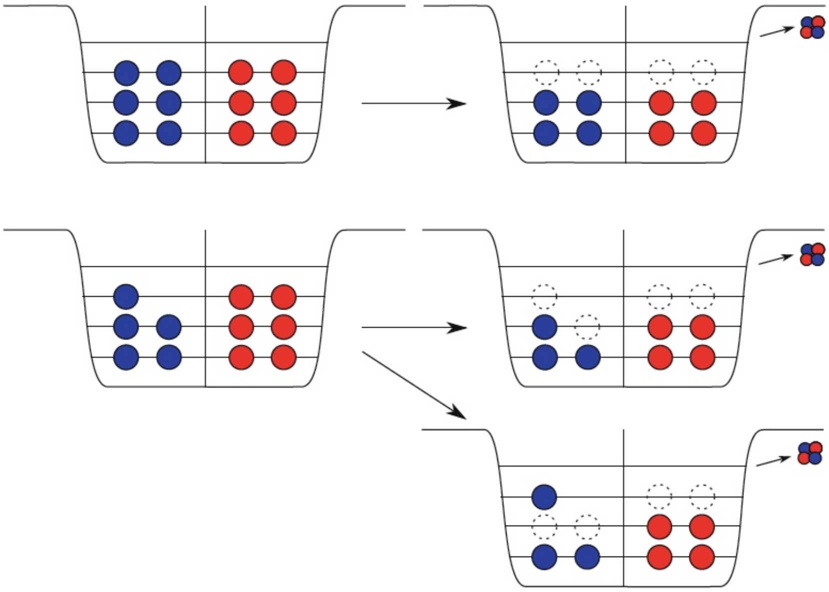

Figure 3.3: A schematic diagram of alpha decay. In an e-e nucleus the last bound pairs can easily form the alpha particle whereas in an e-o system, the alpha particle can be formed by breaking a pair or by the first pairs from the alpha particle leaving the daughter nucleus in an excited state [7].

In general, the hindrance factors for odd A nuclei are classified into five categories based on the influence of the nuclear structures of the both parent and daughter nuclei [59]:

- In a favorable transition, the emitted alpha particle is formed from the two low-lying pairs of nucleons in the parent nucleus, leaving the odd nucleon in its initial orbital. In such a transition, the HF has a value between 1-4.
- If there is a favorable overlap between the initial and final nuclear wave functions, the decay has an HF between 4-10.
- For a transition in which the spin projections of initial and final states are parallel, but the wavefunction overlap is not favorable, the HF takes the value between 10 to 100. Deformation can also cause hindrances in the decay as it affects the overlap of the initial and final wave functions.
- If a transition involves a change in parity, but the spin projections of the initial and final states are parallel, the HF is between 100-1000.
- $HF > 1000$ indicates that there is a change in parity in the transition, and the spin projections of the initial and the final states are antiparallel.

Two methods namely, Preston's spin-dependent method [93] and Rasmussen's method [96, 97] are widely used to calculate the HF. These calculation methods are described briefly in the following sections.

Preston's spin dependent method

M. Alexander Preston [93] re-derived the theory of alpha decay to address some inaccuracies in the formalism for $l \neq 0$. He argued that Gamow's approximations give incorrect numerical results. As in Gamow's original theory, he assumed the alpha particle to be in a rectangular potential $V = U$, a constant, for $r < r_0$ and $V = 2Ze^2/r$, for $r > r_0$, where Z is the charge number of the product nucleus, e is the elementary charge, r is the distance of the alpha particle from the center of the daughter nucleus, r_0 is the radius of the daughter nucleus. The relationship between the variables E_α (the energy with which the alpha particle emerges out of the potential barrier), λ, r_0, and U are expressed in equations 3.21 and 3.22.

$$\mu = -\tan\alpha_0 \tan(\mu k r_0) \tag{3.21}$$

$$\lambda = \frac{2v}{r_0} \frac{\mu^2 \tan\alpha_0}{\mu^2 + \tan^2\alpha_0} \exp(-2\omega_0) \tag{3.22}$$

where

$$\begin{aligned}
\mu &= \sqrt{(1 - \frac{U}{E_\alpha})} \\
\alpha_0 &= \arccos(\frac{mv^2 r_0}{4e^2 Z})^{1/2} \\
k &= \frac{mv}{\hbar} \\
\kappa_R &= \frac{4e^2 Z}{\hbar v} \\
\omega_0 &= \kappa_R (\alpha_0 - \sin\alpha_0 \cos\alpha_0)
\end{aligned}$$

The variable λ can be calculated from the experimentally known E_α and the calculated radius r_0 and potential U. For a given alpha decay transition with corresponding branching ratio Br_i, the partial decay rate can be calculated from the measured $T_{1/2}$ using $\lambda_i = \ln(2) \times Br_i(\text{in }\%)/(100 \times T_{1/2})$. Then the HF of this alpha transition is calculated using equation 3.19.

This approach is adopted in ENSDF (Evaluated Nuclear Structure Data File) to obtain the α-hindrance factors. For odd A or odd odd nuclei, the nuclear radius is estimated as the average radius of the neighboring e-e nuclei for which the HF of g.s. → g.s. alpha transition is defined as $HF = 1$.

$$R(Z,N) = \begin{cases} \frac{R(Z-1,N)+R(Z+1,N)}{2} & \text{for o-e nuclei} \\ \frac{R(Z,N-1)+R(Z,N+1)}{2} & \text{for e-o nuclei} \\ \frac{R(Z-1,N)+R(Z+1,N)+R(Z,N-1)+R(Z,N+1)}{4} & \text{for o-o nuclei} \end{cases} \tag{3.23}$$

If only the radius R_{e-e} of one adjacent e-e nucleus is known, the value is corrected for the $A^{1/3}$ mass dependence.

$$R = R_{e-e}\left(\frac{A}{A_{e-e}}\right)^{1/3} \tag{3.24}$$

where A is the mass number of an o-o nucleus or an odd A nucleus and A_{e-e}, the mass number of the known e-e nucleus.

Rasmmussen method

In one-body formalism (e.g. Gamow's theory), the influence of the nuclear structures of both the parent and the daughter nuclei on alpha decay is ignored completely. By defining a useful concept called the reduced decay width of an alpha transition, the nuclear structure effects are taken into account. The reduced decay width is defined by the overlap integral of the initial and the final states [94]:

$$\delta^2 = | < \psi_i(X)|\psi_f(Y).\phi(\alpha) > |^2 \tag{3.25}$$

By comparing experimental reduced decay width to the theoretical value from a given nuclear structure model, the robustness of the model can be tested.

Experimentally the reduced alpha-decay width is calculated using the experimental decay rate λ and the theoretical barrier penetration factor T (see eq. 3.11) [96]:

$$\delta^2 = \frac{\lambda h}{T} \tag{3.26}$$

The Gamow factor G in eq. 3.12 includes an optical model potential $V(r)$ besides the Coulomb barrier and the centrifugal barrier

$$G = -\int_R^S [\frac{2\mu}{\hbar^2}(V(r) + V_C(r) + V_l(r) - Q_\alpha]^{1/2} dr \tag{3.27}$$

The optical model nuclear potential used in the expression is that of the potential introduced by Igo [95] which has the form:

$$V(r) = -1100\exp(-[\frac{r - 1.17A^{1/2}}{0.574}]) \quad [\text{MeV}] \tag{3.28}$$

Usually, for decays to an excited state in even-even nuclei, the hindrance factor can be defined as the ratio of the rates of decay to the ground state and to the excited state multiplied by the ratio of the corresponding barrier penetration factors calculated without including the centrifugal barrier [96].

$$HF = \frac{\lambda_{g.s.}}{\lambda_{ex.s.}} \times \frac{T_{g.s.}}{T_{ex.s.}} \tag{3.29}$$

In the Rasmmussen's prescription, the reduced hindrance factor $HF_{reduc.}$ is used to take into account the centrifugal barrier effects on the barrier penetration probability. It is calculated as the ratio of $\delta^2_{g.s.}$ for the ground-state transition to the $\delta^2_{ex.s.}(l)$ for the excited state transition [97].

$$HF_{reduc.} = \frac{\delta^2_{g.s.}}{\delta^2_{ex.s.}} \tag{3.30}$$

In the case of odd-mass alpha emitters, the HF is calculated by [97]

$$HF = \frac{\delta^2_1 + \delta^2_2}{2\delta^2_{odd}} \tag{3.31}$$

where δ^2_1 and δ^2_2 are the reduced widths for the ground state transitions in the nearest neighboring e-e nuclei and δ^2_{odd}, the reduced width of the o-o nuclei. HFs are usually normalized relative to the alpha decay of ^{212}Po to ^{208}Pb (which is doubly magic, Z = 82 and N =126) or to a neighboring e-e nucleus. The hindrance factors can also be evaluated from the Viola-Seaborg formula. Details about this method and the results are given in ref. [92, 98].

Alpha decay serves as an important identification tool for discovering new SHEs. It is the most common form of cluster decay (heavy-ion radioactivity). The preformation probability of a cluster $C(z, a)$ heavier than the alpha particle but lighter than a typical binary fission fragment in the parent nucleus drops as follows [99]:

$$\omega(C) = \omega(\alpha)^{(A-1)/3} \tag{3.32}$$

3.2 Spontaneous Fission

In the fission process, an unstable nucleus splits into two nearly equal lighter fragments. This process can either be an induced process by bombarding with a beam called fission reaction or naturally occurring without requiring excitation, a type of radioactive decay known as Spontaneous Fission (SF). It remains a theoretical challenge for a complete understanding of the fission process after eight decades of its first discovery by O. Hahn, L. Meitner and F. Strassman in 1938. Later in 1939 [100, 101], Lise Meitner and her nephew O. R. Frisch explained it theoretically [102, 103]. In the same year, N. Bohr and J. A. Wheeler also gave a detailed theoretical treatment on the mechanism of nuclear fission based on the LDM [104]. SF is observed for very high mass number isotopes and was discovered by G. Flerov and K. Petrzhak in 1940 [105–107]. Classically (LDM), the so-called fissibility parameter x characterizes the feasibility of fission for a given nucleus. It quantifies the competition between the disruptive Coulomb energy that decreases with deformation as opposed to the increase in restoring surface energy. It is given by

$$x = \frac{E_{Coulomb}}{2E_{Surface}} = \frac{Z^2/A}{(Z^2/A)_{critical}} \tag{3.33}$$

where $(Z^2/A)_{critical} \approx 50$. A classical droplet stays stable and spherical if $x \leq 1$, and fissions immediately if $x > 1$ [48]. Since, the LDM fails to describe spontaneous fission process for nuclei with $x < 1$ *e.g.* $^{238}U : x \simeq 0.8$ [48], the observed phenomenon is viewed as a barrier penetration phenomenon in which the nucleus tunnels through the fission barrier similar to the alpha decay. Roughly, the fission barrier is the minimum amount of energy required to deform a spherical nucleus to such a point known as the "saddle point" that the nucleus has no other choice but fission (similar to squashing of a balloon until it burst). The LDM fission barrier disappears around $Z = 104$.

The half-life of a fission decay is expressed as

$$T_{1/2}^{SF} = \frac{ln2}{fP} \tag{3.34}$$

where f is the frequency of impact on the fission barrier by the nucleus and P is its barrier penetration probability. The approximate total kinetic energy of the fission fragments as result of Coulomb repulsion can be estimated by [59]:

$$KE = \frac{Z_1 Z_2 e^2}{r_0(A_1^{1/3} + A_2^{1/3})} MeV$$

where $r_0 = 1.8$ instead of usual 1.2 as the fission fragments at scission are usually deformed. There also exist empirical relations to estimate the kinetic energy released in the process [108].

$$E_K = 0.1166 Z^2/A^{1/3} + 9.0 \quad [\text{MeV}] \tag{3.35}$$

An empirical formula for the spontaneous fission half-life is given in the ref. [86]

$$\log T_{1/2}^{SF} = -3.344 Z^2/A + 133.86 + 6.884\delta_m \tag{3.36}$$

where δ_m represents the fission hindrance (nuclear structure effects) and $T_{1/2}^{SF}$ is given in years. Indeed, observations have shown that the fission half-lives of odd nuclei are longer than those of their e-e neighboring nuclei. In an odd nucleus, the unpaired nucleon hinders the decay because the spin and parity conservation does not allow easy transition, unlike in e-e nuclei. The fission hindrance factor for an odd nucleus is defined as the ratio of experimental fission half-life T_{exp}^{SF} to the unhindered fission half-life T_{ee} calculated as the geometrical mean of the fission half-lives of the neighboring e-e nuclei [109].

$$\delta_m(Z, N) = \frac{T_{exp}^{SF}(Z, N)}{T_{ee}(Z, N)} \tag{3.37}$$

with

$$T_{ee}(Z, N) = \sqrt{T^{SF}(Z, N-1) \times T^{SF}(Z, N+1)}$$

for e-o nuclei,

$$T_{ee}(Z, N) = \sqrt{T^{SF}(Z-1, N) \times T^{SF}(Z+1, N)}$$

for o-e nuclei, and

$$T_{ee}(Z, N) = (T^{SF}(Z, N-1) \times T^{SF}(Z, N+1) \times T^{SF}(Z-1, N) \times T^{SF}(Z+1, N))^{1/4}$$

for o-o nuclei. The dynamics of fission is more complicated than the LDM picture. We can have symmetric and asymmetric fission based on the number of nucleons on each side of the neck (scission point) and fragments, most likely in the excited states. Strutinski's shell correction predicts a double-humped fission barrier for many nuclei. The first minimum is usually the ground state, and the second minimum can harbor quasi-stationary states known as fission isomers or shape isomers. The energy barrier on either side traps the nucleus to retain its elongated shape. These fission isomers either tunnel back to the more spherical ground state by emitting a gamma-ray or tunnel through the remaining fission barrier fissioning spontaneously. As the barrier hindrance is lower in the second well than in the first, a smaller half-life is expected for the isomeric sates than for the ground state.

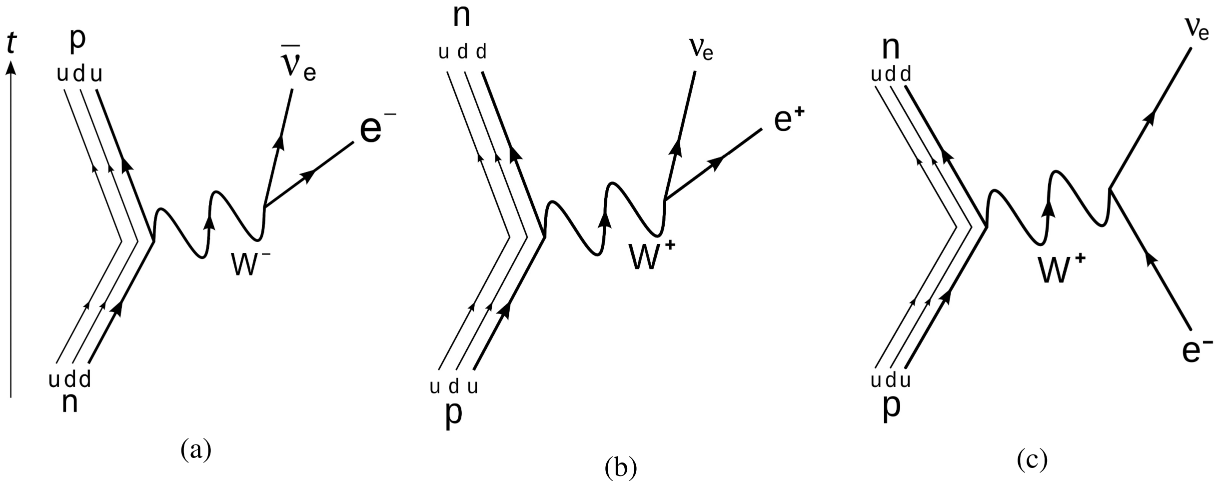

(a) (b) (c)

Figure 3.4: The leading order Feynman diagram of a) β^- decay b) β^+ decay and c) EC decay.

3.3 β decay

A vast majority of nuclei lie in the region where alpha decay is not a predominant decay mode. They become more stable by undergoing a beta decay in which the original nuclei transform into an isobar and either a pair of high energy positron and a neutrino or an electron and an anti-neutrino pair are emitted from the nucleus. Nuclei are said to be unstable against beta decay when protons and neutrons inside are out of balance. Through beta decay, the balance is achieved by converting a proton into a neutron or vice versa inside a nucleus, maintaining a constant mass number. Based on the sign of the charge of the electron, these decays are called beta plus (β^+) and beta minus (β^-) decay. In some cases, when beta plus is not favorable, absorption of one inner atomic orbital electron seems more economical in energy and such decays are called electron capture (EC) decays. These three processes are written as

$$^A_ZX_N \rightarrow ^A_{Z+1} Y_{N-1} + e^- + \bar{\nu}_e \quad \text{for}\, \beta^- \text{ decay}$$

$$^A_ZX_N \rightarrow ^A_{Z-1} Y_{N+1} + e^+ + \nu_e \quad \text{for}\, \beta^+ \text{ decay}$$

$$^A_ZX_N + e^- \rightarrow ^A_{Z-1} Y_{N+1} + \nu_e \quad \text{for EC}$$

And the energy required to occur these decays corresponds to their respective Q-values:

$$Q_{\beta^-} = (M_P - M_D)c^2 \tag{3.38}$$

$$Q_{\beta^+} = (M_P - M_D)c^2 - 2m_ec^2 \tag{3.39}$$

$$Q_{EC} = (M_P - M_D)c^2 - \epsilon \tag{3.40}$$

where the neutrino's mass is neglected, M_P, M_D are the atomic masses of mother and daughter nuclei and ϵ is the binding energy of the electronic orbital from which the electron is captured. Depending on from which shell it is captured, the process is referred to as K-capture, L-capture and so on. EC depends on the properties of the electron cloud around the nucleus and can be inhibited if the atom is fully ionized. Beta-decay is possible because of the fundamental property of nucleons to be able to transform from one to another through Weak interaction. Nucleons are composed of up (u) and down (d) quarks. Fig. 3.4 shows the leading order Feynman diagrams of the three processes showing how a Weak force carrier (either a W^+ or a W^- boson) changes the flavor of a quark inside the nucleon.

The Neutrino hypothesis due to Pauli, is from the shape of the beta energy spectrum energy in which momentum conservation requires beta decay to be a three-body process. Based on the angular momentum L decay radiations carry away, the beta decay transitions are classified as allowed $L = 0$ and forbidden $L > 0$ transitions. Since both electron and neutrino are spin 1/2 particles, their spins can be combined into a total of 0 (singlet case) or 1 (triplet case) hence the classifications called Fermi and Gamow-Teller transitions respectively. For allowed transitions, there is no change in the parity $\Delta\pi = 1$ of the nuclear wave functions. In the singlet case, the electron and the neutrino are emitted in s state, and no change in the total angular momentum $\Delta I = 0$ occurs between the initial and the final states of the nucleus. Whereas in the triplet case, there is an angular momentum change $\Delta I = \pm 1 \, \text{or} \, 0$ between the initial and final states with an exception being 0 to 0 transition.

A transition of Lth degree forbiddenness respects the following selection rules

$$\Delta I = -(L + 1), L, (L + 1)$$

and

$$\Delta\pi = (-1)^L$$

and is slower than a allowed transition.

3.4 Electromagnetic decay

Similar to atomic relaxation process, a nucleus in an excited state can release its excess energy by emission of a photon technically known as gamma decay and the process is represented by

$$^{A}X^* \rightarrow^{A} X + \gamma$$

where $*$ indicates an excited state of the nucleus. The energy of the photon emitted in the transition from a high lying excited state to a low lying state is given by

$$E_\gamma = M^*c^2 - Mc^2 - T_r \tag{3.41}$$

where T_r is the kinetic energy of the recoiling nucleus, M^*, and M masses of the higher and lower nuclear states, respectively. By applying conservation of momentum the kinetic energy of the recoil is

$$T_r = \frac{E_\gamma^2}{2Mc^2} \tag{3.42}$$

which is negligible compared to the photon energy. For example, for a $E_\gamma = 1$ MeV transition in ^{255}Rf, $T_r \approx 1.5$ eV. For this reason, the level energies are usually denoted with the emitted photon energies.

3.4.1 Electromagnetic transition rates

Every nuclear state has charge and current distributions inside the nucleus that are different from one nuclear state to another because of the spatial localization of the orbitals that nucleons occupy. The nucleus emits a photon of either electric or magnetic type when a higher energy state decays to a lower level.

Electromagnetic decays in nuclei are described in terms of the interaction of the nuclear Hamiltonian H_{nucl} with an external electromagnetic field. The total Hamiltonian of the system is then given by

$$H = H_{nucl} + H_{field} + H_{int} \tag{3.43}$$

where the nuclear Hamiltonian has eigenvalues E_i for a given set of eigen fuctions $\Psi_i(1, .., A)$

$$H_{nucl}\Psi_i(1, .., A) = E_i\Psi_i(1, .., A)$$

The Hamiltonian of the electromagnetic field is the integral of the energy density:

$$H_{field} = \frac{1}{8\pi}\int (E^2(r,t) + B^2(r,t))d^3r \tag{3.44}$$

where E and B are the electric and magnetic fields derived from the four-potential $A^\mu = (\phi, \vec{A})$. And the interaction Hamiltonian is

$$H_{int} = -\frac{1}{c}\int j_\mu A^\mu d^3r \tag{3.45}$$

with four-current $j_\mu = (c\rho, \vec{j})$ where ρ and $\vec{j}$ are the nuclear charge and current densities. The current density is related to the the magnetic moment $\vec{\mu}$ by

$$\vec{j}(\vec{r},t) = c\nabla \times \vec{\mu}(\vec{r},t). \tag{3.46}$$

The nuclear magnetic moment has two sources: the orbital motions of the protons and the intrinsic spin of the protons and the neutrons. It is expressed as

$$\vec{\mu} = \sum_{i=1}^{A}\left[g_{l,i}\vec{l}_i + g_{s,i}\vec{s}_i\right]\frac{\mu_N}{\hbar} \tag{3.47}$$

where $\mu_N = \frac{e\hbar}{2m_pc}$ is the nuclear magneton, m_p, the rest mass of a proton, g_s, the spin g-factor of a nucleon whose value is $g_s = 5.586$ for protons and $g_s = -3.826$ for neutrons, and g_l, the orbital g-factor with values $g_l = 0$ for neutron and $g_l = 1$ for proton. The interaction Hamiltonian can be expanded in multipole forms

$$H_{int} = \sum_{\lambda\mu} a_{\lambda\mu}\hat{Q}_{\lambda\mu} + b_{\lambda\mu}\hat{M}_{\lambda\mu} \tag{3.48}$$

with the electric operator

$$\hat{Q}_{\lambda\mu} = \int \rho(\vec{r})r^\lambda Y_{\lambda\mu}(\theta,\varphi)d^3r = \sum_{i=1}^{A} e_i r_i^\lambda Y_{\lambda\mu}(\theta_i,\varphi_i) \tag{3.49}$$

and magnetic operator

$$\hat{M}_{\lambda\mu} = \int \mu(\vec{r}).\nabla(r^\lambda Y_{\lambda\mu}(\theta,\varphi))d^3r = \frac{\mu_N}{\hbar}\sum_{i=1}^{A}\left[\frac{2}{(\lambda+1)}g_{l,i}\vec{l}_i + g_{s,i}\vec{s}_i\right].\nabla_i(r_i^\lambda Y_{\lambda\mu}(\theta_i,\varphi_i)) \tag{3.50}$$

The transition probability denoted by T_{fi} per unit of time, from an initial nuclear state $|\Psi_i>$ to a final state $|\Psi_f>$ which proceeds by a multipole component of degree λ and order μ of the radiation field from either an electric or a magnetic source, designated by σ, is given by Fermi golden rule:

$$T_{fi}^{\sigma\lambda\mu} = \frac{2\pi}{\hbar}| < \Psi_f|H_{int}(\sigma\lambda\mu)|\Psi_i > |^2\rho(E_f) \tag{3.51}$$

where $H_{int}(\sigma\lambda\mu)$ is the perturbative interaction between the nuclear and electric fields that stimulates the transition and $\rho(E_f)$ is the product of the densities of the final nuclear and electromagnetic states. After some rigorous mathematical treatment, the expression reduces to (see for eg. ref. [48])

$$T_{fi}^{\sigma\lambda\mu} = \frac{8\pi(\lambda+1)}{\hbar\lambda[(2\lambda+1)!!]^2}\left(\frac{E_\gamma}{\hbar c}\right)^{2\lambda+1} |<\Psi_f|\hat{O}_{fi}(\sigma\lambda\mu)|\Psi_i>|^2 \tag{3.52}$$

where E_γ is the energy of the transition and $\hat{O}_{fi}(\sigma\lambda\mu)$ is the multipole transition operator whose form is given in eq 3.49 and 3.50, $|\Psi>=|\xi Im>$, a nuclear state with I and m as the total angular momentum and the magnetic quantum numbers, and ξ representing the rest of the quantum numbers.

Since different orientations of the angular momenta are usually not observed separately when the initial state is not polarized, hence averaging over the initial substates and summing over all the final magnetic substates (m-values) and all the μ-values of the field the transition probability becomes

$$T_{fi}^{\sigma\lambda} = \frac{1}{2I_i+1}\sum_{m_i,m_f,\mu} T_{fi}(\sigma\lambda\mu) \tag{3.53}$$

It is useful to define a quantity called the reduced transition probability $B(\sigma\lambda; I_i \rightarrow I_f)$ which is the sum over of all the final states $|\xi I_f m_f>$ and the μ-values of the transition operator $\hat{O}(\sigma\lambda\mu)$ for a given initial state $|\xi I_i m_i>$

$$B(\sigma\lambda; I_i \rightarrow I_f) = \sum_{\mu m_f} |<\Psi_f|\hat{O}(\sigma\lambda\mu)|\Psi_i>|^2 = \frac{1}{2I_i+1}|<\Psi_f||\hat{O}(\sigma\lambda)||\Psi_i>|^2 \tag{3.54}$$

where $<\Psi_f||\hat{O}(\sigma\lambda)||\Psi_i>$ is referred as the reduced matrix element. The equation 3.52 becomes

$$T_{fi}^{\sigma\lambda} = \frac{8\pi(\lambda+1)}{\hbar\lambda[(2\lambda+1)!!]^2}\left(\frac{E_\gamma}{\hbar c}\right)^{2\lambda+1} B(\sigma\lambda; I_i \rightarrow I_f) \tag{3.55}$$

The B values contain information about the nuclear wave function and is often expressed in Weisskopf single-particle estimates (WE). Weisskopf assumed that the transition in the nuclear states results from a change in the electric charge and electric current distributions due to a single proton inside a nucleus with a uniform mass density. The reduced transition probabilities from the single-particle limit are given by:

$$B_{sp}(E,\lambda) = \frac{1}{4\pi}\left[\frac{3}{(\lambda+3)}\right]^2 r_0^{2\lambda} A^{2\lambda/3} \quad [e^2 fm^{2\lambda}] \tag{3.56}$$

$$B_{sp}(M,\lambda) = \frac{10}{\pi}\left[\frac{3}{(\lambda+3)}\right]^2 r_0^{(2\lambda-2)} A^{(2\lambda-2)/3} \quad [\mu_n^2 fm^{(2\lambda-2)}] \tag{3.57}$$

These estimates serve as references for the observed transition rates. A transition occurring more rapidly than the single-particle rate is said to be more collective as many particles participate in the process. On the contrary, if a slower transition rate than the WE suggests a smaller overlap between the initial and final nuclear states. It is a common practice to designate a transition in Weisskopf units (W.u.) by taking the ratio of the observed decay rate to the WE rate.

The following selection rules (from angular momentum and parity conversations) apply for a transition from an initial state $|I_i m_i>$ to $|I_f m_f>$:

$$\begin{gathered} |I_i - I_f| \leq \lambda \leq I_i + I_f \\ m_f - m_i = m \\ \pi_i \pi_{\sigma\lambda} \pi_f = 1 \end{gathered} \tag{3.58}$$

EL	$T(E\lambda)\,[s^{-1}]$	$B_{sp}(E\lambda)\,[e^2 fm^{2\lambda}]$	$T_{sp}(E\lambda)\,[s^{-1}]$
$E1$	$1.587\times10^{15}E^3B(E1)$	$6.446\times10^{-2}A^{2/3}$	$1.023\times10^{14}E^3A^{2/3}$
$E2$	$1.2233\times10^{9}E^5B(E2)$	$5.940\times10^{-2}A^{4/3}$	$7.265\times10^{7}E^5A^{4/3}$
$E3$	$5.698\times10^{2}E^7B(E3)$	$5.940\times10^{-2}A^{2}$	$3.385\times10^{1}E^7A^{2}$
$E4$	$1.694\times10^{-4}E^9B(E4)$	$6.285\times10^{-2}A^{8/3}$	$1.065\times10^{-5}E^9A^{8/3}$
$E5$	$3.451\times10^{-11}E^{11}B(E5)$	$6.928\times10^{-2}A^{10/3}$	$2.391\times10^{-12}E^{11}A^{10/3}$

(a)

ML	$T(M\lambda)\,[s^{-1}]$	$B_{sp}(M\lambda)\,[\mu_n^2 fm^{(2\lambda-2)}]$	$T_{sp}(M\lambda)\,[s^{-1}]$
$M1$	$1.779\times10^{13}E^3B(M1)$	$1.790\times A^{0}$	$3.184\times10^{13}E^3$
$M2$	$1.371\times10^{7}E^5B(M2)$	$1.650\times A^{2/3}$	$2.262\times10^{7}E^5A^{2/3}$
$M3$	$6.387\times10^{0}E^7B(M3)$	$1.650\times A^{4/3}$	$1.054\times10^{1}E^7A^{4/3}$
$M4$	$1.899\times10^{-6}E^9B(M4)$	$1.746\times A^{2}$	$3.316\times10^{-6}E^9A^{2}$
$M5$	$3.868\times10^{-13}E^{11}B(M5)$	$1.924\times A^{8/3}$	$7.442\times10^{-13}E^{11}A^{8/3}$

(b)

Table 3.2: Most significant (a) Electric and (b) Magnetic transition probabilities of multipolarity λ. The transition energies are given in [MeV].

where, $\pi_{\sigma\lambda}$ is the parity of the multipole radiation; for electric transition $\pi_{E\lambda} = (-1)^{\lambda}$ and $\pi_{M\lambda} = (-1)^{\lambda+1}$ for magnetic transition. Also, note that since the spin and parity of a photon is $1^{(-1)}$, $\Delta\lambda = 0$ transitions are forbidden. E0 transition proceeds via internal conversion process (discussed below). Since no magnetic monopole is known to exist, there are no M0 transitions. From table 3.2, few observations can be made. The transition probabilities decrease with increasing multipolarity. For transitions with small energy differences, the transition probabilities also decrease, and the internal conversion process becomes more and more important. For a given transition energy, the magnetic transition is weaker than its electric counterpart. Often there is a competition between electric and magnetic transitions; for example, E2 transitions compete with M1 transitions. This competition is expressed using a quantity called the multipole mixing ratio $\Delta(E2/M1)$. It is defined as [110]

$$\Delta(E2/M1) = \frac{<\Psi_f||\hat{Q}2||\Psi_i>}{<\Psi_f||\hat{M}1||\Psi_i>} \quad \left[\frac{efm^2}{\mu_N}\right] \tag{3.59}$$

This ratio is an important measurable quantity which serves as a test for nuclear models. Experimentally, a dimensionless quantity $\delta(E2/M1)$ is used which is related to the mixing ratio by

$$\delta(E2/M1) = \sqrt{\frac{T_{i\to f}(E2)}{T_{i\to f}(M1)}} = 0.835E_{\gamma}|\Delta(E2/M1)| \tag{3.60}$$

where, E_{γ} is given in MeV and since the sign of the mixing ratio is not known a priori, absolute value of $|\Delta(E2/M1)|$ is taken.

3.4.2 Electromagnetic transitions in deformed systems

The electric multipole moments describe the charge distribution of the nucleus. In an axially symmetric deformed nucleus because of parity conservation, the odd moments vanish. For the lowest order deformation

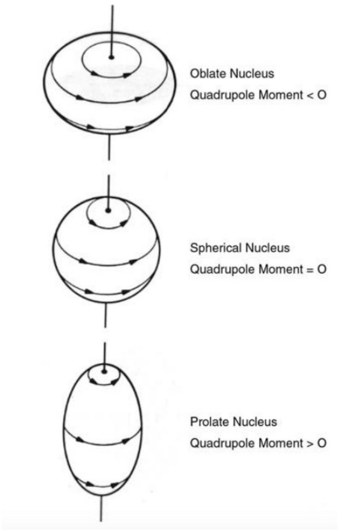

Figure 3.5: Schematic representations of quadrupole deformations [59].

the electric quadrupole moment becomes the primary measure of the deviation of the nuclear charge distribution away from spherical symmetry. Hence, the observation of large quadrupole moments is a direct proof of the existence of stable deformed nuclei. The intrinsic quadrupole moment Q_0 in the body-fixed frame of an ellipsoid nucleus is given by:

$$Q_0 = \int (3z^2 - r^2)\rho_e(r) d^3r \tag{3.61}$$

where $\rho_e(r)$ is the charge distribution in the nucleus, sensitive to the nuclear shape. The intrinsic quadrupole moment can be related to the deformation parameter β by

$$Q_0 = \frac{3}{\sqrt{5\pi}} Z R_0^2 \beta (1 + 0.36\beta) \quad [eb] \tag{3.62}$$

where R_0 is the average nuclear radius. By convention, Q_0 is positive for a prolate nucleus and negative for an oblate nucleus (see fig. 3.5). The experimentally measured quadrupole moment Q (in the laboratory frame) is related to the intrinsic value by

$$Q = Q_0 \frac{3K^2 - I(I+1)}{(I+1)(2I+3)} \tag{3.63}$$

To make the quadrupole moment independent of charge and radius, the reduced quadrupole moment

$$Q_{red} = \frac{Q}{ZeR_0^2}$$

is used to compare the deformations of nuclei with different mass numbers.

Experimental transition rates provide a measure of the quadrupole moment of the nucleus. For transitions between two members of a rotational band with M1 or E2 transitions, the $B(L, I_i \rightarrow I_f)$- values are given by the following equations:

$$B(M1; I_i \rightarrow I_f) = \frac{3}{4\pi} (g_K - g_R)^2 K^2 < I_i K 10 | I_f K >^2 \quad \text{for} K > 1/2 \quad [\mu_n^2] \tag{3.64}$$

$$B(E2; I_i \rightarrow I_f) = \frac{5}{16\pi} Q_0^2 < I_i K 20 | I_f K >^2 \quad [(eb)^2] \tag{3.65}$$

where, the last terms in <> are the Clebsch-Gordon coefficients, g_R is the gyromagnetic ratio which corresponds to the magnitude of the magnetic moment of the nucleus because of the rotating core, $g_R \approx qZ/A$ with q in the range [0.7, 1] called the quenching factor and g_K, the gyromagnetic ratio due to the valence particle(s).

In a deformed and axially symmetric nucleus, collective rotation of many particles around an axis perpendicular to the symmetry axis can construct high angular momentum states. If the Coriolis effects are large, breaking of pairs can occur, and the individual angular momenta of unpaired particles are aligned with the rotation. Nucleons in high j orbitals and small projection of j on the symmetry axis (Ω) experience more Coriolis force than the nucleons with large Ω. Coupling of the projections of all individual quasiparticles results in the total projection K on the symmetry axis:

$$K^\pi = \sum_{i=1}^{n} \Omega_i^{\prod \pi_i}$$

where n is the number of quasiparticles equal to the number of unpaired nucleons.

If there are n quasiparticles, then g_K in expression 3.64 becomes $K g_K = \sum_{i=1}^{n} \Omega_i g_{\Omega^i}$ and the following angular momentum coupling rules (Gallagher rules) [111, 112] apply to the Nilsson states represented by the quantum numbers N, n_z, Λ, and Σ (defined in section 2.2.3)

$$\Omega = |\Omega_1 - \Omega_2|, \quad \text{if} \quad \Omega_1 = \Lambda_1 \pm \frac{1}{2} \Omega_2 = \Lambda_2 \pm \frac{1}{2};$$

$$\Omega = \Omega_1 + \Omega_2, \quad \text{if} \quad \Omega_1 = \Lambda_1 \pm \frac{1}{2} \Omega_2 = \Lambda_2 \mp \frac{1}{2};$$

The calculated g_K values relevant to this study are given in table 3.3. Experimentally, the ground state magnetic moment of ^{253}No is $\mu = -0.527(33)\,\mu_N$ and the quadrupole moment is $Q = +5.9(1.4)\,eb$ [65]. The g_K value is related to the magnetic moment by

$$\frac{\mu}{\mu_N} = g_K \frac{I^2}{I+1} + g_R \frac{I}{I+1} \tag{3.66}$$

where the rotational g factor is limited to $0.7Z/A \geq g_R \geq Z/A$ giving an average value $g_K = -0.22(5)$ [65] which agrees with the theoretical value for the 9/2$^-$[734] configuration given in table 3.3.

Configuration	g_K
neutron	
9/2$^-$[734]$_\nu$	-0.246
7/2$^+$[624]$_\nu$	0.275
5/2$^+$[622]$_\nu$	-0.406
11/2$^-$[725]$_\nu$	-0.406
proton	
7/2$^-$[514]$_\pi$	0.63
9/2$^+$[624]$_\pi$	1.296
1/2$^-$[521]$_\pi$	-0.828

Table 3.3: Relevant single-particle g_K values (Woods-Saxon).

For transitions from an initial state i to different final states $f_1, f_2, f_3, ...$ of a rotational band due to a given multipole radiation $L < K_i + K_f$, the branching ratios depend only on the geometrical factors, written as follows [113]

$$\frac{B(\sigma L, I_i \to I_{f_1})}{B(\sigma L, I_i \to I_{f_2})} = \frac{< I_i L K_i \Delta K | I_i L I_{f_1} K_f >^2}{< I_i L K_i \Delta K | I_i L I_{f_2} K_f >^2} \tag{3.67}$$

where, $\Delta K = K_f - K_i$ and $< I_i L K_i \Delta K | I_i L I_f K_f >$ is the Clebsch Gordon (vector addition) coefficient for $I_i + L = I_f$.

3.4.3 Internal conversion process

Besides γ-ray decay, an excited nucleus can de-excite through another competing process known as internal conversion (IC). This process occurs when an excited nucleus interacts electromagnetically with an orbital electron thereby ejecting it. Emission of characteristic X-rays or Auger electrons follows subsequently. The transfer of the nuclear excitation energy to the electron is a direct radiationless process that occurs via the Coulomb interaction, not a two-step process in which the nucleus first de-excite by emitting a gamma ray that knocks out an orbital electron in the second step. The IC probability depends entirely on the density of the atomic electrons inside the nucleus. The kinetic energy of the internally converted electron is given by:

$$T_{ICE} = E_{transition} - B_{Se-} \tag{3.68}$$

where B_{Se-} corresponds to the electron binding energy in shell S.

As the Coulomb interaction drops with increasing distance between the orbital electron and the nucleus, so does the IC transition probability. Hence, in general we find conversion of K electrons to be more dominant than the L electrons than the M electrons and so forth. The competition with the gamma-ray emission is characterized by the internal conversion coefficient defined as:

$$\alpha = \frac{\text{no of internal conversion decays}}{\text{no of gamma decays}} = \frac{T_{IC}}{T_\gamma} \tag{3.69}$$

The total enhanced electromagnetic transition rate is then given by

$$T_{I_i \to I_f} = T_\gamma + \sum_{i=K} T_{ICE,i} = T_\gamma(1 + \alpha_{tot}) \tag{3.70}$$

where i represents the electronic shell from which an electron is ejected and α_{tot} is the total conversion coefficient calculted by summing the internal conversion coefficients of all the shells involved in the IC transition:

$$\alpha_{tot} = \alpha_K + \alpha_L + \alpha_M + ... \tag{3.71}$$

The observed lifetime $T_{1/2}^{observed}$ of an excited nuclear state is then given by

$$T_{1/2}^{observed} = \frac{ln(2)}{(1 + \alpha_{Tot})T_\gamma} \tag{3.72}$$

If there are N branches of γ decay, the partial half-life of an individual transition j, $T_{1/2}^{\gamma,j}$ is given by [114]:

$$T_{1/2}^{\gamma,j} = T_{1/2}^{observed} \times \frac{\sum_{i=1}^{n} I_\gamma^i (1 + \alpha_{Tot}^i)}{I_\gamma^j} \tag{3.73}$$

For a mixed multipolarity transition, such as E2 and M1 which compete significantly, the conversion coefficient is obtained from the formula:

$$\alpha_{mixed}(\sigma,\sigma') = \frac{\alpha(\sigma L) + \delta^2 \times \alpha(\sigma' L')}{1+\delta^2}, \quad L' > L. \tag{3.74}$$

where σ represents electric or magnetic character of the transition and δ is the mixing ratio defined in equation 3.60

It can been seen that the IC process becomes important for high Z nuclei, low energy transitions and high multipolarity transitions from the following equations derived from a non-relativistic calculation [59, 115]

$$\alpha(EL) = \frac{Z^3}{n^3}\left(\frac{L}{L+1}\right)\left(\frac{e^2}{4\pi\varepsilon_0\hbar c}\right)^4\left(\frac{2m_ec^2}{E}\right)^{L+5/2} \tag{3.75}$$

$$\alpha(ML) = \frac{Z^3}{n^3}\left(\frac{e^2}{4\pi\varepsilon_0\hbar c}\right)^4\left(\frac{2m_ec^2}{E}\right)^{L+3/2} \tag{3.76}$$

where Z is the atomic number, n is the principal quantum number of the ejected electron, $\left(\frac{e^2}{4\pi\varepsilon_0\hbar c}\right)$ is the fine structure constant. In an experiment, the X-ray intensity often serves as a good indication of the IC process when the ICE is not detected.

In this work, the conversion coefficients are calculated using the BRICC software [116], which incorporates the relativistic aspect as well. By comparing the ratio of the experimental ICE intensity and γ-ray intensity to the theoretical values, one can deduce the multipolarity and mixing ratio of the transition.

Atomic processes

The internal conversion process creates a vacancy in one of the inner shells or subshell (level) of the atom. The ionized atom relaxes through either a radiative or a non-radiative process. The vacancy created can be filled by electrons from higher energy levels emitting either a characteristic X-ray or an Auger electron. The energy of the emitted radiation is the electronic binding energy difference between two atomic levels involved in the process.

$$E_{Xray:i-j} = BE_i - BE_j \quad j > i \tag{3.77}$$

In the Auger electron emission process, the energy released in filling the vacancy in level i from a higher level j is transferred to an electron located in even more higher-level k, which then escapes from the atom

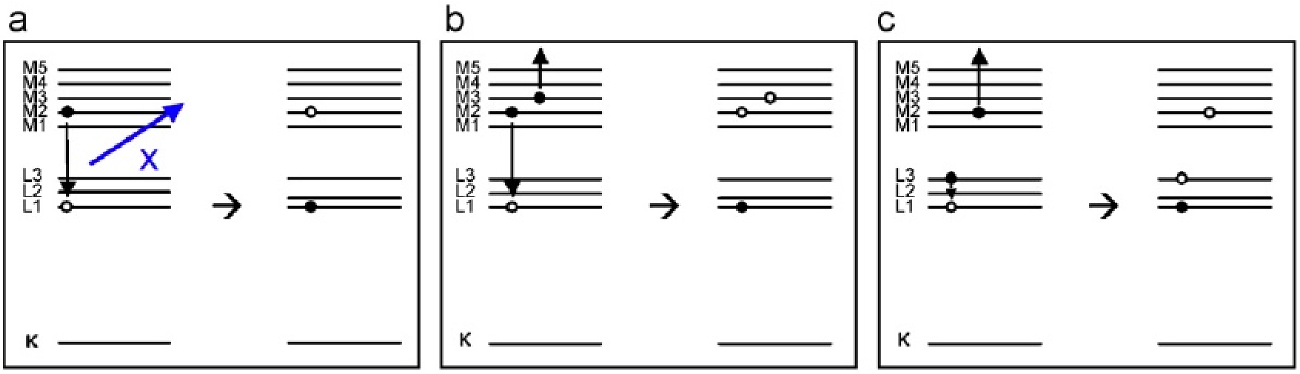

Figure 3.6: A schematic illustration of the processes to fill a vacancy in L1 subshell: a) X-ray fluorescence b) Auger process and b) Coster-Kronig process [117].

with an energy

$$E_{Ae-:i-jk} = BE_i - BE_j - BE_k \quad k > j > i \tag{3.78}$$

creating two secondary vacancies in the levels j and k. There is a special type of Auger process called the Coster-Kronig process in which the initial vacancy is filled from a higher subshell of the same shell instead of transition from a different shell, as in the case of Auger process. Fig. 3.6 illustrates these three atomic relaxation processes. A cascade of the vacancy filling processes follows after the creation of an initial vacancy. In the end, multiple vacancies are created in the outermost shell of the atom, leaving it highly ionized. If a vacancy is created in level i, then the probability to be filled by one of the processes is:

$$\omega_i + \alpha_i + f_i = 1 \tag{3.79}$$

where ω_i is the fluorescence yield, α_i is the Auger yield and $f_i = \sum_{j=i+1}^{k} f_{ij}$ is the sum of the Coster-Kronig yields f_{ij}. ω_i represents the probability of filling the vacancy in subshell i through a radiative transition, α_i corresponds to the probability of filling the vacancy through a non-radiative transition by an electron from the higher shell and f_{ij} is the probability that a vacancy in the subshell i is filled via the non-radiative transition from a higher subshell j located in the same major shell.

3.5 Isomers

An electromagnetic transition between two states with very different angular momenta is strongly hindered, stretching the decay lifetime significantly. These long-lived nuclear meta-stable states are called isomers, and their decays are formally known as isomeric transitions. In chemistry, the term isomers refer to ions or molecules with the same elemental composition but have different physical arrangements giving rise to distinct properties. In 1917, F. Soddy [118] first suggested the existence of states having "different stability and mode of disintegration" in a given nuclide. G. Gamow [119, 120] later refers to them as nuclear isomers analogous to chemical isomers. In 1921, O. Hahn [121] discovered nuclear isomerism in Uranium. And later in 1936, C. F. v. Weizsäcker [122] provided the theoretical explanation of the phenomenon. It then became an established fact that the protons and neutrons in nuclei can have different arrangements in their quantum orbits molding different metastable excited states (The history of nuclear isomerism can be found in ref. [123]). There are mainly three types of nuclear isomers: spin isomers, K

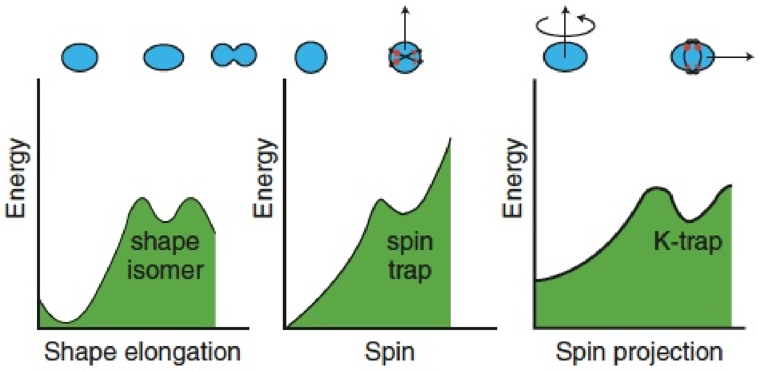

Figure 3.7: Secondary minima in the potential energy of a nucleus as a function of various nuclear variables lead to differentiate kinds of isomers [124].

isomers, and shape isomers (see fig. 3.7). Spin isomerism occurs when the decay from a higher excited state to a lower state is hindered because the transition requires a large change in nuclear spin. Therefore, to satisfy the spin selection rules, a high multipolarity L radiation needs to be emitted. The transition rate (see eq. 3.58) decreases with increasing L, forming spin traps. K isomers are observed in well-deformed nuclei and the isomerism occurs when a large change in the angular momentum orientation is required.

In axially deformed nuclei, the K quantum number is approximately conserved. For a transition from an initial state (K_i, I_i, π_i) to a final state (K_f, I_f, π_f) that involves a change in K, larger than the multipole order L, the transition are usually forbidden. K isomers are thereby formed. The multipolarity L of the transition must satisfy the K-selection rules:

$$\begin{gathered} |I_i - I_f| \leq L \leq I_i + I_f \\ \pi = \pi_i \pi_f \\ |K_i - K_f| = \Delta K \leq L \end{gathered} \tag{3.80}$$

The last selection rule is not as strict as the preceding ones and it is understood in terms of K mixing mechanism caused by Coriolis mixing, deviation from axial symmetry and level density [125]. The transitions that violate the last rule are called K-forbidden transitions, and the degree of K-forbiddenness is characterized by:

$$\nu = \Delta K - L \tag{3.81}$$

The other type of isomer is called the shape isomers, in which, the inhibition to the decay comes from the associated shape changes requiring substantial rearrangement of individual nucleon orbits. All the above three mechanisms influence, with varying degrees, the half-life of a given isomer that depends on the competing decay branches, transition energies, and multipole orders. The inhibition to the decay process is usually characterized by the Weisskopf hindrance factor defined as

$$F_W = \frac{T^{\gamma}_{1/2}}{T^{W}_{1/2}} \tag{3.82}$$

where $T^{\gamma}_{1/2}$ is the partial γ-ray half-life determined experimentally and $T^{W}_{1/2}$ is the half-life calculated from Weisskof single-particle estimates. In particular, for K isomers, a reduced hindrance factor (the hindrance

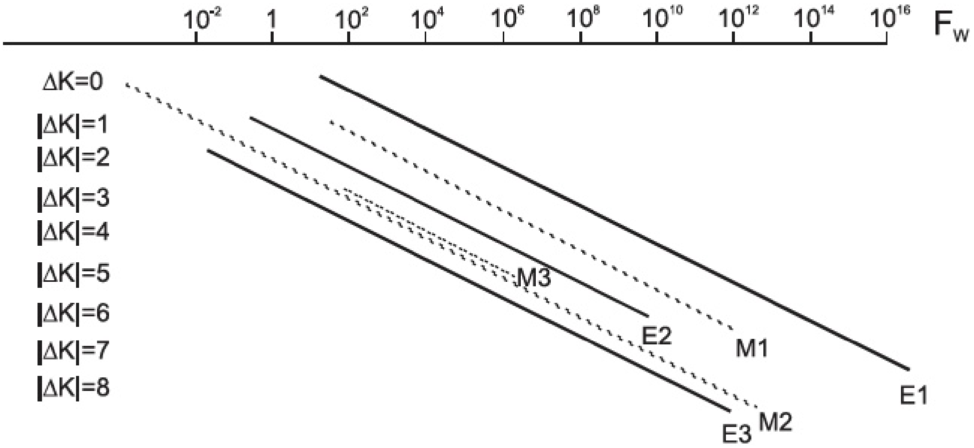

Figure 3.8: Trends of the hindrance factor F_W from the systematics of Lobner [125] for electromagnetic transitions of different multipolarities as functions of ΔK [126].

per degree of K-forbiddenness) is generally used which is defined as:

$$f_\nu = (F_W)^{1/\nu} \tag{3.83}$$

Based on Lobner's systematics [125] shown in fig. 3.8 and Rusinov's empirical rule given by equation 3.84, as a rule of thumb, one considers with each additional unit of ΔK, the hindrance factor F_W is increased by approximately a factor of 100.

$$\log F_W = 2(\Delta K - L) \tag{3.84}$$

Hence the reduced hindrance factor within the range $f_\nu \sim 30 - 300$ is usually used for assigning spin of a state [75]. However, small reduced hindrances $2 < f_\nu < 10$ observed in several cases (in ^{179}W [127], ^{172}Hf [128] for example), question the validity of the K quantum number [124]. Instead of a nuclear reorientation required for ΔK, involvement of a shape change was found to be a reason for such a rapid transition. The f_ν values can also become small for highly excited isomers as the level density increases with excitation energy resulting in more K mixing. The Coriolis effects can also induce K-mixing resulting in lower f_ν values (see ref. [124]).

3.5.1 Quasiparticle states in neighboring nuclei

The study of K isomers is important not only to access the single-particle structure near the Fermi level but also to access the states that cannot be populated in alpha decay. We expect to observe High-K quasiparticles states in ^{255}Rf as such states have been already observed in the neighboring even-even and odd A nuclei. See figs. 3.9 - 3.11, for instance, in ^{252}No, an 8^- isomer having configuration $\nu^2(7/2^+[624], 9/2^-[734])$ was observed feeding on to a vibrational band [129]. Similarly, in ^{254}No an 8^- isomer decaying to a 3^+ intermediate state was observed [13, 130].

And, analysis of recent data from Dubna has identified a 5^- isomer in ^{256}Rf, which previously was interpreted as K = 6 or 7 decaying to an intermediate 2^- structure [133]. In ^{254}Rf, two isomers were also observed and have been interpreted as two- and four-quasiparticle states that are highlighted in figure 3.10a which shows the energy and configurations of calculated high K states. In the isotone ^{253}No, the existence of a high-K isomer was first reported in ref. [41] and later in ref. [42]. The half-life of the isomeric state was found to be 0.7 ms and it was suggested that the decay goes through an intermediate structure based on the coupling of the odd neutron to the 3^+ 2-quasiparticle state observed in ^{254}No. The tentative partial level scheme is shown in fig. 3.11 where the high energy lines (802 keV and 714 keV) were observed in prompt emission at the target [126].

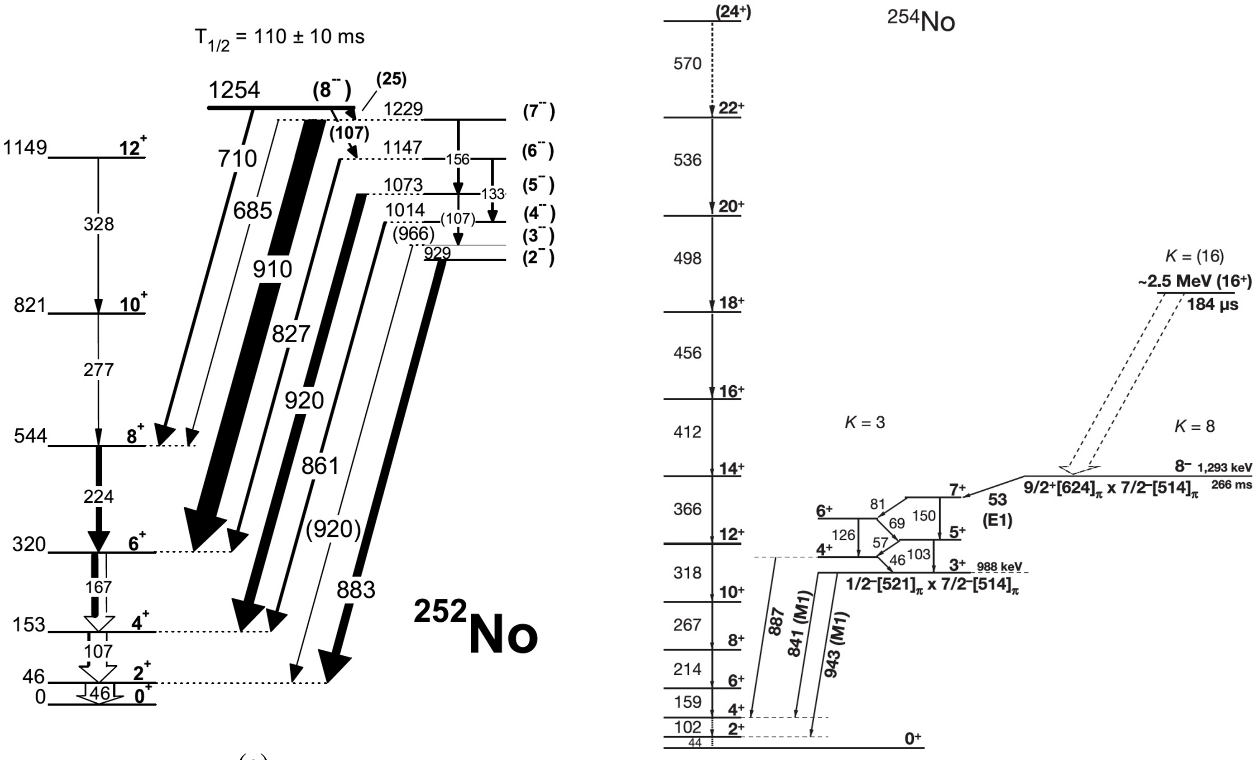

(a)

(b)

Figure 3.9: a) Decay scheme of the 8^- isomer in ^{252}No [129]. b) Decay scheme of the 8^- isomer in ^{254}No [13].

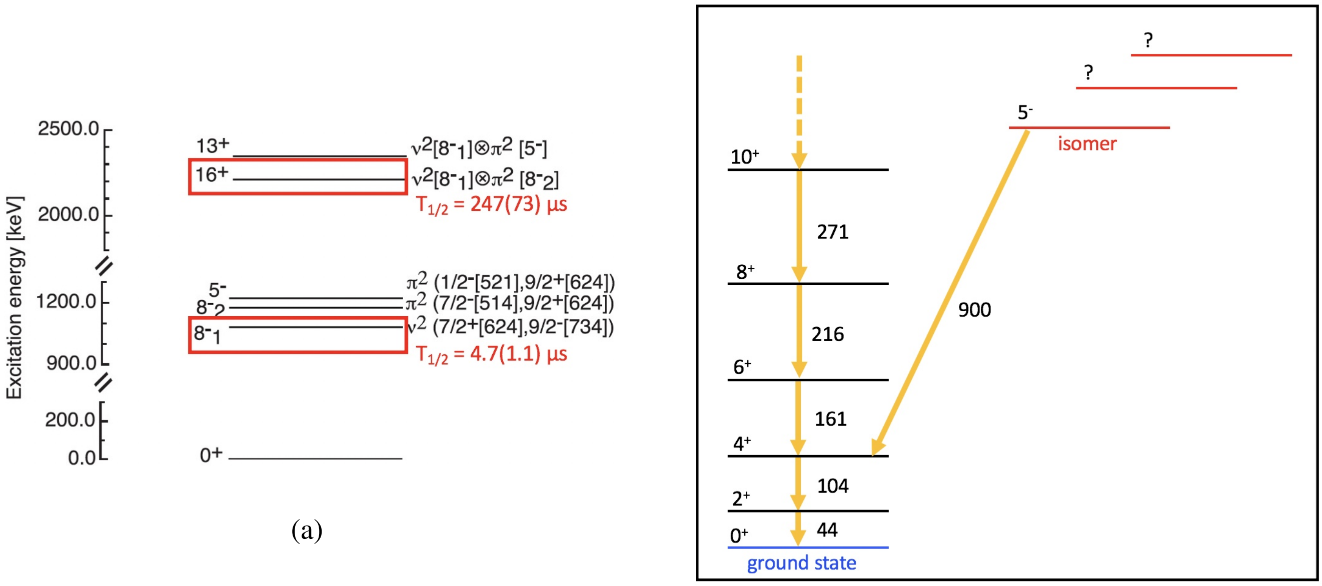

(a)

(b)

Figure 3.10: a) Suggested (highlighted with red square) two and four quasiparticle configurations for the isomers observed in ^{254}Rf [131]. b) Decay scheme of the lowest isomer observed in ^{256}Rf [134].

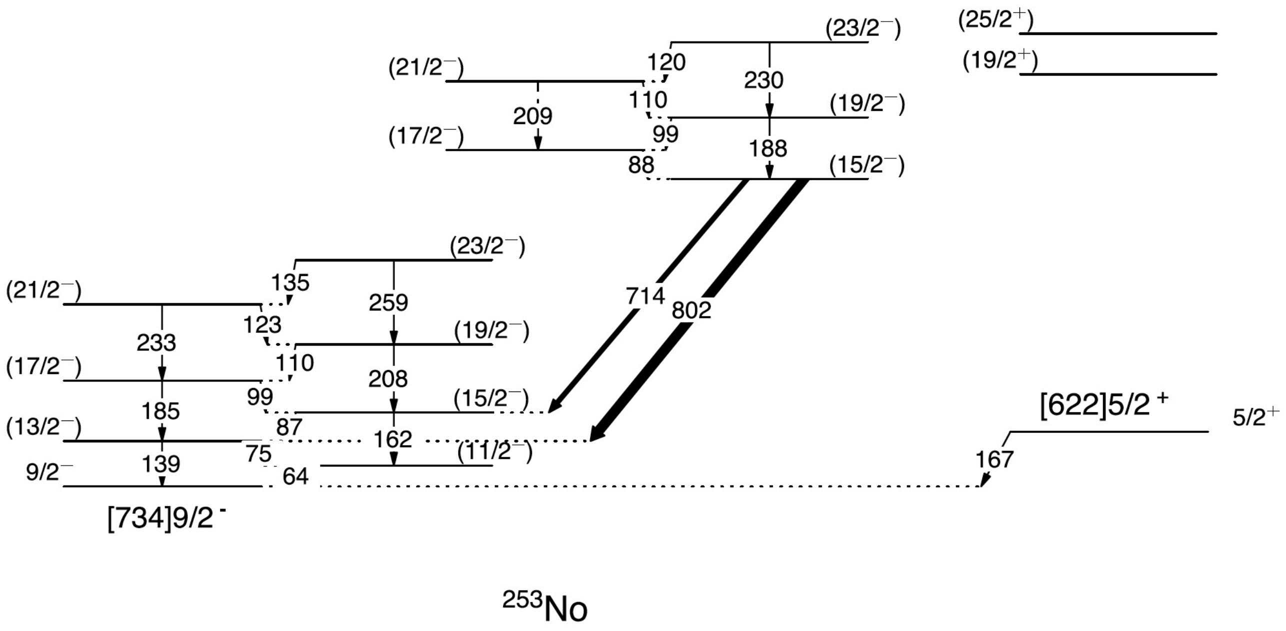

Figure 3.11: Tentative level scheme of ^{253}No [42].

Chapter 4

Experimental Techniques

The experiment was performed in two runs, first in May then in October (Oct) of 2017 at the Flerov Laboratory of Nuclear Reactions (FLNR), JINR, Dubna. The U400 cyclotron delivered an intense ^{50}Ti beam of average intensity 7.42(5) eμA in May and about 7.92(5) eμA in Oct. Using the following relation

$$\text{p}\mu\text{A} = \text{e}\mu\text{A}/\text{charge state}$$

the beam intensities are ≈ 337-370 pnA in May, and ≈ 360-396 pnA in Oct with $\approx 20^+ - 22^+$, the charge state of the ^{50}Ti ions. This also means about $\sim (2.1 - 2.3) \times 10^{12}$ ions/s were delivered in May and $\sim (2.2 - 2.5) \times 10^{12}$ ions/s in Oct. The beam impinged on a rotating ^{207}PbS target of thickness 0.4 mg/cm^2 (≈ 0.353 μm) mounted on a target wheel (see fig. 4.1). The target is deposited on a 1.5 μm thick Ti backing that faces the beam. The nuclei of interest, the evaporation residues (ERs) were produced in fusion evaporation reactions ^{207}Pb(^{50}Ti, xn), which were filtered and transported through the recoil separator SHELS [38] and delivered into the GABRIELA [37] detection system (see fig. 4.2). After passing through a Time of Flight (ToF) detector, the ERs are implanted into a position-sensitive detector located at the focal plane of the recoil separator, where their kinetic energies and their radioactive decays (alpha, spontaneous fission, gamma and IC) are measured.

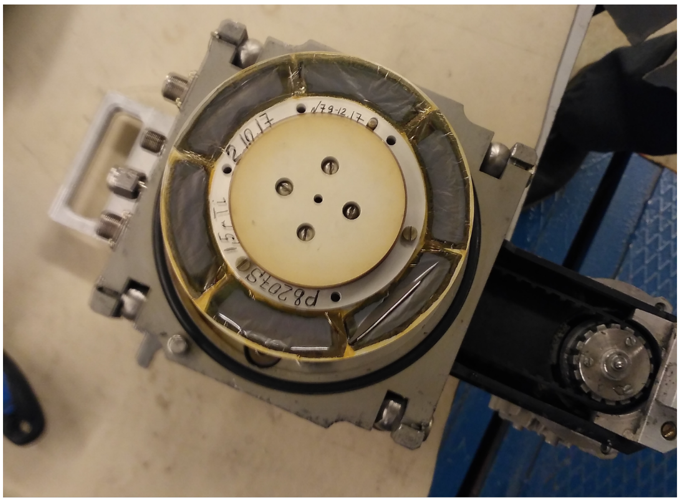

Figure 4.1: 6 ^{207}Pb target foils mounted on the rotating target wheel.

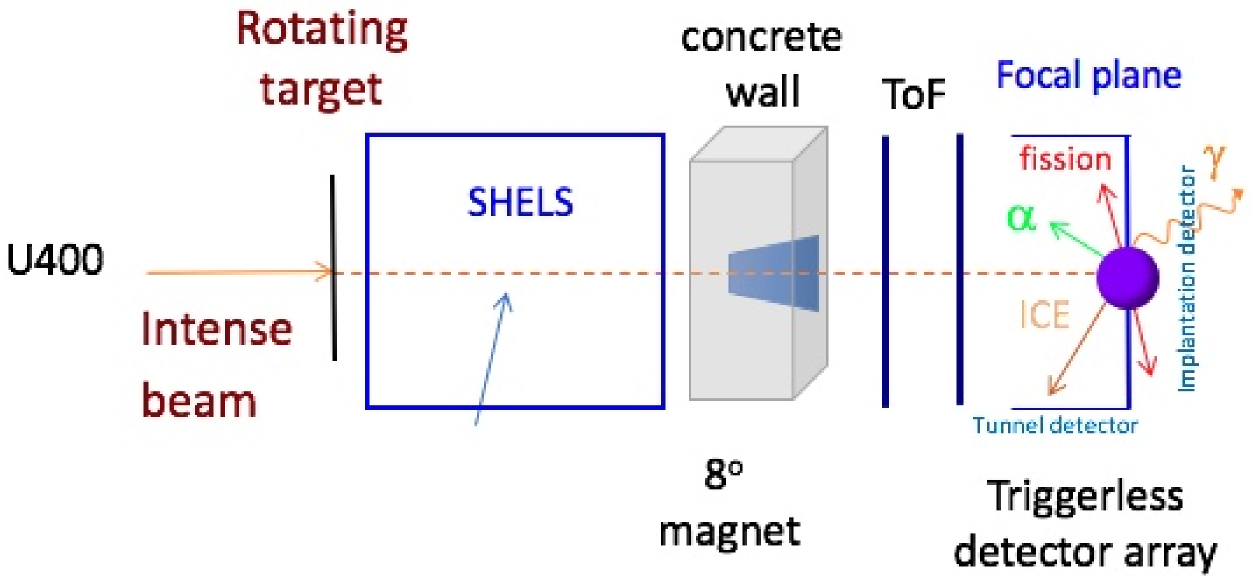

Figure 4.2: A schematic of the experimental setup.

4.1 Production: Fusion evaporation reactions

The first induced nuclear reaction in a laboratory was carried out by Rutherford in 1919 by colliding alpha particles with nitrogen [135]. Similar to a chemical reaction, the final products must be different from the initial ones in a nuclear reaction. Otherwise, the process is said to be a scattering process if the reactants only interact with no change in their nature. The possibilities of different induced nuclear reactions were limited as the alpha particles remained the only available projectile until the advent of accelerators around 1930. Depending on the entrance channel and the exit channel(s), many different kinds of reactions can take place. These are summarized in fig. 4.3a. The probability of each exit channel is measured by a quantity known as the cross-section of that channel. The reaction type we are interested in is known as fusion evaporation reaction. A projectile nucleus fuses with a target nucleus forming a compound nucleus (CN) in a highly excited state. The newly formed CN then cools down predominantly through the emission of neutrons, protons, and alpha particles depending on the excitation energy much like the cooling of water hence the term "evaporation". After most of the excitation energy is released the leftover nucleus is known as the evaporation residue. The deexcitation process can lead to the ground state or to an isomeric state. The basic mechanism is illustrated in fig. 4.3b. Complete fusion undergoes three stages: 1) the Coulomb barrier is overcome by the colliding nuclei. At this stage, usually quasi-elastic and deep-inelastic reactions channels dominate, resulting in projectile-like and target fragments in the exit channel. 2) The Captured system *Cap* is formed, the colliding nuclei can re-separate at this point i.e., quasi fission directly without the formation of a CN. 3) the excited CN cools down by emission of neutrons, charge particles, and gamma rays with a strong possibility to fission [137]. Fusion evaporation reactions have been the primary method of producing heavy elements in the past half a century. During the deexcitation process, the survival probability of the CN against fission determines the production cross-section of the heavy elements. The survivability of the CN is determined by its nuclear structure and the excitation energy. In the case of SHE, this probability is diminished as the fission barrier height is small because of the contribution from just the shell effects. It is therefore of paramount importance that the beam energy must be chosen optimally so that the maximum cross-section can be reached. Heavy nuclei production requires heavier targets and heavier projectiles, hence, powerful accelerators are needed to overcome the large Coulomb barriers. These days

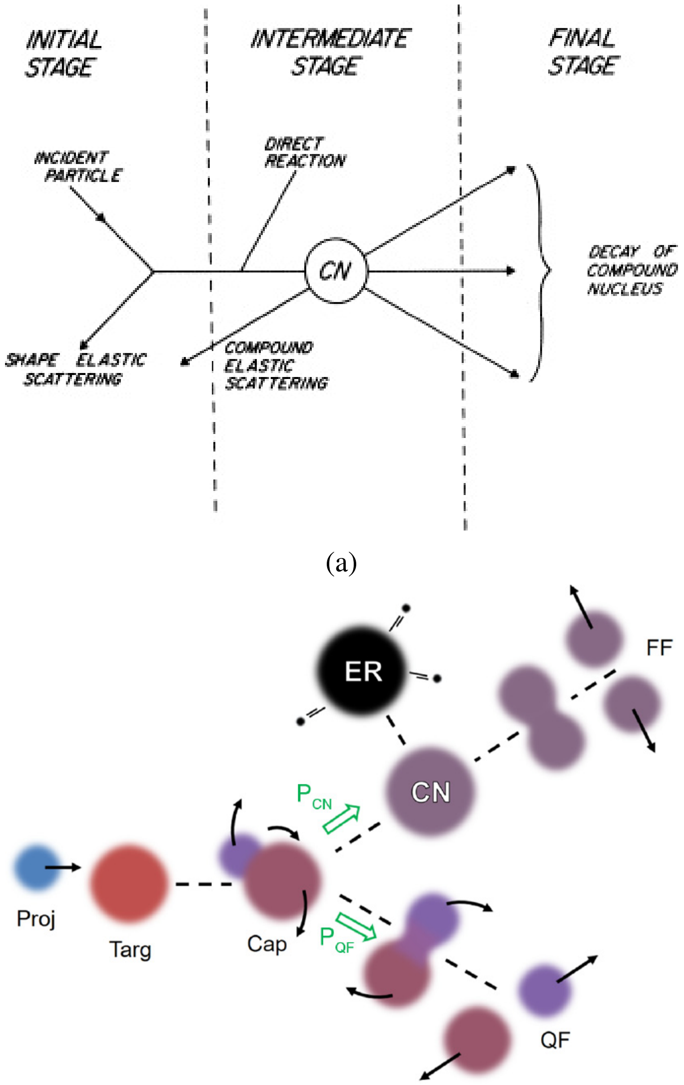

(a)

(b)

Figure 4.3: A schematic representation of (a) different reaction modes [136] (b) fusion evaporation reaction [137] (see the text for details).

a variety of beam and target combinations are available. Ion beams such as ^{22}Ne,^{40}Ar, ^{48}Ca, ^{50}Ti are used in combination with heavy-targets such as ^{208}Pb, ^{209}Bi, ^{238}U in our experiments. A sufficient amount of kinetic energy must be endowed to the projectile nucleus to overcome the Coulomb barrier between the two positively charged particles to form the compound nucleus. The excess collision energy then appears as excitation energy of the compound nucleus.

The Q value of a reaction whether it is an exothermic or endothermic reaction is:

$$Q = (M_{initial} - M_{final})c^2 = \Delta_{initial} - \Delta_{final} \tag{4.1}$$

where M represents mass and Δ represents mass-defect. The Q value is also equivalent to the difference in the kinetic energies (KE [MeV])

$$Q = KE_{final} - KE_{initial} = \Delta KE. \tag{4.2}$$

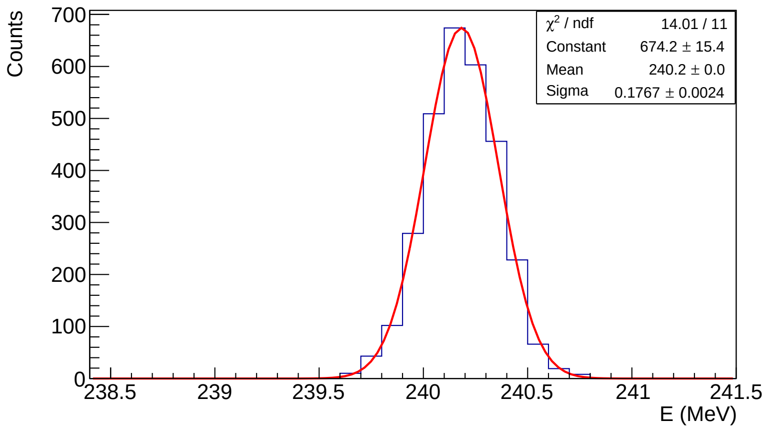

Figure 4.4: Energy distribution of 253 MeV ^{50}Ti ions after Ti backing and half lead target in SRIM [139] calculation. The red-curve is a Gaussian fit.

In an exothermic case ($Q > 0$), the kinetic energy of the final products is greater that of initial reactants implying that mass is converted into kinetic energy whereas in an endothermic case ($Q < 0$), the kinetic energy converts into mass hence a minimum threshold energy is required. In fusion evaporation reactions, the CN is left in an excited state and this excitation energy E^* can be easily determined from the above two relations in which $M^*_{CN} = M_{CN} + E^*$

$$E^* = \Delta KE + Q \tag{4.3}$$

Explicitly in terms of mass defect Δ [MeV], the excitation energy of the CN is given by

$$E^* = \Delta_{beam} + \Delta_{target} - \Delta_{CN} + KE_{beam} - KE_{CN} \tag{4.4}$$

The beam energy is known and the kinetic energy of the CN derived from the momentum conservation principle in non relativistic approach is

$$KE_{CN} = KE_{beam}\frac{M_{beam}}{M_{CN}}. \tag{4.5}$$

During the deexcitation process, in every stage of the neutron evaporation cascade the fission process competes. Hence, the production cross-section σ is often plotted as a function of the excitation energy. In our experiments, the average energy of the beam was about 253 MeV, and it loses about ≈ 11 MeV while passing through the Ti backing and about 1 MeV in half of the target material. These energy losses were estimated from SRIM [139] calculations (see fig. 4.4). Therefore, at the mid target, only about 240.2 MeV was available effectively for the reaction. From equation 4.5, we have,

$$KE_{CN} = 46.7 \quad \text{MeV}$$

and

$$Q = \Delta_{50Ti} + \Delta_{207Pb} - \Delta_{257Rf} = -169 \quad \text{MeV}$$

Using mass-defect values listed in AMDC mass table [140]. Hence, the excitation energy of the compound nucleus is found to be 23.7 MeV from equation 4.4.

In fig. 4.5 one can see that 2n evaporation channel is more probable than any other channel at the beam energy of ~ 240 MeV. Depending on the excitation energy of the CN, the fusion evaporation reactions

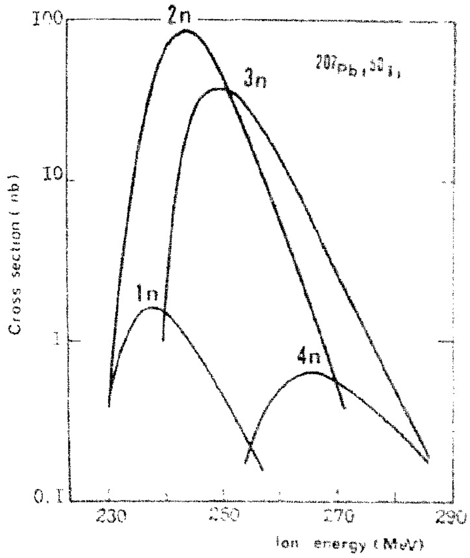

Figure 4.5: Calculated excitation functions of the reaction ^{207}Pb(^{50}Ti, xn)$^{257-\mathrm{xn}*}$Rf [138].

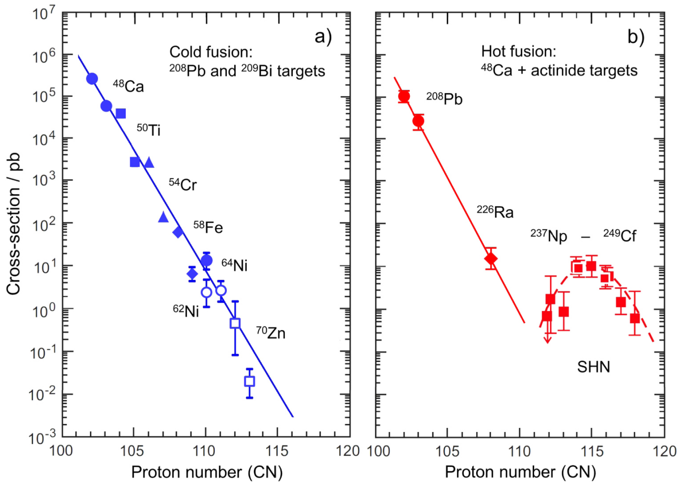

Figure 4.6: Measured cross sections for a) cold and b) hot fusion reactions [142].

are categorized into two types: cold fusion and hot fusion. In the hot fusion, the CN has high excitation energy and 3 to 5 neutrons are evaporated whereas, in cold fusion, the excitation energy is only sufficient to evaporate one or two neutrons [141]. Fig. 4.6 shows that the cross-section drops rapidly in both hot and cold fusion with increasing projectile proton number about an order of magnitude as Z increases by 2. In the case of hot fusion, the production cross-section is enhanced around $Z = 115$ of the CN from shell stabilizing effects.

4.2 Separation: SHELS

The separation of fusion reaction products can be performed by velocity filters. The separator SHELS [38] is comprised of two identical velocity filters, two focusing lenses and a deflector. It is an upgrade from VASSILISSA [143–145], which was a kinetic energy-based separator. The ion optical scheme of SHELS (shown in the fig. 4.7) can be described as QQQ-E-D-D-E-QQQ-D, where Q denotes magnetic Quadrupole lenses, E stands for Electrostatic dipole deflectors and D for magnetic dipoles. Each filter consists of a parallel flat plate electrostatic dipole and a magnetic dipole. The distance between the plates can be adjusted to optimally match the angular distribution and electric rigidity of the evaporation residues (ERs). The nominal deflection angle of ERs in the electric field is 8° and in the magnetic field ≈ 22°.

Each focusing lens consists of three quadrupole magnets. The first quadrupole triplets converge the beam of ERs emerging from the target, and the second triplet focuses the ERs onto the focal plane detector. The last dipole magnet with a deflection angle ≈ 8° situated inside a thick wall places the GABRIELA spectrometer away from the direct view of the target and the beam dump. This arrangement certainly drastically reduces a large fraction of beam-type background. SHELS has a transmission and detection efficiency of 40 % for ^{48}Ca and ^{50}Ti induced reactions [146–148].

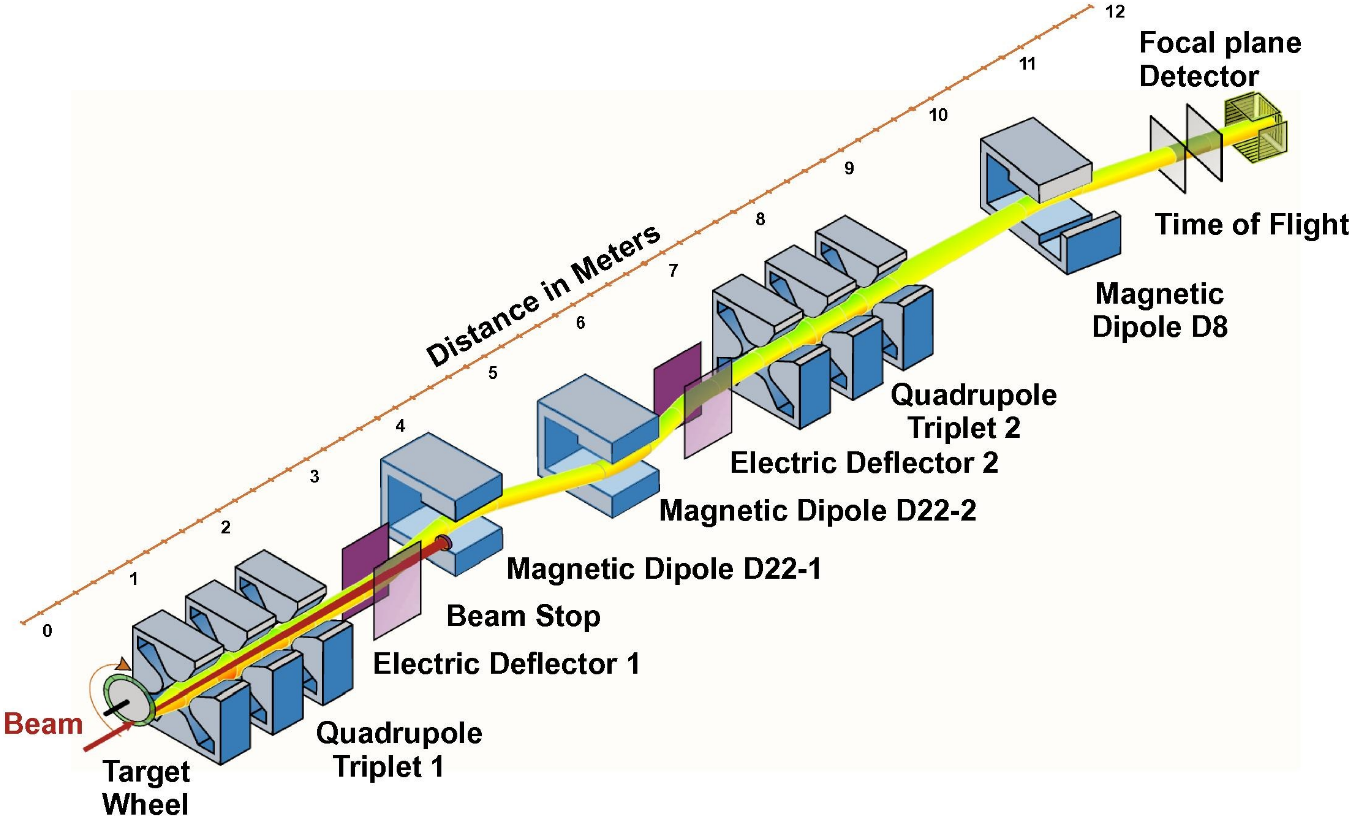

Figure 4.7: Ion optical scheme of SHELS [38].

4.3 Detection Setup: GABRIELA

The detection system is installed at the focal plane of the recoil separator. The detection system is sensitive to all the radioactive decay modes and capable of detecting gamma rays, alpha particles, beta particles, spontaneous fission fragments, and the kinetic energies of the ERs. Hence the detection system is rightly called GABRIELA [37] (Gamma Alpha Beta Recoil Investigations with the electromagnetic Analyser). It is composed of a Time of flight detector, a position-sensitive silicon detector where ERs are implanted shallowly, an array of silicon detectors forming a tunnel structure to detect escaping decay particles from the implantation detector and an array of germanium (Ge) detectors for detecting gamma radiations. The Ge detectors are equipped with bismuth germanate crystals represented by the chemical formula $Bi_4Ge_3O_{12}$, hence BGO in short. The setup is described in more detail in the following sections.

4.3.1 Time of Flight detector

After going through the separator and the bending magnet, the evaporation residues pass through a Time of Flight (ToF) detector in the experimental hall before their implantation into a silicon detector. The ToF detector serves as an identifier by providing a "flag" (MCP flag) to distinguish the recoil implants from the subsequent decays in the implantation detector. Although the resolution of the ToF does not allow the identification of similar mass nuclei, it is useful in separating the ERs from scattered beam and transfer products that have very different mass numbers from that of ERs. The ToF detector consists of two emissive foils made of 30-40 μg/ cm^2 of gold deposited on 40-50 μg/ cm^2 of polypropylene. Each foil is 102 mm wide and 90 mm long. In the experiment, the distance between the two foils can be changed as there are three foil slots in the ToF "box". Two microchannel plates (MCP) are placed perpendicular to each of the foils for collecting the secondary electrons released during the passage of an ER through the foil. The MCPs plates are made of highly resistive material and have ~ 5-10 μm diameter holes distributed over the surface. The holes on the MCPs are about ~ 15 μm apart from one another. When an ER ion passes through an emissive foil, a large number of electrons are emitted, which are then accelerated using an electric field and guided to the MCP plates by a magnetic field.

4.3.2 Implantation detector

After passing the ToF detector, the ERs pass through a Mylar foil. The Mylar foil is useful in reducing the background of scattered beam and the kinetic energies of the ERs for shallow implantation in the focal plane detector. A shallow implantation of the ERs is desirable to perform conversion electron spectroscopy in the tunnel detectors (see section 4.3.3 and 4.7). The implantation depths in the silicon detector can vary

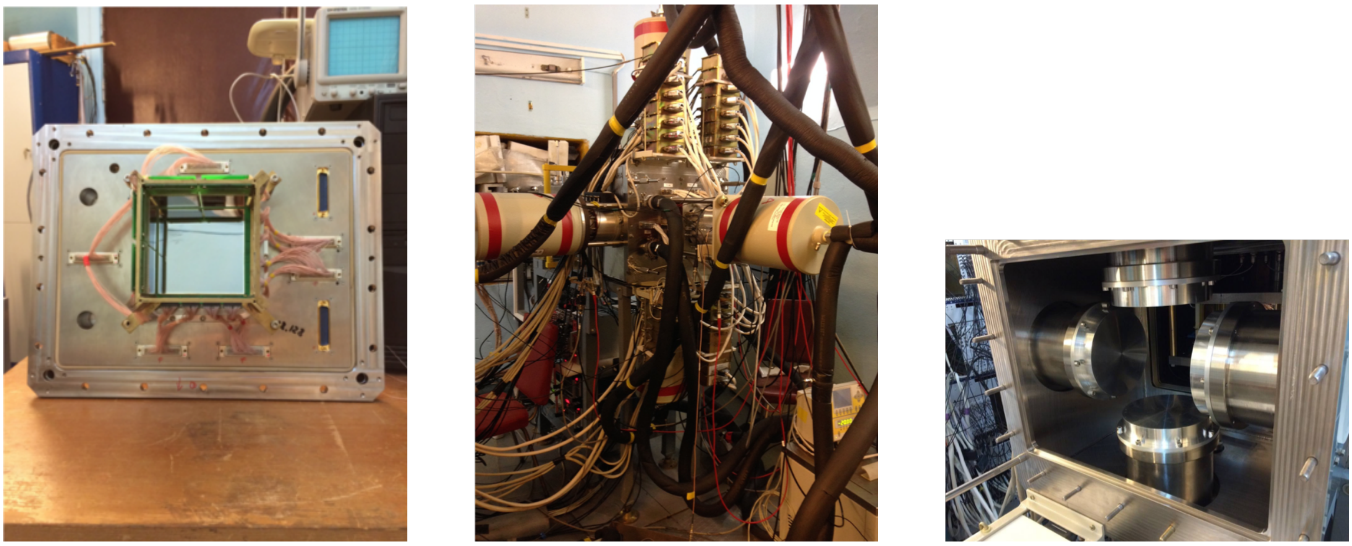
(a) (b) (c)

Figure 4.8: Photographs showing the components of the GABRIELA setup:(a) Implantation detector and tunnel DSSDs (b) Ge array and (c) Inside of the vacuum chamber showing 4 of the 5 inserts.

between 1-5 μm depending on the mass and the velocity of an ER. A method to estimate an average implantation depth is described in section 4.7.1. The implantation detector is a double-sided silicon strip detector (DSSD), providing position-sensitivity to an event, a requirement for genetic correlations among the events occurring in the detector. The DSSD has a dimension of 100.4 × 100.4 mm^2 with 128 vertical and 128 horizontal strips, constituting 16384 pixels for time and position correlations. In the May experiment, the DSSD had a thickness of 300 μm and in the Oct run, a 500 μm thick DSSD was utilized. The DSSD is sensitive to the incoming recoils and the decay particles: alpha particles, internal conversion electrons, and fission fragments. The thickness of the DSSD allows the detection of the decay particles emitted in the upstream directions. Hence, just from the geometrical argument, the efficiency of the implantation detector to detect alpha particles is roughly about 50% assuming the decay radiation emission is isotropic.

4.3.3 Silicon detector array for *ICE*-spectroscopy

In the upstream direction of the implantation detector, eight small DSSDs are arranged in a tunnel configuration and mounted perpendicular to the implantation detector (see fig. 4.8a). A brass cooling frame supports the Si detector array in this tunnel structure. They are designed to detect the alpha particles, electrons, and fission fragments that escape from the implantation detector. Each of the 50 × 60 mm^2 tunnel detectors is ∼ 0.7 mm thick and has 16 horizontal and 16 vertical strips. Angular correlations can be established for the decay particles that escape the implantation detector and get detected in the tunnel detectors. Taking into account the energy loss in the dead layers of the implantation detector and the tunnel detector, the energies of these escaped particles (especially applicable to α particles) can then be reconstructed from the angles of these events. Such event reconstructions have not been performed in this work.

4.3.4 Germanium detector array for gamma-spectroscopy

The gamma rays and X-rays are detected in the array of germanium detectors surrounding the focal plane of the separator. The array consists of four coaxial, cylindrical, large volume Hyper Pure Germanium detectors plus one clover [149]. The coaxial detectors are placed on each lateral side of the implantation detector and the clover is placed behind it (see fig. 4.8b). The clover consists of four tapered crystals, each 50 mm in diameter and 70 mm long. Two of the coaxial detectors are 73.1 mm long and 72.9 mm in diameter and the other two have a diameter of 72 mm and a length of 71.9 mm. The Ge detectors are equipped with uncollimated BGO Compton shields. The BGOs are 15 cm long and 15 mm thick. Special inserts into the vacuum chamber with 1 mm thick Aluminum windows (see fig. 4.8c) allow the Ge detectors to be placed close to the implantation detector. The BGO shields, when used in 'suppressed' mode, improve the peak-to-total (P/T) ratio by rejecting the gamma-ray events which Compton scatter out of the Ge detectors. They are also used in 'tagged' mode' when such Compton scattered gamma-ray events are tagged with a flag. The flag is ON only when the energy deposition in the BGO shields of the same detector is greater than the threshold set for the BGOs, which is about ≈30 keV. The Compton suppression mode allows identification of low energy and low intense gamma lines that could otherwise get submerged in the Compton background of higher energy and more intense lines when no such rejection is preferred. The use of BGO shields increases the "search" times for long-lived isomers by filtering out radiation coming from the concrete walls (natural radioactivity at higher energies for example ^{40}K) reducing the background radiation rate. Experimentally, the average P/T is extracted from the gamma-ray spectrum due to a single transition (obtained by using either gamma or electron coincidences) by taking the ratio of the peak intensity over the intensity of the whole spectrum. The average P/T with beam on target was found to be ~ 40-45 % (see section 4.9 and fig. 4.47).

Interaction of radiation with matter

Heavy charged particles traversing through matter primarily interact via the Coulomb force with the electrons and ions within the absorber material. Depending on the strength of the interactions, the medium's atoms can become excited or ionized at the expense of kinetic energy by the charged particle. The charged particle slows down in the absorber medium and finally comes to rest after traveling a particular range.

In addition to Coulomb interactions, a fast electron can lose energy through the bremsstrahlung radiative process, which is negligible in the case of heavy charged particles. The electrons also suffer backscattering as they can be deflected easily in large angles along their tracks. It becomes more significant for electrons with low incident energy and absorber with a high atomic number. This phenomenon has a significant impact on the response of a detector as the backscattered electrons escape complete detection.

Gamma rays lose their energies mainly via photoelectric effect, Compton scattering, and pair production. In the photoelectric process, a photon is absorbed in an atom followed by emission of an electron with energy equal to $E_{e-} = E_\gamma - E_{shell}$ where E_{shell} is the binding energy of the atomic shell from where the photoelectron is emitted. As the energy and momentum cannot be simultaneously conserved, this phenomenon cannot occur with free electrons and, therefore, the radiation is always absorbed by bound electrons as the nucleus can absorb the recoil momentum. However, Compton scattering of photons can occur on free electrons. The electrons in matter can be approximated as free when the photon energy is very high compared to the binding energy. In this process, a portion of the photon's energy is transferred to the electron that deflects it from its original course. The energy loss ΔE_γ by the incident photon can vary from zero to a large fraction of the original energy E_γ since the scattering of the photon by the electron is possible in every direction. Assuming the electron is at rest, this energy loss is given by the expression:

$$\Delta E_\gamma = E_\gamma \left(1 - \frac{1}{1 + \frac{E_\gamma}{m_e c^2}(1 - cos\theta)} \right)$$

where m_e is the rest mass of the electron and θ is the angle with which the photon has defected from its original direction.

For a photon with energy greater than twice the rest-mass energy of an electron, its transformation into an electron-positron pair is energetically favorable given that the conservation of momentum is facilitated by the presence of a third body, which is usually a nucleus. The excess energy of the photon $E_\gamma - 2m_e c^2$ appears as the kinetic energy of the $e^- e^+$-pairs. The positron travels through the medium losing its energy and finally annihilates after coming in contact with an electron producing two annihilation photons having energy equal to 511 keV. Fig. 4.9 describes which of these three processes become important at different photon energies in different absorbing materials.

4.3.5 Basic working principles of the semiconductor detectors

In many radiation detection applications, solid-state detectors are preferable simply because their sizes can be kept smaller as the high energy radiation can give off their energy in a relatively small dimension. Semiconducting materials (Si, Ge) are generally used to make solid-state ionization chambers. Semiconductors are normally poor electrical conductors. However, the charged particles created by ionizing radiation can be collected by applying external voltage. A block of metal cannot be used as a detection medium because even without ionizing radiation, a large current would flow through the material. In the other extreme case,

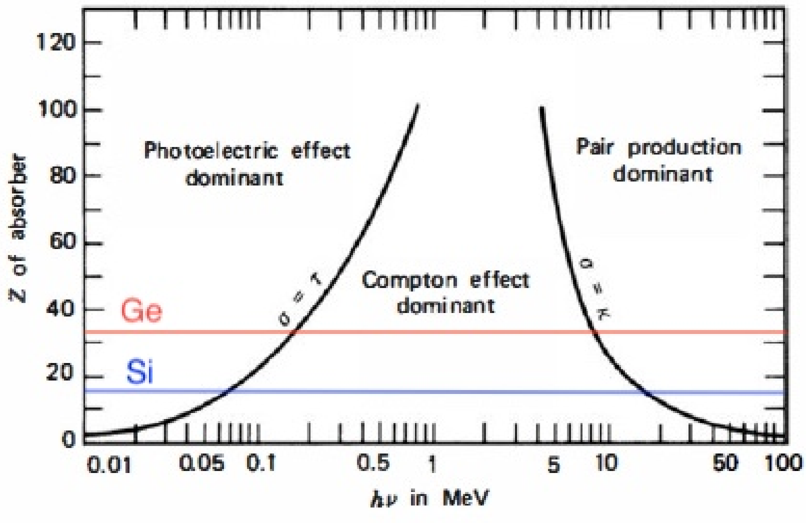

Figure 4.9: Variation of the relative dominance of the three types of gamma-ray interactions at different gamma-ray energies *hv* for different absorber of atomic number Z [150].

insulators are not suitable detector materials either, because they do not conduct even in the presence of ionizing radiation. An energy band structure (consisting of a valence band, a forbidden energy gap, and a conduction band) for the electrons originates from the arrangements of atoms in the solid. Electrons in the valence band are bound to the parent atoms; however, if they are promoted to the conduction band, they become free to roam about the entire crystal. At room temperature, a few electrons thermally excited electrons to jump into the conduction band, leaving vacancies (holes) in the valence band. From a neighboring atom, a valence electron can fill up the original hole, leaves a hole in the neighboring position. Repetition of this process causes the hole to appear moving through the crystal. In a semiconductor, therefore, there are two charge carriers: free electrons in the conduction band and holes in the valence band. The number of one kind of the charge carriers in the intrinsic semiconductor is increased by doping with small amounts of trivalent or pentavalent atoms. If the dopant is pentavalent, the extra electron of the impurity atom that could not participate in 4 covalent bond formation resides in a discrete energy level close (0.01 eV for germanium and 0.05 eV for silicon) to the conduction band. Since the majority charge carriers are electrons (holes being the minority carriers), this kind of doped semiconductors are known as n-type semiconductors. With the trivalent dopant, there is one less valence electron and an additional energy level close to the valence band. The valence electrons can easily migrate into this extra level, leaving more holes in the valence band. As a result, the holes become the majority charge carriers and the electrons minority carriers, and such materials are called p-type semiconductors. When these two types of semiconductors are combined into a pn junction, the majority charge carriers from both materials diffuse until the resulting electric field gradient across the junction is strong enough to stop the process. This is illustrated in fig. 4.10. A special region known as the depletion region with no mobile charge carriers is created at the interface between the two materials. Radiation entering the depletion region creates electron-hole pairs that get pulled by the electric field. The liberated charges can be collected with electrical contacts placed on either end of the junction, and a current signal proportional to the ionization can be detected. The width of the depletion region (the sensitive volume of a radiation detector) can be increased by applying a reverse bias voltage.

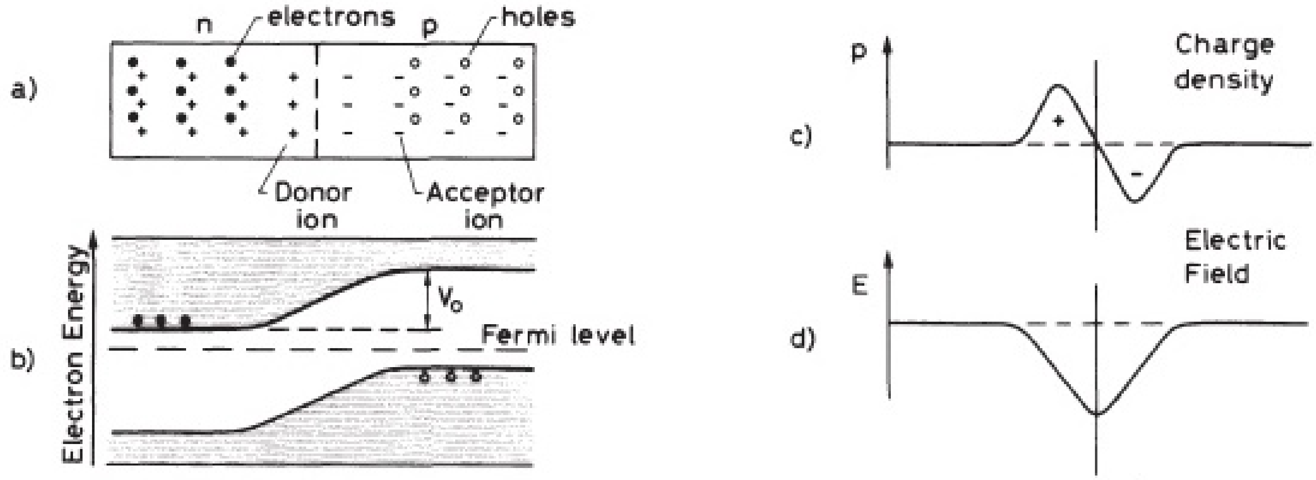

Figure 4.10: (a) Schematic diagram of an pn junction, (b) diagram of electron energy levels showing the creation of a contact potential V_0, (e) associated charge density, and (d) the electric field intensity [151]

4.4 Instrumentation

The interaction of radiation in a detector instantaneously liberates an amount of charge proportional to the energy deposited within the detector's active volume. With opposite-polarity electrodes, the produced charge moves under the influence of the electric field and produces a current signal $i(t)$ lasting up to the charge collection time t_c typically about a few tens-hundreds nanoseconds in semiconductor detectors depending on the volume.

$$\int_{t=0}^{t_c} i(t)dt = Q \propto E$$

As the signal produced is too small for direct treatment, a charge sensitive preamplifier is used to magnify it before sending it to the processing electronics. The preamplifier produces a voltage step ΔV proportional to the amount of charge. The output signal of the preamplifier is then transformed into a desirable form by a shaping amplifier. The shaping amplifier produces an output voltage pulse with a height V_{peak} proportional to the deposited charge Q. At this stage, the signal is amplified, and using a high-pass filter and a low-pass filter the signal-to-noise ratio is improved. If an output of the shaping amplifier does not quickly return to the baseline, overlapping with another signal can occur if the signals occur close in time. This pile-up effect can distort the energy measurement as the pulse height is associated with the deposited energy of the radiation. It is therefore desirable for a shaping amplifier to have a shorter shaping time constant to minimize the pulse pile-up effect. The shaped pulse then passes through a discriminator which selects pulses above a certain threshold to reduce unwanted signals. The selected signals are then transferred to an analog-to-digital converter (ADC) that converts the signal into a corresponding digital number at its output. For example, a 12-bit (resolution) ADC can give $2^8 = 4096$ channels. After the preamplifier, the signals pass through the shaping amplifiers. At this stage, the signals from the silicon detectors are amplified with two different gains [153] for simultaneous measurement of conversion electrons ranging from 70 keV to 2 MeV and alpha particles up to 25 MeV (another possibility is to measure alpha particles up to 25 MeV and fission fragments up to 250 MeV). To lower the thresholds to detect low energy electrons, the outputs of the implantation detector preamplifiers go through additional fast linear amplifiers before the spectroscopic amplifiers. It was stated in the previous sections that there are

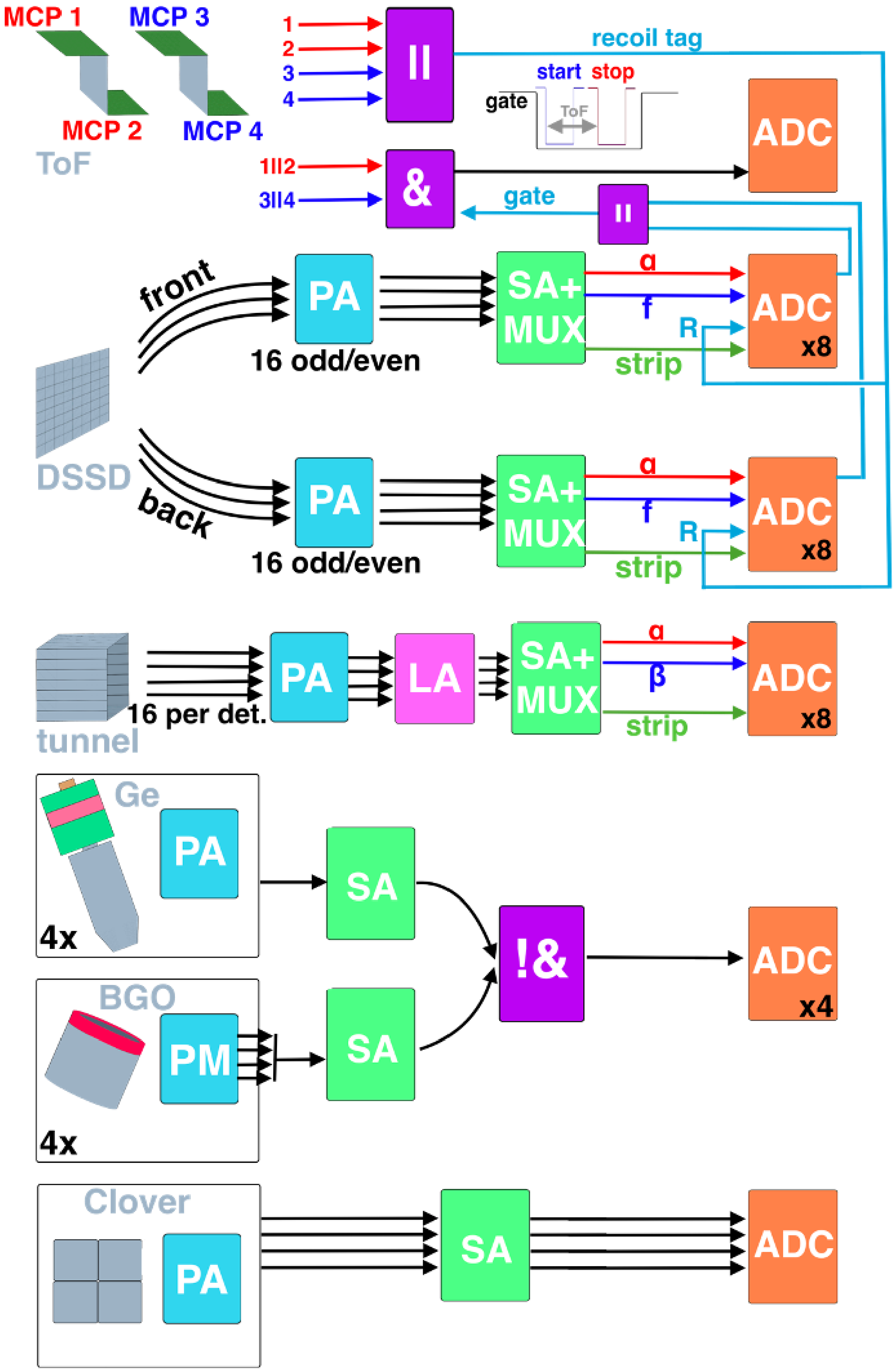

Figure 4.11: A schematic drawing of GABRIELA's instrumentation as it was in 2016 [152]. The only difference with the setup used in this work is that the Clover detector has also a BGO shield.

256 strips in total in the implantation detector and the tunnel detectors. To reduce the cost of back-end electronics (number of ADCs), signals from several strips are multiplexed to share one ADC. Hence, after the shaping amplifier, the signals pass through a 16-channel multiplexer that selects one output among 16 analog signals and sends the signal to an ADC. The front and back strips of the implantation detector are arranged in an even-odd fashion so that the events in the neighboring strips of the implantation detector do not get processed by the same ADC. Starting from strip number 0, sixteen successive even number strips share the first ADC, and the sixteen successive odd number strips share the second and so on requiring eight ADCs for the frontside and eight for the backside of the implantation detector. Similarly, the tunnel detectors also require 16 ADCs. However, in the case of tunnel detectors, such an even-odd strip arrangement was not used. For each tunnel detector, 16 frontside strips share one ADC, and the 16 backside strips share another ADC. The signals from eight Ge crystals are not multiplexed, hence require 8 ADCs. The outputs of the ADCs are sent to the data acquisition system. To distinguish an implantation event from a decay event in the DSSD a ‘recoil tag’ from the ToF detector is used. The recoil marker (MCP flag) is ON if there is a coincident signal in any of the four MCP plates. The ToF signal is the time difference between the signals in two emissive foils and taken within a gate generated by the DSSD to reduce the occupation time in the ToF electronics (see fig. 4.11).

All the ADCs are placed in two Computer Automated Measurement and Control (CAMAC) crates. Each crate has a 1 MHz timing module that synchronizes the signals of the whole crate. A lower-level time "timeL" is set for all the ADCs in the crate. The timer has a 16-bit memory, hence every 65536 µs the clock resets, and a higher-level 16-bit timing module counter is incremented by 1 given by "timeH". The higher-level clock also resets in every 65536 ticks, and a software highest-level clock "nLoops" can count the number of times the "timeH" passes through zero. The absolute time of a given signal can be calculated by

$$t = (nLoops \times 2^{32}) + (timeH \times 2^{16}) + timeL \quad [\mu s] \tag{4.6}$$

A signal in one of the ADCs and the resetting of the timing module triggers a look-at-me flag (LAM), and

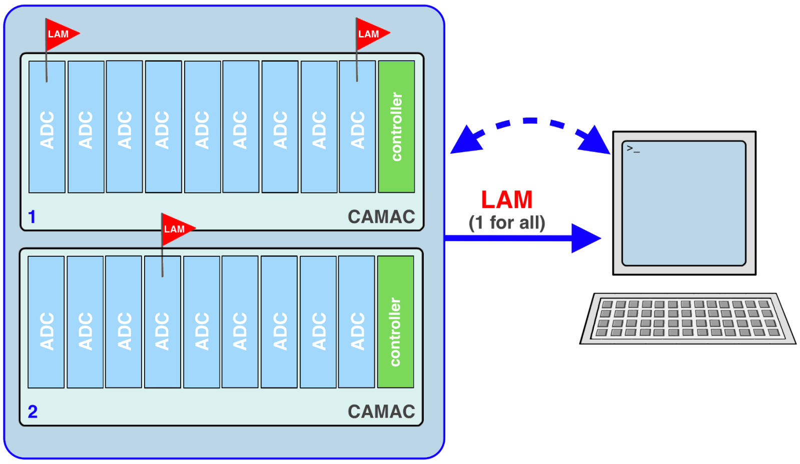

Figure 4.12: A schematic of data acquisition system [152].

a signal is sent to the crate controller. The LAM is then transmitted to the computer and remains ON until the signal is readout. A schematic of the data acquisition system is shown in fig. 4.12. While the LAM flag is ON, no signal in the same ADC can be recorded. This inactive period is called the dead time of the ADC. The dead time of a detector arises from the limiting time set by the detector (charge collection time) and from delays in the associated electronics and can be defined as the minimum amount of time required for two events to be recorded separately. Therefore, the effects of the dead time can particularly become severe if the counting rate is high as the detector is blind to the events occurring within this characteristic time.

4.5 Data Format

The data from an ADC is written in binary format. For each ADC, there are four 16-bit words. The first word corresponds to the number of the ADC from where the signal is registered. The second word provides the lower-level time "timeL" given by the timer in the same CAMAC crate. In the third word, the 12 lower-bits give the low gain amplification data "dataL" ranging from 0 to 4095 values, and the 4 most significant bits give the multiplexer output number varying from 0 to 15. The strip number of the DSSDs can then easily be constructed from the ADC number and the multiplexer output number. To do so, one needs to know the grouping of the ADCs given as follows:

- ADC no. [1-8] corresponds to the front-strips of the implantation detector.
- ADC no. [9-16] corresponds to the back-strips of the implantation detector.
- ADC no. [17-24] corresponds to the front-strips of the tunnel detectors.
- ADC no. [25-32] corresponds to the back-strips of the tunnel detectors.
- ADC no. [33-40] corresponds to the 8 Ge crystals.
- ADC no. [41] corresponds to the ToF detector.
- ADC no. [42] corresponds to the high-level clock "timeH".

Similarly, in the fourth word, the 13 lower-bits give the high-gain data of the same signal, and the higher 3-bits correspond to different flags used to identify the nature of the signal. For example, the MCP flag associated with the ToF detector is set ON for an implantation type signal in the DSSDs and OFF for decay type events. For the signals from the Ge detectors, the second-bit used as a BGO signal coincidence flag. In the case of Si detectors, the second bit is used as beam ‘chopper flag’. The beam needs to be turned ON and OFF to avoid the spoke on the target wheel. When a First in, First out buffer (FIFO) is used to queue ADC signals before they can be read out by the acquisition system, the pile-up flag is used. Fig. 4.13 illustrates the data format succinctly.

There are also computer-generated data written to the disc that includes beam energy, beam intensity, beam integral, and background information. Since the above data layout can be varied from one experiment to another, there is a .pro file associated with every data set. This file provides information not only about the data format but also the location of the ADCs in the crates. It is, therefore, necessary to consult the .pro file before beginning the analysis of the data. The data are written in near time-order fashion because of the CAMAC readout mechanism the close by time-events can be swapped. The detailed data analysis procedure is discussed in the following section.

4.5.1 Data Analysis Methodology

The primary objective of the data analysis is to establish the decay properties of the ERs implanted in the implantation detector and of their subsequent daughters. This objective can be realized by establishing

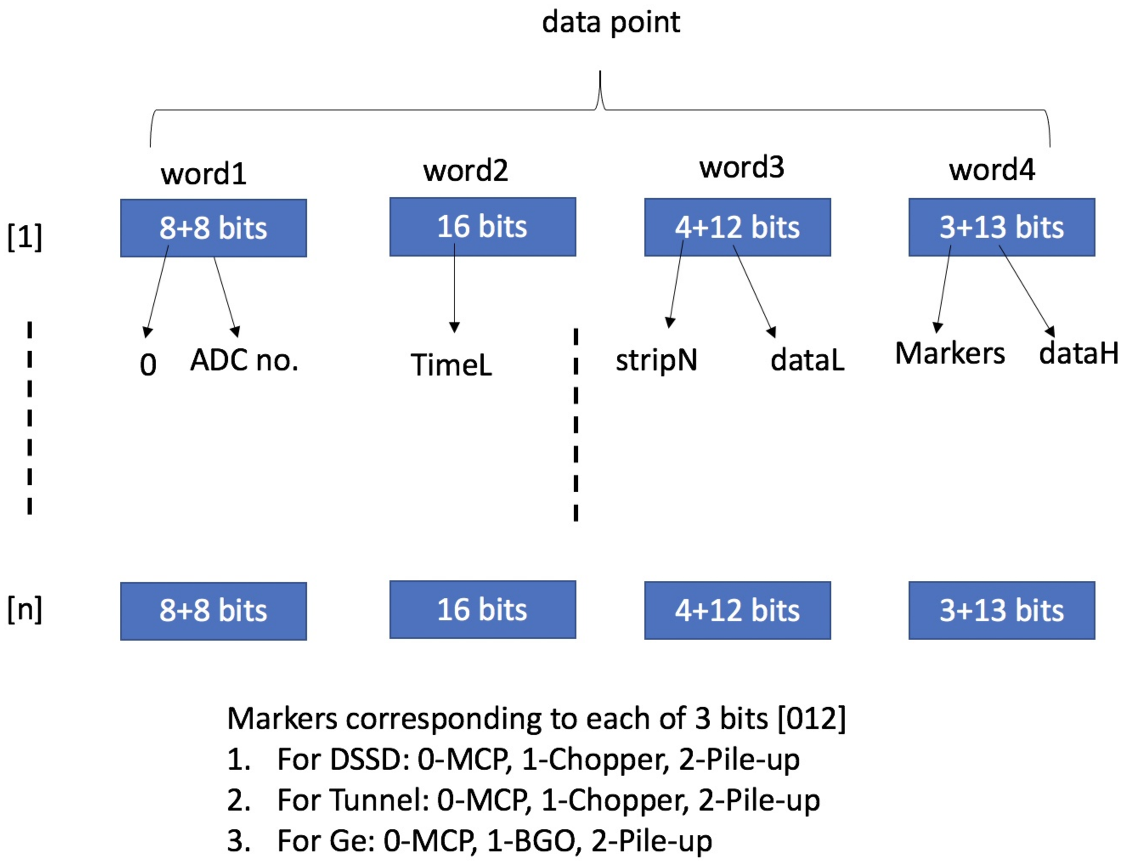

Markers corresponding to each of 3 bits [012]

1. For DSSD: 0-MCP, 1-Chopper, 2-Pile-up
2. For Tunnel: 0-MCP, 1-Chopper, 2-Pile-up
3. For Ge: 0-MCP, 1-BGO, 2-Pile-up

Figure 4.13: A schematic of the data format.

Particle	Energy [MeV]	Range in Si [µm]
α particle	8	~48
fission fragment	120	~18
electron	0.2	~242

Table 4.1: Ranges of ionizing particles in Si.

position-time correlations of the decay events following every recoil (implantation) event. It is, therefore, necessary to define ‘pixels’ as the smallest units of the implantation detector that form the basis of the whole genetic correlation procedure. Unlike in a display device, there are no physical pixels in a DSSD. The pixels are constructed based on the event sequence and therefore are transient. Before going into the detailed data analysis procedure, it is apt to give justification for the pixel size in the implantation detector with lateral dimension $\approx 760 \times 760$ µm^2. Let an event in the implantation detector is represented by the X-Y coordinates where the X value corresponds to the front strip and Y value to the back strip, where the opposite charges created by the radiation in the detector’s active volume are collected. Table 4.1 justifies that the pixel size is large enough for the ionizing particles with typical energies such as alpha particles, fission fragments, and low energy electrons as their ranges are small compared to the size of a pixel assuming their sources are placed at the center of the pixel. Since the ERs are implanted randomly, there is always a finite probability that two front strips or two back strips would share the charges of the same event. Such events are called inter-strip events, and in such cases, we will consider the strips with the highest energies as the position of that event. A comparison of energies of two coincident signals in two neighboring front or back strips requires calibration of the whole detector as different amplifiers are associated with different strips of the detection. Needless to say, the calibration of detectors is the first and foremost task that needs to be done before beginning the analysis of the data.

Fit Function

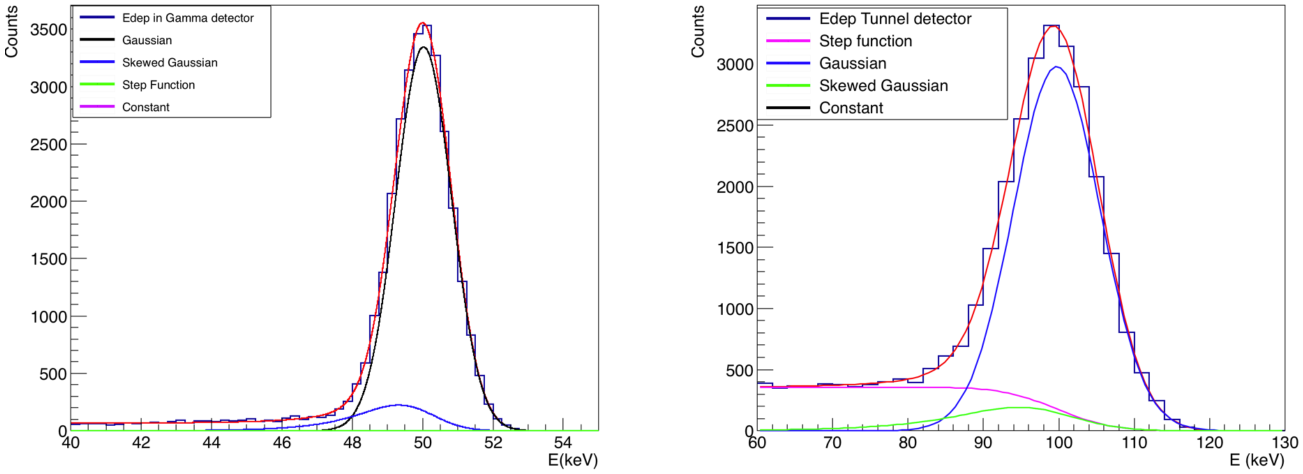

(a) Fit of 50 keV gamma-ray peak

(b) Fit of 100 keV electron peak

Figure 4.14: Figures showing the components of the fits used for gamma-ray and electron peaks.

The gamma and electron and alpha full energy peaks are fitted with the following RadWare type function [154]:

$$\text{Fit Function} = \text{Step Function} + \text{Gaussian} + \text{Skewed Gaussian} + \text{Flat Background}$$

$$F(x,\mu,\sigma,\beta) = h_1 Erfc\left(\frac{x-\mu}{\sigma\sqrt{2}}\right) + h_2 e^{-\frac{1}{2}(\frac{x-\mu}{\sigma})^2} + h_3 e^{(\frac{x-\mu}{\beta})} Erfc\left(\frac{x-\mu}{\sqrt{2}\sigma} + \frac{\sigma}{\sqrt{2}\beta}\right) + const \tag{4.7}$$

where x is the energy, μ, the mean energy, σ, the standard deviation, β, the decay constant and h_1, h_2 and h_3 are the heights related to step function, Gaussian and skewed-Gaussian distributions. The fits of gamma and electron spectra obtained from GEANT4 simulation are shown in the fig. 4.14. The Gaussian component can be attributed to full energy deposition in the detectors. Incomplete charge collection can be described by a skewed Gaussian component. The step function describes the back scattering of electrons as well as the Compton scattering (scattering out of the detector volume, scattering back from outside materials into the detector and multiple Compton scattering) of gamma rays and a flat background if any is described by a constant.

Calibration

The detectors are calibrated using well-known radioactive sources. The high gain data of the implantation detector and tunnel detectors are calibrated using a ^{133}Ba source (figs. 4.15a and 4.15c show the alignment of the strips of the implantation detector and the tunnel detectors respectively and figs. 4.16a and 4.16c

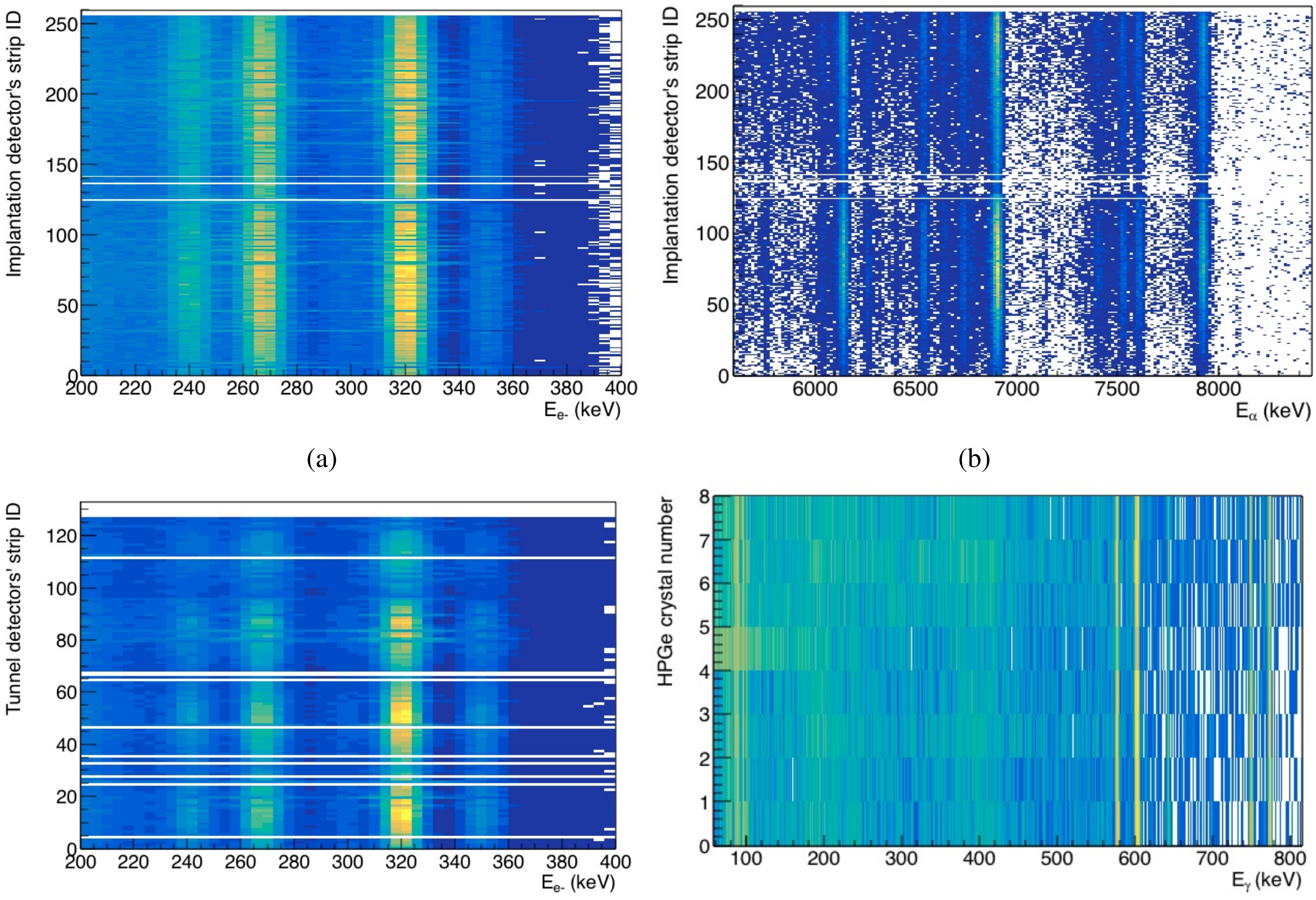

(a) (b)

(c) (d)

Figure 4.15: Calibrated spectra after the calibration procedure for (a) DSSD high gain (b) DSSD low gain (c) tunnel detectors (d) Ge detectors.

show the corresponding energy spectra of 127 front strips). The low gain data of the implantation detector are calibrated using known alpha-emitting nuclei produced at the target and implanted into the implantation detector (see figs. 4.15b and 4.16b). Care needs to be taken while calibrating the DSSD using different implanted alpha emitters as the energy detected is the sum of the energy deposited by the alpha particle and a fraction of the recoil energy of the daughter nucleus $E_{daughter} = E_\alpha \frac{4}{A-4}$. To obtain the true alpha energies of SHE, one needs to correct for the mass differences in the recoil term (~ 30 % of which goes into ionization [155].)

The Ge detectors are calibrated using standard calibration sources namely ^{60}Co, ^{133}Ba, ^{152}Eu, and checked with in-beam sources, for example, the isomeric decay of ^{210}Ra nuclei produced in the reaction ^{164}Dy(^{50}Ti, 4n)^{210}Ra (see figs. 4.15d and 4.16d). Since there were two experimental campaigns, the detectors needed calibration for each run. This amounts to the calibration of a total of 2 Experiments x (2 Gains x (256 DSSD + 256 Tunnel) + 8 Gamma) = 1552 channels. In both the experimental campaigns there were strips in the silicon detectors that could not be calibrated either because they had bad resolutions or had noise or had no structure whatsoever. Such uncalibrated strips are referred to as missing strips as they were excluded from the experimental analysis. There were also gain drifts during the experiments in

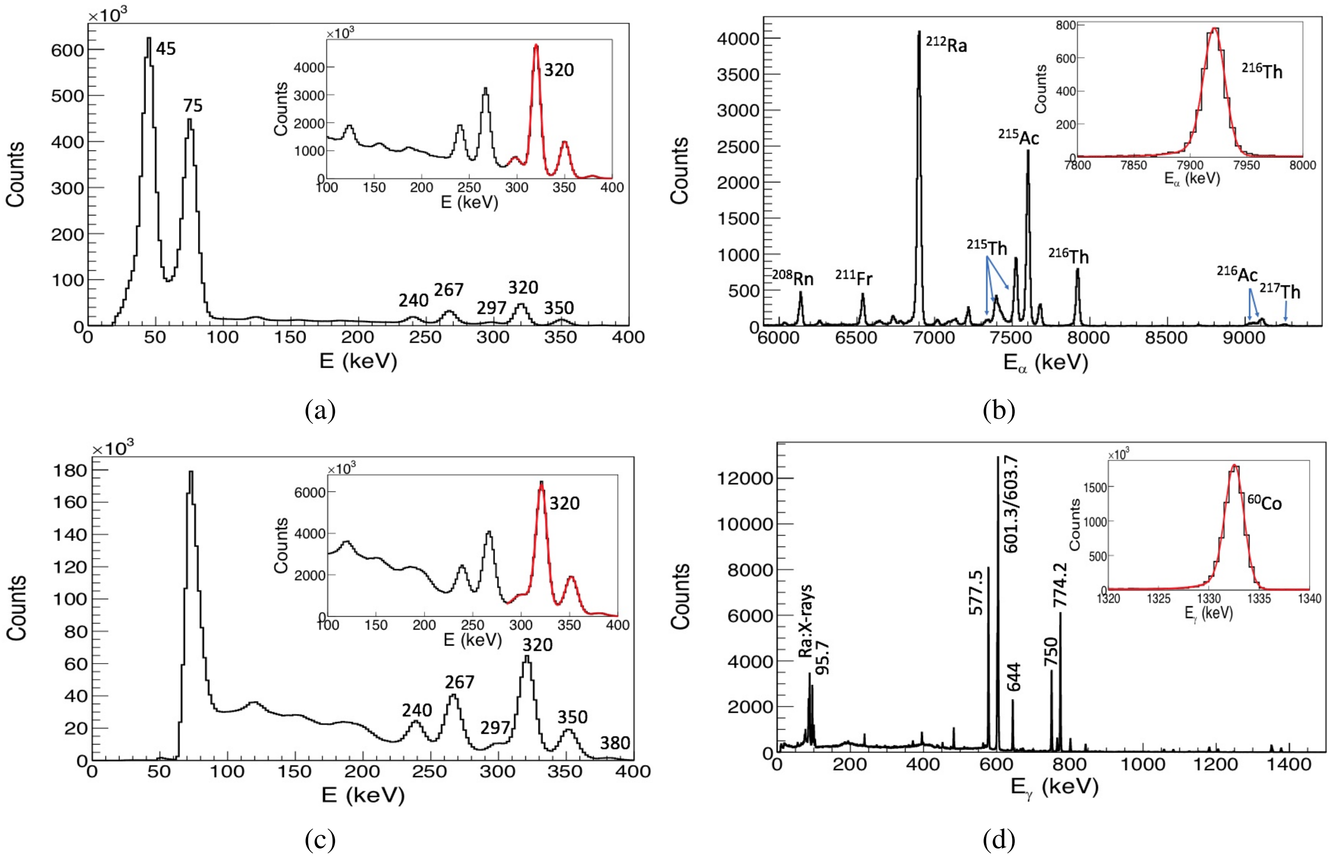

Figure 4.16: The energy spectra of the electrons emitted from a ^{133}Ba source detected in all the strips of (a) the implantation detector and (c) the tunnel detectors. (b) Spectrum of alpha-particle energies emitted by the nuclei produced in the reaction ^{170}Er(^{50}Ti, xn yp) (d) Energy spectrum of the Compton suppressed gamma rays detected within 24 µs from the implantation of ^{210}Ra nuclei. The insets in the figures show the corresponding fits (red curves) of the peaks, from which the resolutions of table 4.3 have been extracted. The histograms of insets a) and (c) have been scaled up by 100 to show their differences. The inset of figure (d) shows the fit on the 1332.5 keV peak of ^{60}Co since gamma-ray resolutions are often quoted at this energy.

the DSSD which were corrected using ^{211}Po alpha peak as reference. The DSSD signals also suffer from pole-zero effect. If a decay signal is not well separated in time from the larger recoil implantation signal, it can ride on the back of the implantation signal, thus increasing its energy artificially. Whereas, if it occurs at the undershoot of the implantation signal, its signal can be reduced. These effects are responsible for the arch shapes seen in fig. 4.17 in the case of ^{209}Ra isomeric decay.

We have also encountered some low energy signals in the Clover detector, which appear $\sim$ 30 µs after a decay event in the implantation detector. Such signals could be related to punch-through events and could not be removed in software (see fig. 4.18). As a prospect, the punch-throughs can be rejected by placing a veto detector in between the implantation detector and the Clover. However, this solution comes with a drawback as the veto detector will impact on the efficiency of the low energy gamma rays. Another problem that appeared is related to the cross-talk in the tunnel (at the level of the vacuum feedthroughs) leading to spurious low-energy signals which could only be partially removed.

In the Oct experiment, in addition to missing strips in the Si detectors, one Ge ring detector was

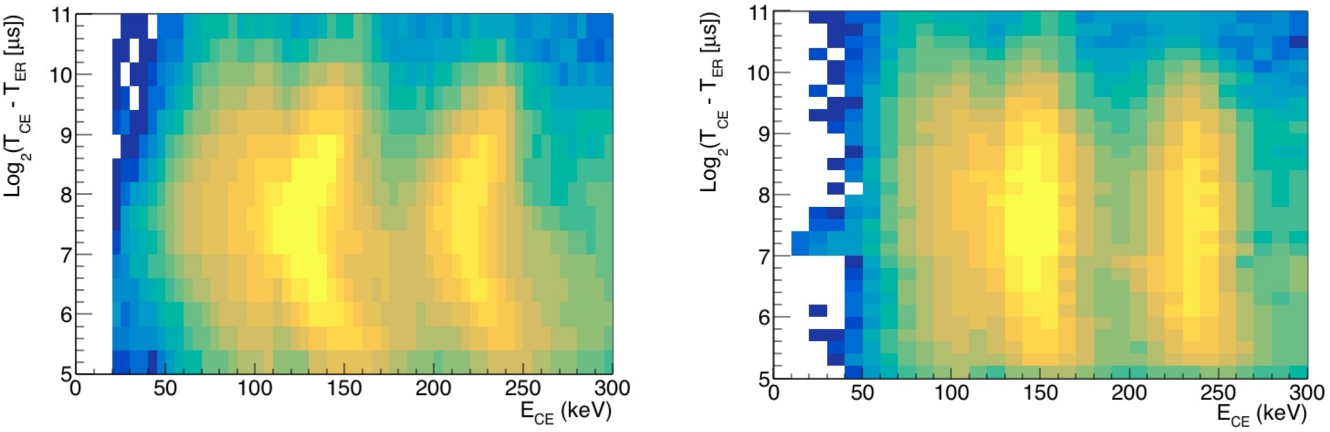

(a) (b)

Figure 4.17: Spectrum of low energy signals (CE) observed in the implantation DSSD in the decay of the 117 µs isomer in ^{209}Ra (a) before and (b) after pole-zero software correction.

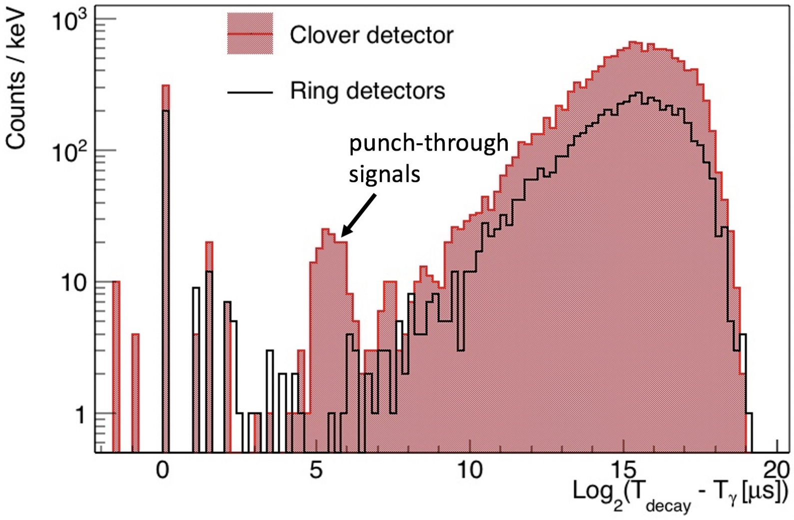

Figure 4.18: Punch-through signals in the Clover detector appearing ~ 30 µs after a decay signal in the implantation DSSD.

Detector	May	Oct
Implantation Detector	124, 136, 141	–
Tunnel Detector	4, 24, 27, 32, 35, 46, 64, 66, 67, 111, 114, 122, 123, 125, 127	4, 24, 27, 48, 51, 62, 64, 66, 67, 79, 111, 127
Ge detector	–	1

Table 4.2: List of Missing strips or detectors in the two experiments.

not present as well. Table 4.2 lists the missing strips/detector in each experiment. In a spectroscopic measurement using a detector, there can be many lines/peaks in the energy spectrum of a radiation source. For a given type of detector, the widths of the peaks in the energy spectrum can vary depending on the energy and nature of the incident particle. The energy resolution is the ability to distinguish between two incident radiations with slightly different energies. The narrower the peaks, the better is the resolution. It is defined as the full width at half maximum (FWHM) of the full energy peak at a certain energy. The resolution depends on the number of charge carriers which are produced per unit energy deposited in a detector. The resolution can be affected by many factors such as a drift of the operating characteristics of the detector during the course of the measurements, random noise within the detector and instrumentation system, and statistical noise arising from the statistical nature of the processes by which the radiation interacting with the detector medium produces the charge carriers [150].

$$(FWHM_{overall})^2 = (FWHM_{statistical})^2 + (FWHM_{noise})^2 + (FWHM_{drift})^2 + ...$$

The statistical noise is inherent in nature and therefore will always be present and in most detector systems, it is the dominant source of fluctuation in the signal, thus, limiting the performance of the detector. This fluctuation is proportional to the square root of the average number of charge carriers.

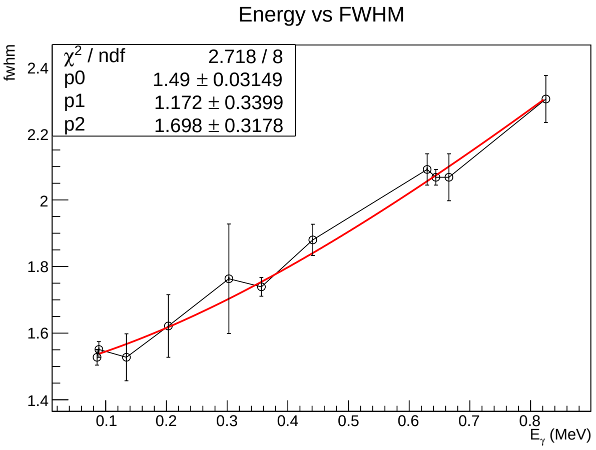

Figure 4.19: Measured FWHM for the Ge array.

For Ge detectors, the overall resolution as function of energy can be expressed as [154]

$$FWHM = (A^2 + B^2 \times E_\gamma + C^2 \times E_\gamma^2)^{1/2} \tag{4.8}$$

with E_γ in MeV and A, B, and C coefficients that are obtained from a fit on the experimental data. Fig. 4.19 shows the fit and parameters obtained from the our data.

The measured resolutions and the typical thresholds of the detectors in our setup are given in table 4.3.

Detector	FWHM (keV)	Threshold (keV)
Implantation	10.8 ± 0.6 at 320 keV 23.2 ± 1.7 at 7922 keV	60 - 100
Tunnel	14.4 ± 1.2 at 320 keV	60 - 100
Gamma	2.26 ± 0.17 at 1332.5 keV	~15

Table 4.3: The resolutions and the typical thresholds of the GABRIELA detectors. The fits at these energies are shown in the insets of fig. 4.16.

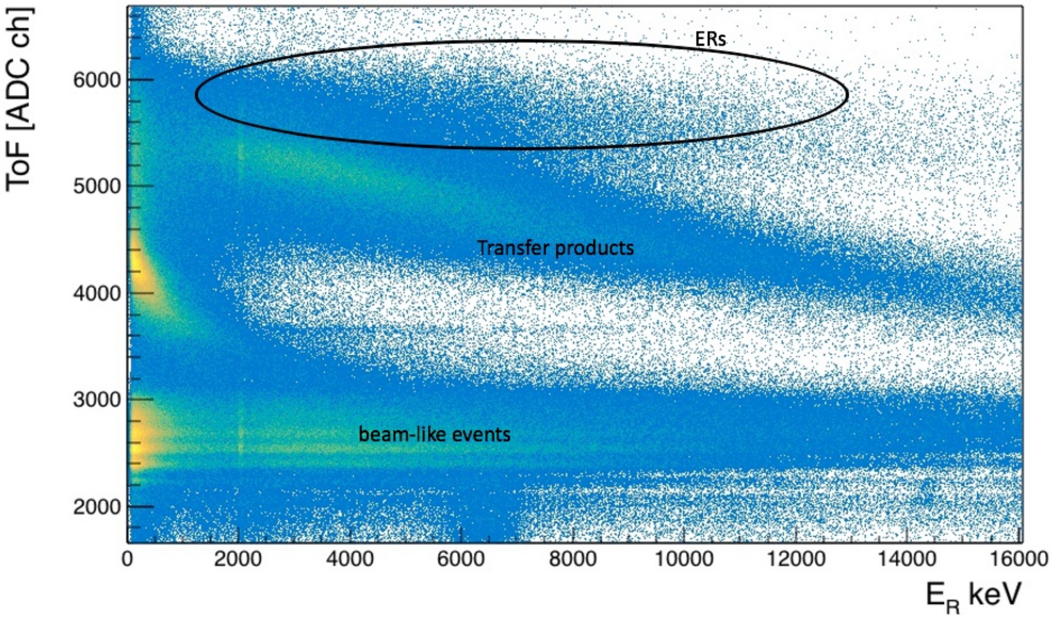

Figure 4.20: ToF in ADC channel number as a function of Recoil Energy (E_R) in the reaction ^{207}Pb(^{50}Ti,xn)$^{(257-\mathrm{xn})*}$Rf

Event Construction and Correlation

After calibrating the detectors, it is now possible to construct pixelized events of the implantation detector. The time difference between two signals in two front strips occurring subsequently in the data set gives the corresponding coincidence window. Similarly, the other coincidence windows for two back strips, one front strip and a back strip, and the vice-versa need to be obtained to construct pixelized events. While reading a given data set, the DSSD events of either decay or recoil type are constructed separately from the coincident signals in the front and back strips of the detector. In any event, if signals from multiple strips on either side of the detector are coincident because of charge sharing, then the strips with maximum energies that reflect more proximity to the event are considered. For any DSSD event, the energy detected in the corresponding front strip is considered to be the energy of the event in our analysis. As a result, the energy values for inter-strip events are smaller than those of the single-strip events. After assigning each DSSD event with a physical position, it is necessary to associate each recoil type event with a ToF signal. This can be done by demanding a coincidence between a ToF signal and a recoil event. The time of flight is different for different types of recoil events namely scattered beams, ERs, and transfer products, hence, ToF information can be used to distinguish them from one another. Fig. 4.20 shows a plot where recoil energy is plotted against the ToF value [in ADC channel number]. By constraining the ToF value and the recoil energy only the ERs can be selected. A proper selection of ERs is important not only to associate decay events to the proper recoil event but also to have a longer correlation time.

Since ERs can decay in a variety of ways as discussed in chapter 3, it is pertinent to seek correlations not only with subsequent events in the same pixel but also with events in the Ge and tunnel detectors. These correlations are established in the following manner keeping the DSSD as the reference:

- The decay events appearing before a recoil event are generally ignored. These events occur randomly from the decay of some long-lived isotopes accumulated in the implantation detector from earlier experiments.

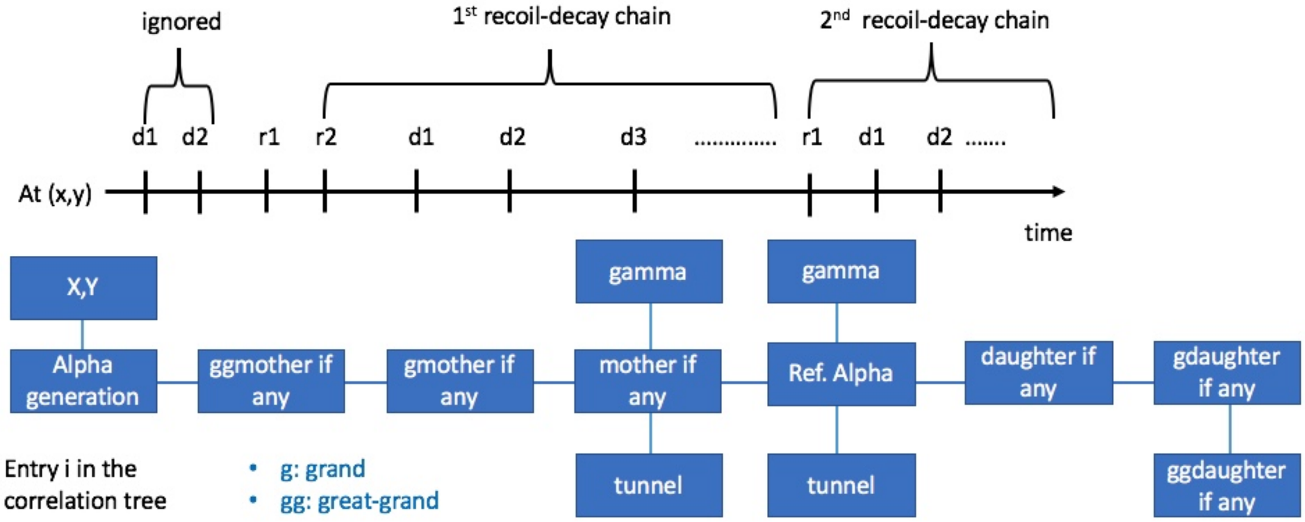

Figure 4.21: Schematic of the sequence of implantation and decay signals observed in the implantation detector and an entry of the correlation tree based on these decay chains.

- If multiple recoil events occur in sequence, the decay events are correlated to the last recoil. By selecting ERs with proper ToF value and recoil energy (see fig.4.20) it is possible to associate the decay events to associate the decay events to the real recoil event.
- A recoil decay correlation chain continues until another recoil event is observed in the same pixel which marks the beginning of another new chain.
- For every recoil event, the coincident and subsequent events in the tunnel and Ge detectors occurring before another recoil event are associated with the former. In this way the detected gamma rays and electrons emitted from isomeric decays can be easily produced.
- For every decay event, the coincident and subsequent events in the tunnel and Ge detectors occurring before another decay or recoil event are associated with the former decay event. This allows prompt and delayed decay-gamma ray and decay-electron spectroscopy can be easily performed.

Note that, some events of the Ge and tunnel detectors that are coincident with a DSSD event are recorded before the DSSD event. Hence, a backward search of these time-flipped events is necessary while seeking correlations. These correlated events can be structured into a ROOT Ttree (correlation tree) to avoid sorting of data every time a specific selection of events is required while analyzing the data. While sorting the data at the end of every recoil-decay chain the correlation tree is filled. The structure of the tree built for this work is displayed in fig. 4.21. Each entry of the Ttree contains the following information:

- X and Y positions
- The generation number (Alpha generation) of the reference (or current) DSSD decay event. It is equal to the position number of the alpha or fission decay event (reference) with respect to the recoil event, starting from 1 to the end of the decay chain. Alpha generation number equal to 0 is assigned to the recoil event(s) for convenience. In fig. 4.21, the number associated with ‘d’ in the schematic of the sequence of events at a given pixel represents the generation number.

- In a given pixel, a decay event can have multiple preceding (mother) decay events and multiple subsequent (daughter) decay events before another recoil starts a new recoil-decay chain. The energy and time information of the preceding decay events up to the great-grandmother are stored in the Ttree and similarly for the daughter events up to the great-granddaughter. For alpha generation = 1, the mother corresponds to the recoil event and since there are no grandmothers or great-grandmothers, the corresponding branches are filled with an arbitrary value say -100. Similarly, if no subsequent decay events are found the daughter branches are filled with an arbitrary value.

- For every reference decay event, the information (energy, time, detector or strip number, BGO marker) of the correlated gamma rays detected in the Ge detector and electrons detected in the tunnel detectors are stored in variable containers. The information of the gamma rays and electrons correlated with the recoil is also stored only if mother = recoil (i.e., alpha generation = 1) to save memory. The recoil-gamma ray and recoil-electron information can be easily obtained by moving up in the tree as this information is stored in alpha generation = 1 entry of the same recoil-decay chain. For instance, entry j corresponds to alpha generation = 3, implying that recoil is the great-grandmother in the recoil-decay chain (see fig. 4.21), the containers for mother gamma rays and electrons are kept empty. Then to access the recoil-gamma ray and recoil-electron information, one calls the entry (j-2) in which the reference decay event is of alpha generation = 1.

This correlation tree structure allows one easy forward and backward movement in time on the DSSD-event plane. It may seem computationally expensive as the same information is written multiple times in different entries of a recoil-decay chain. However, this structure facilitates the application of selection cuts and easy manipulation of data. The usefulness of this tree structure is illustrated in 4.22a and 4.22b, where, by selecting the ^{251}No alpha peak and fission events, a clean spectrum of the mother ^{255}Rf alpha decay is obtained. Similarly, by selecting ^{255}Rf alpha-peak events, it is possible to get the ^{251}No daughter events (see fig. 4.22c and 4.22d).

4.6 GEANT4

A brief introduction

[1] GEANT4 [159] is a Monte Carlo simulation toolkit written in object-oriented C++ language primarily developed for simulating high energy physics experiments and quickly found applications in a variety of domains such as space science, medical applications, and so on. Nuclear physics is one domain where GEANT4 is extensively used these days to interpret experimental data, especially when complex setups are involved. GEANT4 provides many components, and it rests upon the user for their uses to build the desired application. The GEANT4 kernel forms the skeleton for geometrical modeling and the physics processes. It also controls the runs, events, tracks, steps, hits, and trajectories. To perform a GEANT4 simulation, one first defines the experimental setup, the physics processes, and the primary particles associated with the experiment. In a Run (G4Run), a collection of events share the same detector and physics conditions which cannot be changed during a Run. In analogy with real experiments, a Run starts with "Beam On" and managed by the G4RunManager class. The kernel loops over the number of events of a Run. In every event (G4Event), the G4PrimaryGenerationAction class first creates primary particles that are pushed into a stack. G4EventManager class manages the processing of an event in which the primaries are looped over. The primary particles can be generated using various utilities such as G4ParticleGun, G4GeneralParticleSource, and user-defined source (derived

---

[1] This section is based on ref. [156–158] and the GEANT4 course held at LAL Orsay in May 2018

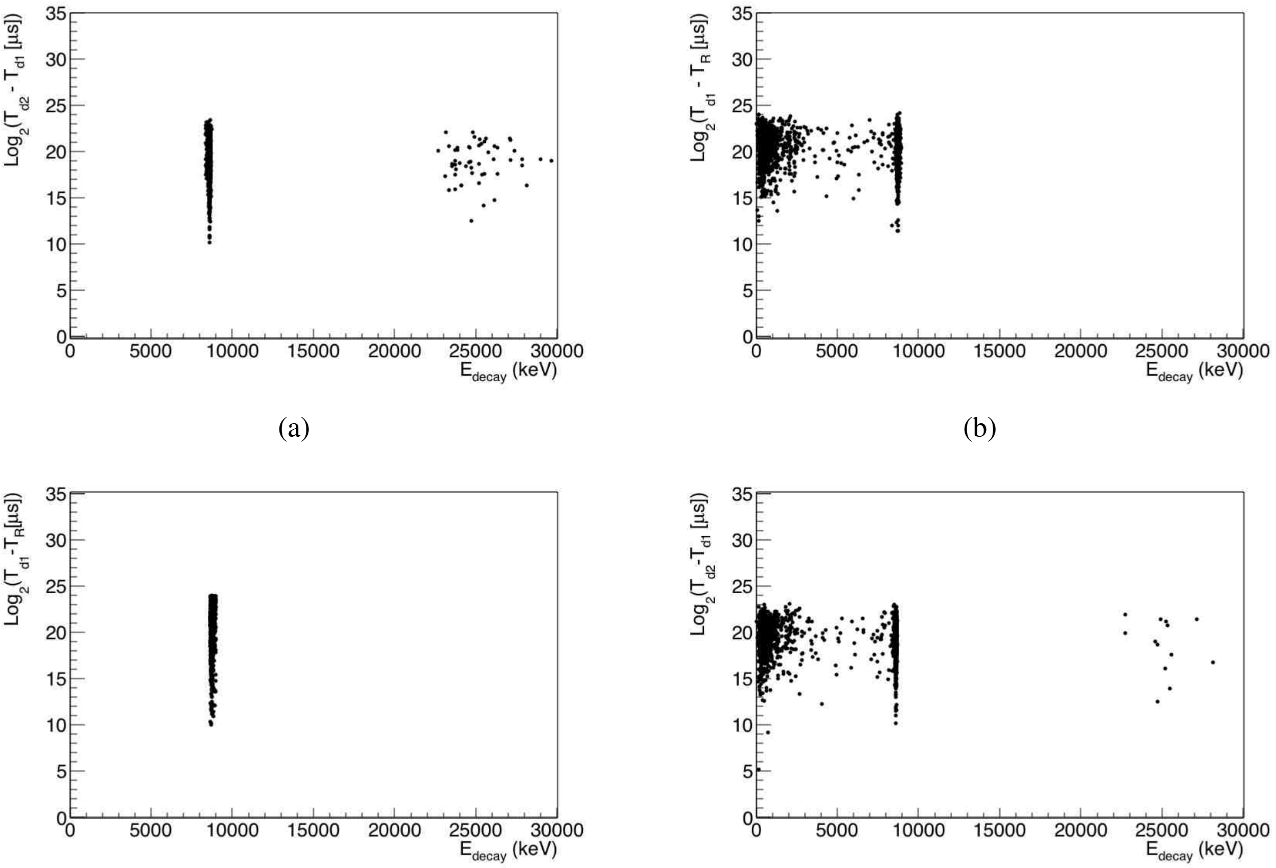

(a) (b)

(c) (d)

Figure 4.22: By selecting a) ^{251}No alpha-peak and fission events in the correlation tree b) ^{255}Rf mother decay events can be obtained. Similarly, by selecting mother c) ^{255}Rf alpha-peak events d) daughter ^{251}No events can be obtained.

from G4VUserPrimaryGeneratorAction). GEANT4 tracks the primary particles that undergo the registered physics processes throughout the detector volume. The secondary particles created from the interaction of the primary with the detector material are also tracked. Each track (G4track) is a snapshot of a particle composed of many "delta information" called steps (G4Step), and the track is updated with every step. Tracks and steps of a particle are managed by the G4TrackingManager and the G4SteppingManager, respectively. As there are no default physics processes registered, the user must define the physics processes explicitly. For this, one derives a user-defined class from the G4VUserPhysicsList abstract base class, where one defines all the essential particles and physics processes (such as electromagnetic, hadronic, nuclear, decay processes, etc.) they can undergo. In this class, one can also define production threshold cuts in terms of range. No secondary particles are created if particle energy falls below the cuts. These cuts can also be applied at the level of a region of a detector as the production thresholds can vary from material to material. The physics processes are model-driven and sometimes rely on experimentally evaluated data. The physics models have different energy range applicability, and one can use complementary models to cover a wide range of energy as desired for an experiment.

The detector geometry can be constructed using different types of solids and operations available in GEANT4. The procedure contains conceptual layers of volume construction: 1) the shape and size are

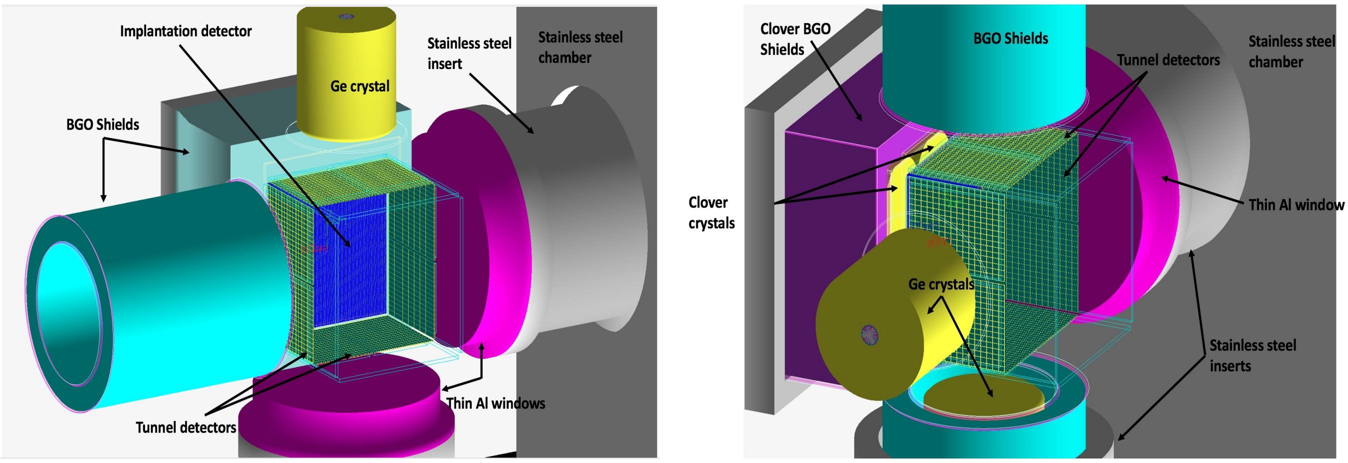

(a) (b)

Figure 4.23: 3D rendering of the various elements of GABRIELA, as described in GEANT4 (courtesy of K. Hauschild).

defined by G4VSolid class, 2) material, sensitivity, and other characteristics are endowed to the solid by G4Logicalvolumes class 3) the position and orientations are defined by G4VPhysicalVolume class. Using the G4SensitiveDetector class sensitive detectors are instantiated corresponding to the logical volumes of the detectors. When a particle passes through a sensitive detector Hits (G4Hits) are created using the information provided by the G4step. Various types of information can be stored in a Hit such as energy deposition, position and time of the step, momentum and energy of the track, and so on.

Simulations for GABRIELA setup

The geometry of the GABRIELA's setup was constructed meticulously under the GEANT4 framework taking care of the active areas, the dead layers, and the gaps between the detectors. Other additional components such as the chamber, the PCB boards for mounting the silicon detectors, the support frame, etc. were also included (see the visualization in fig. 4.23). The active areas of the detectors were defined as sensitive detectors. The energy deposited in a sensitive volume by a step is collected in the Hits defined in that sensitive detector class. For every sensitive detector class, a corresponding hit class was defined to store relevant information such as strip number, crystal number, total energy deposited, and so on. Every strip of a silicon detector is associated with a hit in its respective sensitive detector class. In the case of Ge detectors and BGOs, for every crystal, a corresponding hit is instantiated. When the processing of an event is over, event number, detector identity, strip, or crystal number and total energy deposited are saved to a ROOT tree for post-processing. The data generated for each run has a similar format to the experimental data and thus treated as such. A C++ program is written to read the simulated data where the effects of electronics such as the multiplexing, the missing channels, the experimental energy resolutions, and the typical thresholds of the detectors are added. For a given Run, $\gamma - \gamma$, $\gamma - e^{-}$, $\gamma - \alpha$, $e^{-} - e^{-}$, $e^{-} - \alpha$ and other correlations are established similarly as for the experimental data allowing a better comparison of experimental and simulated results.

Radioactive decays in GEANT4

The software package for the simulation of radioactive decays in the GEANT4 Monte Carlo simulation code is well established and validated [160] against the Evaluated Nuclear Structure Data File (ENSDF) database [78]. User-defined photon evaporation files and radioactive decay files can be added to the simulations to test various radioactive-decay schemes (see appendix B for details about the format of these files). However, atomic relaxation processes are limited to $Z = 100$ in the current GEANT4 versions. Hence, simulation of radioactive decay of elements $Z > 100$ is not practical. For instance, in the internal conversion decay of a $Z > 100$ isotope, a single electron is emitted with the total transition energy. This certainly affects the energy spectra obtained using a compact detector setup like ours, as summing in the detectors plays a big role. This inadequacy of GEANT4 is tackled carefully using different methods. One approach is to hard-code the whole atomic relaxation process as a part of the Primary Generator Action of GEANT4. Another technique is to disguise heavy nuclei as lighter ones (i.e., to the heaviest element available in GEANT4) by modifying their atomic properties [161, 162]. Another approach is to modify the GEANT4 source code so that the internal conversion for heavy elements is taken into account. In this study, the third approach was adopted after realizing that some modifications in the GEANT4 source code and addition of new data can solve the problem from a study of the radioactive decay classes and atomic-relaxation classes. The following modifications were introduced in the source code to allow atomic-relaxation processes up to Rf. First, In G4AtomicDeexication, G4AugerData, G4ITDecay, AtomicTransitionManager and G4ECDecay classes, the atomic number limits were changed from $5 < Z < 100$ to $5 < Z < 105$. In the G4AtomicShell class, the limit of Z needed modification accordingly with the inclusion of the binding energies of all the atomic shells and electronic configuration for each additional element. Besides, for every electronic shell, an index number and the number of electrons it can have were also included in this class. Electronic shell binding energies of these elements need to be added as well in the file called binding.dat located in the "fluor" directory. The G4ShellData class reads binding energies from this file. The binding energy values of the atomic subshells designated by ENDL notations are from the Table of Isotopes (ToI) [163] (see appendix B for ENDL notations). It is also required to add Fluorescence and Auger data files in the "fluor" and the "auger" directories for every element up to Rf. The extrapolation is limited to Rf since my thesis's primary objective is to study the decay properties of ^{255}Rf isotope. Since the atomic structures of $Z = 90$ to $Z = 104$ can be approximated to be similar except at the outermost electronic shell, the existing atomic data files in GEANT4 from $Z = 90$ to $Z = 104$ can be used to extrapolate Fluorescence and Auger data files

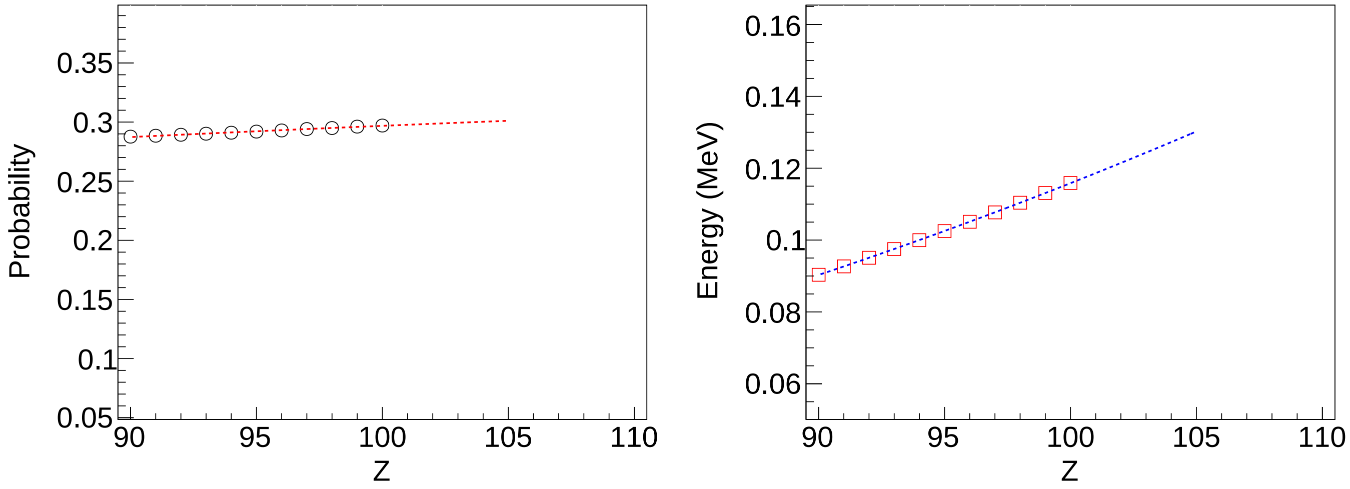

(a)

(b)

Figure 4.24: Fluorescence transition (a) probability and (b) energy as a function of atomic number for a K vacancy.

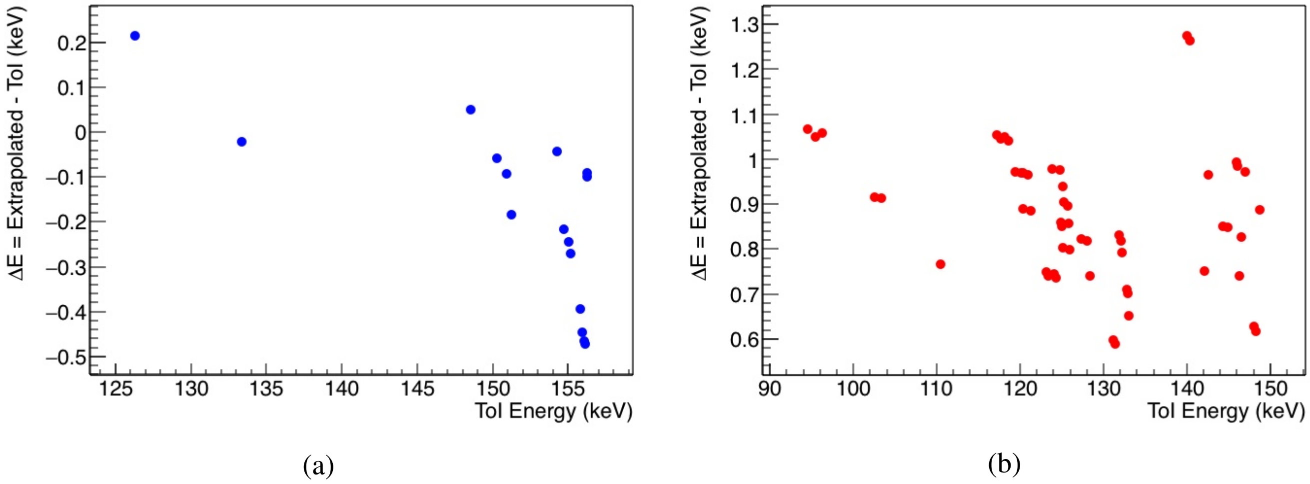

(a) (b)

Figure 4.25: The difference between the extrapolated Energy in (a) Fluorescence and (b) Auger transitions and the corresponding calculated value given in ToI for K shell vacancy in ^{255}Rf.

up to Rf. Two C++ programs were written to extrapolate these data files and produce GEANT4 readable formats (see appendix B). In a given element, for every atomic transition, the data from $Z = 90$ to $Z = 104$

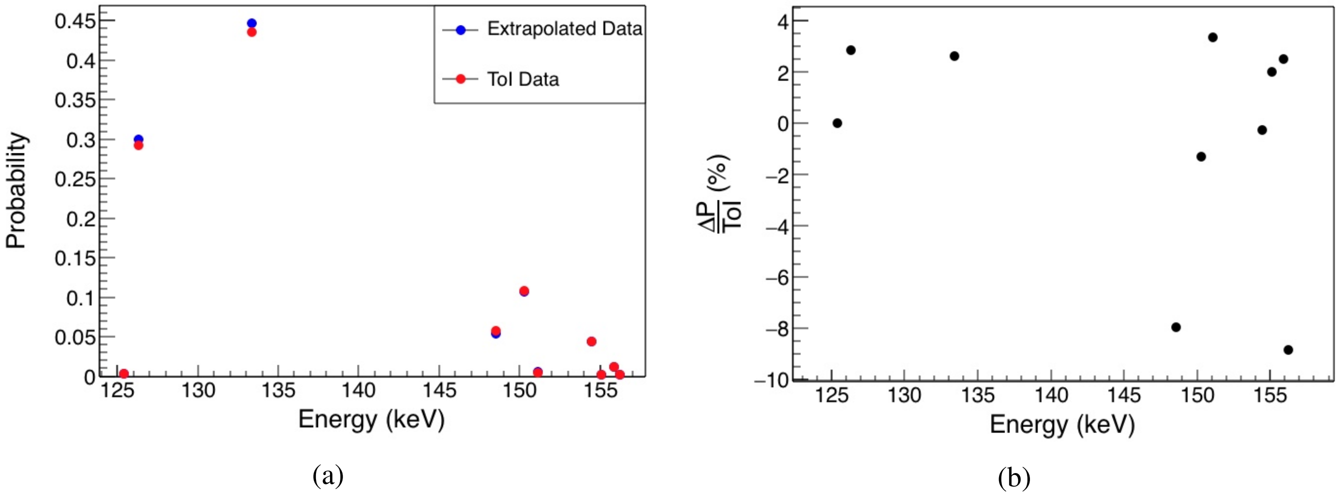

(a) (b)

Figure 4.26: (a) Comparison of extrapolated and Fluorescence emission probabilities with calculated values given in ToI for K shell vacancy in ^{255}Rf after correcting the transition energies. (b) shows the relative differences with $\Delta P = Extrapolated - ToI$.

is fitted with a cubic Polynomial Function. In the first attempt, both the transition probabilities and the energies were extrapolated (see fig. 4.24). However, a comparison of the extrapolated values of Rf to the standard values given in the ToI revealed a few keV shifts in some extrapolated energies (see fig. 4.25). Even though these shifts are within our detector resolution, the transition energies were calculated in the second attempt using equation 3.77 and 3.78. A better agreement of the extrapolated values is visible in fig. 4.26). Note that with these changes, it is no longer possible to utilize all the built-in Electromagnetic physics lists (see appendix C for more detail). It is because some physics lists require models whose data files were not extended up to Rf likewise.

4.7 Efficiency Characterization

The response of a detector to incoming radiation is dependent on a few factors: the constituent materials, the detector's geometry, its position relative to the source, and on nature and the energy of the incoming particle. In an experiment like ours, detection of radiations emitted by a sample of radioactive nuclei and the analysis of their decay energy and time spectra are not enough to conclude on their nuclear structures. The structural information is hidden in branching ratios, internal conversion coefficients, mixing ratios, and so on. Their determination requires accurate knowledge of the behavior of each detector involved in the experiment. Certainly, not every ionizing particle incident onto the detector's surface is fully absorbed. Many of them scatter out of the detector volume, some of them deposit only a fraction of the incident energy due to the escape of secondary particles produced from the interactions of the primary particle with the detector's material. Hence, it is required to distinguish a detector's total detection efficiency for a particular radiation from its corresponding absolute detection efficiency, "absolute" in the sense that the particles are detected completely (*i.e.* with their full energies), also known as the peak efficiency[2]. The absolute detection efficiency of a detector to detect an ionizing particle with energy E is the fraction of counts in the full energy peak N_p for the total number N_e emitted by the source

$$\varepsilon(E) = \frac{N_p}{N_e} = \epsilon_i(E).\epsilon_g \tag{4.9}$$

where $\epsilon_i(E)$ is the interaction probability that a particle hitting the detector will appear in the full energy peak and ϵ_g being the geometrical efficiency. The interaction probability is the ratio of the number of particles detected in the peak region over the number of particles hitting the detector: $\epsilon_i(E) = \frac{N_p}{N_{\text{particles hitting the detector}}}$ and the geometrical efficiency is the fraction of the solid angle Ω subtended by the detector's aperture over 4π: $\epsilon_g = \frac{\Omega}{4\pi}$ relative to the source. Similarly, the total detection efficiency is the fraction of the number of particles detected N_d out of the total number of emitted particles.

$$\varepsilon_{Tot} = \frac{N_d}{N_e} \tag{4.10}$$

Another useful quantity called the peak to total ratio (P/T) can be defined as:

$$P/T = \frac{N_p}{N_d} = \frac{\varepsilon_p}{\varepsilon_{Tot}} \tag{4.11}$$

There are two ways to determine the efficiency of a detector. The obvious one is to experiment with a standard radioactive source whose activity A in (in Bq) and the intensity I of the radiation of interest are well known, the eq. 4.9 in this case then

$$\varepsilon_p(E) = \frac{N_p}{A \times I(E)} \tag{4.12}$$

Such measurements may not be useful at all for the analysis of experimental data as the relative positions of the detectors from the source can differ between the calibration run and the main experiment. Even if we chose to measure the efficiencies using an in-beam source, the number of measured points could be very few suggesting that interpolation or extrapolation on these points can induce huge error and lead to wrong interpretation as a result. Furthermore, the efficiencies vary with the incident multiplicity (the number of

---

[2] It is worth to mention that many authors refer to absolute efficiency to the total detection efficiency and full energy detection efficiency as peak efficiency.

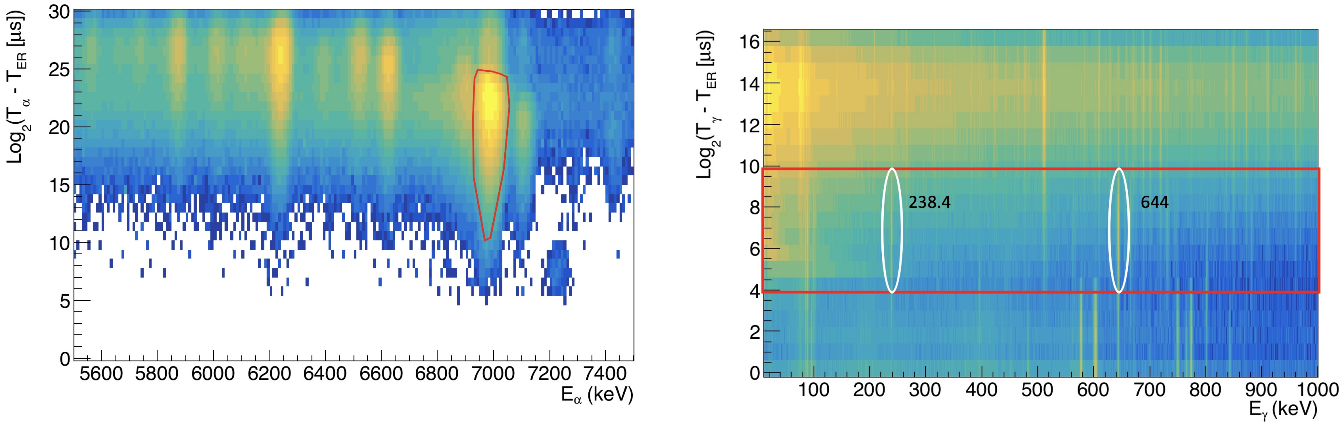

(a) Recoil-decay correlations for the ^{50}Ti+^{164}Dy reaction. The red contour indicates the alpha decays used to select ^{209,210}Ra ERs.

(b) Time and energy distribution of gamma rays following the ERs.

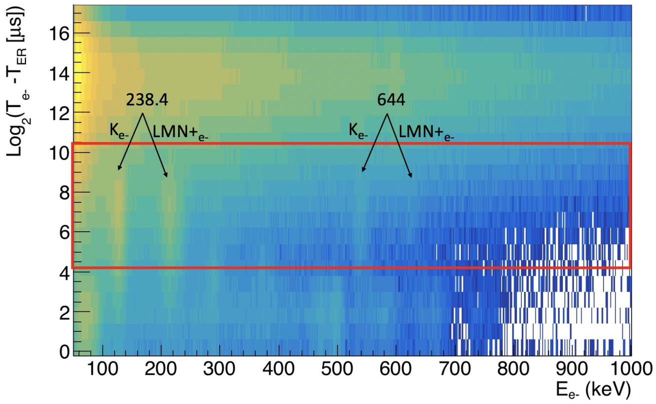

(c) Time and energy distribution of electrons following the ERs.

Figure 4.27: Cuts applied to select ^{209}Ra ions implanted in an isomeric state.

incident radiations at the same time) due to summing effects (see section 4.9). The other possible way is to perform simulations with the proper geometry (discussed before) and then validate the simulation results with some experimental values. To do so, a number of simulations were performed using two experimental XY (Z: beam direction) distributions of the source in the implantation detector (one, slightly off-centered, measured for ^{209}Ra during a calibration run and the other one centered, measured for ^{255}Rf during an experiment, see fig. 4.28) and a point source centered in the middle of the detector (X=Y=0) were used.

The ^{209}Ra distribution was obtained by selecting full energy deposition events of $^{209-210}$Ra alpha decay (they have similar alpha energies and lifetimes [see fig. 4.27a]). ^{209}Ra has an isomer having half-life 117 ± 5 µs [164] (see fig. 4.40a). The ^{209}Ra implantation events were selected by requiring either a gamma ray or an electron be detected after the implantation event within the time window from 16 to 956 µs. The upper limit was set to exclude the random correlations whereas the lower limit excluded the isomeric decay events of 2.24 µs isomer in ^{210}Ra [165] (see fig. 4.27). Similarly, the X-Y distribution of ^{255}Rf was obtained by selecting events followed by the characteristic α-decay of ^{255}Rf and the subsequent detection of full energy α-decay of ^{251}No. These distributions are compared in fig. 4.28.

It was shown in an earlier study of GABRIELA [37] that the depths at which the electron-emitting

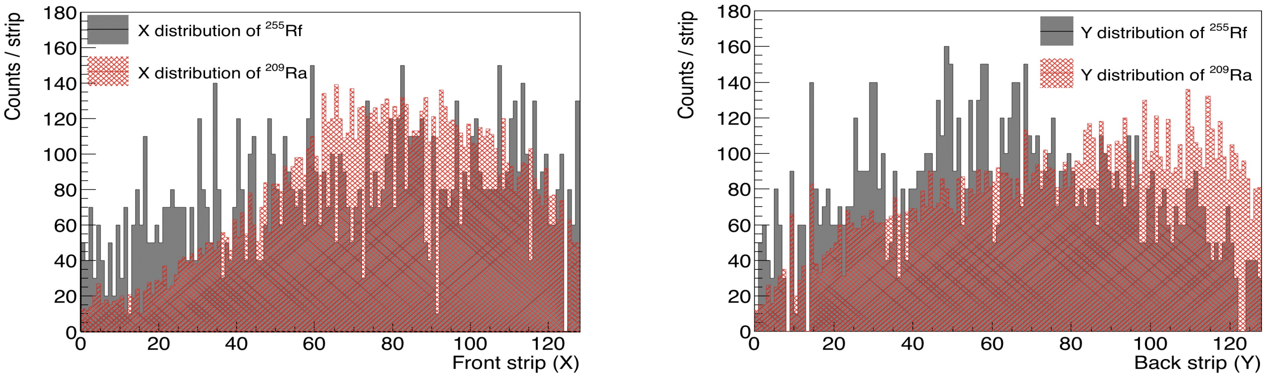

(a) X position

(b) Y position

Figure 4.28: position distribution comparison between ^{209}Ra isomers and ^{255}Rf nuclei.

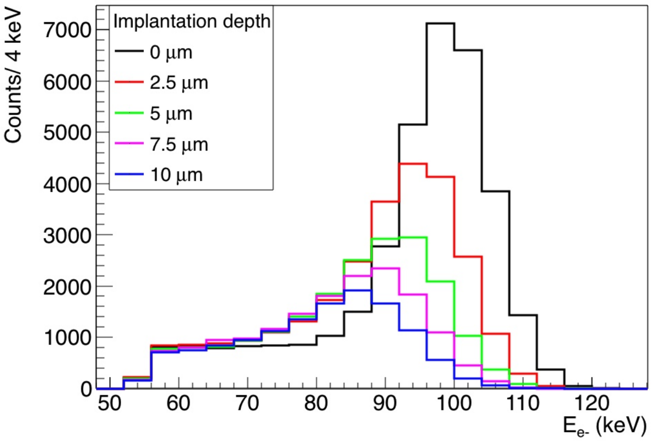

Figure 4.29: Effect of implantation depth on peak shape and intensity in the tunnel detector.

sources are positioned in the DSSD affect the tunnel detectors' energy resolutions (fig. 4.29 shows how implantation depth affects the FWHM) hence their absolute electron detection efficiency. A similar study was undertaken in this work. Several simulations were executed by placing an isotropic point source centered in the middle of the implantation detector (X=Y=0) at various depths (Z). The source emits either a gamma-ray or an electron with a given energy. In fig. 4.30, it is noticeable that the effect of the implantation depth on the gamma ray detection efficiency is not significant but substantial for the electron detection efficiency. Therefore, it is important to estimate the implantation depth profile of the evaporation residues of interest for every experiment.

4.7.1 Method to estimate the implantation depth of evaporation residues

The energy deposited by an alpha particle escaping the implantation detector is directly proportional to the thickness of the silicon it traverses, in other words, it depends on the Z position of the source inside the concerned. Hence, the experimental Z distribution of all the decaying nuclei is determinable from the energy spectrum of the escaping alpha particles using the following χ^2 test against simulation results.

$$\chi^2 = \sum_{i=1}^{M} \left(\frac{N^i_{exp} - N^i_{sim}}{\sigma^i_{exp}} \right)^2 \tag{4.13}$$

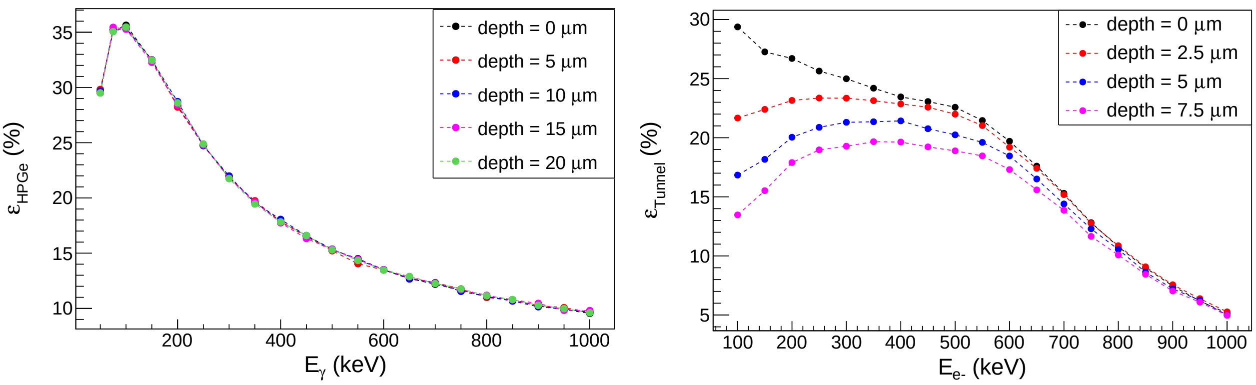

(a) (b)

Figure 4.30: Absolute efficiency to detect (a) gamma rays in the Ge array and (b) electrons in the tunnel detectors that are emitted from a point source at (0, 0, depth) various implantation depths in the implantation detector.

where, M is the number of bins, N^i_{exp} and N^i_{sim} are the experimental and simulated number of counts in bin i respectively, and $\sigma^i_{exp} = \sqrt{N^i_{exp}}$. As a starting point for simulations, one needs to know the depth distribution profile of the alpha-emitting sources in the DSSD. As described before, the experimental alpha sources are implanted inside the DSSD hence detected with finite energies. The depth profile of the recoils is proportional to the energies with which they are detected and their measured energies are dependent on the calibration procedure. But, the response of a semiconductor is different for an alpha particle and a heavy ion. There is ample evidence that for the same energy, the observed pulse height is substantially lower for a heavy ion than that of a light ion. This difference between the true energy of the heavy ion and its apparent energy as determined from an energy calibration of the detectors using alpha particles is known as the pulse height defect (PHD). It arises due to higher energy loss by the heavy ions than an alpha particle in the entrance window and the dead layer of the detector. Additionally, as the velocity of the ion decreases, nuclear collisions increase, which in turn increases the effective-charge of the ion. This effect reduces the electronic interactions resulting in a net decrease in electron-hole pair production. Also, the high rate of electron-hole recombination in the dense plasma created along the ion track contributes to the pulse height defect [150].

The pulse height defect for a heavy-ion can be estimated using the following manner [166]:

$$PHD = (E_{true} - E_{loss}) - E_\alpha = E_d - E_\alpha \tag{4.14}$$

Where E_{true} is the total energy of the ion before entering the target, E_{loss}, the amount it lost in the detector window as well as in the dead layer, E_d, the deposited energy in the detector and E_α, the apparent value from alpha calibration. A simple power-law derived from the fitting of experimental measurements of PHD in silicon for a range of elements with different energies is [166]

$$PHD(Z) = 10^b E_d^a \tag{4.15}$$

where Z is the atomic number of the incident ion, E_d is given in MeV and the parameters are obtained from the following relations:

$$b(Z) = -0.1425(100/Z) + 0.0825 \tag{4.16}$$

$$a(Z) = 0.02230(Z^2/10^3) + 0.5682 \tag{4.17}$$

Ignoring the E loss by the ion in the dead layer and the entrance window, the actual deposited energy by heavy-ions in the silicon can be estimated by adding the pulse height defect to the detected energy.

$$E_{true}(Z) = E_d + PHD \tag{4.18}$$

The true energy distribution of the ^{255}Rf ERs obtained after correcting for pulse height deficit is shown in fig. 4.31a. This energy distribution was taken as the input energy distribution for ^{238}U projectiles in SRIM calculations with Si as the target and assuming a perpendicular incidence of the beam onto the target. In the SRIM calculations, the dead layer was not taken into account as the energy loss by the incoming heavy-ions in the dead layer was not considered while estimating their true energy depositions (since experimentally measured energy corresponds only to the energy deposited in the active volume of the detector). The depth profile shown in fig. 4.31b is obtained from the position of the ion in the target along the projectile direction when it comes to rest. This distribution is then fitted with a Gaussian function to determine the mean depth and the standard deviation.

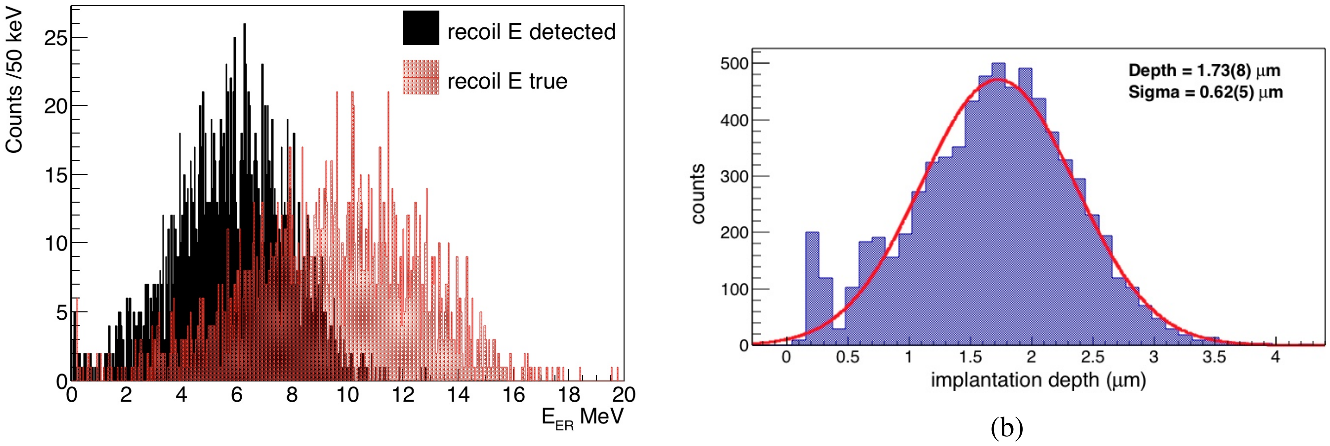

(a)

(b)

Figure 4.31: (a) Estimated true recoil E distribution: SRIM input energy for 238U projectiles. (b) Depth profile of ^{238}U beam in Si from SRIM calculation. The incident energy of the beam was the recoil energy detected for ^{255}Rf ERs after PHD correction (see fig. 4.31a).

Motivated by this result, we assume the implantation depth distribution of the ^{255}Rf in the DSSD to be Gaussian. For each run of the simulation of the alpha decay of ^{255}Rf, the XY distributions of the ^{255}Rf nuclei were the same, only the mean depth and the standard deviation of the Z distribution were varied. From the χ^2 test mentioned before, it is possible to determine the experimental mean implantation depth and the standard deviation of the depth profile. As seen in fig. 4.32a, a clear minimum is obtained for an average implantation depth of 2.7 µm. Using this average depth and the standard deviation of 0.8 µm, which minimizes the χ^2 test, the energy spectrum of the escaping alpha particles emitted by ^{255}Rf (shown in fig. 4.32b) is well reproduced by the simulation.

The justification for considering only the energy spectrum of the escaping alpha particles instead of the total sum energy is two-fold. First, the energy spectrum of the escaping alpha particles is dependent on the thickness it traverse and, as a result, sensitive to the depth at which the source is placed inside the detector. Second, in alpha decay from the mother's ground state to an excited state in the daughter followed by an internal conversion process, the summing of the energy of the electron and the alpha particle can be ignored, because a 200 keV electron escaping from the mean depth in the DSSD loses about 4 keV energy, which is very small compared to the resolution of the DSSD.

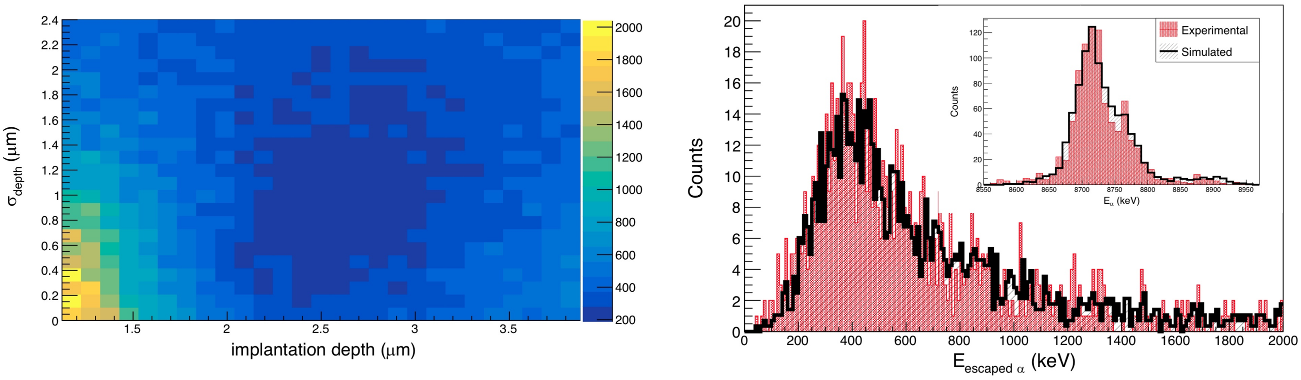

(a)

(b)

Figure 4.32: (a) Plot showing the χ^2 difference (see equation 4.13) between the experimental and simulated energy spectra of ^{255}Rf alpha particles that escape the DSSD as a function of the mean and the standard deviation of a Gaussian implantation depth distribution. (b) Experimentally observed and simulated spectra of ^{255}Rf alpha particles at minimum χ^2 value. The inset shows the comparison of the alpha peaks in the spectra. In the simulation, the decay scheme of ^{255}Rf was taken from ref. [185] with alpha decay to additional levels (see chapter 5 section 5.7).

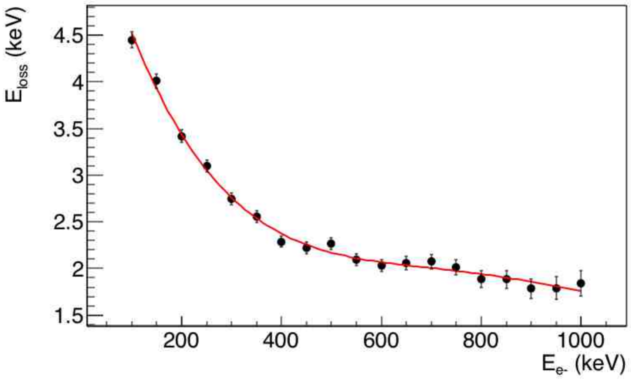

Figure 4.33: Energy loss by an electron in the DSSD as a function of its energy .

The average energy loss by an electron in the range from 100 keV to 1 MeV while traversing the mean implantation depth of the DSSD is shown in fig. 4.33. The energy loss in the DSSD can be parametrized with a polynomial function

$$E_{loss} = p_0 + p_1 \times E_{e-} + p_2 \times E_{e-}^2 + p_3 \times E_{e-}^3 + p_4 \times E_{e-}^4 \tag{4.19}$$

The fit parameters are $p0 = 6.17974 \pm 0.229795$, $p1 = -0.0198854 \pm 0.002408$, $p2 = (3.64747 \pm 8.21613) \times 10^{-06}$, $p3 = (-2.9957 \pm 1.11334) \times 10^{-08}$, $p4 = (8.94348 \pm 5.17532) \times 10^{-12}$.

Using these parameters, the energy losses by the electrons are estimated and added back to their energy depositions in the tunnel detector so that experimental and simulated electron spectra can be compared.

4.7.2 Electron detection efficiency of the Tunnel Detectors

The absolute electron detection efficiency of the tunnel detectors as a function of the electron energy was extracted from simulations in the following manner. In the simulations, a single monoenergetic electron

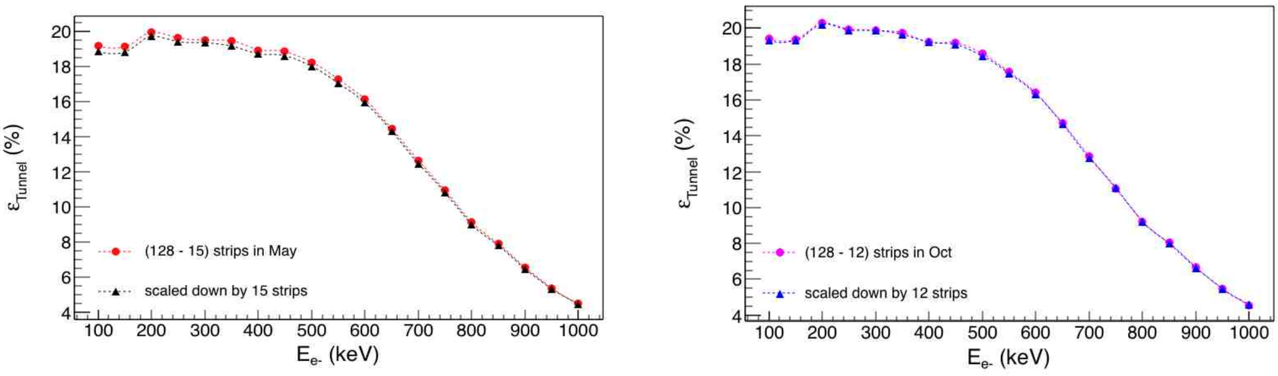

Figure 4.34: Comparison between the scaled-down and original efficiency curves

emitted isotropically by a particle gun. The position distributions of the ERs (described before) in the implantation detector set the position of the particle gun inside the implantation detector at every event of a simulation run of 100000 events. The energy of the particle gun was varied from 100 keV to 1 MeV with an interval of 50 keV resulting in 3 distributions × 19 simulation runs. For a given tunnel detector, a strip is chosen randomly from the strips with energy depositions above the threshold to simulate the multiplexing of the tunnel detectors. In real electronics, different strips of a tunnel detector can have different threshold levels, in the simulations however an average threshold of 55 keV was set for all the strips. It was mentioned before that there are some missing strips in both the experimental campaigns. The difference in the IDs and the number of these missing strips reflect their position with respect to the source. The post-processing of the simulated data allows the exclusion of the missing strips separately for each case. The average relative loss of the detection efficiency due to these missing strips is 10.6 % for the May experiment and 9 % for the Oct experiment from the total detection efficiency. The efficiency loss as a function of the electron energy can be quantified by

$$\varepsilon_{loss}(E) = \frac{\varepsilon_{allstrips}(E) - \varepsilon_{lessstrips}(E)}{\varepsilon_{allstrips}(E)}$$

In different experiments, the number of missing strips and/or their IDs in the tunnel detectors might change. It is of interest to investigate whether by comparing an efficiency scaled by the number of strips to the true efficiency simulated by taking into account the missing strips. A difference between the two would signify a dependence on the efficiency with the strip position. The scaled efficiency can be obtained by

$$\varepsilon_{128-n} = \varepsilon_{all} - n\frac{\varepsilon_{all}}{128}$$

A comparison of the scaled efficiency curves against the efficiency curves obtained originally by excluding the specific strips missing in the experiment shows that they are equivalent within the error bars (see fig. 4.34). Hence, one can conclude that from the total detection efficiency and the number of missing strips it is possible to obtain the efficiency for that configuration by simply scaling down efficiency curves.

It is also interesting to see the variation of the efficiency in different configurations of the tunnel detectors. For this reason, the absolute detection efficiency at a given energy was computed for a single multiplexed strip, energy summing in all the strips of a detector, and energy summing across all the tunnel detectors. Fig. 4.35 compares the efficiency in each case. As expected, the efficiency of the per detector is more than the individual strip case because of energy sharing among multiple strips. The efficiency of

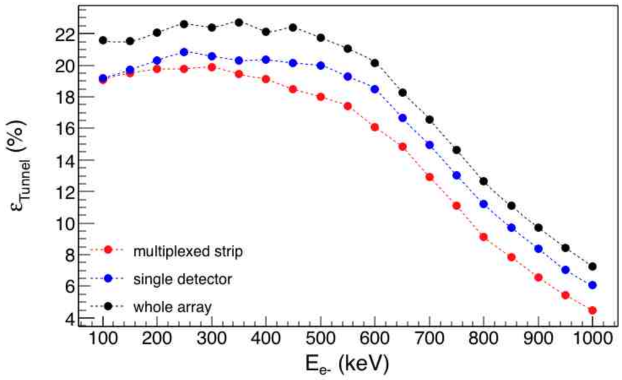

Figure 4.35: Electron detection efficiency as a function of energy for various ways of treating the signals from the tunnel detector.

the whole tunnel detector is even greater as the energy shared among different tunnel detectors due to the electron backscattering phenomenon is summed together.

4.7.3 Gamma-ray detection efficiency

The absolute gamma detection efficiency of the Ge array is obtained similarly. An isotropic particle gun emits a monoenergetic gamma ray in every event of a simulation run that consists of 100000 events. The position of the gun in the implantation detector is determined by the distributions mentioned before. The energy of the gun is varied from 50 keV to 1.5 MeV with an interval of 50 keV. Hence, a total of 3 distributions × 30 runs were simulated in this case. An average cutoff of 30 keV energy was set for all the BGO shields. In any event, if the energy deposition in a BGO is more than this threshold value, the energy deposition in the corresponding Ge detector is neglected in the "suppression" mode. It is also interesting to obtain the spectra in fully "unsuppressed mode", i.e., when all the gamma rays registered in the Ge detectors are considered. The energy depositions in each crystal of the clover detector [149] can be treated as separate events (singles mode) or summed in the so called addback mode. In this way, the full energy of the photons, which scatter from one crystal to the neighboring crystals can be recovered. This procedure

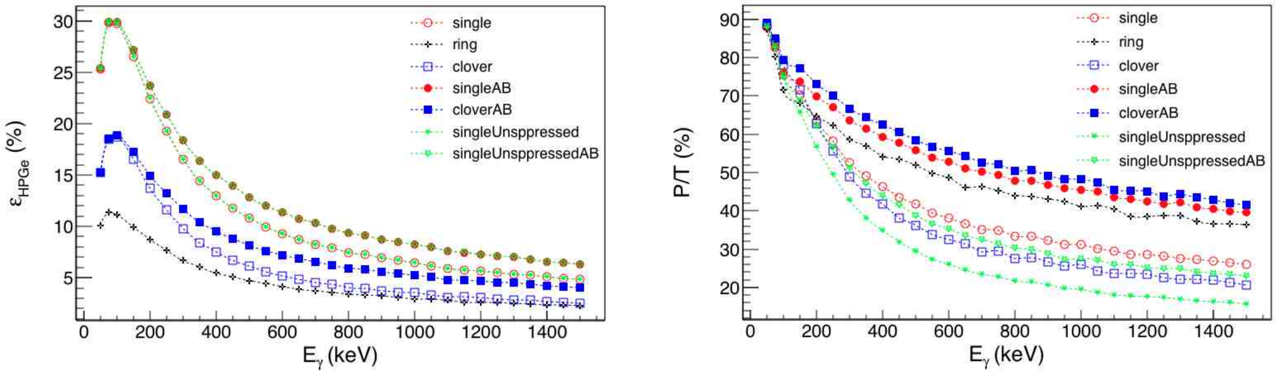

(a)

(b)

Figure 4.36: (a) Absolute gamma-ray detection efficiency of the components of the Ge array and (b) the corresponding peak to total ratio.

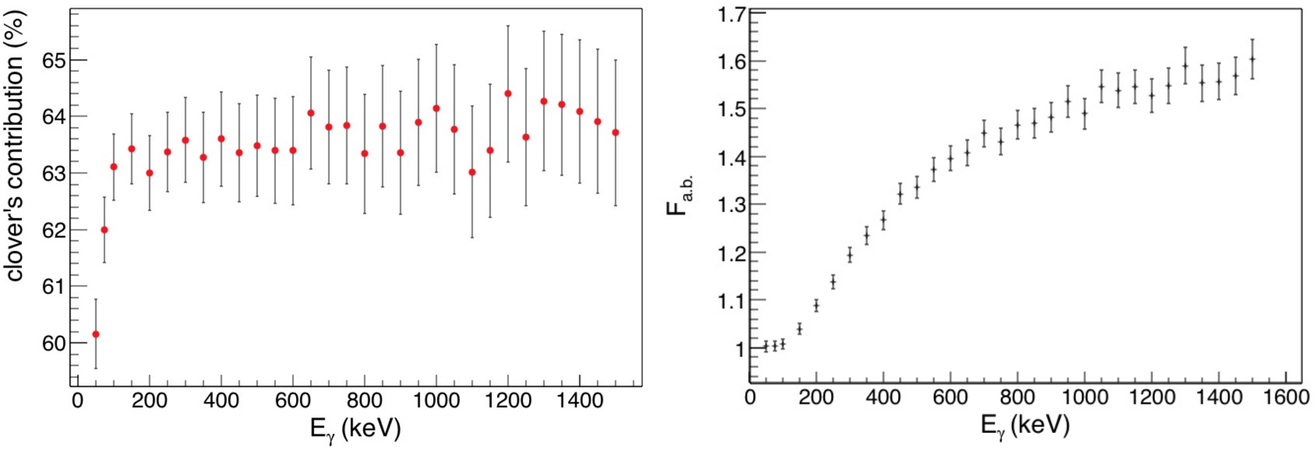

(a) (b)

Figure 4.37: (a) The contribution of the clover detector to the total efficiency with its (b) addback factor as a function of gamma-ray energy.

increases the clover efficiency by an addback factor defined as $F = \frac{\epsilon_{AB}}{\epsilon_{singles}}$, which grows with photon energy (see fig. 4.37b). The asymptotic value of the addback factor is found to be 1.52(1). The absolute gamma detection efficiency is compared for various configurations in fig. 4.36:

- the four coaxial detectors are represented by "ring".
- the clover detector in the single-mode by "clover".
- the clover detector in the addback-mode by "cloverAB".
- ring + clover in single-mode by "singles".
- ring + clover in addback-mode by "singlesAB".
- ring + clover in singles and unsuppressed mode by "singlesUnsuppressed".
- ring + clover in addback and unsuppressed mode by "singlesUnsuppressedAB".

In addback mode, the absolute gamma-ray efficiency of GABRIELA peaks at 30% at 100 keV and drops to 8% at 1332 keV (63% of which comes from the contribution of the clover alone as shown in fig. 4.37a).

In the Oct experiment, one ring detector was not functioning. The decrease of the efficiency is illustrated in the figs. 4.38. The loss of efficiency at a given energy is quantified as :

$$\varepsilon_{loss}(E) = \frac{\varepsilon_{alldetector}(E) - \varepsilon_{n-1missingring}(E)}{\varepsilon_{alldetector}(E)}$$

We notice that about 10 % (relative) of the total efficiency is lost due to the absence of one ring detector.

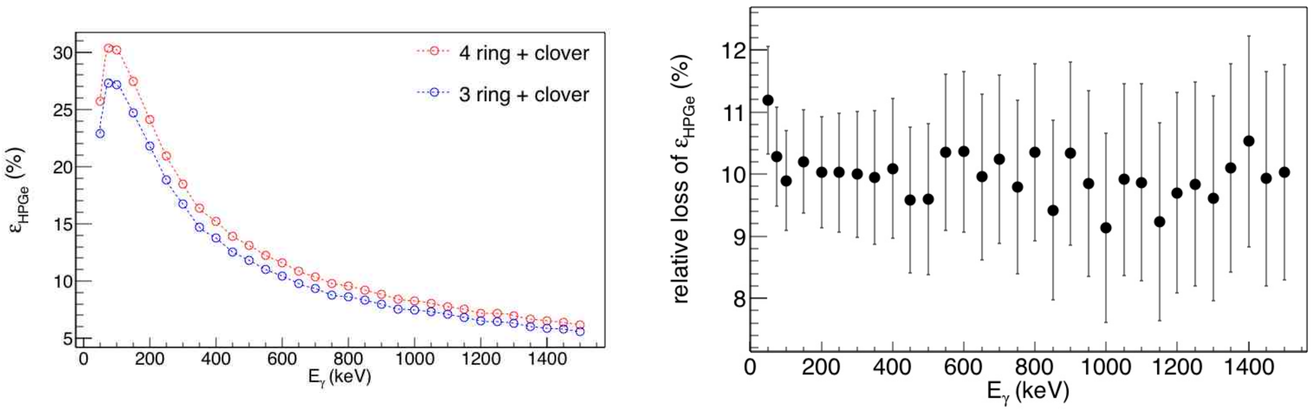

(a)

(b)

Figure 4.38: (a) Effect of missing 1 ring detector in the Ge array on the gamma-ray detection efficiency. (b) Relative loss of efficiency due to the absence of 1 ring detector.

4.8 Effects of distributions

To check how the position distributions of the source on the x-y plane of the implantation detector might affect the efficiency, we compared the electron, and the gamma-ray detection efficiency curves for the distributions mentioned earlier. In figs. 4.39a and 4.39b, the simulated efficiencies for a point source positioned at the center of the implantation detector and for the 2 distributed sources mentioned above are compared. It can be concluded that a little variation in the position distributions (^{255}Rf and ^{209}Ra), in general, does not have such drastic effects on efficiency. This severity is only observed when compared to the point distribution (X=Y=0). Thus, in principle, these efficiency curves could be useful for other experiments if the position distributions of ERs remain somewhat similar. The efficiency of the tunnel

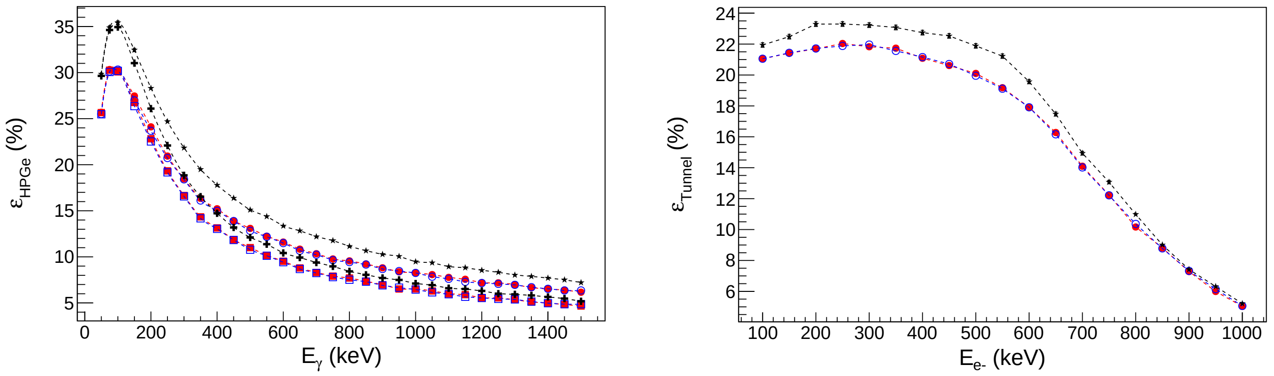

(a)

(b)

Figure 4.39: Absolute efficiency curves as a function of energy for different XY-distributions in the implantation detector with the same implantation depth profile, which minimizes the χ^2 test on the ^{255}Rf escaped alpha-particle energy spectra. (a) Ge-array Compton-suppressed efficiencies for a point source in addback mode ★ and in singles mode ✚, for the ^{209}Ra distribution in addback mode ● and in singles mode ■, and for the ^{255}Rf distribution in addback mode ○ and in singles mode □; (b) Tunnel detector efficiencies in the case of a point source ★, for the ^{209}Ra ● and ^{255}Rf ○ distributions.

detectors remains flat around 21% for electron energies ranging from 100 to 550 keV. The gradual loss of efficiency at higher electron energies is due to the finite thickness of the detector. Compared to the previous version of GABRIELA, the absolute gamma-ray detection efficiency of the present setup is simulated to be a factor of ~ 3 - 4 higher, while the electron detection efficiency shows an increase of 5 - 7 %. The gamma detection efficiency curves can be described with a Radware type function to obtain the efficiency at any energy [154]

$$\varepsilon(E_\gamma) = exp\left(\left[(A + Bx + Cx^2)^{-G} + (D + Ey + Fy^2)^{-G}\right]^{(-1/G)}\right) \tag{4.20}$$

where $x = \log(E_\gamma/E1)$, $y = \log(E_\gamma/E2)$, $E1 = 100$ keV, $E2 = 1$ MeV and C is usually set to 0, and the parameters A,B,C,D,E,F and G obtained from a fit. The fit parameters are given in table 4.4.

Parameter	4 ring + clover	3 ring + clover
A	4.26498	4.2623
B	1.09247	1.20863
C	0	0
D	2.10553	2.00214
E	-0.647628	-0.648445
F	0.0800258	0.0798024
G	3.5729	3,28612

Table 4.4: Fit parameters of the gamma efficiency curves in addback mode.

4.9 Validation

To check if the geometry constructed for GEANT4 simulations is valid, a simple 2-transition cascade stemming from the 117 µs isomer of ^{209}Ra was used (see the level scheme of fig. 4.40a [164]). Experimentally, the isomeric gamma or ICE decays were selected by requiring that they occur between 16 to 956 µs after the implantation of ^{209}Ra nuclei. The experimental and simulated isomeric gamma-ray and ICE spectra are compared in figs. 4.41 and 4.42. In the experimental spectra, we notice some contributions from ^{207}Rn

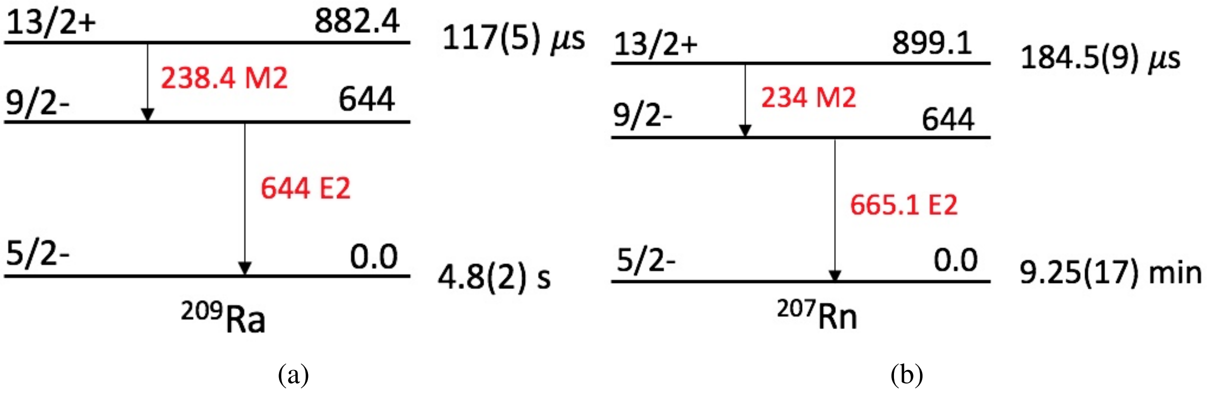

(a) (b)

Figure 4.40: Partial level schemes of (a) ^{209}Ra [164] and (b) ^{207}Rn [167] showing the low-lying 13/2+ isomer, whose decay has been used to validate the GEANT4 simulations.

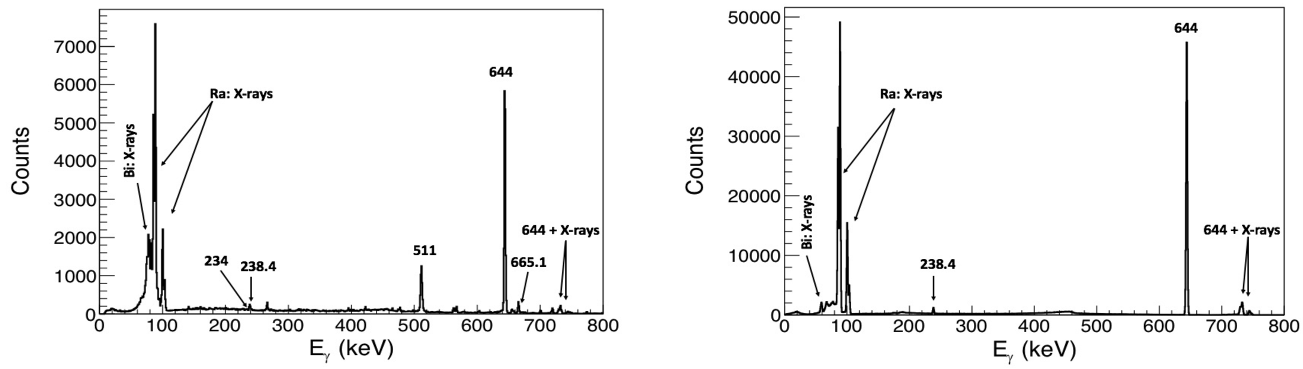

(a) (b)

Figure 4.41: (a) Experimental and (b) simulated spectrum of gamma rays emitted in the isomeric decay of ^{209}Ra.

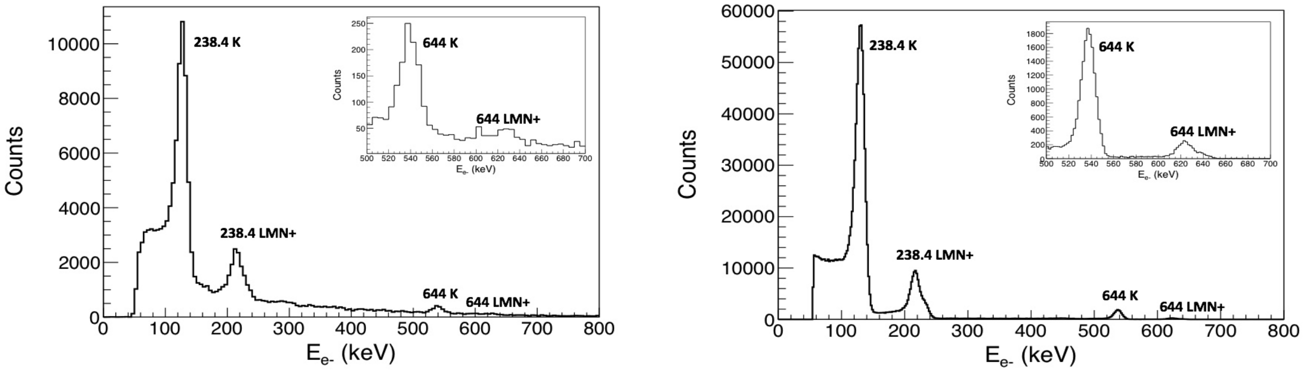

(a) (b)

Figure 4.42: (a) Experimental and (b) simulated spectrum of ICE emitted in the isomeric decay of ^{209}Ra.

isomer whose half-life is close to the half-life of ^{209}Ra isomer (see the partial level schemes of these isomers in fig. 4.40). The internal conversion coefficients and the energy of the electrons from BRICC [116] corresponding to the transitions for these two isomers are given in table 4.5. The tails of random correlations present in the recoil-gamma and recoil-tunnel correlation spectra of fig. 4.27 are responsible for extra lines in the gamma-ray energy spectrum and exponential background in the electron energy spectrum of the tunnel detectors.

In a simple decay consisting of a cascade of two transitions, the gamma-ray and electron detection efficiencies can be measured using two methods. One is called the "singles method" as the values are measured from the singles spectra, while the other method is called the "coincidence method". The disadvantage of the singles method is that the number of decaying isomers (N_{isomer}) needs to be known. Hence, it cannot be applied to the experimental data. The efficiency values in the singles method are calculated using the following simple equations

$$\varepsilon(E) = \frac{N_{peak}}{N_{emitted}} \tag{4.21}$$

where, N_{peak} is the integral of the peak in the single spectrum and, $N_{emitted}$ for gamma rays and electrons are calculated as follows

$$N_{emitted,\gamma} = \frac{N_{isomer}}{(1+\alpha_{Tot})} \tag{4.22}$$

	^{209}Ra				^{207}Rn			
	238.4 keV		644 keV		234 keV		665.1 keV	
Shell	Ece(keV)	α (M2)	Ece(keV)	α (E2)	Ece(keV)	α (M2)	Ece(keV)	α (E2)
Tot		5.38		0.0219		4.94		0.0185
K	134.48	3.81	540.08	0.01555	135.6	3.55	566. 7	0.01354
L	219.57	1.164	625.43	0.00473	216.33	1.042	647.63	0.00374
M	233.72	0.298	639.43	0.00119	229.66	0.264	660.85	0.000932
N+	237.44	0.108	643.079	0.00043	232.96	0.084	664.1	0.000288

Table 4.5: Internal conversion coefficients and electron energies of the isomeric transitions obtained from BRICC [116].

$$N_{emitted,Se-} = N_{isomer}\frac{\alpha_S}{(1+\alpha_{Tot})} \tag{4.23}$$

where α is the internal conversion coefficient and S represents the shell from which the electron is emitted. In the experiment, the L, M, and N+ peaks could not be resolved as individual peaks, hence, they were treated as a single LMN+ peak with conversion coefficient $\alpha_{LMN+} = (\alpha_{Tot} - \alpha_K)$.

In the coincidence method, the values are extracted from gamma-electron coincidences using equations 4.24 and 4.25, where for instance, $\varepsilon_\gamma(T1_\gamma)$ is the absolute gamma-ray detection efficiency for photons emitted in the T1 transition and $N(T1_\gamma \otimes T2_{Se^-})$ indicates the number of gamma rays emitted in the T1 transition detected in coincidence with electrons emitted from the shell S in the T2 transition.

$$\varepsilon_\gamma(T1_\gamma) = \frac{N(T1_\gamma \otimes T2_{Se^-})}{N(T2_{Se^-})}(1+\alpha_{Tot}(T1)) \tag{4.24}$$

$$\varepsilon_{e^-}(T1_{Se^-}) = \frac{N(T1_{Se^-} \otimes T2_\gamma)}{N(T2_\gamma)}\frac{(1+\alpha_{Tot}(T1))}{\alpha_S(T2)} \tag{4.25}$$

In these expressions, if $T1$ transition represent the 238.4 keV transition then $T2$ transition represents the 644 keV transition or vice versa, $N(T2_{Se-})$ and $N(T2_\gamma)$ are the total number of internally converted electrons from the S shell and gamma rays detected from the T2 transition in the corresponding singles spectra.

Following this procedure, the efficiency values extracted from a simulation run consisting of 10 million ^{209}Ra isomeric decays. The measured values are listed in table 4.8 and found to disagree with the expected values of figs. 4.39a and 4.39b obtained by simulating individual gamma rays and electrons. This discrepancy can be attributed solely to summing in the detectors. Indeed, the 238.4 keV photon can sum with the 644 keV gamma ray. Each of the gamma rays can also sum with X rays emitted in the atomic relaxation process following the internal conversion of the other transition or with X rays emitted by the BGO shields. In the Compton suppressed mode, full-energy events in one detector may be suppressed when other gamma rays enter the BGO shield and deposit energy above the detection threshold. Similarly, summing of conversion electrons with other conversion electrons, Auger electrons, or X rays can occur in the tunnel detectors.

In the singles method, the gamma-ray efficiencies can be corrected by excluding the influence of one transition on the other. In principle, this correction should be applied per detector as the detection probability of every detector is different

$$N^i_{peak}(T1_\gamma) = \frac{N_{decay}}{(1+\alpha_{Tot}(T1))}\varepsilon_{T1} \times Probability\ of\ not\ detecting\ any\ of\ T2\ in\ detector\ i$$

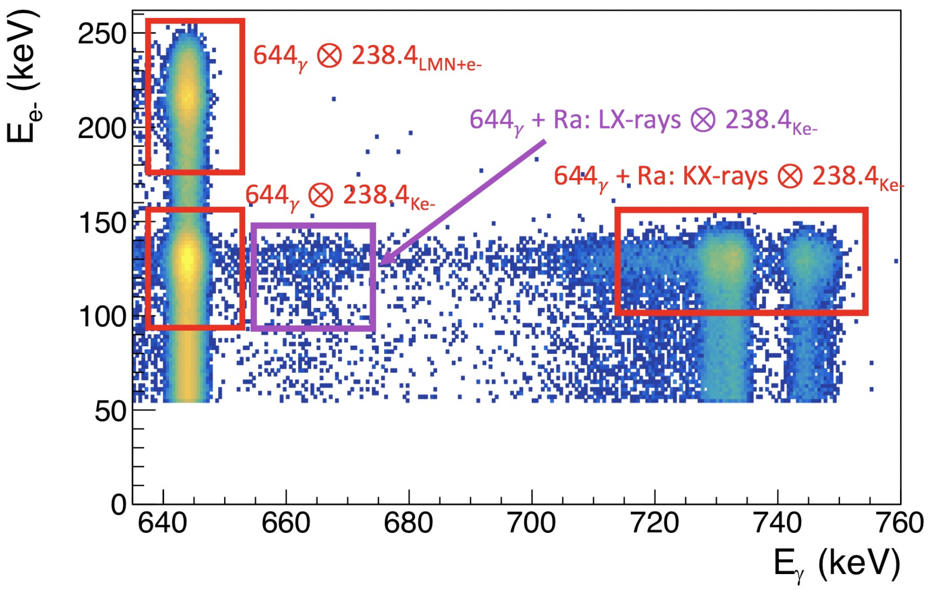

Figure 4.43: Selected region of the simulated gamma-ray and ICE coincidence matrix measured in the isomeric decay of ^{209}Ra, showing the effect of summing.

the total efficiency is then given by

$$\varepsilon_\gamma(T1_\gamma) = \sum_{i}^{no.\,of\,detectors} \frac{N^i_{peak}(T1_\gamma)}{N_{emitted} \times (1 - \varepsilon^i_{Tot}(T2))} \tag{4.26}$$

where $\varepsilon^i_{Tot}(T2)$ is the detection probability in detector i of any radiation emitted in $T2$. This probability is obtained by simulating the decay of $T2$ alone. Similar corrections can be applied to the electron efficiencies as well, however, due to a relatively large number of strips involved, this correction was not carried out in our study.

In the coincidence method, corrections can be made by integrating the peaks formed due to summing. As an example, consider the coincidence between K converted electrons (Ke^-) from the 238.4 keV transition and photons from the 644 keV transition, they are denoted by $644_\gamma \otimes 238.4_{Ke^-}$ in the gamma-electron coincidence matrix shown in fig. 4.43. The Ke^- of the 238.4 keV transition are seen not only in coincidence with 644 keV gamma rays but also with photon events of apparent energies of 644 + KX rays. The modified gamma-ray efficiency equation for a given transition is then, to first order, given by:

$$\varepsilon_\gamma(T1_\gamma) = \frac{\Delta N}{N(T2_{Ke^-})}(1 + \alpha_{Tot}(T1)) \tag{4.27}$$

where,

$$\Delta N = N(T1_\gamma \otimes T2_{Ke^-}) + N((T1_\gamma + KXrays) \otimes T2_{Ke^-})$$

In fig. 4.43, other much smaller contributions below photon energy 644 + KX rays are also visible, but since they are not solely due to summing with full energy 644 keV depositions, they have been neglected here.

Similarly, the electron efficiency equations can also be corrected to account for summing effects. For Ke^-, the equation becomes:

$$\varepsilon_{e^-}(T1_{Ke^-}) = \frac{N_1}{N_2} \frac{(1 + \alpha_{Tot}(T1))}{\alpha_K(T1)} \tag{4.28}$$

where,

$$N_1 = N(T1_{Ke^-} \otimes T2_\gamma) + N(T1_{Ke^-} \otimes (T2_\gamma + KXrays))$$

and

$$N_2 = N(T2_\gamma) + N(T2_\gamma + KXrays)$$

In order to extract the efficiency to detect $LMN + e^-$, the contribution to the $T1_{LMN+e^-}$ peak from the summing of $T1_{Ke^-}$ and X rays or summing of $T1_{Ke^-}$ and Auger electrons in the tunnel detectors needs to be subtracted. This contribution can be estimated by:

$$\Delta N(T1_K) = N(T2_\gamma)\frac{\alpha_K(T1)}{(1+\alpha_{Tot}(T1))} \times \varepsilon^t_{Ke^-}(\omega_K \varepsilon^t_{KXrays} + a_K \varepsilon^t_{KAuger})$$

where, $\varepsilon^t_{Ke^-}$ is the probability of detecting a Ke^- in the tunnel detector with full energy, ω_K and a_K are the fluorescence and Auger yields following a K shell vacancy in Ra, and, ε^t_{KXrays} and ε^t_{KAuger} are the full-energy peak efficiency of KX rays and KAuger electrons in the tunnel detectors, respectively. These probabilities are obtained by simulating a single photon and an electron with weighted mean KX-ray energy (74.76 keV) and KAuger electron energy (90.63 keV) of Ra respectively. There is also summing of partial energy depositions of L converted electrons with the X rays following L vacancies, which yields counts in the full energy peak, which must also be subtracted. This increase is calculated by:

$$\Delta N(T1_L) = N(T2_\gamma)\frac{\alpha_L(T1)}{(1+\alpha_{Tot}(T1))}\varepsilon^t_{Le^-}(C_{L1} + C_{L2} + C_{L3}) \tag{4.29}$$

where

$$\begin{aligned}
C_{L1} &= \omega_{L1}\varepsilon^t_{L1Xrays} + f_{12}(\omega_{L2}\varepsilon^t_{L2Xrays} + f_{23}\omega_{L3}\varepsilon^t_{L3Xrays}) + f_{13}\omega_{L3}\varepsilon^t_{L3Xrays}\\
C_{L2} &= \omega_{L2}\varepsilon^t_{L2Xrays} + f_{23}\omega_{L3}\varepsilon^t_{L3Xrays}\\
C_{L3} &= \omega_{L3}\varepsilon^t_{L3Xrays}
\end{aligned}$$

where similarly, $\varepsilon^t_{Le^-}$ is the probability of detecting an Le^- in the tunnel detector with full energy, ε^t_{iXray} is the absolute detection efficiency of the tunnel detectors for X rays emitted from the Li subshell determined from simulations, ω_{Li} is the fluorescence yield of subshell Li (see table 4.6), and f_{12},f_{13}, f_{23} are Coster-Kronig yields taken from the ToI. Simulations showed that the efficiency to detect L1, L2 and L3 Auger electrons in the tunnel detectors is close to zero, hence their summing contributions are ignored. The efficiency equation then becomes:

$$\varepsilon_{e^-}(T1_{LMN+e^-}) = \frac{N'}{N(T2_\gamma)}\frac{(1+\alpha_{Tot}(T1))}{\alpha_{LMN+}(T1)} \tag{4.30}$$

where,

$$N' = N(T1_{LMN+e^-} \otimes T2_\gamma) - \Delta N(T1_K) - \Delta N(T1_L)$$

Accounting for all the summing contributions, the simulated efficiency values obtained by the singles and coincident methods are tabulated in table 4.8 and displayed in fig. 4.46. They are consistent with the efficiencies obtained by simulating individual electrons or gamma rays (figs. 4.39a and 4.39b).

Summing in the detectors has one advantage, as it is possible to deduce the KX-ray efficiency of a Ge detector from the $\gamma_{detector\,i} - e^-$ coincidences. Solely for computational time, we limited ourselves to the clover detector and KX rays as K conversion is more dominant. Suppose there are N_{644} gamma rays of 644 keV in the clover detector in coincidence with K converted electrons of 238.4 keV transition detected in

subshell	energy (keV)	ε^t in (%)	ω
L1	15.74	22.63 ± 0.15	0.146
L2	15.82	22.63 ± 0.15	0.456
L3	9.59	24.54 ± 0.16	0.437

Table 4.6: The absolute detection efficiency of tunnel detector for X rays emitted from each subshell of L having intensity weighted energy. The fluorescence yield, ω is taken from ToI [163].

the tunnel detectors. Let N_0 be the number of counts in 644 keV peak if there were no KX-ray emission, then N_{644} can be simply expressed as

$$N_{644} = N_0 \times (1 - \text{Probability to detect KX rays}) \tag{4.31}$$

and number of N_{644} in coincident with KX rays is

$$N_{644+Xrays} = N_0 \times \text{Probability to detect KX-rays in the peaks} \tag{4.32}$$

dividing eq 4.31 by eq 4.32 gives

$$\frac{N_{644}}{N_{644+x-rays}} = \frac{(1-\omega_K) + \omega_K(1 - \varepsilon_{Tot}(KXrays))}{\omega_K \varepsilon_{peak}(KXrays)} \equiv r$$

where ε_{Tot} can be obtained if the P/T of the detector at the mean KX ray energy is known

$$\varepsilon_{Tot} = \frac{\varepsilon_{peak}}{P/T}$$

For the clover detector

$$P/T_{clover} = 83.45 \pm 0.81\%$$

determined from simulation (see fig. 4.36b).

$$\varepsilon_{peak}(KXrays) = \frac{1}{\omega_K(r + 1/P/T)}$$

In general, for any Ge detector i the KX ray efficiency can be obtained by

$$\varepsilon^i_\gamma(KXrays) = \frac{1}{\omega_K(\frac{N^i_\gamma}{N^i_{\gamma+Xrays}} + \frac{1}{(P/T)^i})} \tag{4.33}$$

where N_γ is the number of counts in the T2 transition gamma-ray peak coincident with K shell electrons emitted in the T1 transition, $N_{\gamma+Xrays}$ is the number of counts in the peaks formed from summing of T2 gamma rays with KXrays radiated in the T1 transition and P/T denotes the peak-to-total ratio at the mean energy of the Ra X rays.

Note that in table 4.8, without correction for summing, the extracted value of the KX-ray efficiency is larger than the expected value. This is because the summing of Ke^- with the X rays and the Auger electrons in the tunnel detectors reduces the integral of the Ke^- peak. Hence the apparent number of photons N_γ detected in coincidence with Ke^- is artificially reduced. Hence, the ratio r is modified to

$$r = \frac{N_{644} + \Delta N(238.4K)}{N_{644+Kxrays}}$$

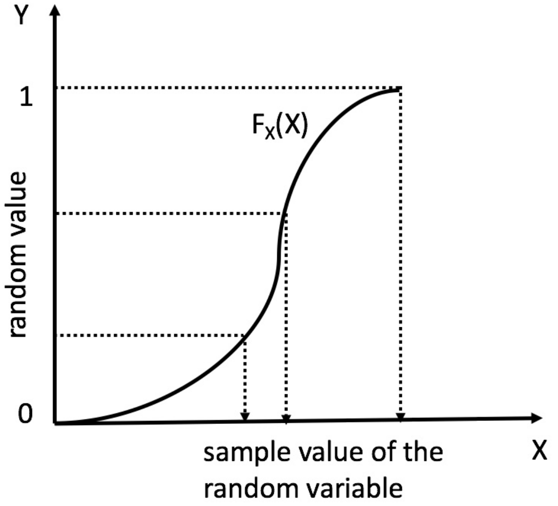

Figure 4.44: An illustration of inverse transform sampling method.

with $\Delta N(238.4K) = N_{644} \times f$ and f is the fraction of counts in the Ke^- peak removed due to summing in the tunnel detectors. f is determined to be 8.6(2)% by applying the 'inverse transform sampling method' on the Ke^-, KX rays, and KAuger electrons energy spectra that are obtained from simulations of individual radiation at the corresponding energies. The principle of this method is that if a random variable Y has a uniform distribution on [0,1] and a continuous random variable X has a cumulative distribution function $F_X(X)$, then the random variable $F_X^{-1}(Y)$ has the same distribution as X (see fig. 4.44).

In this method, the steps followed are given below:

- Convert the energy spectra of Ke, KX rays, and KAuger electrons into probability distributions (PDFs). The PDF of a given spectrum can be obtained by dividing the counts in every bin of the histogram by the total number of entries.
- Convert the pdfs into cumulative distribution functions (CDFs). To obtain the CDF of a given distribution, at every bin the probability is cumulatively incremented.
- Invert the CDF of the Ke^- distribution by generating a random number p of uniform distribution whose value lies between [0,1]. The energy value Ee corresponding to the probability p is obtained (see fig. 4.44). At this stage, the influence of the KX rays and the KAuger electrons can be added. To add the KX ray contribution, if $p \leq \omega_K$ another random number q in the range [0,1] is generated and the KX ray energy value Ex corresponding to probability q is obtained. The summed energy is obtained by summing Ee + Ex. Similarly, the effect of the KAuger electrons on the energy of the Ke^- can be obtained. The summed electron spectrum is shown in fig. 4.45.
- By scaling the summed histogram with the original Ke^- histogram, the fraction that is removed from the peak as a result of summing in the tunnel detectors can be determined.

To extract the experimental efficiency values, a similar treatment was performed on the experimental data. However, in the experimental data analysis there is an added complications from the isomeric decay of ^{207}Rn (the decay scheme is shown in fig. 7b). It is because the electrons emitted from the M2 transition in the isomer decay of ^{207}Rn and ^{209}Ra have quite similar energies and cannot be resolved in the tunnel detectors. Hence, intensity-weighted internal conversion coefficients (see table 4.7), fluorescence and Auger yields and KX-ray and Auger electron energies were used in the equations 4.27-4.33.

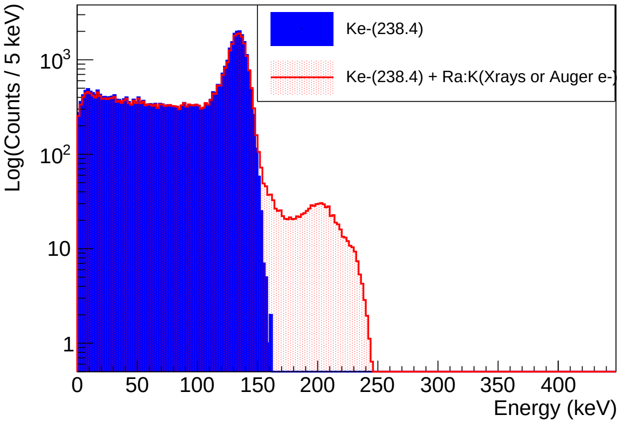

Figure 4.45: Summing of Ke^- of 238.4 keV transtions with KX rays and KAuger electrons in the tunnel detectors.

Shell	α (M2)	α (E2)
Tot	5.34±0.08	0.0216 ±0.0003
K	3.79 ± 0.05	0.0154 ± 0.0002

Table 4.7: Intensity-weighted conversion coefficients used in this work (see text for details).

The experimentally measured efficiency values obtained using coincidence method are compatible with the simulation results (see the table 4.8 and fig. 4.46) except for the electron efficiency at Ke^-(238.4) energy. This lower-than-expected value is due to a threshold effect, as some of the tunnel strips had higher thresholds than others. In our study, only the KX-ray efficiency of the clover detector was measured solely for statistical reasons. Also note that the large error bars in fig. 4.46 are due to low number of recorded 238.4 keV gamma-ray events in coincidence with 644_{Se^-}. We have also extracted from gamma-electron

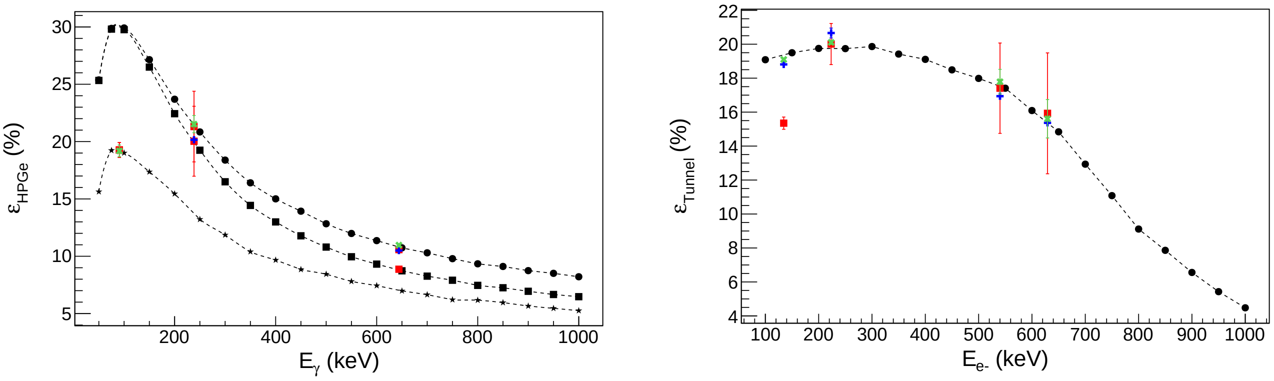

(a) (b)

Figure 4.46: Absolute efficiency curves for the (a) Ge and (b) Tunnel detectors. (a) ■, ● and ★ denote the simulated efficiencies in singles and add back mode for the whole Ge array and the clover detector alone. (b) ● represent the simulated electron efficiency for the 113 active strips during the ^{209}Ra calibration run. ✚ and ✖ correspond to the simulated efficiencies extracted from simulated ^{209}Ra isomeric data using the singles and coincidence methods. 🟥 correspond to the measured gamma-ray or electron efficiencies.

	Simulated single gamma-ray or electron emission	Simulated ^{209}Ra isomeric decay				Experimental	
	Singles Method	Singles Method		Coincidence Method		Coincidence Method	
Energy (keV)	ε (%)	ε_0 (%)	ε^* (%)	ε_0 (%)	ε^* (%)	ε_0 (%)	ε^* (%)
Gamma							
KXrays (clover)	19.40±0.14	-	-	20.46±0.35	19.19±0.51	20.54±0.66	19.27±0.65
238.4	21.60±0.15	16.03±0.03	20.16±0.04	17.78±0.68	21.52±0.75	16.44±2.06	21.31±3.08
644	10.98±0.10	8.96±0.01	10.50±0.01	9.39±0.03	10.97±0.03	9.28±0.15	10.58±0.17
Electron							
134.48	19.04±0.14	18.81±0.02	-	17.72±0.07	19.10±0.07	15.48±0.24	15.35±0.36
223.48	20.15±0.14	20.66±0.29	-	25.46±0.11	20.13±0.12	24.09±0.39	20.03±1.21
540.08	17.71±0.13	16.94±0.11	-	18.06±0.73	17.79±0.73	18.70±2.59	17.41±2.66
629.25	15.30±0.12	15.37±0.16	-	19.73±1.12	15.61±1.13	19.79±4.18	15.93±3.56

Table 4.8: The measured gamma-ray and electron efficiency values obtained from singles and coincidence methods: ε corresponds to efficiency from a ^{209}Ra distributed source emitting either a single gamma or an electron isotropically with the given energy. ε_0 and ε^* indicate values extracted without or with summing corrections (see the text) for ^{209}Ra isomeric decay.

coincidences the addback factor of the clover detector at 644 keV in the simulated and the experimental data. The values were also found to be in good agreement: 1.36 ± 0.01 (simulation) and 1.34 ± 0.05 (experimentally), and the P/T behavior is well accounted for (see fig. 4.47). This compatibility of the simulation and experimental results proves that the geometry of GABRIELA described in GEANT4 is quite accurate. This is further confirmed by the ability to reproduce the decay spectrum of the isomer observed in ^{257}Rf [168] (see fig. 4.48).

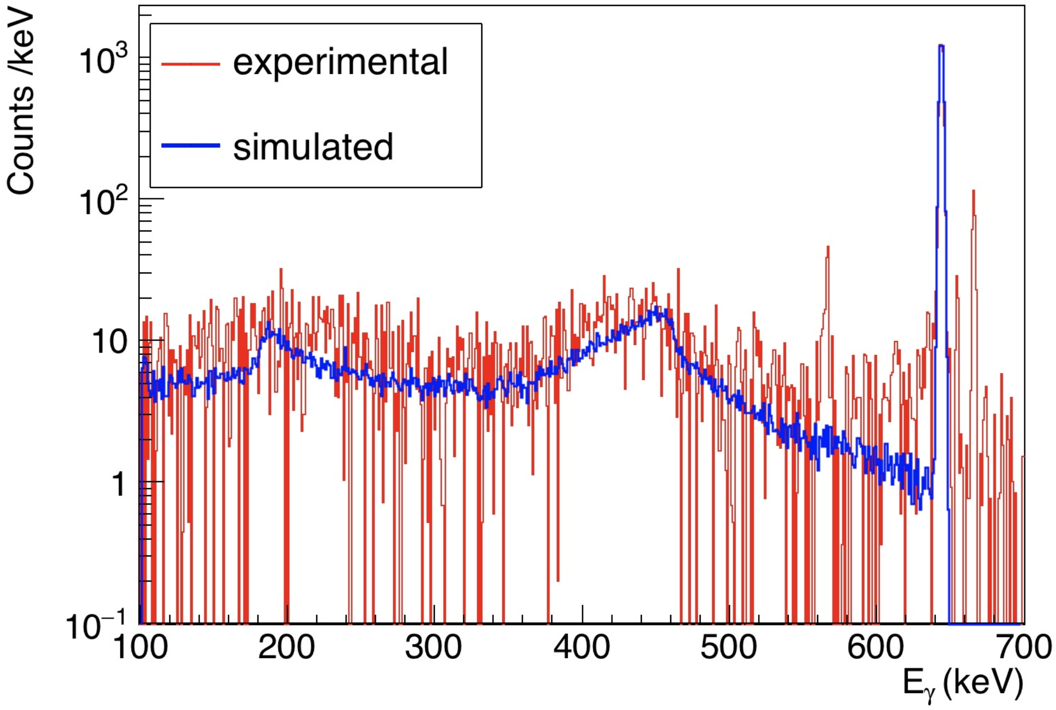

Figure 4.47: P/T measurement on the 644 keV peak.

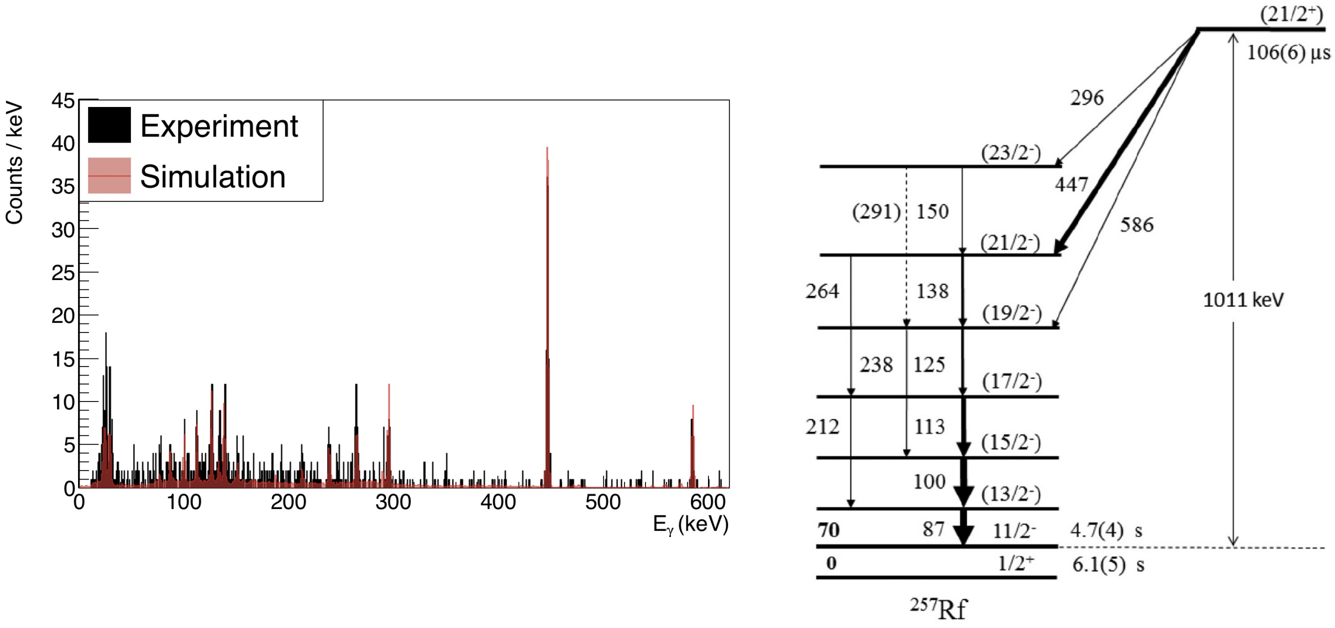

Figure 4.48: Using the decay scheme established by Rissanen et al. [168], the spectrum of isomeric gamma rays observed in Dubna could be reproduced with the GABRIELA GEANT4 program. The excess L X ray intensity is due to the contribution of a second isomer which was also observed in the data [K. Hauschild et al. to be published].

Chapter 5

Decay Spectroscopy of ^{255}Rf and ^{251}No

5.1 Discovery of Rf

Like many Transfermium elements, the discovery of element Z = 104, which eventually was named rutherfordium has a controversial history. In 1964, the earliest claim came from the JINR team in Dubna when G. N. Flerov and his co-workers bombarded ^{242}Pu with ^{22}Ne ions, and the resulting isotope fissioned spontaneously with a half-life ~ 0.3 sec. Based on nuclear reaction systematics, this nuclide was assigned to be ^{260}104 [169]. The name kurchatovium (Ku) was suggested by the Russian group to this newly discovered element, in honor of the Soviet physicist Igor Kurchatov. The half-life of this nuclide remained inconclusive as the same group later suggested it to be 0.1 sec., then 80 ms and most recently 28 ms [170]. In 1966, the identification of the atomic number of this new element was claimed by I. Zvara and her team based on the thermochromatography experiment. However, it raised a doubt because the 28 ms half-life of the ^{260}104 nuclide was not enough to survive the passage through the apparatus used in the experiment which is 1.2 s [170, 171]. Thus, a definitive conclusion on the discovery of the 104 element could not be reached as the half-life and the atomic number remained undetermined. Five years later, A. Ghiorso and his team at Berkeley claimed to have convincing evidence on the synthesis of the Z =104 element via ^{249}Cf(^{12}C,4n)^{257}Rf with a half-life ~3.8 s by identifying its daughter ^{253}No from alpha decay. A similar experiment was performed in the same period with ^{13}C projectiles ^{249}Cf(^{13}C,3n)^{259}Rf with a half-life ~3.4 s in which case as well they detected daughter nuclei ^{255}No from the alpha decays [172]. In honor of Ernest Rutherford, this group later proposed that the element 104 to be named rutherfordium. In 1973, physicists at Oak Ridge National Laboratory confirmed the claim of the Berkeley group from X-ray spectroscopy of the nobelium daughter. They observed photons coincident with the alpha decays of ^{257}Rf that match in energy and intensity of the theoretical KX-ray spectrum of Z =102 [173]. A controversy broke out between the American and the Russian groups regarding the discovery or the first clear identification of the element Z =104, hence the right to name the element. This conflict caused great difficulty for the International Committee on Nomenclature of the International Union of Pure and Applied Chemistry (IUPAC) in naming the element. Only in 1977, IUPAC had decided to formally name the element 104 as rutherfordium.

5.2 Discovery of No

In 1957, at the Stockholm's Nobel Institue of Physics, a group of Swedish, American, and British physicists bombarded a sample of curium with a beam of ^{13}C. They identified an alpha emitter with a half-life about 10 min and alpha energy 8.5 MeV presumably due to either ^{13}C(^{244}Cm,6n)^{251}No or ^{13}C(^{244}Cm,4n)^{253}No reaction because of the absence of spontaneous fission, and the method of preparation [174–176]. They claimed it to be nobelium as the new alpha-emitter had the expected chemical properties of the element 102. They suggested the name nobelium with chemical symbol No for the new element in recognition of Alfred Nobel's contributions to the advancement of science. The discovery created a lot of sensation in the European media as well. One British physicist of the group has noted that nobelium was the first of the trans-uranium elements to be discovered on European soil and the first from an international effort. However, later this discovery became highly controversial as the Berkeley group lead by G. T. Seaborg and the Dubna group of G. Flerov failed to reproduce the results from Stockholm. A year later, the Berkely group initially set out to confirm the Stockholm group's discovery reported that they could not verify this result [177] but claimed to have created ^{254}No from the reaction ^{12}C(^{246}Cm,4n)^{254}No [178]. Their claim is based on the observation that the new element alpha decay with a 3 s half-life and confirmation from the daughter nucleus ^{250}Fm whose radioactive properties were known. The Dubna group in the early 1960s also failed to duplicate the Nobel Institute's work. They not only disbelieved the Stockholm results but also cast doubt on Berkeley's findings, which they consider to be a mere indication of the Z =102 element. It is because they suspect that the American group had misidentified the reaction products hence incorrectly claimed to have produced ^{254}No isotope. To the Russian group, this incorrect assignment of the isotope could not be considered a discovery. The American group later admitted that their earlier isotope identification was wrong, and their new findings align with the Dubna results [179]. The Dubna group maintained that element 102 was discovered in their studies from 1963-1966 in which they had identified five isotopes of 102 (see ref. [180] for details about the experiments and results). They asserted the name joliotium (Jo) for element Z =102 to IUPAC, in honor of the French scientist Frédéric Joliot-Curie. Much later, in 1992, when IUPAC was reassessing the controversial claims of discovery of several elements, the Dubna team was declared to have correctly detected and assigned decays to nuclei of element 102 in 1966. And two years later, the IUPAC ratified the name nobelium (No) for this element, as it had become well-established in the literature over 30 years, and also because Alfred Nobel is commemorated well in this way (see ref. [170, 179, 181] for more historical overviews).

5.3 What is known in ^{255}Rf

Several experiments before our study have shed some light on the nuclear structure and decay properties of ^{255}Rf. The first investigation was carried out in Dubna in 1975 by Oganessian and his team. They bombarded Pb isotopes with ^{50}Ti ions producing two isotopes of Rf with mass numbers 255 and 256. The spontaneous fission half-lives they measured for these isotopes are > 1 s in the case of ^{255}Rf and 5 ms for ^{256}Rf. The hindrance factor influencing the lifetime of the odd nucleus is about 10^3 [138].

Then a decade later, Heßberger and his coworkers at GSI using the same reactions produced ^{255}Rf and ^{256}Rf isotopes and confirmed the previously reported spontaneous fission activities with improved half-lives 1.4 ± 0.2 s and $7.4^{+0.9}_{-0.7}$ ms. The evaporation residues were separated using the SHIP velocity filter and implanted into position-sensitive detectors, where their alpha and spontaneous fission decay were measured. They also found that ^{255}Rf alpha decays B_α = 48(7) % of the time, and in the case of ^{256}Rf, a small alpha-decay branch $2.2^{+7.3}_{-1.8}$% of ^{256}Rf was noticed [182].

The GSI group again carried out a similar study in 1997. In this experiment, the ^{255}Rf nuclei were produced in the reactions ^{208}Pb(^{50}Ti,3n)^{255}Rf and ^{206}Pb(^{50}Ti,1n)^{255}Rf. They carried out alpha-alpha correlation and tentatively suggested an isomeric state with a half-life 0.8 ± 0.3 s from an observation of correlations 8722 keV→ 8471 keV → 8126 keV which they assigned to ^{255m}Rf → ^{251m}No → ^{247m}Fm. Their new fission branching ratio was B_f = 45(6)% [183].

In 2001, the GSI group, through α and $\alpha - \gamma$ spectroscopy, improved the decay data of ^{255}Rf produced int the reaction ^{207}Pb(^{50}Ti,2n)^{255}Rf [184]. In this study with more statistics, the isomeric chain observed in the earlier study was not found. They observed 203 keV and 142 keV gamma lines to be in coincident with alpha-decays and established the decay scheme shown in fig. 5.1. The Q alpha for a transition to the ground state they obtained is 9109 ± 15 keV. Their new spontaneous fission branching is B_f = 52(6)% and a half-life 1.63 ± 0.11 s.

In 2006, their improved data confirmed their previous measurements on the transitions found in coincidence with alpha decays of ^{255}Rf. They determined the energies, intensities, and multipolarities of these transitions. The measured half-life of the ground-state decay is 1.68 ± 0.09 s, which agrees with the previous measurements. The 203.6 ± 0.2 keV and 143.3 ± 0.2 keV transitions were interpreted as E1 transitions like in the alpha decay of other known isotones (^{251}Fm, ^{253}No, see fig. 5.2 and ^{247}Cm, ^{249}Cf). The alpha decay populates the excited state ($9/2^-$) in the daughter nucleus ^{251}No, which then gamma decay to the ($7/2^+$) ground state and the $9/2^+$ state, a member of the rotational band built upon the ground state. The branching ratios of these two transitions were reported as 49 (6) % and 51 (6) % respectively to the $7/2^+$ and $9/2^+$ state. The alpha decay fine structure obtained is given in table 5.1. It has been suggested that 8906 keV could be g.s. → g.s. transition plus summing of 8716 with conversion electrons because the HF for g.s. → g.s. transition is substantially lower than values obtained in the lighter isotones that are HF = 3800-8700. The 8678 keV transition was assumed to populate the $11/2^-$ member of the $9/2^-$ band. As the alpha decay of ^{255}Rf can populate some excited states in ^{251}No, alpha decay of ^{259}Sg can also give access to some low lying excited states in ^{255}Rf. The GSI group performed such an experiment in 2010 by producing ^{259}Sg isotopes in the reaction ^{206}Pb(^{54}Cr,1n)^{259}Sg. Two alpha emitting states with different half-lives were observed and inferred as an $11/2^-$ g.s. and $1/2^+$ isomer. From the decay properties of the $11/2^-$ g.s., the $11/2^-$ state in ^{255}Rf was tentatively identified at an excitation energy (E*) of ~ 600 keV.

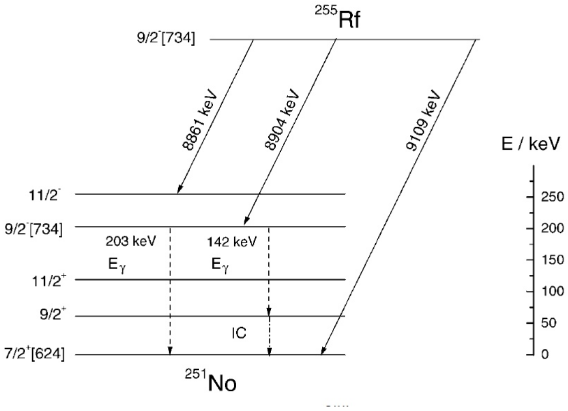

Figure 5.1: Decay scheme proposed for ^{255}Rf. The numbers denote the Q values [184].

E_α	i_{rel}	HF
8906 ±8	0.025 ±0.01	1344
8716±4	0.92 ±0.05	2.4
8678±8	0.03 ±0.01	56
8646±5	0.015 ±0.005	90
8575±5	0.01 ±0.005	80

Table 5.1: α fine structure observed in the study of ref. [185].

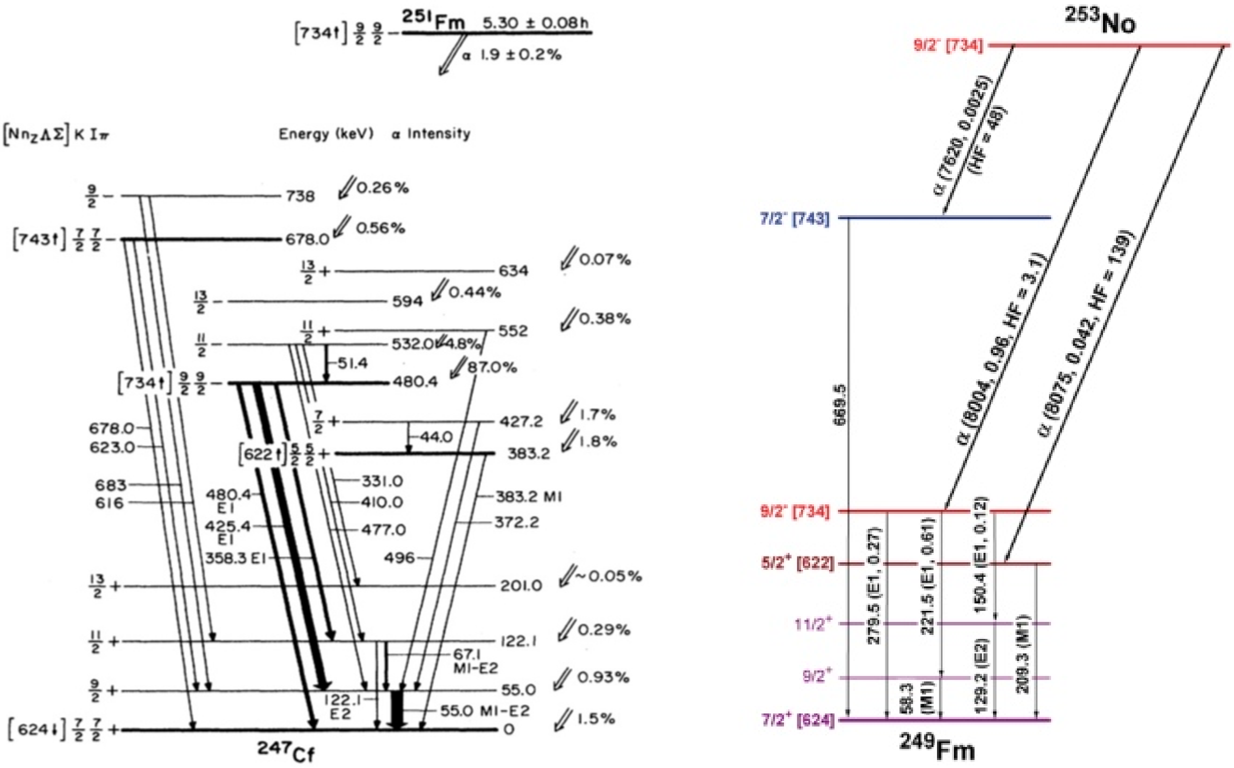

(a) (b)

Figure 5.2: a)^{251}Fm α-decay scheme [189] b) ^{253}No α-decay scheme [190].

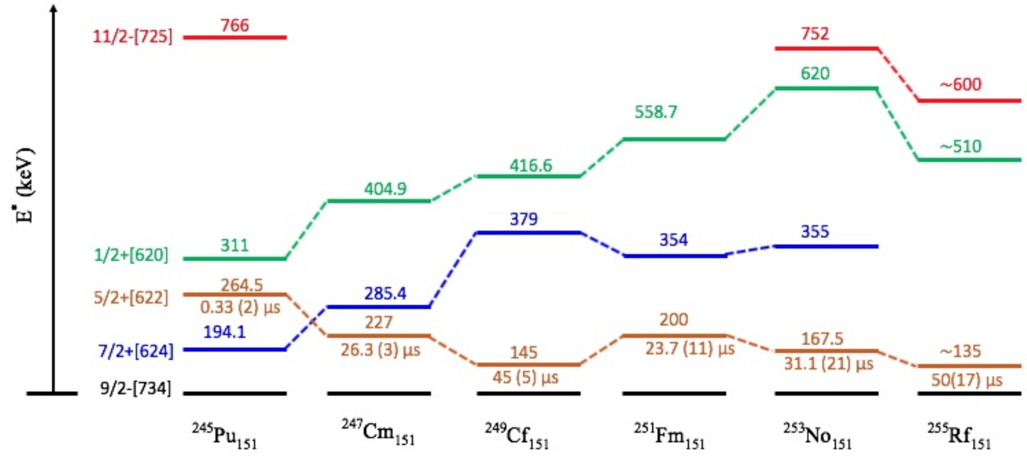

Figure 5.3: Systematics of low-lying states in N= 151 isotones.

By performing triple correlation searches in chains consisting of an ER, an alpha decay and a low energy signal , a short-lived ($T_{1/2}$ = 50 ± 17µs) isomeric state in ^{255}Rf was observed. The average energy of the low energy signals (CE, a sum of conversion electrons, Auger electrons and low energy X rays) in the 42 ER-α-CE chains was ≈ 105 keV. Since no gamma or X rays were observed in coincidence with these electrons, it was concluded that the isomer lies below the K binding energy of rutherfordium. The isomer was interpreted as the $5/2^+$ state as in the systematic shown in fig. 5.3 and the decay proceeds via M2

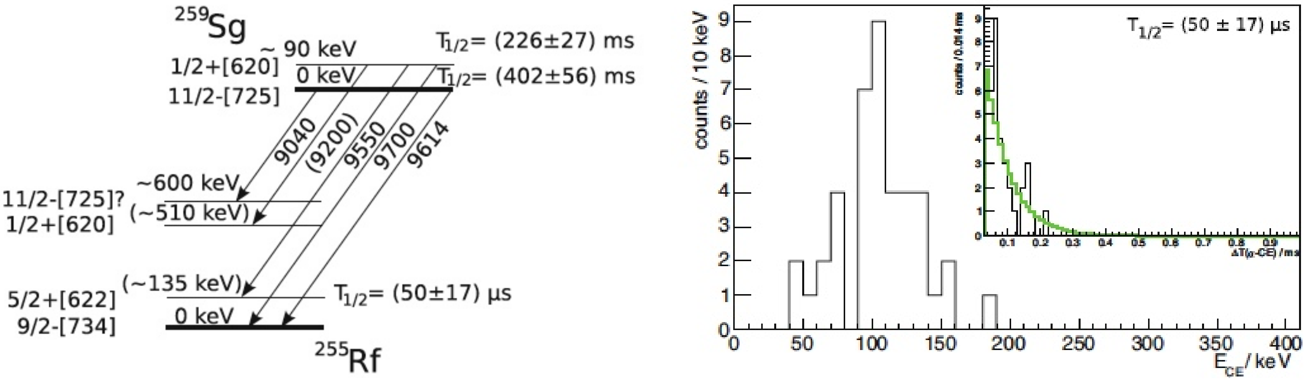

(a)

(b)

Figure 5.4: (a) Suggested alpha decay scheme of ^{259}Sg. (b) Energy spectrum and the lifetime fit (inset) of the isomeric conversion electrons following the alpha decay of ^{259}Sg [186].

transition to the ground state. Considering the L shell binding energy in Rf is 30 keV, the isomer is placed at excitation energy ≈135 keV (see fig. 5.4) [186].

Isomeric decays with a half-life > 30μs were observed from pulse shape analysis in a recent experiment at GSI. The rutherfordium isotopes were produced in the reaction ^{206}Pb(^{50}Ti, 1n) and separated using the TASCA gas-filled recoil separator. A half-life of 1.9 ± 2 s was measured with estimated branching ratios for alpha decay and spontaneous fission of 46 ± 8 % and 53 ± 8 %, respectively, which are in agreement with the previously reported values. The isomeric state observed in this experiment was interpreted as the 135 keV isomer [187].

More recently [188], in another experiment, the GSI group reported high K isomers in ^{255}Rf. They used ^{207}Pb(^{50}Ti,2n) reaction to synthesize the isotopes. They observed a total of 144 ER–CE–SF/alpha correlations. A broad CEs energy distribution (up to 800 keV) and several CEs in coincidence with gamma rays were observed. They found 3 ER–CE-CE–SF/alpha correlations, for which, the decay time of the first electron burst is significantly longer than the decay time of the second one. Out of a total of 147 correlations, 19 CEs were seen in coincidence with gamma ray. The spectra of CEs and the gamma rays are shown in fig. 5.5. The half-life of the lower-energy electrons below 370 keV is found to be 35± 6 μs, and for the higher-energy group (above 370 keV) is 15^{+6}_{-4} μs. When coincidence with gamma rays is demanded, the half-life for the lower-energy group CEs becomes 38^{+12}_{-7} μs. As can be seen from the gamma energy spectra, they could not identify any distinct gamma line either in singles or in addback mode. A maximum of 1050 keV was reached, after summing the energies of electrons and coincident gamma rays. They concluded to have observed new high-energy high-K isomer(s) in ^{255}Rf, as these results are in contrast with the previously reported $5/2^{+}$[622] single-particle isomer where the CE energy spectrum has a narrow peak at 105 keV with no coincident gamma ray. Therefore, they assumed that besides the direct population of the 15 μs isomer during the production of the ER, the decay of the longer-lived 38 μs isomer probably also feed the 15 μs isomer. From the energies of the first CEs in the chain plus the electronic binding of K and L shells in Rf, the gap between the two isomeric levels was estimated to be 150–300 keV. The proposed decay scheme of K isomers in ^{255}Rf observed in this experiment is shown in fig. 5.6.

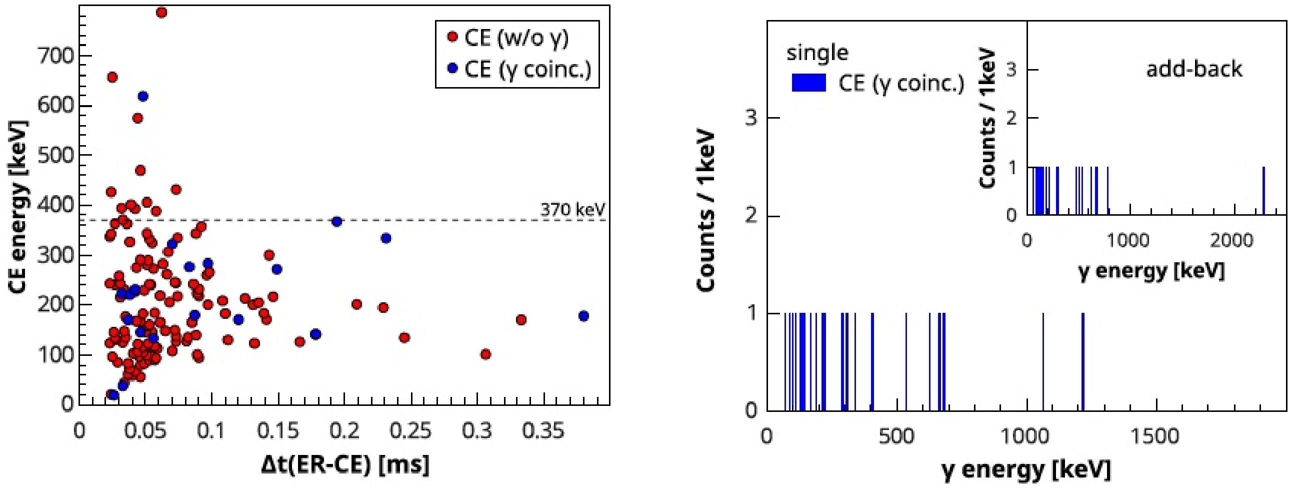

(a) (b)

Figure 5.5: a) CE energies as a function of the time difference between the implantation of an ER and the detection of a CE. Red dots, electrons not in coincidence with gamma rays; blue dots, electrons in coincidence with gamma rays. b) Energy spectrum of coincident gamma rays [188].

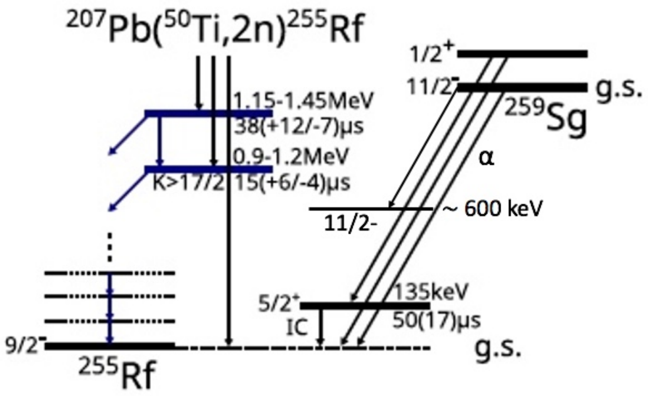

Figure 5.6: Proposed decay scheme of K isomers in ^{255}Rf (left) along with the alpha decay scheme of ^{259}Sg (right). Adapted from ref. [188].

5.4 Ground state decay properties of ^{255}Rf

In our study, the ^{255}Rf nuclei were produced in the reaction ^{207}Pb(^{50}Ti,2n)^{255}Rf from two experimental campaigns in May and Oct of 2017. Some details of these two experimental runs are given in table 5.2.

Run	duration (days)	E_{beam} (MeV)	$dose^*$	$N_{produced}$	cross section (nb)
May	20.58	253	5.045×10^{18}	4208 ± 83	1.71(9)
Oct	23.36	253	6.622×10^{18}	3769 ± 81	1.16(6)

Table 5.2: Details of the 2 experiments: duration, average beam energy, total beam dose, number of ^{255}Rf ions detected and corresponding production cross section (assuming a 22^+ charge state for the Ti ions and a transmission and detection efficiency of SHELS of 40%).

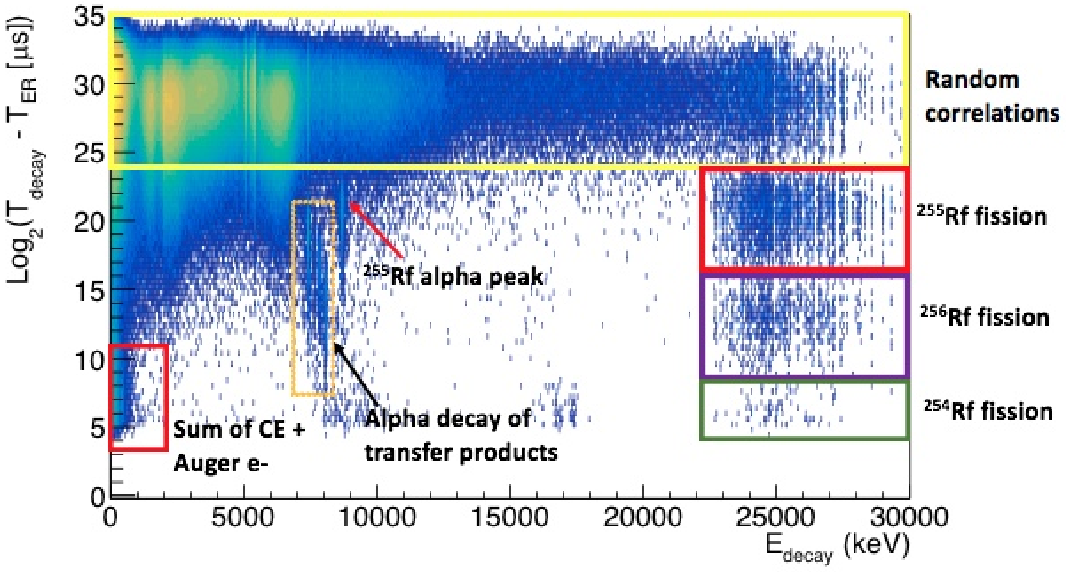

Figure 5.7: Log_2 of the time difference between a recoil implant and subsequent decay vs energy of the decay observed in the reaction ^{207}Pb(^{50}Ti,xn)$^{257-xn}$Rf.

For statistical reasons, the two data sets were treated as one. The recoil-decay correlation matrix is shown in fig. 5.7, where the vertical axis represents the time difference between the implantation of recoil and its subsequent decay in the same pixel, and the horizontal axis gives the decay energy in keV. The top region of the plot shows random correlations. On the high energy side, the fission events are recorded as overflows as the signal amplification gains were set to detect electron and alpha particles, thus do not reflect the proper fission energy of ≈ 200 MeV. Besides the 2n evaporation channel, 1n and 3n channels were also open which can be confirmed from the fit to the time distributions of fission events (shown in the right panel of fig. 5.8). The measured fission half-lives of ^{255}Rf and ^{256}Rf are 1.69 ± 0.03 s and 6.82 ± 0.37 ms, which agree to the values given in the literature. Because of our long deadtime, only a small portion of ^{254}Rf nuclei produced in the experiment is visible. We also measured the half-life of the alpha decay branch by gating only on the full energy peak in the range [8660-8850] keV and found it to be

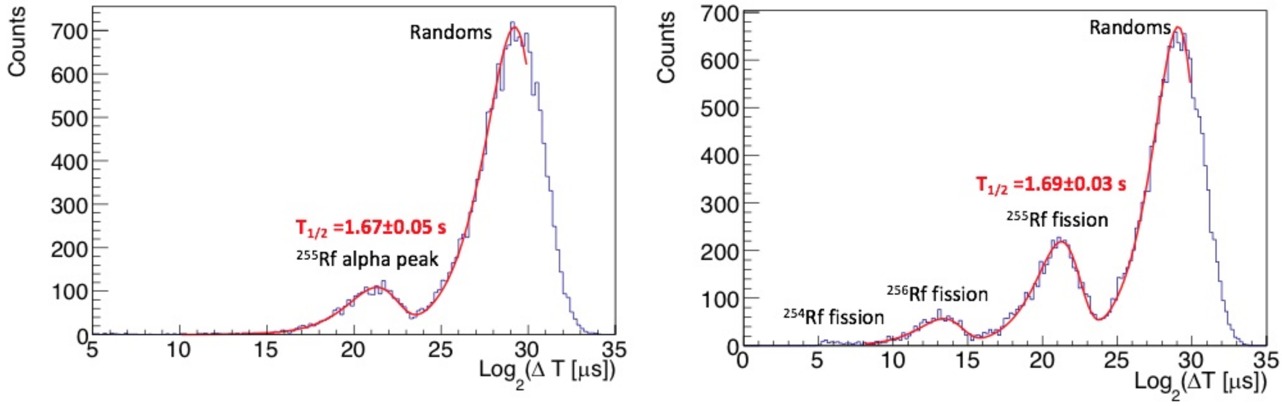

(a) (b)

Figure 5.8: Lifetime fit of the ^{255}Rf (a) the alpha peak and (b) the fission events of fig. 5.7.

$T^{\alpha}_{1/2} = 1.67 \pm 0.05$ s.

A total of ≈ 7880 ± 112 ^{255}Rf nuclei were produced, out of which ≈ 3866 ± 92 of them were observed to decay via alpha transition and 4013 ± 65 via spontaneously fission. The corresponding branching ratios thus estimated are $B_\alpha = 49.1 \pm 1.3\%$ and $B_f = 50.9 \pm 1.1\%$ that are compatible with the values values given in the literature. Since no ^{255}Lr alpha decay was identified we deduced an upper limit for the β^+/EC decay branch to be 0.009 %.

5.5 Alpha decay of ^{255}Rf

In our experiments, we observed both gamma rays and ICEs in coincident with the alpha decays of ^{255}Rf. In addition to the fact that ICEs were never measured directly before, we also have more statistics than in any earlier studies. The spectra of gamma rays and conversion electrons detected in coincidence with alpha decays of ^{255}Rf were obtained in the following manner.

- E_α(any gen) < 9.5 MeV to exclude fission events (where, gen corresponds to the generation number of ^{255}Rf decay in the decay chains of the correlation tree).
- $11 > \mathrm{Log}_2(T_\alpha - T_{recoil}) <= 24.2$, the upper limit excludes most of the random correlations whereas the lower limit excludes isomeric events.
- the daughter lifetime lies within $10 > \mathrm{Log}_2(T_{\alpha 2} - T_{\alpha 1}) <= 23.8$ (the lifetime range of ^{251}No).

The spectra are shown in fig. 5.9, where the energies of the coincident gamma rays and electrons are plotted against the energies of the alpha particles. Fig. 5.10a and 5.10b show the γ-ray and e- spectra observed in coincidence with the alpha peak of energy in the range 8.6-9 MeV. We observe two strong lines at $E_\gamma = 203$ keV and $E_\gamma = 143.2$ keV as seen by the GSI group. Some KX rays and weak lines (e.g 70 keV) are also seen in fig. 5.10a. Furthermore, we notice that the energies of the coincident electrons detected in the tunnel detectors are below 220 keV.

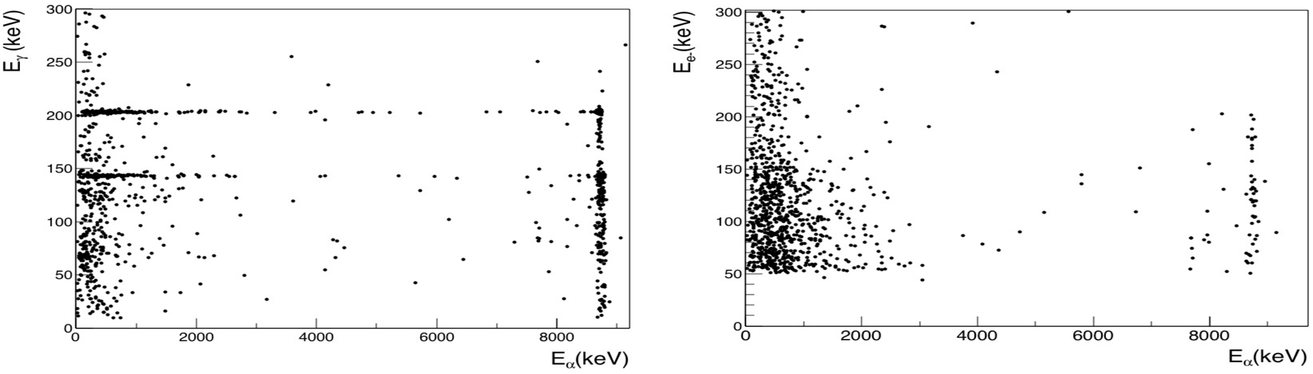

(a) (b)

Figure 5.9: Experimental a) $\alpha - \gamma$ and b) $\alpha - e^-$ coincidence matrices.

5.6 Determination of relative γ-ray branching ratios

To interpret these findings, we shall first assume that the level scheme GSI proposed is correct. However, we will modify the energies of the levels to adapt them to our data. Taking energy difference between the

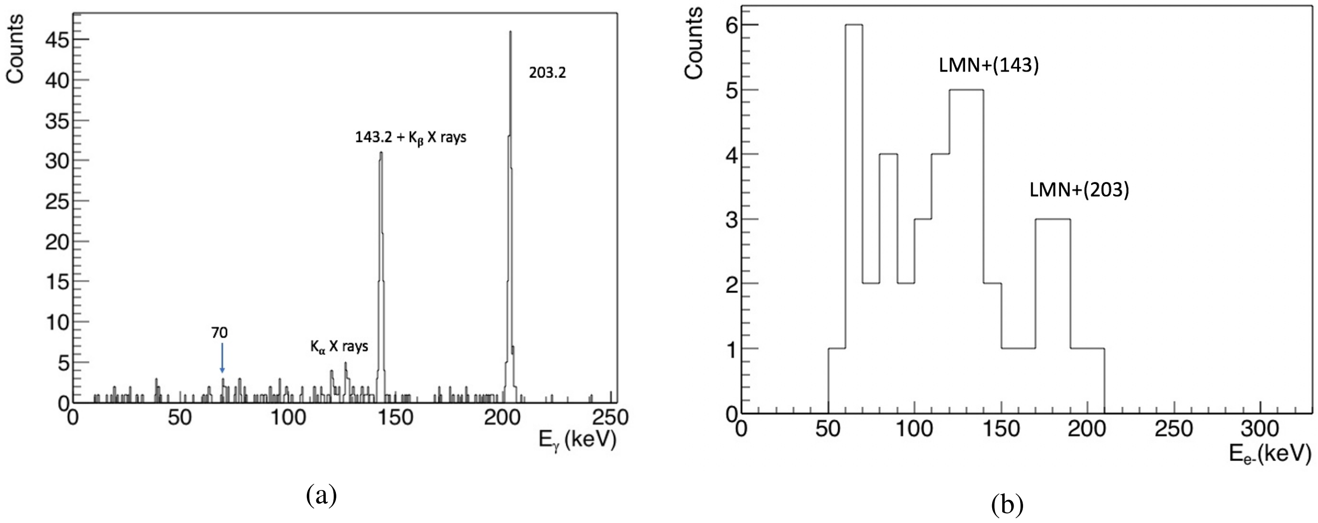

(a)

(b)

Figure 5.10: Spectra of the a) γ rays and b) electrons in coincidence with $^{255}Rf - \alpha$ peak.

203.2 keV and 143.2 keV transitions gives the excitation energy of the first member of the ground state rotational band. This energy also fixes the moment of the inertia parameter in equation 2.71, which defines the energies of a rotational band. The 60 keV energy spacing gives $\frac{\hbar^2}{2\mathcal{J}} = 6.67$. The energy of the $11/2^+$ state in fig.5.11 was determined using constant moment of inertia yielding a $9/2^- \rightarrow 11/2^+$ transition of ∼ 70 keV, which fits well with the energy of a weak line obtained in the γ-ray spectrum. The Q_α value (see eq. 3.6) of the alpha decay to the $9/2^-$ state can be extracted from the full energy alpha peak in coincidence with 203 keV gamma rays. The mean energy was found to be $E_\alpha = 8709 \pm 2$ keV giving the Q-value equal to 8855 ± 2 keV taking into account the mass dependence of the ionization signal of the daughter recoil. The Q value to the ground state can then be easily found by adding the 203.27 ± 0.07 gamma transition energy to the $Q(9/2^-)$, which is Q_α(g.s.) = 9058 ± 2 keV. This value is consistent with the value of 9055 keV obtained from mass differences between ^{255}Rf and ^{251}No (see eq. 3.5). Previously, it was reported that the relative intensities of 203 keV and 143 keV gamma transitions to be 0.94(5) and 1 respectively, and by including the conversion, the corresponding intensities are 0.49(6) and 0.51(6). In an attempt to determine the branching ratios of the gamma transitions, we start with the basic decay scheme shown in

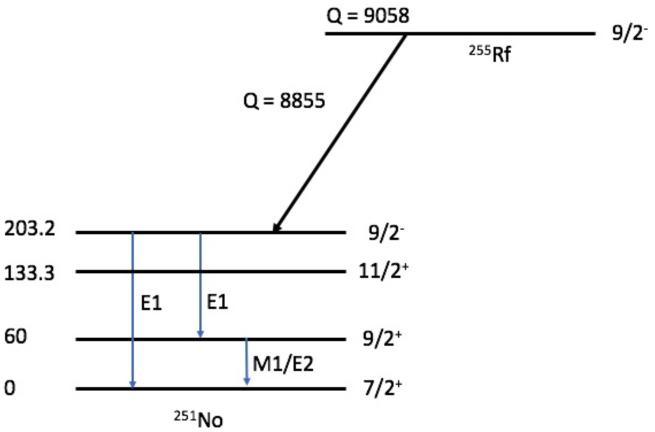

Figure 5.11: Simple ground state decay scheme of ^{255}Rf.

fig. 5.11. The gamma transition rates within the band can be calculated using equations given in table 3.2. The reduced transition rates B(M1) and B(E2) are computed using equation 3.64 and 3.65 respectively. To calculate B(E2), first, the intrinsic quadrupole moment of ^{251}No is calculated using equation 3.62 with quadrupole deformation parameter $\beta = 0.25$ as per ref. [44]. The calculated quadrupole moment is 12.05 eb. Using equation 3.4.1 the mixing ratios for $\Delta I = 1$ transitions are obtained. The calculated branching ratios and the mixing ratios corresponding to the first three states of the $7/2^+$ band are given in table 5.3. Note that, for mixed transitions, the conversion coefficients need to be modified using equation 3.74.

Spin	E (keV)	br (E2) %	br (M1+ E2) %	δ
$\frac{7}{2}^+$	0	0	0	0
$\frac{9}{2}^+$	60	0	100	16.15
$\frac{11}{2}^+$	133.3	80.79	19.21	16.01

Table 5.3: Calculated excitation energies and branching ratios of the first three rotational states in the the ground-state band.

If we consider the basic scheme for the ^{255}Rf ground state alpha decay as shown in fig. 5.11, the only unknowns are the branching ratios of 203 keV and 143 keV transitions from the $9/2^-$ state. Since both these transitions stem from the same $9/2^-$ state, the summing of these two transitions cannot occur. We can, therefore, simulate each gamma transition individually and normalize to the experimental peak integrals to extract their branching ratios in the manner discussed below. We know that absolute detection efficiency is evaluated by:

$$\epsilon = \frac{N_{peak}}{N_{emitted}} \tag{5.1}$$

where N_{peak} is the peak integral and $N_{emitted}$ is the number of radiation quanta emitted by the source. Equating simulated and experimental efficiency,

$$\epsilon = \frac{N_{peak}(sim)}{\frac{N_{decay}(sim)}{(1+\alpha_{Tot})}} = \frac{N_{peak}(exp)}{br \times \frac{N_{decay}(exp)}{(1+\alpha_{Tot})}} \tag{5.2}$$

where α_{Tot} is the total internal conversion coefficient of the transition and br is its branching ratio. Multiplying and dividing by a scaling factor $SF = \frac{N_{peak}(exp)}{N_{peak}(sim)}$ on the left hand side in order to normalize to the experimental peak, we get

$$\frac{SF \times N_{peak}(sim)}{SF \times N_{decay}(sim)} = \frac{N_{peak}(exp)}{br \times N_{decay}(exp)}$$

which implies that,

$$SF \times N_{decay}(sim) = br \times N_{decay}(exp) \tag{5.3}$$

Hence, the relative gamma emission intensities of 203 keV and 143 keV transitions can be obtained simply from the ratio of the corresponding scaling factors.

$$\frac{br(143)}{br(203)} = \frac{SF(143)}{SF(203)} \tag{5.4}$$

The conversion coefficients and electron energies of these two transitions taken from BRICC are tabulated in the table 5.4. To make sure we only consider ^{255}Rf α-decay events, we have restricted ourselves to the alpha peak energy in the range $8.6\text{MeV} \geq E_\alpha \geq 9\text{MeV}$. Comparison between the experimental $\alpha - \gamma$ and $\alpha - e^-$ coincident spectra with the corresponding simulated spectra was carried out on the ^{255}Rf alpha

	143.2 keV		203.2 keV	
Shell	Ece(keV)	α (E1)	Ece(keV)	α (E1)
Tot		0.067		0.1148
K	0		53.9	0.0861
L	115.82	0.05	175.47	0.0214
M	136.18	0.0125	196.06	0.00533
N+	141.70*	0.0045	201.67*	0.00197

Table 5.4: Conversion coefficients and electron energies from BRICC. The Ece_{N+} are weighted by the conversion coefficients and indicated by *.

E_γ	$N_{peak}(exp)$	$N_{peak}(sim)$
203.2	150	10885
143.2	122 - N(203:Xray)	11718

Table 5.5: gamma in coincident with ^{255}Rf alpha peak.

peak only. The peak integrals of these two transitions from the experimental (May+Oct) and simulated data ($N_{decay}(sim) = 100000$) are given in table 5.5. In table 5.5, N(203:Xray) is the number of KX rays in the range between 140-145 keV from the K conversion of the 203 keV transition. The number KX rays contributing to the 143 keV peak can be estimated using the following relation.

$$N(203 : Xray) = N_\gamma(203) \times \alpha_K(203) \times Prob(143) \times \varepsilon(143) \tag{5.5}$$

where $Prob(143)$ is the probability of emitting 143 keV X rays due to K vacancy, $\varepsilon(143)$ is the detection efficiency at 143 keV, $N_\gamma(203)$ is the number of 203 keV gamma rays actually emitted, which can be estimated by dividing the peak integral of 203 with the detection efficiency $\varepsilon(203)$. Fluorescence yields of $K_{\beta1}$, $K_{\beta3}$ and $K_{\beta5}$ X rays due to K conversions can be usually found in the ToI [163], but in this case we have taken the extrapolated values (see section 4.6). Hence, we find $N(203 : Xray) \approx 2.5$. This number can also be estimated from the $K_{\alpha1}$ X-ray intensity

$$N(143) = \frac{N(127)}{\varepsilon(127) \times Prob(127)} \times Prob(143) \times \varepsilon(143)$$

where $N(127)$ is the peak integral of 127 keV peak, the energy of $K_{\alpha1}$ X rays. We find $N(143) = 4.7(5)$. Care needs to be taken in estimating the background as under or over estimation will influence the branching ratio extracted using equation 5.4. Note that, the number obtained using $K_{\alpha1}$ intensity is greater than the number obtained using 203 keV intensity. This will be revisited later in this section. Using equation 5.4, the relative gamma branching ratio of 143 with respect to 203 is then 72.5(8.9) %. The decay scheme of the fig. 5.11 was simulated for 100000 events. To compare the simulated γ-spectrum and e- spectrum with the experimental ones, we have normalized them using a scaling factor $SF = \frac{N_{exp}(203)}{N_{sim}(203)}$, they are displayed in fig. 5.12 and the peak integrals in the e- spectra are quantified in table 5.6. We noticed that in the simulated spectra, there are fewer X rays and electrons than in the experimental ones. We conclude that the internal conversion coefficients for the E1 transitions must be greater than the theoretical BRICC values. Such anomalous behavior of the E1 transitions has been reported in other nuclides as well such as in ^{177}Hf [191] and also in ^{249}Fm [39]. Therefore, we have estimated the internal conversion coefficients and adjusted the branching ratios accordingly. First, we needed to evaluate the integrals of the LMN+ peak of 143 keV transitions since the summing of electrons from the 143 keV transition and 60 keV can

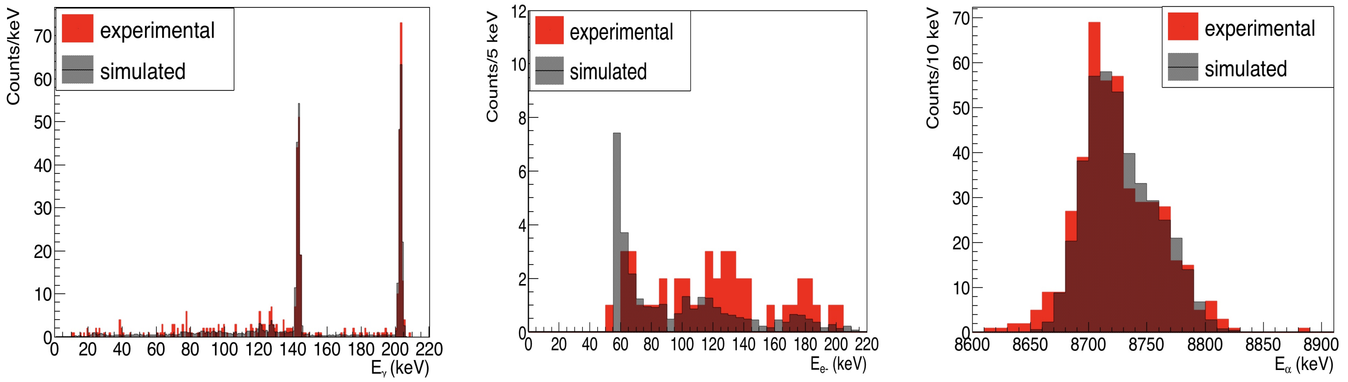

(a) (b) (c)

Figure 5.12: Energy spectra of a) gamma rays and b) electrons coincident with ^{255}Rf alpha-peak events. c) The full energy peak of the alphas in coincident with gamma rays. Note that in the γ-ray spectrum the apparent mismatch between the experimental and simulated peak intensities of 203 keV and 143 keV lines is a visual rendering.

E_{LMN+e}	Range	N(exp)	N(sim)
203.2	154-210	10	4.7
143.2	94-150	21	8.5

Table 5.6: electron in coincident with ^{255}Rf alpha 8.6-8.85 MeV.

increase the count in the LMN+ peak of 203 keV transition. Also, the backscattered electrons of the 203 keV transition can form a background for the LMN+ peak of the 143 keV transition. Simulations of these two transitions individually gave the ranges of the peaks of the alpha particles that are coincident with the conversion electrons (see fig. 5.13). The peak integral values are given in table 5.7.

Transition	N	ε %	$N_{emitted}$
203.2	10(3)	19.95	50
143.2	15(4)	18.46	81

Table 5.7: Measured LMN+e intensities.

The conversion coefficients α_{LMN+} can be estimated using the following equation

$$\alpha_{LMN+} = \frac{N_{LMN+e-}}{N_\gamma}$$

The measured conversion coefficients are summarized in the table 5.8 where we have assumed that α_K of 203 keV can also be scaled by the same factor $\alpha_{measured} \div \alpha_{theory}$. To obtain the conversion coefficient of 143 keV, $N_\gamma(143)$ needs to be evaluated again by subtracting the new KX-ray contribution from the 203 transition in the 143 keV peak using the equation 5.5. The number KX rays in the 143 keV peak obtained using the modified conversion coefficient α_K is $\sim$ 4.2, which is now equivalent to the number obtained using $K_{\alpha 1}$ intensity.

Repeating, the procedure discussed before, the new relative gamma branching ratio of the 143 keV transition is 66.3(8.3) %. Note that in the photonevaporation file, one needs to provide the conversion

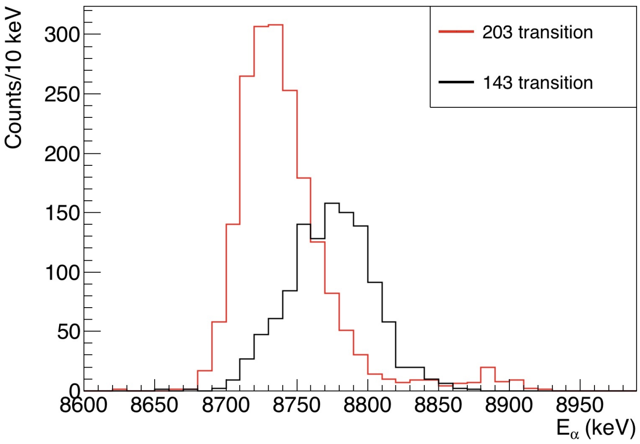

Figure 5.13: Simulated energy spectra of alpha particles coincident with ICE. The simulations of 143 keV and 203 keV were carried out individually.

	measured			BRICC		
Transition	α_K	α_{LMN+}	α_{tot}	α_K	α_{LMN+}	α_{tot}
203.2	0.234(34)	0.078(11)	0.312(36)	0.0861	0.0288	0.1148
143.2	0	0.200(24)	0.200(24)	0	0.067	0.067

Table 5.8: Measured conversion coefficients. Since the K conversion electrons of the 203 keV transition have energy below the thresholds of the tunnel detectors, $\alpha_K(203)$ was scaled using the same factor as for the $\alpha_{LMN+}(203)$.

coefficients from the inner K shell to the outer N+ shell separately. We have scaled the conversion coefficients of each subshell given in the BRICC by the same factor. Simulating the decay scheme of fig. 5.11 with the new branching ratios and conversion coefficients, we observed a good agreement between the simulated and experimental data. The spectra are compared in fig. 5.14.

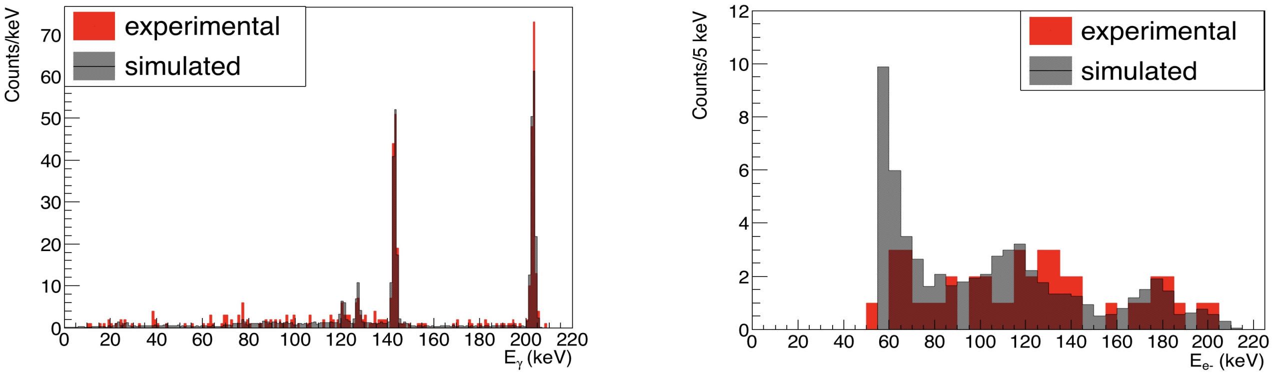

(a) (b)

Figure 5.14: Comparison of a) γ and b) e^-energy spectra gated by α peak.

We can conclude that our assumption of scaling $\alpha_K(203)$ by the same factor as $\alpha_{LMN+}(203)$ is valid as long as no other sources are contributing significantly to the X-ray intensities. We have mentioned in our discussion about the transition from $9/2^-$ to $11/2^+$ state that we observed a weak 70 keV transition, which

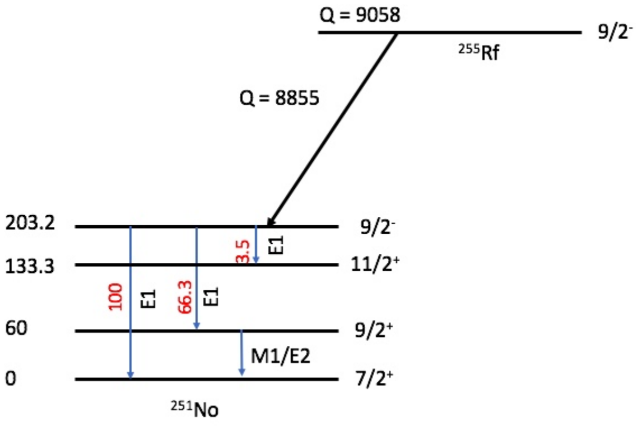

Figure 5.15: Relative gamma branching ratios from 9/2$^-$ state.

fits well in the scheme. Following a similar procedure as described above, the relative branching ratio of the 70 keV transition was estimated to be 3.5(1.5) %. Note that, for this transition, no change to BRICC coefficients could be made because of low statistics and high threshold in the tunnel detectors. The results from the simulation of the decay scheme shown in fig. 5.15 are compared with the experimental results in fig. 5.16.

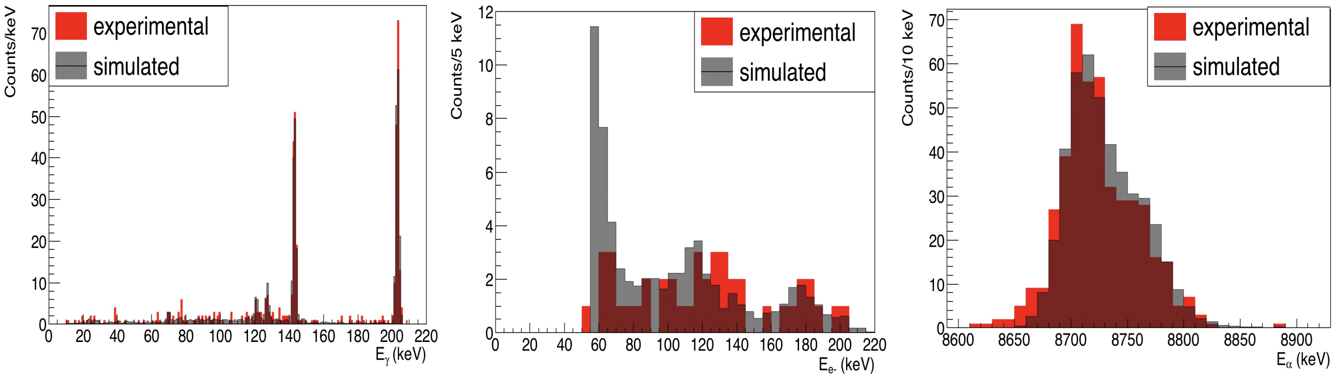

(a) (b) (c)

Figure 5.16: Energy spectra of a) gamma rays b) electrons coincident with ^{255}Rf alpha peak and c) alpha particles coincident with gamma rays.

5.7 Determination of alpha-decay branching ratios

The alpha particles are detected in the implantation detector, which suffers the most from summing and distorted peak shape as a consequence. Hence, the determination of alpha branching can be a challenging task. We know that if all the input parameters in both the photoevaporation file and the radioactive decay file are the true values, then simulations should in principle reproduce the experimental spectra provided the geometry of the experimental setup is properly imitated in the simulations. Hence, by performing simulations with different decay schemes and comparing the simulation results with the experimental results, one could estimate the alpha-decay branching ratios. One could tune the input parameters (in this case, the branching ratios) for every simulation run and compare the experimental and simulated spectra until a full agreement is reached. But such a trial and error method can be very time-consuming, especially for complicated decay schemes. This trial and error method can involve a few hundreds of simulation runs, if not thousands. To avoid such a scenario, one could perform individual simulations with 100 % alpha decay to every single level in the daughter nucleus involved in the decay scheme and then adjust the branching ratios in a post-processing phase to obtain the total simulated spectra from the corresponding contributions of each transition. Let there be m states in the daughter nucleus in which alpha decay populates from a particular state in the parent nucleus. We know that,

$$br_{tot} = \sum_{i=1}^{m} br_i = 1 \quad \text{where, br stands for branching ratio} \tag{5.6}$$

and conservation of alpha peak integrals allow

$$N_{sim} = \sum_{i=1}^{m} br_i \times N_{sim,i} \tag{5.7}$$

We can then perform χ^2 tests to compare the results

$$\chi^2 = \sum_{i=1}^{M} \left(\frac{N^i_{sim} - N^i_{exp}}{\sigma^i_{exp}} \right)^2 \quad M = \text{no. of bins, } N^i = \text{counts in bin i} \tag{5.8}$$

and $\sigma^i_{exp} = \sqrt{N^i_{exp}}$. In this work, the empty bins $N^i_{exp} = 0$ with $N^i_{sim} < 0.5$ are ignored while if $N^i_{sim} > 0.5$, σ^i_{exp} is set to 1.

5.7.1 Decay to $9/2^-$ state band

As a starting point, we first look at the alpha decay schemes in the neighboring isotones to see which states are populated. Fig. 5.2a shows the decay scheme of ^{251}Fm to ^{247}Cf. We see that $11/2^-$ and $13/2^-$ states of the $9/2^-$ rotational band have small feeding branches onto them. The GSI group also hinted for such decay branches in ^{251}No. With a similar spirit, we have attempted to investigate alpha decay to these levels in ^{251}No. Our first decay model is shown in fig. 5.17, which includes feeding into the first three states of the $9/2^-$ band. First, we shall estimate the energy spacing between $11/2^-$ and $9/2^-$ by scaling the values given in fig. 5.2a. In fig. 5.2a, the $\Delta E(9/2^+,7/2^+)$ is 55 keV, and the ΔE(11/2–, $9/2^-$) is 51.4 keV. For ^{251}No, $\Delta E(9/2^+,7/2^+)$ is 60 experimentally. Therefore, we estimate the spacing $\Delta E(11/2^-, 9/2^-)$ to be $= \frac{51.4}{55} \times 60 = 56$ keV. From equation 2.71, we obtain a corresponding moment of inertia parameter $\frac{\hbar^2}{2\mathcal{J}} = 5.1$. We also assume that Q_0 and β are the same as the ground state. As was done for the $7/2^+$ band,

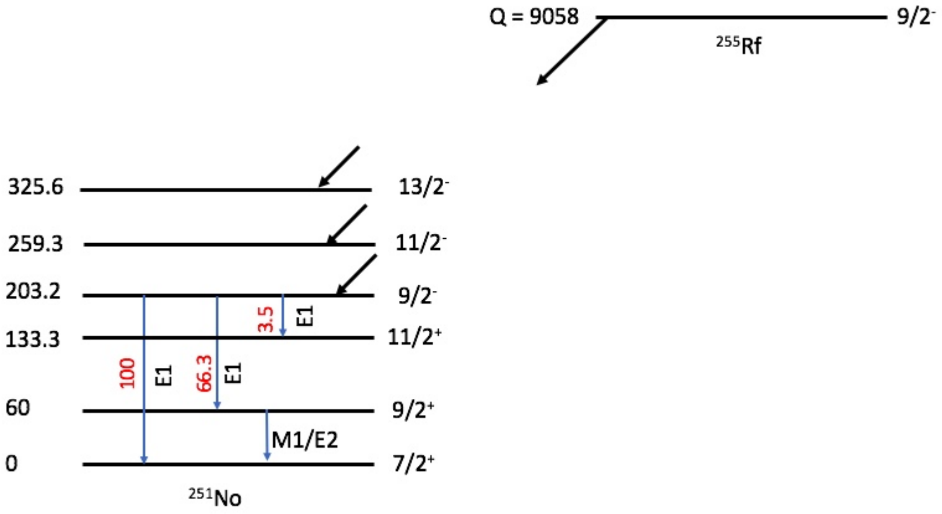

Figure 5.17: additional levels of the 9/2$^-$ band.

Spin	E (keV)	br (E2) %	br (M1+ E2) %	δ
$\frac{9}{2}^-$	203.2	0	0	0
$\frac{11}{2}^-$	259.3	0	100	0.22
$\frac{13}{2}^-$	325.6	13	87	0.22

Table 5.9: Calculated excitation energies, branching ratios (br in %) and mixing ratios (δ) of the first three rotational states in the 9/2$^-$ band.

the transition energy, gamma branching ratios, and mixing ratios of the first three rotational members of the 9/2$^-$ band are computed. These values are given in table 5.9.

We have simulated 100 % alpha decay to 9/2$^-$, 11/2$^-$ and 13/2$^-$ separately. The 11/2$^-$ state, if populated, is expected to decay to the 9/2$^-$ via a highly converted M1 transition. The corresponding alpha energies will then sum with the energies of the conversion electrons and the emissions accompanying the atomic relaxation process. Similarly, the 13/2$^-$ to 11/2$^-$ transition is also expected to be a highly converted M1 transition. Hence more shift in the energies of the alpha particles is expected if the 13/2$^-$ level is populated as illustrated in fig. 5.18. The energies of the conversion electrons in the three in-band transitions of the 9/2$^-$ band are given in table 5.10.

Energy (keV)	L	M	N+*
56.1	27.02	48.50	54.46
66.3	37.02	58.50	64.45
122.4	96.15	115.67	120.98

Table 5.10: Energy of the conversion electrons for the three in band transitions of the 9/2$^-$ band. * values are the weighted values.

Based on the fact that the population of these higher-lying states would affect the peak shape of the total α-particle spectrum, $\alpha - \gamma$, and $\alpha - e^-$ coincident spectra, the alpha branching was extracted. Experimentally, the total α-particle spectrum was obtained by selecting the daughter ^{251}No alpha peak and fission events and looking back in time for the Rf events. The experimental and simulated spectra were

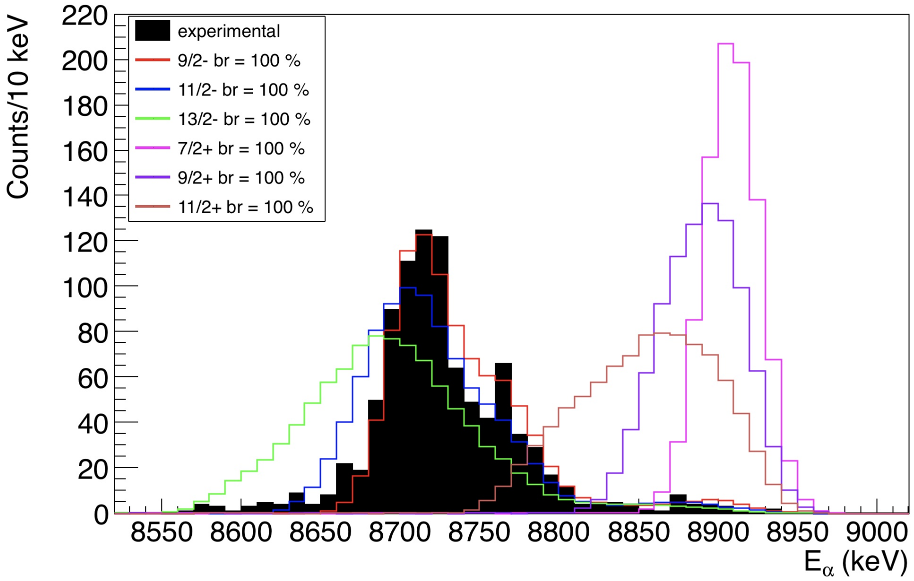

Figure 5.18: Simulated alpha particle energies when 100 % branching is given to each level. For each case, the simulated peaks are normalized to the experimental peak.

compared within the energy range from 8.6 MeV to 9 MeV since, beyond these limits, there are lots of empty bins that would skew the χ^2 value. The tunnel spectra are compared above a safe value, above the average threshold from 120 keV up to 250 keV. The γ-ray spectra are compared from 15-300 keV. Since 2D plots of alpha-gamma and alpha-electron have a lot of empty bins and computationally expensive as well, we have instead used their projections for χ^2 tests. Thus, we have 5 1D histograms on which χ^2 tests were performed. Note that, for performing χ^2 tests, the corresponding histograms from experimental data and simulations must have identical binning. To reduce skewness in the χ^2 value, the bins in a histogram were regrouped into categories such that each category contains at least five counts. If in the bin ‘i’, the counts in simulated and experimental histograms are 0, that bin was excluded from χ^2 evaluation. For the experimental spectra, if the counts in a bin is less than 5 then the counts in the next bins are added until the total count is more than 5.

We have 3 constraints for each histogram namely,

- $\sum N^i_{sim} = N_{exp}$ where N^i_{sim} is the number of counts contributing to the total simulated spectrum and N_{exp} is the total number of counts in the corresponding experimental spectrum.
- $\mu_{sim} = \mu_{exp}$, the mean energies of the simulated and experimental histograms are equal.
- $\sigma^2_{sim} = \sigma^2_{exp}$, the variations of the simulated and experimental histograms are equal.

Hence, the number of degrees of freedom for every spectrum ν = number of bins - 3. We have a total of 80 bins in 5 histograms and another additional constraint come from the branching ratios, i.e. $\sum br_i = 100\%$. Therefore, the total number of degrees of freedom is 64. Using equation 3.8, it is possible to limit the branching ratios into the $11/2^-$ and $13/2^-$ states with respect to the branching to the $9/2^-$ state. The relative alpha decay rates for ^{255}Rf nuclei are given in table 5.11 as the angular momentum carried away by the alpha particle is increased by 1 unit.

If we assume that alpha decay of ^{255}Rf only populates these 3 states of $9/2^-$ band, we can write

$$br_{9/2^-} + b_{11/2^-} + b_{13/2^-} = 100\,\%$$

Δl	k_l	$\frac{\lambda_{l\neq0}}{\lambda_{l=0}}$ (%)
1	k_1	85.40
2	k_2	62.28
3	k_3	38.78

Table 5.11: Relative alpha decay rates k_l as a function of angular momentum carried away by the alpha particle.

$$br_{9/2^-} = \frac{100}{1 + k_1 + k_2}\,\%$$

where k_1 and k_2 values are given in table 5.11. This gives $br_{9/2^-} = 40.4\%$, $br_{11/2^-} = 35.5\%$ and $br_{13/2^-} = 25.7\%$. Hence, we have varied the branching ratio for the 11/2$^-$ state from 0 % to a maximum value of 40 % with an increment of 0.1 % in each step. At each step of $br_{11/2^-}$, $br_{13/2^-}$ was varied from 0 % to $k_2/k_1 \times br_{11/2^-} = 0.73 \times br_{11/2^-}$ in steps of 0.1 %. At each step of variation, the branching ratio for the 9/2$^-$ state is obtained from:

$$br_{9/2^-} = 100 - (br_{11/2^-} + br_{13/2^-})\,\% \tag{5.9}$$

and, a χ^2 value is evaluated. The χ^2 distribution contour plots are shown in figs. 5.19a, 5.19b and 5.19c. The black region in each plot give the limits for the branching ratios beyond which $\chi^2 > \chi^2_{critical}$. The critical values $\chi^2_{critical}$ of the χ^2-distributions can be obtained from standard statistics handbooks. We have taken the conventional significance level $\alpha = 0.05$ and the limits of acceptance are given in table 5.12.

state	E_α (keV)	χ^2_{min}	$br_{lower-limit}$ (%)	$br_{upper-limit}$ (%)
9/2$^-$	8716	78.9	72.8	83.5
11/2$^-$	8660	12.2	9.5	19.8
13/2$^-$	8595	8.9	5.8	10.8

Table 5.12: Table showing the branching ratios extracted from the χ^2 comparison test for the alpha decay to the 9/2$^-$ band. The branchings are given at the minimum χ^2 value and for the χ^2 values at the limits of acceptance.

The null hypothesis (the simulation input parameters reproduce the experimental results) is rejected if the test statistic is greater than the upper critical value or less than the lower critical value. For 64 degrees of freedom, the upper and the lower critical values are $\chi^2_{upper-critical} = 88.0$ and $\chi^2_{lower-critical} = 43.8$, obtained from WolframAlpha online calculator. Minimization of χ^2 occurs at $br_{9/2^-} = 78.9\%$, $br_{11/2^-} = 12.2\%$ and $br_{13/2^-} = 8.9\%$. At the minima, the experimental and simulated alpha peak spectra are compared in fig. 5.19d.

5.7.2 Decay to ground state band

To determine feeding into the ground state band following the same procedure described above, we included the 7/2$^+$, 9/2$^+$ and 11/2$^+$ states of the ground state band for χ^2 evaluation. Their branching ratios were varied from 0 % to 2 % in step of 0.2 %. The minimization of the χ^2 still occurred at the same values obtained in the previous section, i.e., with $br_{7/2^+}, br_{9/2^+}, br_{11/2^+} = 0\%$. Hence, we estimated an upper limit for the ground state by comparing the high energy tail of alpha peak $E_\alpha > 8850$ keV in the α_{Tot} energy spectra (see fig. 5.18). Feeding to the 7/2$^+$ state would decrease the branching into the 9/2$^-$ band. Hence, we re-normalized the χ^2_{min} branching ratios of the 9/2$^-$ band in accordance with $br_{7/2^+}$. Table 5.13 gives the

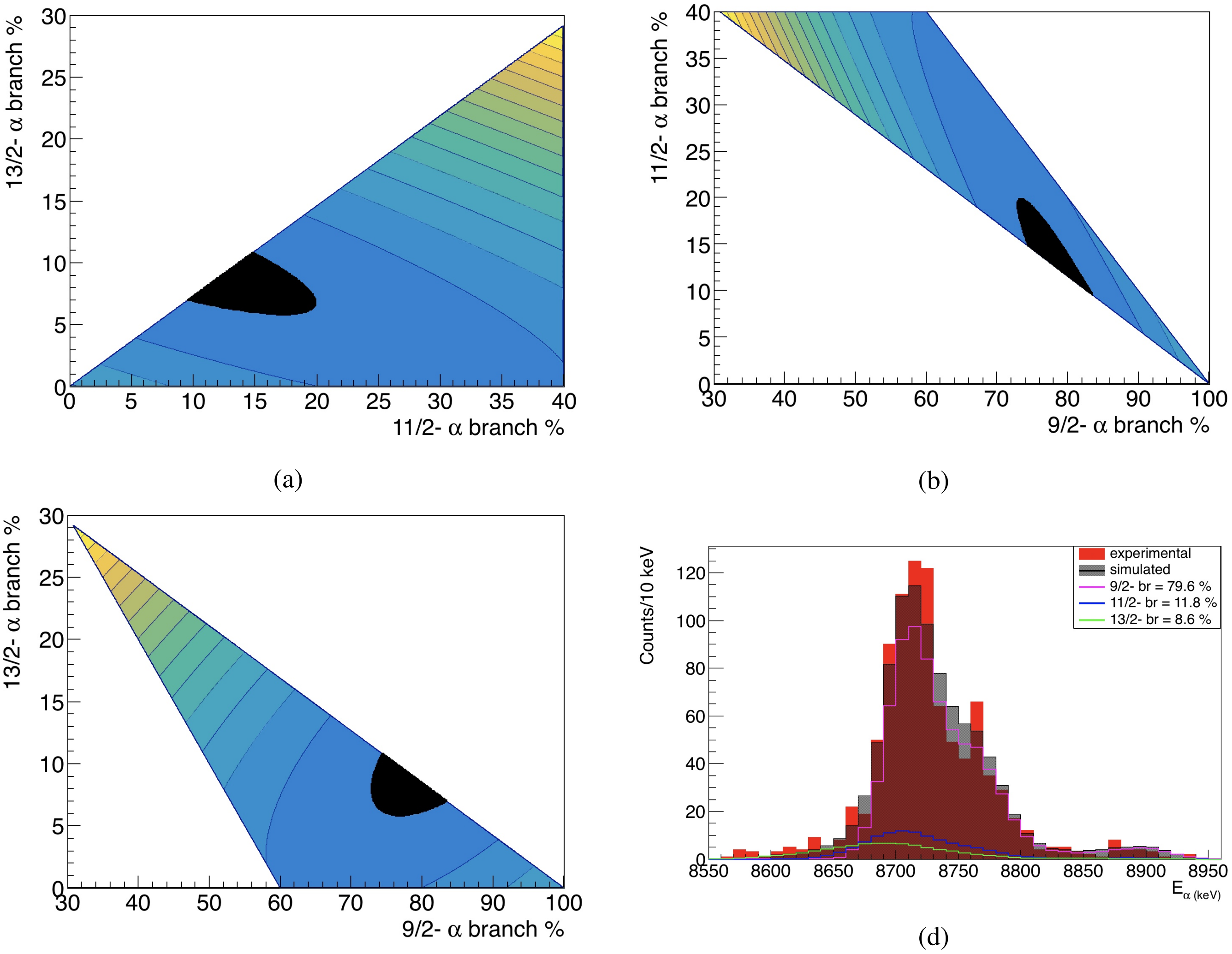

(a)

(b)

(c)

(d)

Figure 5.19: χ^2 value: a) $11/2^-$ vs $13/2^-$ b) $9/2^-$ vs $11/2^-$ c) $9/2^-$ vs $13/2^-$. The dark area is the limit beyond which $\chi^2 > \chi^2_{critical}$ d) Comparison of experimental and simulated alpha peak shapes at the minimum χ^2 value. The contribution due to each decay branch is shown separately. The experimental and simulated peak integrals are 937 and 931 respectively.

counts of the alpha particles with energy in the range 8850 - 9000 keV for different values of $br_{7/2^+}$. From table 5.13, we see that there could be a maximum of 0.1 % branching to the ground state. Since, feeding to the ground state is very small we did not check alpha decay branching to the higher lying states in the band.

5.7.3 Decay to $5/2^+$ state

In the neighboring isotones, there is a small branch to the $5/2^+$ band. Assuming that the $5/2^+$ state lies above K binding (at an excitation energy greater than 149 keV) in ^{251}No, we have estimated an upper limit for the branching to the $5/2^+$ state. Since, we do not know the exact position of this state, we only compared the X-ray counts within the range from 118-131 keV and ICE energy above 100 keV. As for the $7/2^+$ state, we also varied the branching to the $5/2^+$ state in step of 0.2 % from 0% to 5%. The X-ray

br(9/2$^-$) band	br(g.s.)	N_{exp}	N_{sim}
100	0.0	25 ± 5	35 ± 6
99.8	0.1		36 ± 6
99.8	0.2		37 ± 6
99.6	0.3		38 ± 6
99.6	0.4		37 ± 6
99.4	0.6		40 ± 6
99.2	0.8		42 ± 6
99	1.0		44 ± 7

Table 5.13: Table showing how the intensity of the simulated alpha peak between 8850 and 9000 keV varies according to the relative branching to the 7/2$^+$ ground state.

9/2$^-$	5/2$^+$	$N_{exp}(x-ray)$	$N_{sim}(x-ray)$	$N_{exp}(e-)$	$N_{sim}(e-)$
100	0	40 ±6	47 ±7	31± 6	31± 6
99	1		48 ± 7		31 ± 6
98	2		50 ± 7		32 ± 6
97	3		52 ± 7		33 ± 6
96	4		55 ± 7		34 ± 6
95	5		57 ± 7		34 ± 6

Table 5.14: Table showing how the intensity of the X rays and electrons vary with branching to the 5/2$^+$ state. A maximum of 3 % branching can be accommodated.

and the electron counts are given in table 5.14. By comparing the integrals we see that a maximum of 3 % can be fed to the 5/2$^+$ state. We cannot rule out the possibility that the 5/2$^+$ lies below the K binding. This would require performing the χ^2 minimization with two unknowns: the true conversion coefficient of the 143 transition and the intensity of the 5/2$^+$ → 9/2$^-$ transition. Such a multiparameter study could be envisaged in the future. The final decay scheme established for the alpha decay of ^{255}Rf is shown in fig. 5.20.

5.8 Hindrance Factors

Hindrance factors are calculated using Preston's method described in section 3.1.1. To calculate the hindrance factor we need to get the total decay branching to these states. From our measurements $br_\alpha = 49.1 \pm 1.3\%$ and $br_{fission} = 50.9 \pm 1.1\%$, $T_{1/2} = 1.67 \pm 0.05$ s. The nearest even-even nucleus is ^{256}Rf with $T_{1/2} = 6.67 \pm 0.01$ ms, $br_\alpha = 0.32 \pm .017\%$ and $E_\alpha = 8790$ keV. The calculated radius of ^{256}Rf is $\rho = 9.27$ fm. After mass dependence correction using eq. 3.24, the radius of ^{255}Rf is found to be $\rho = 9.26$ fm. The HF to the states in ^{251}No are reported in table 5.15.

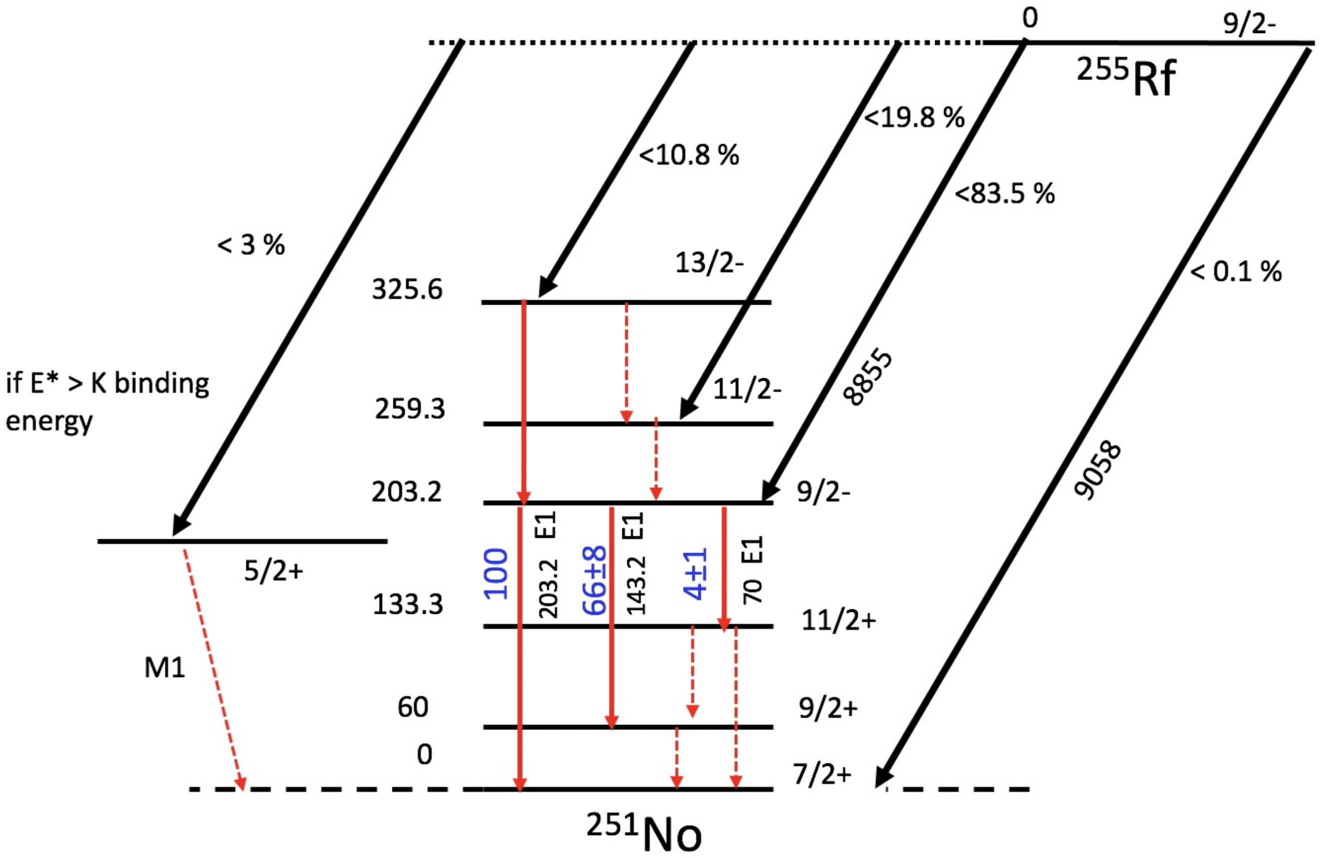

Figure 5.20: Proposed decay scheme of ^{255}Rf where the given alpha branching ratios are the maximum limits and the energies correspond to Q values.

state	E_α (keV)	br_α %	br_{decay} %	HF
$9/2^-$	8716	78.9	38.74	1.3
		72.8^-	35.74	1.4
		83.5^+	41	1.2
$11/2^-$	8660	12.2	6	5.5
		9.5^-	4.66	7.1
		19.8^+	9.72	3.4
$13/2^-$	8595	8.9	4.37	4.7
		5.8^-	2.85	7.2
		10.8^+	5.3	3.9
$7/2^+$	8916	0.1^+	0.049	4114
$5/2^+$	8753	3^+	1.47	43.8

Table 5.15: HF calculated using Preston's Method. + and - indicate maximum and minimum values as discussed in the text. The alpha particle energies have been corrected for mass dependence of the contribution of the recoil daughter to the detected energy.

5.9 Investigation of isomeric states in ^{255}Rf

In section 5.3, we have discussed how the single-particle $5/2^{+}[622]$ spin isomer and possible multi-quasiparticle isomers were identified in ^{255}Rf by the GSI group. In our study, we have detected 27 events where 2 consecutive low energy signals in the implantation DSSD are observed before the characteristic alpha decay or fission of ^{255}Rf. This an indication of the presence of at least two isomers. In the following sections detailed analysis for establishing the characteristics of these isomers is presented. First we shall present the spectroscopic information obtained from the experiment and then we will discuss the decay scenarios we have tested with GEANT4 simulations to explain the observations. We have looked at isomeric decays in several ways, i.e., through the detection of :

- low energy signals occurring in the same pixel as the recoil and subsequent alpha- or fission decays. These events will be denoted by CE.
- Signals in the Ge or tunnel detectors either in coincidence with the CEs or not. They will be denoted by γ or e- respectively.

5.9.1 Isomer spectroscopy of ^{255}Rf

Detection of single isomeric events

The events where only 1 CE was detected in the implantation detector are referred to as ER*-[CE]-^{255}Rf, where * correspond to the event with respect to which the lifetime of the event enclosed in [ ] is measured and these symbols will be used in the rest of the sections. The energy and time distribution of these CEs are shown in fig. 5.21a. The time distribution has been fitted with the 1 lifetime component fit function given in Appendix A. In fig. 5.21b, we can notice the dead time of the ADCs, which is about $2^5 = 32\,\mu$s. Due to this dead time only 663 CEs were detected out of $N_{fit} = 1024 \pm 45$, an estimation from the lifetime fit. The measured half-life of these CEs is $T_{1/2} = 53 \pm 2\,\mu$s. The spectra of gamma rays and electron observed in coincidence with the CEs are shown in fig. 5.22a and 5.22b respectively. In the γ-ray spectrum, the

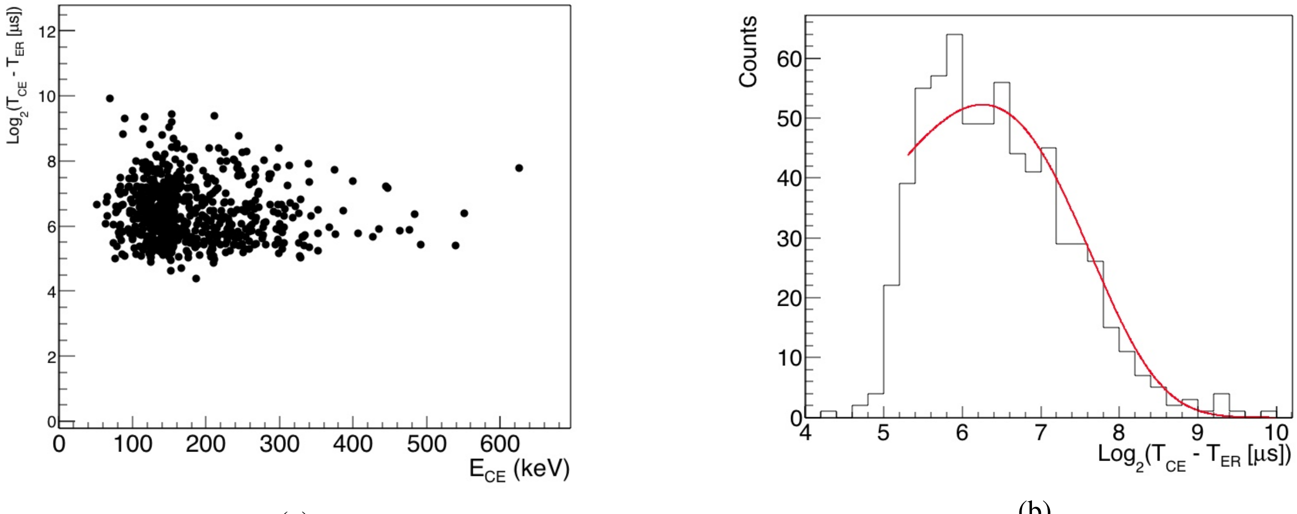

(a) (b)

Figure 5.21: a) Energy and time distribution plot, and b) the fit on the lifetimes of the CEs in the decay chains ER*-[CE]-^{255}Rf.

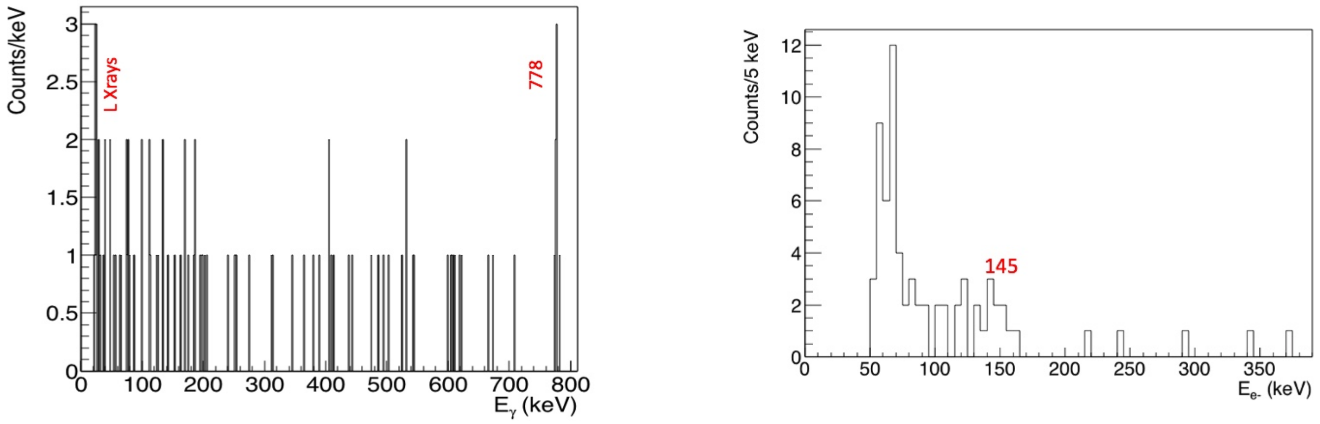

(a)

(b)

Figure 5.22: (a) 103 gamma rays and (b) 69 electrons(tunnel) observed in coincidence with CEs in the decay chains ER-[CE]-^{255}Rf.

most intense line is the 778 keV transition and some LX rays around 24 keV are visible. While in the e- spectrum, two structures < 100 keV and around ~ 145 keV are observed. We have attempted to disentangle the CE events on the basis of whether a gamma ray and/or an electron is seen in coincidence with them. Table 5.16 gives the half-lives, mean energy and counts of these CEs in different conditions. We can

Condition	mean E (keV)	Fit	Schmidt	Counts
w γ	202	75 ± 8	96^{+111}_{-9}	97
wo γ	174	49 ± 2	72^{+3}_{-3}	566
w e-	184	71±9	91^{+13}_{-10}	63
wo e-	177.4	51 ± 2	74^{+3}_{-3}	600
w γ and e-	177.8	105± 23	124^{+32}_{-21}	24
wo γ and e-	172.7	49±2	72^{+3}_{-3}	527
w γ wo e-	211	65±8	87^{+12}_{-9}	73
wo γ w e-	189.3	50±8	70^{+13}_{-10}	39
w γ or e-	198.4	68± 6	89^{+8}_{-7}	136

Table 5.16: Half-lives (in µs) of conversion electrons for the chain ER*- [CE]-^{255}Rf in different conditions. Here 'w' and 'wo' refer to with and without coincidence respectively. Since CE events suffer from deadtime, the $T_{1/2}$ values should be considered as upper limits.

notice that the half-lives of the CEs without coincident gamma rays and/or electrons have similar half-lives as the one established for the $5/2^+$ isomer from the work of the GSI group in contrast to the ones with coincident gamma rays which tend to have longer lifetimes. We have summed the energies of the CEs with the energies of the coincident gamma rays and electron on event-by-event basis to get an idea of the total energy (E_{max}) removed. This E_{max} would then set a constraint on the energy step involved in the deexcition of the supposed isomer. Since, ground state alpha and fission decays follow these CEs, the E_{max} would than correspond to the the excitation energy of the isomer with respect to the ground state. Fig. 5.23 shows the E_{max} for these CEs with their corresponding detection times. One can notice that except for 1 high energy event most of the events lie below 1100 keV.

One can also detect single isomeric decays when no CEs are recorded in the implantation detector. We

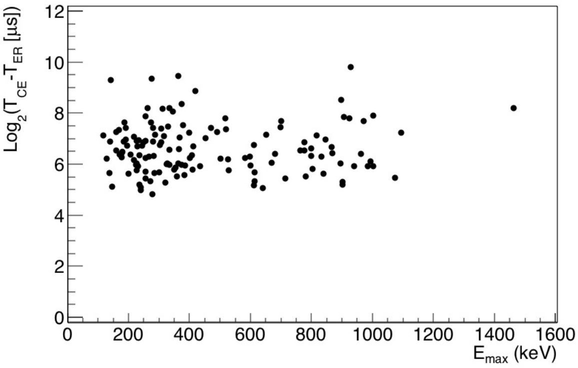

Figure 5.23: CE time with respect to recoil implant vs the total energy E_{max} obtained by summing all the energies detected in coincidence on an event-by-event basis.

have thus looked at the gamma rays and electron that follow the recoil with a subsequent alpha or fission decay in the same pixel. These correlations shall be denoted by ER-$\gamma/e-$-^{255}Rf. The energy spectra of these gamma rays and electron are shown in fig. 5.24. We have measured the half-lives of the prominent gamma rays lines at 778 keV, 708 keV, 666 keV, 543, 170 and 102 keV. Although some of the peaks are not 3 σ peaks and the counts are very low, we have fitted their time distributions. The half-lives of these gamma transitions were also determined using the method of Schmidt [192] (see Appendix A) as it is appropriate for very low statistics. The mean energy, counts without background subtraction and the half-lives from a fit and from Schmidt's method are given in table 5.17. The last three columns in table

	ER-γ ^{255}Rf$_{\alpha/f}$			ER*-[γ] -CE-^{255}Rf$_{\alpha/f}$		
E (keV)	Counts	Fit	Schmidt	Counts	Fit	Schmidt
778.4	33	32±6	$35^{+7.4}_{-5.2}$	43	42±7	46^{+8}_{-6}
708	7	66±27	$66.6^{+40.5}_{-18.3}$	8	33±19	63.9^{+35}_{-17}
666.3	6	14±6	$14.7^{+10.1}_{-4.3}$	7	35±15	35.4^{+21}_{-10}
610.4	5	44±24	$62.2^{+50.4}_{-19.2}$	7	83 ± 43	78.6^{+48}_{-22}
543.8	9	55±36	$57.6^{+28.8}_{-14.4}$	12	59±29	59.1^{+24}_{-13}
170	30	44±8	$35.8^{+8}_{-5.5}$	33	49±8	$42.1^{+8.9}_{-6.2}$
102.7	13	89±54	$96.9^{+37.2}_{-21}$	17	116±39	$101.9^{+32.6}_{19.9}$

Table 5.17: Half-lives (in µs) of prominent gamma lines observed (see fig. 5.24a) before the ground-sate decay of ^{255}Rf. [CEs] indicates that gamma rays in coincident with the CEs in the implantation detector were also included.

5.17 under the heading ER*-[γ]-CEs-^{255}Rf correspond to the gamma rays observed before the ground state decay irrespective of whether a CE is detected or not in the implantation detector. We notice that for each transition, the half-life measured in both the cases ER-γ-^{255}Rf and ER-γ-[CEs]-^{255}Rf is compatible, at least from Schmidt's method for the weak lines. We can also notice that the 102 keV transition has a very different half-life, an indication that it must originate from a different isomer. To inspect more closely, whether decay from more than one isomeric states were contributing to the γ-ray spectrum, we have performed a weighted mean analysis. Fig. 5.25 shows the spread of the half-lives. The weighted mean half-life of all the gamma transitions was found to be 30.78 µs (denoted by a black straight line) with a standard deviation σ = 3.8 µs. Bands corresponding to 1 σ to 5 σ are drawn to identify abnormality in the half lives, fit $T_{1/2}$ and mean $T_{1/2}$ correspond to the fit and Schmidt values given in table 5.17. The

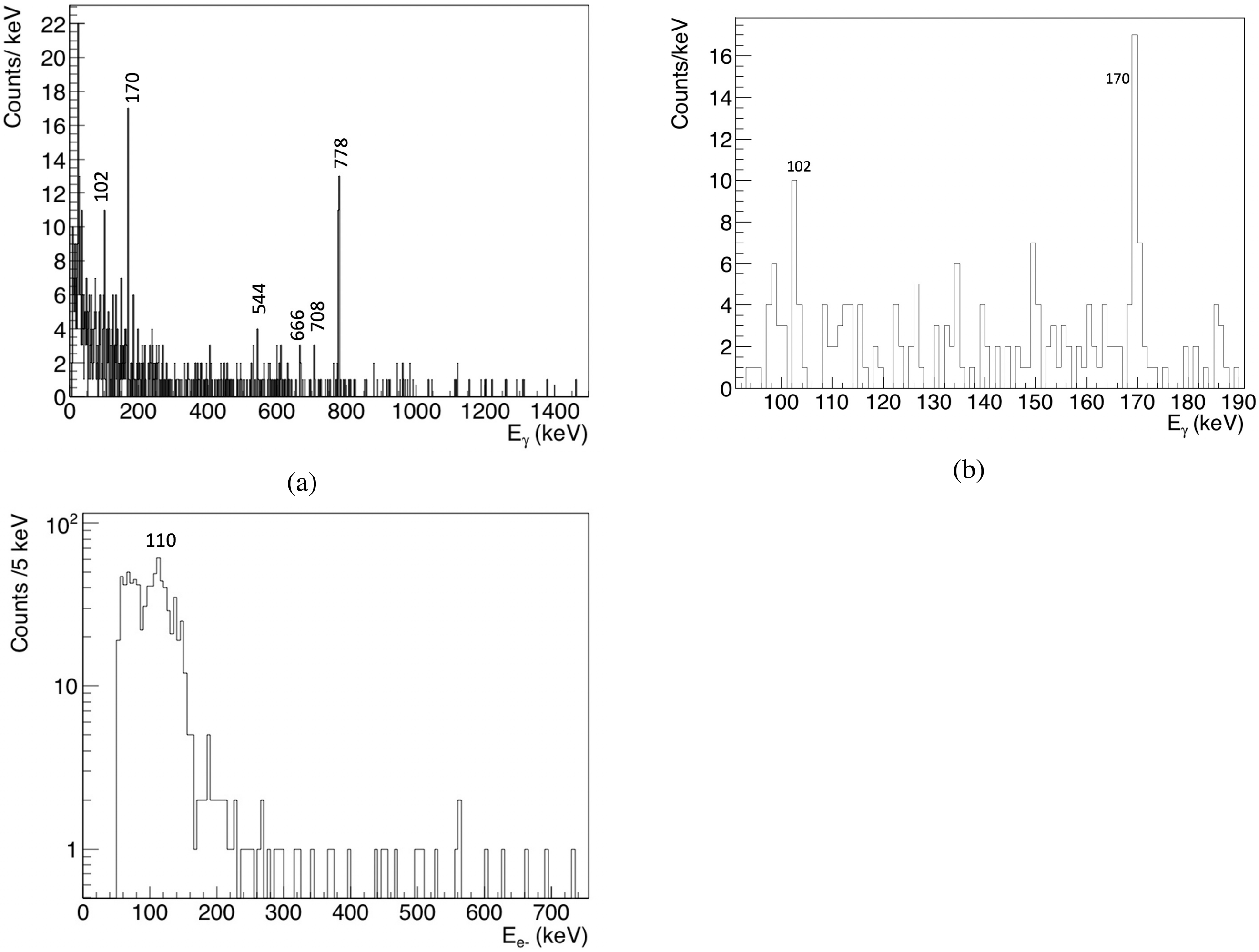

(a)

(b)

(c)

Figure 5.24: (a) Spectrum of gamma rays (b) zoomed at low energy and (c) spectrum of tunnel electrons observed in the chains ER-$\gamma/e-$- ^{255}Rf.

errors on the Schmidt values are reflected in the asymmetric band drawn for mean $T_{1/2}$. From this figure we can notice that the 102 keV transition is very far from the weighted lifetime whereas, the other transitions fall within 5 σ. The half lives obtained for the electron detected in the tunnel detector are given in table 5.18. Here in particular, we have separated the electron in energy intervals to look for different behaviors in the lifetimes.

The $\gamma - \gamma$ and $\gamma - e-$ coincidence plots are shown in fig. 5.26 in which the coincidence of the few high energy transitions at 778 keV, 708 keV and 610 keV with electron of energy < 200 keV can be ascertained. We have summed the energies of the coincident gamma rays and electron to get E_{max}. This allows a comparison of the isomeric properties in the two types of correlations: ER*-[CE]-^{255}Rf and ER*-[$\gamma/e-$]-^{255}Rf. In fig. 5.27, we see that the E_{max} in both the correlations are comparable. Aside from the dead time cut for the CEs, the time distributions seem to be compatible.

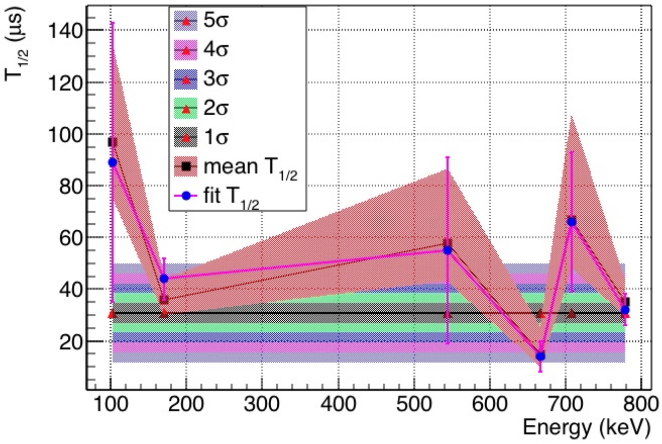

Figure 5.25: Measured lifetime of prominent gamma-ray lines for ER- γ correlations with or without CEs (i.e low-energy signals in the implantation DSSD) followed by the ground-state decay of ^{255}Rf.

	ER-e-^{255}Rf$_{\alpha/f}$				ER*-[e-]-CE-^{255}Rf$_{\alpha/f}$			
E Range (keV)	mean E	Fit	Schmidt	Counts	mean E	Fit	Schmidt	Counts
0-90	70	29±4	63.1^{+4}_{-4}	242	70	44±4	52.9^{+3}_{-3}	310
90-130	110	41±2	$41.9^{+2.5}_{2.2}$	316	110	42±2	39.8^{+2}_{-2}	336
130-170	142	43±4	44.9^{+5}_{-4}	106	143	48±4	39^{+4}_{-3}	123
>170	328	29±8	$64.5^{+10}_{-7.8}$	52	324	33±9	58^{+9}_{7}	58
Tot	117	41±2	51.2^{+2}_{-2}	716	114	44±2	46^{+2}_{-2}	827

Table 5.18: Energy ranges and associated half-lives (in µs) of electrons detected in the tunnel detectors (see fig. 5.24c) before the ground-sate decay of ^{255}Rf (see text for details on the last 3 columns of the table).

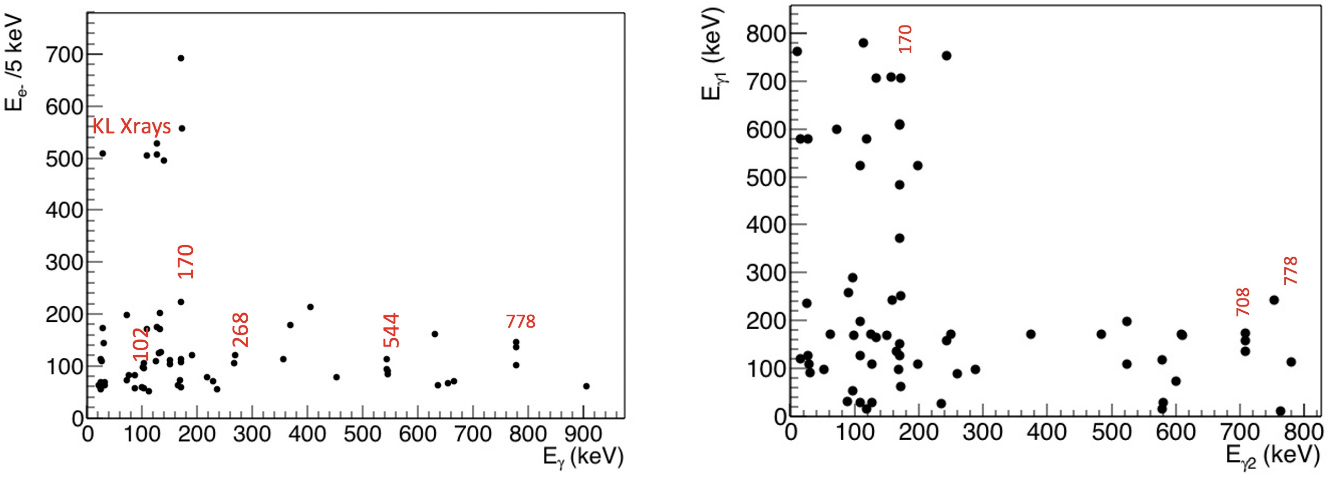

(a)

(b)

Figure 5.26: a) 65 $\gamma - e^{-}$ coincidences and b) 66 $\gamma - \gamma$ coincidences observed in the decay chains ER-$\gamma/e-$ - ^{255}Rf decay.

2 isomeric decays

It was mentioned before that two CEs cascades were detected in the implantation detector,these are denoted by ER-CE-CE-^{255}Rf. The energy and the time distributions of the first and second CEs are compared in fig.

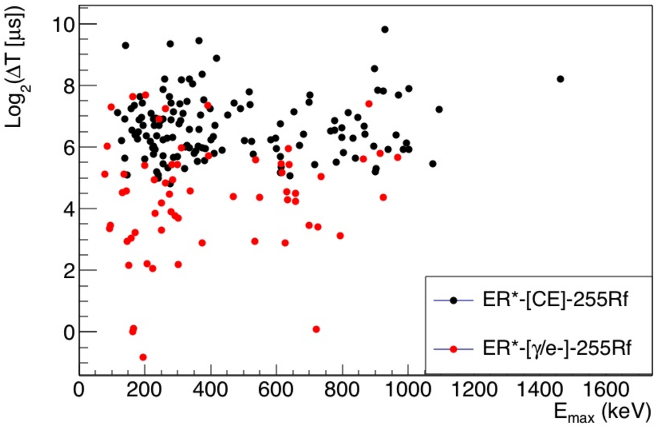

Figure 5.27: Comparison of E_{max} and lifetime of the isomer detected in two different correlations.

5.28. Two conclusions can be immediately drawn from this figure: (1) the first isomer (iso1) is relatively longer-lived than the second (iso2), (2) the detected signal for the first isomer is of much smaller energy than the second. The measured half-lives of isomers iso1 and iso2 are given in table 5.19 for different energy ranges. The half-life of iso2 with respect to the recoil is also given to compare with the CEs in the ER*-[CE]-^{255}Rf correlations where we may have contributions from many possible sources: iso1 when iso2 is missed and iso2 when iso1 is missed resulting in an apparent longer lifetime, iso2 alone and from possibly the 5/2^{+} isomer, which is known to be populated in the reaction in other isotones. Incidentally, neither a gamma ray nor an electron was detected in coincident with isomer iso1 CEs. However, 6 gamma rays and 8 electrons were detected in coincident with the iso2 CEs. Their energy spectra are shown in fig. 5.29. Interestingly, from fig. 5.29 we can identify the 543 keV and 778 keV gamma transitions that are seen in coincidence with the CEs of the ER-CE-^{255}Rf chains and in the ER-$\gamma/e-$-^{255}Rf correlations. This suggests that in all the three decay chains, the decay of the second isomer has been observed. Again for the second CE, based on whether a gamma ray and/or an electron was observed with it, the half-lives are presented in table 5.20. We can notice that under all the conditions, the half-lives of second CEs are

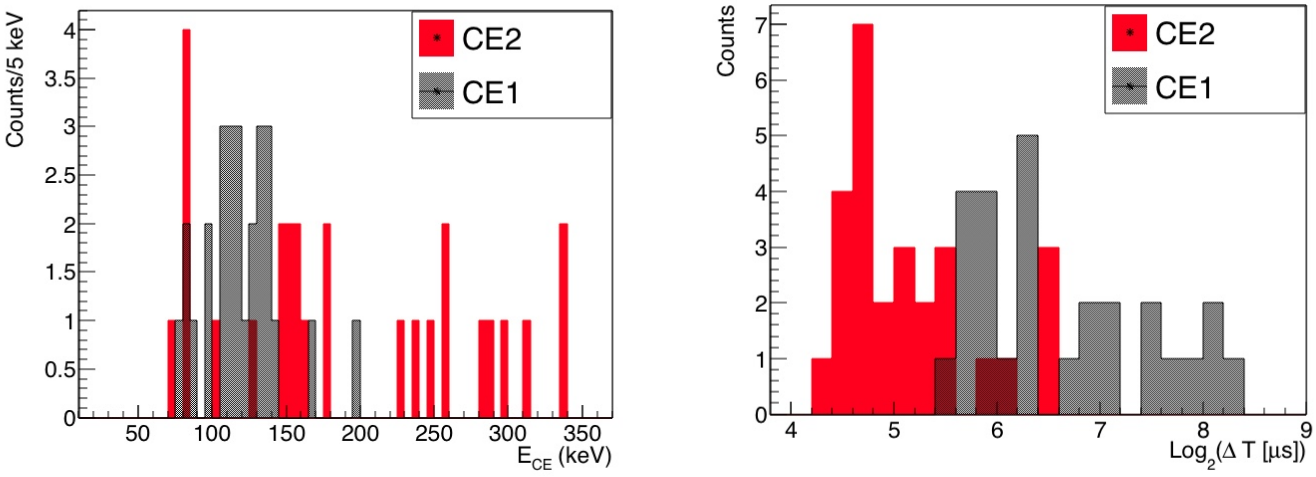

(a) (b)

Figure 5.28: a) Energy and b) time distribution comparisons between the CE observed in the 27 decay chains ER-CE-CE-^{255}Rf.

	E Range (keV)	mean E (keV)	Fit	Schmidt	Counts
ER*-[CE]-CE-^{255}Rf	< 200	119.8	53± 11	$83.7^{+19.9}_{-13.5}$	27
	0 – 100	88.2	-	$71.5^{+49.3}_{-20.7}$	6
	100 – 200	128.8	-	$87.1^{+24.3}_{-15.6}$	21
ER-CE*- [CE]-^{255}Rf	< 350	190.8	13 ± 3	$27.2^{+6.5}_{-4.4}$	27
	0 – 200	129.4	10 ± 3	$24.5^{+8.2}_{-4.9}$	16
	>200	280	27 ± 16	$31^{+13.4}_{-7.2}$	11
ER*-CE- [CE]-^{255}Rf			84 ± 24	$110.8^{+26.4}_{-18}$	27

Table 5.19: Half-lives (in µs) of the CEs measured in different conditions.

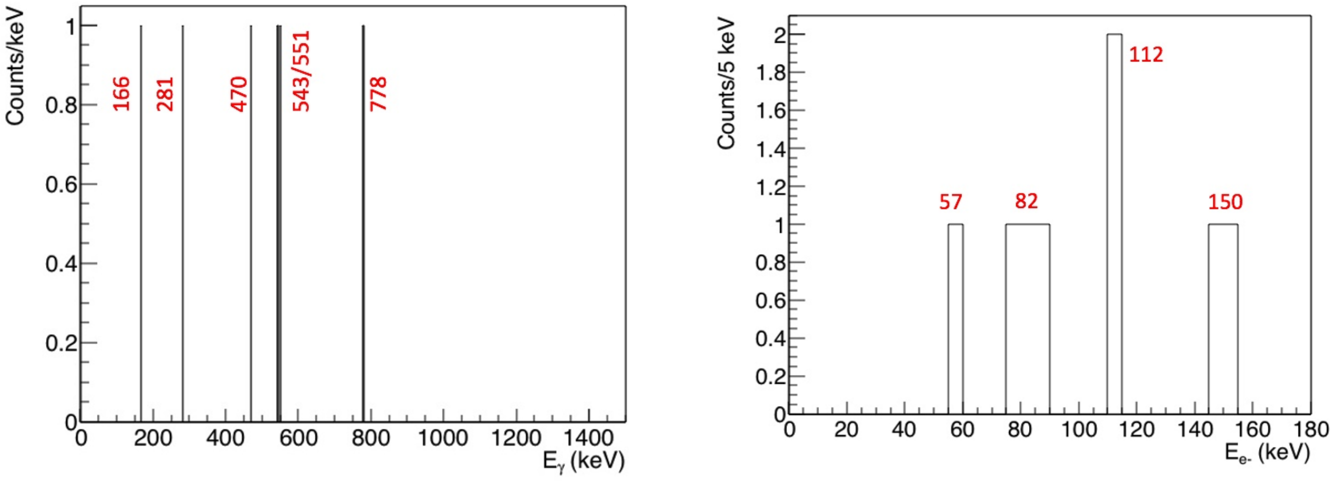

(a) (b)

Figure 5.29: a) 6 gamma rays and b) 8 electrons(tunnel) observed in coincidence with 2nd CEs in the chains ER-CE-[CE]-^{255}Rf.

similar suggesting that they are stemming from the same isomer. The time distribution vs E_{max} of iso2 is shown in fig. 5.30a.

Summing the energies of the two cascading CEs and the coincident gamma rays and electron, we can obtain the excitation energy E_{max} of the isomer iso1, which is shown in fig. 5.30b. The E_{max} obtained is below 1.1 MeV similar to the limits obtained before.

Isomeric decays were also observed in the correlations ER-$\gamma/e-$-CE-^{255}Rf. 19 such gamma rays and 23 electrons were detected before a CE signal. Their energy and time distributions are shown in fig. 5.31. In the γ-ray spectrum we observe some LX rays around 26 keV, and a 102 keV transition and no KX rays, suggesting no transition in the decay from iso1 to iso2 is above the K binding energy. Except for the 2 gamma rays above 200 keV and an electron around 250 keV, both the electron and γ rays have energies less than the E_{max} of the iso1 in ER-CE-CE-^{255}Rf correlations. The higher energy events could be due to our selection of ^{255}Rf ground state decays which lies very close to the randoms (see fig. 5.7). The half lives of iso1 and iso2 in these correlations are given in table 5.21. In the case of gamma rays and electron all the events were taken into consideration to obtain the half-lives. By analogy with the ER-CE-CE-^{255}Rf correlations, we expect the first isomer to have a longer lifetime than the second and from table 5.21, this is indeed what can be inferred.

The energy and time distributions of the CEs in these decay chains are shown in fig.5.32a. From

Condition	mean E (keV)	Fit	Schmidt	Counts
w γ	224.2	19 ± 17	$24.1^{+16.7}_{-7}$	6
wo γ	181.3	15 ± 4	$28^{+7.8}_{-5}$	21
w e-	153.5	20±11	$30.3^{+16.6}_{-7.9}$	8
wo e-	206.5	13 ±4	$25.8^{+7.7}_{-4.8}$	19
w γ and e-	197.2	-	$23.9^{+57.7}_{-10}$	2
wo γ and e-	198.2	13±4	$26.2^{+9.1}_{-5.4}$	15
w γ wo e-	237.7	12±7	$24.26^{+24.3}_{-8.1}$	4
wo γ w e-	139	-	$32.46^{+22.4}_{-9.4}$	6
w γ or e-	1281.6	28±8	$28.3^{-11.5}_{-6.3}$	12

Table 5.20: Half-life (in µs) of conversion electrons for the chain ER-CE*- [CE]-^{255}Rf in different conditions.

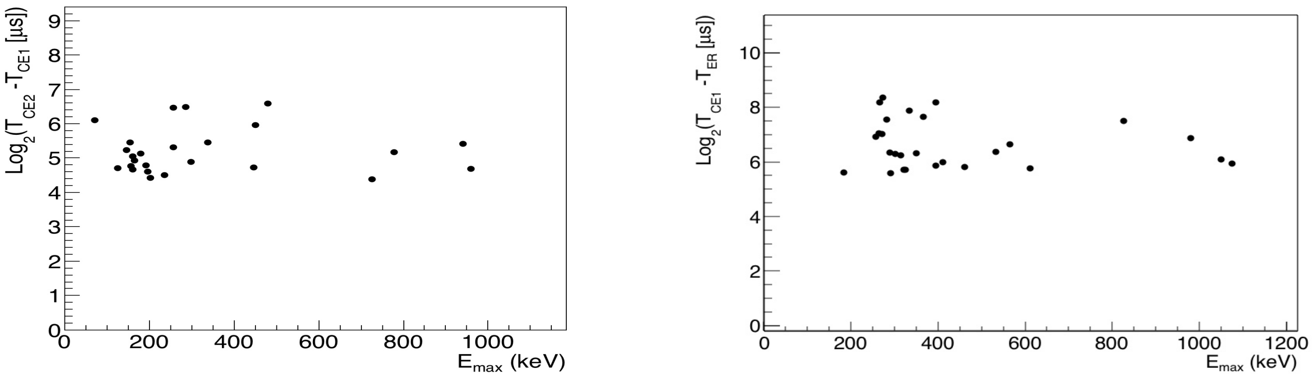

(a)

(b)

Figure 5.30: (a) E_{max} obtained by summing the energy of the (a) 2nd CE and the coincident gamma rays and electron. (b) + CE1 on event-by-event basis.

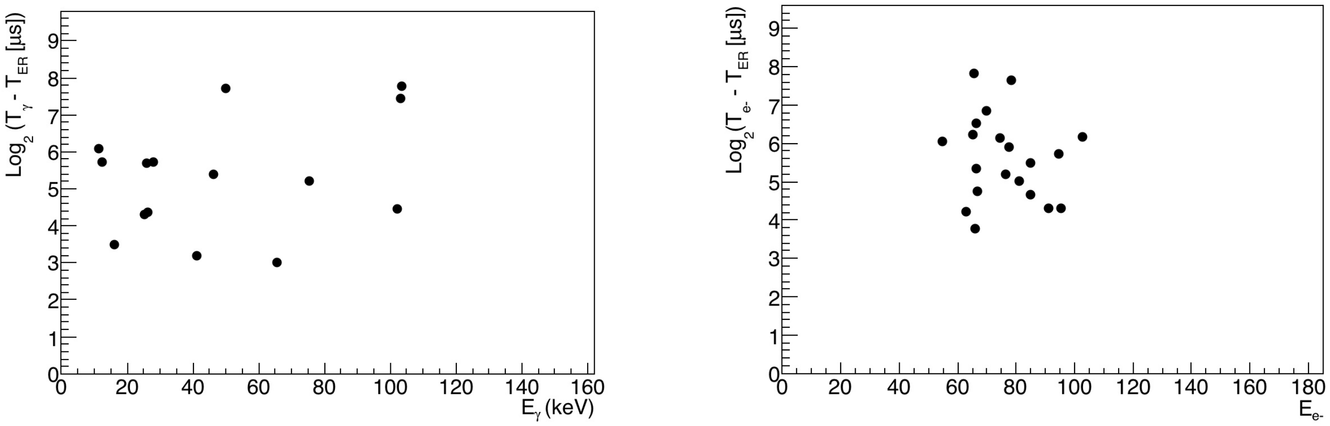

(a)

(b)

Figure 5.31: Energy and time distributions of the a) gamma rays and b) electron seen before the detection of the CE in the decay chains ER-$\gamma/e-$-CE-^{255}Rf.

correlation	Fit	Schmidt	Counts
ER*-[γ]-CE-^{255}Rf	36±8	$45.6^{15.8}_{-9.4}$	15
ER*-[e-]-CE-^{255}Rf	40 ± 8	$46.3^{+13}_{-8.5}$	20
ER-γ*-[CE]-^{255}Rf	49±12	41^{+16}_{-9}	13
ER-e-*-[CE]-^{255}Rf	22±6	$25.2^{+7.2}_{-4.6}$	20
ER*-γ/e−e-[CE]-^{255}Rf	55±9	$78.4^{+16.8}_{-11.8}$	32

Table 5.21: Half-lives (in µs) of gamma rays and electrons in the tunnel and in the DSSD of fig. 5.31 and 5.32a.

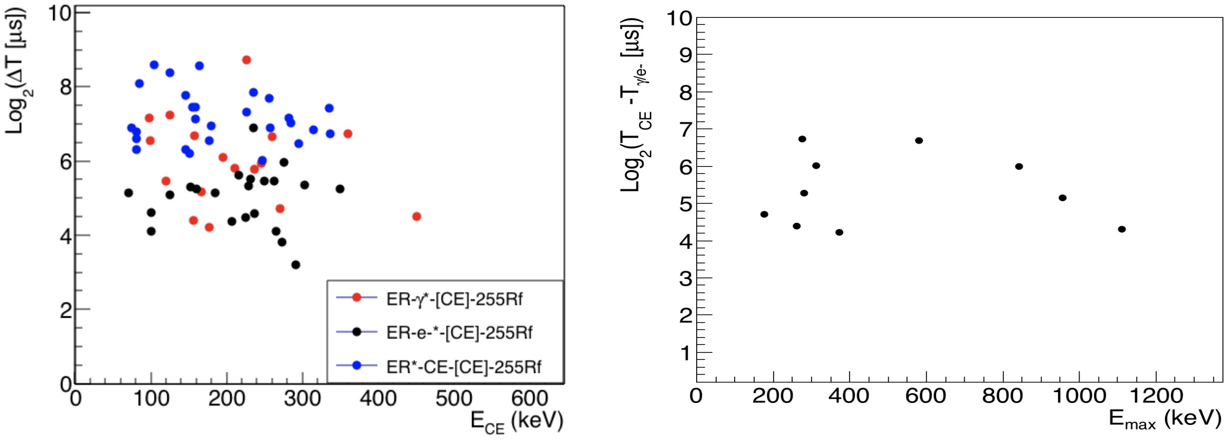

(a)

(b)

Figure 5.32: a) Energy and time distributions of the CEs in the decay chains ER-γ/e−-CE-^{255}Rf. Their lifetimes have been compared with the lifetime of iso2 mocking the non detection of iso1 in the ER*-CE-[CE]-^{255}Rf decay chains. b)Energy step of the 2nd isomer (CE) in the decay chain ER-γ/e−*-[CE]-^{255}Rf.

energy arguments these cannot stem from iso1 as the E_{max} in the decay step from iso1 to iso2 is less than 200 keV, suggesting that their origin could be from iso2 decay. However, their lifetime seems longer than the lifetime of iso2 which might be due to the poor statistics.

In these correlations as well, 6 gamma rays and 10 electrons were observed in coincidence with the CEs, in particular the 778 keV line was observed. Again, to inspect whether more than two isomers are contributing to these spectra we have measured the half-lives of the CEs under different conditions and found them to be equivalent (see table 5.22). The E_{max} in the decay step of iso2 to the ground state is shown in fig. 5.32b.

No ER-CE-γ-^{255}Rf were investigated because of overwhelming punch through signals in the Clover detector. For similar reason, no ER-γ-γ-^{255}Rf correlations were investigated. It was also not possible to investigate ER-CE-[e-]-^{255}Rf correlations because of the limit set by random correlations. Since we have detected only 2 isomers in cascade in whichever way we look, we can now compare them on the basis of their generation in the decay correlation chains. The properties of the 1st, higher-lying isomers are compared in fig. 5.33a and the low lying ones in fig. 5.33b. From there figures, we can conclude that the energy gap between iso1 and iso2 is of the order of 150-200 keV and that iso2 lies ~ 1.1 MeV above the ground state. The various studied correlations indicate that the longer-lived iso1 feeds a shorter lived iso2 that emits a 778 keV gamma ray. There results confirm the GSI result of fig. 5.6.

Condition	mean E (keV)	Schmidt	Counts
w γ	182.9	21^{+17}_{-7}	5
wo γ	218	34^{+8}_{-6}	27
w e-	182.3	27^{+16}_{-7}	7
wo e-	221.6	33^{+8}_{-7}	25
w γ and e-	166.2	17^{+17}_{-6}	4
wo γ and e-	220.4	33^{+9}_{-6}	24
w γ wo e-	249.7	$40^{+\infty}_{-20}$	1
wo γ w e-	203.8	40^{+55}_{-15}	3
w γ or e-	190.8.6	28^{+16}_{-7}	8
tot	213	32^{+7}_{-5}	32

Table 5.22: Half-lives (in µs) of CEs for the chain ER- $\gamma/e-$*-[CE]-^{255}Rf in different conditions.

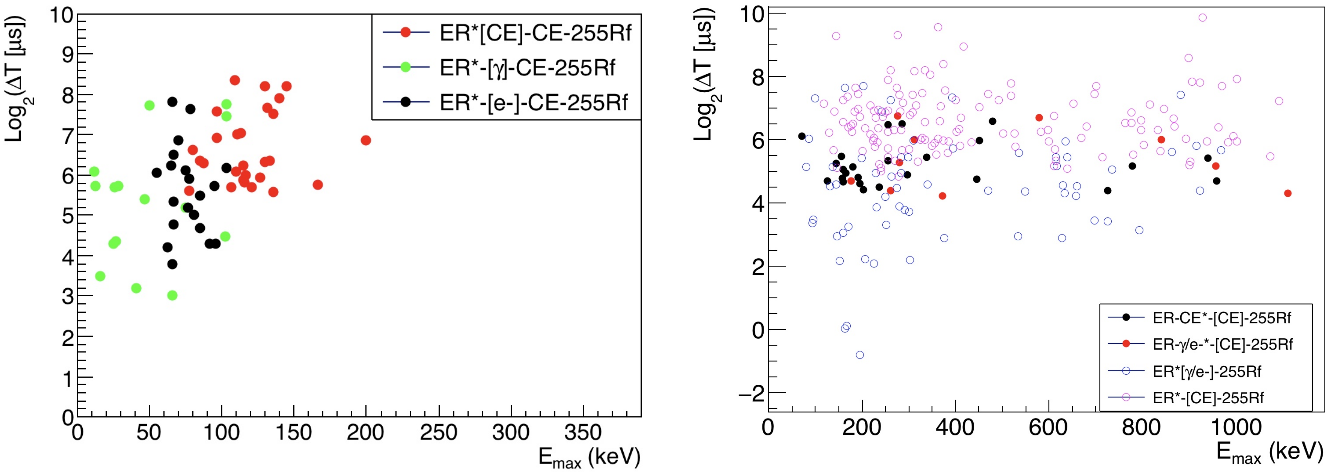

(a) (b)

Figure 5.33: Lifetime and E_{max} compared for the a) 1st isomer and b) the 2nd isomer.

5.9.2 Discussion

There are several possibilities for the 2 isomers at excitation energies around $\sim 1.1 - 1.25$ MeV. The odd neutron ($9/2^-$ $[734]_\nu$) can couple to the 5^-, 8^- or 3^+ 2-quasiproton states observed and/or suggested in ^{254}No and ^{254,256}Rf, or the odd neutron can couple to the 2^- and 8^- 2-quasi-neutron states observed in ^{252}No. The 5^- and 8^- configurations are expected to be the lowest (see table VII in ref. [168]) and lie close in energy and because of the microsecond lifetimes, the ΔK involved in the isomeric transitions must not be greater than 5 (see figs. 5.34a, 5.34b and 5.35 where transitions lifetimes as a function of transition energy are plotted for ΔK = 3 - 5). Possible high-K and low-lying 1-neutron $\otimes$ 2-proton configurations for the isomers are therefore $\{9/2^-\ [734]_\nu \otimes 1/2^-\ [521]_\pi \otimes 9/2^+\ [624]_\pi\}$ and $\{9/2^-\ [734]_\nu \otimes 7/2^-\ [514]_\pi \otimes 9/2^+\ [624]_\pi\}$ yielding states with K^π=$19/2^+$ and $25/2^+$. We have constructed several decay scenarios keeping in mind the constraints set by observables such as E_{max}, $T_{1/2}$ and the intensities in the γ-ray and e- spectra. These scenarios were then simulated in GEANT4 and the simulation results were compared to the experimental results. The comparison between the simulated spectra and experimental ones is however not as straightforward as in the case of the α decay of ^{255}Rf. This is due to 2 factors: the first one is the dead time between 2 subsequent events in a pixel of the DSSD and the second is related to the experimental thresholds. As

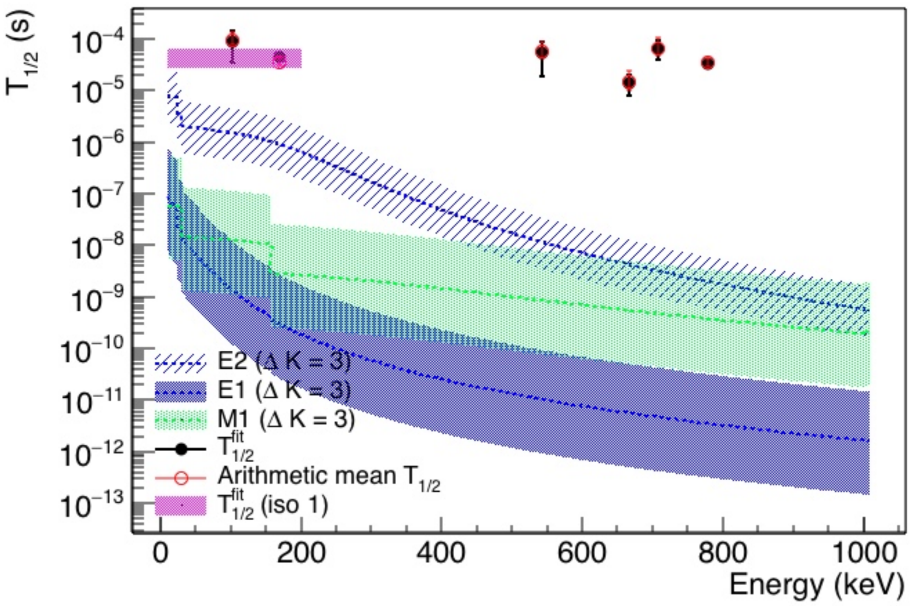

(a)

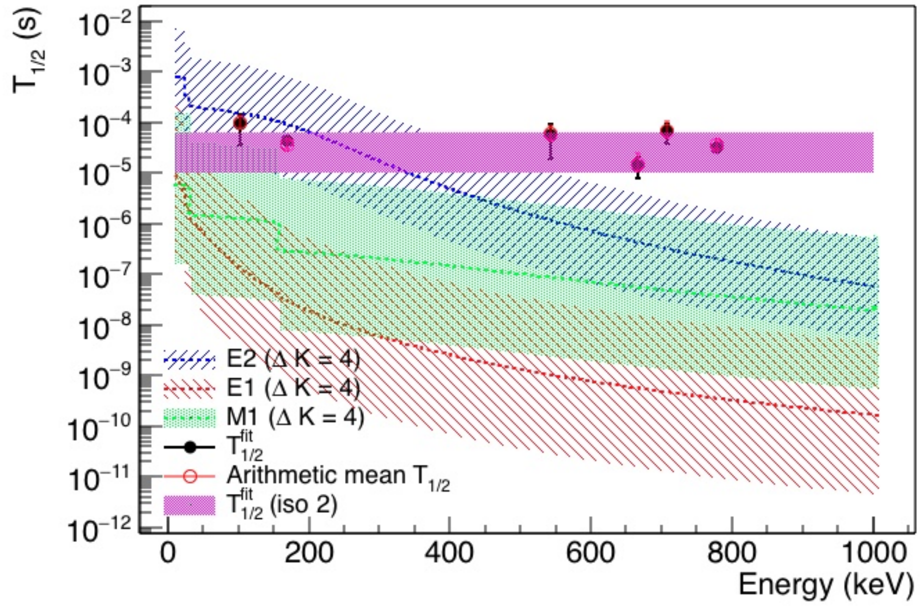

(b)

Figure 5.34: Experimental half-lives of the prominent gamma transitions listed in table 5.17 for ER- γ - ^{255}Rf decay compared with Weisskof estimates including a K-hindrance a) $\nu = 3 - L$ and b) $\nu = 4 - L$. The Weisskof estimates have been corrected for the internal conversion coefficients. For each transitions in the figures, the band corresponds to $f_\nu = 30 - 300$ with a line corresponding to $f_\nu = 100$. The upper and lower limits on the half-life of iso1 and iso 2 are from table 5.19 and 5.21. A band has been drawn to highlight its half-life in the visible range.

an example, gamma rays which are emitted by one or the other isomer may not be detected in coincidence with a CE in the DSSD, not because the particles contributing to the CE signal were not emitted, but simply because they were not detected. For our study, an effective threshold of ~ 80 keV and a dead time of

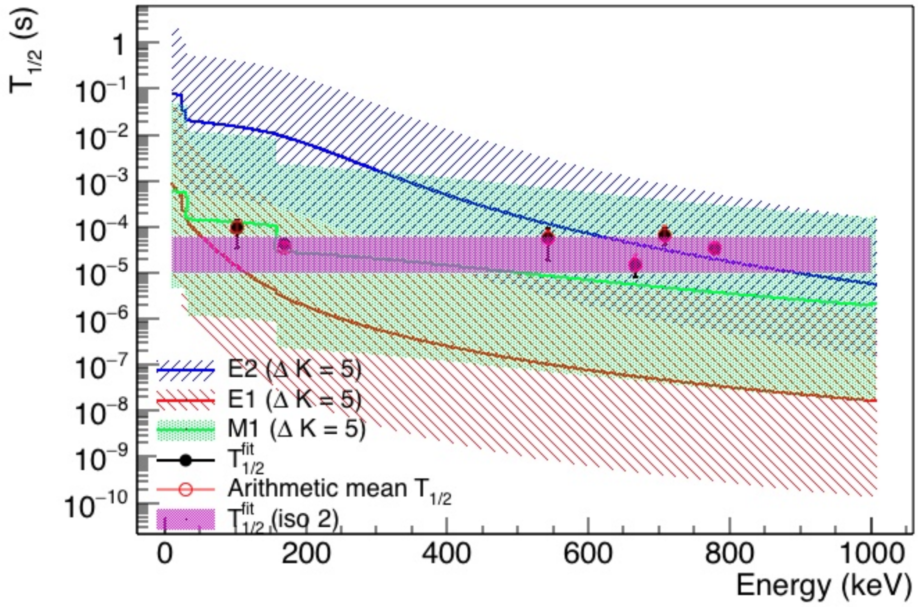

Figure 5.35: Same as for fig. 5.34 for $\nu = 5 - L$.

32 μs were used for the implantation detector.

In scenario 1, we suppose that the $19/2^+$ isomer decays directly to the ground state $9/2^-$ band. Fig. 5.36 shows the corresponding decay scheme. Using a typical value of $\frac{\hbar^2}{2\mathcal{J}} = 6.1$ in equation 2.71, a 170 keV can be obtained for the E2 cross-over transition at spin $15/2^-$ in the ground state band and a few of the observed high-energy lines may also be placed in the decay scheme. The K hindrance for such high

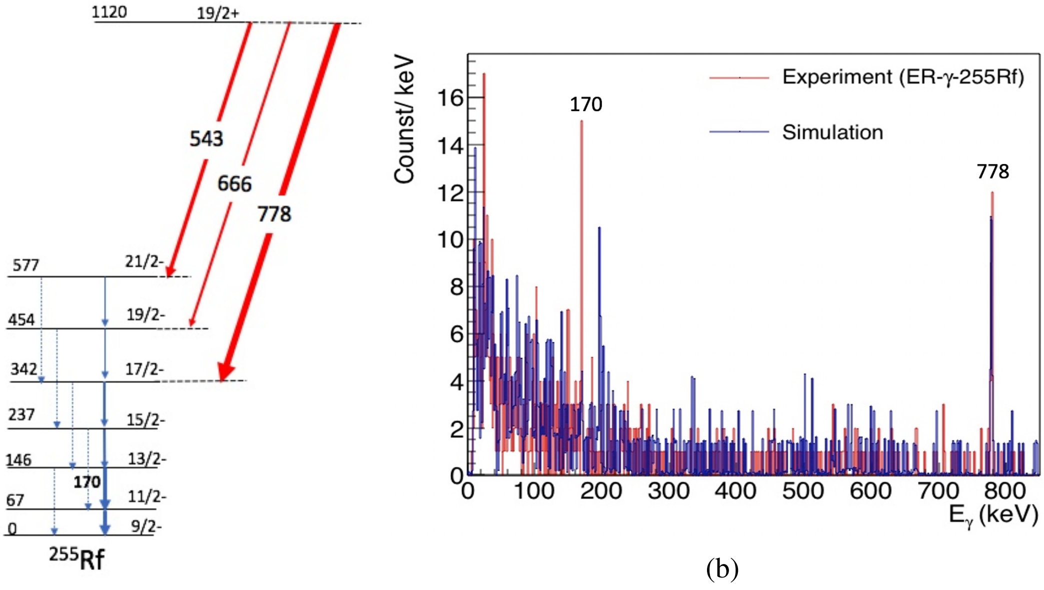

(a)

(b)

Figure 5.36: Scenario 1: a) Decay scheme b) simulated γ ray spectrum where experimental background has been added.

energy E1 transitions is of the order of 400, which is not uncommon for E1 transitions and is in line with the f_ν=804 measured in the decay of the 8^- isomer in ^{254}No [130].

The simulated spectrum shown in fig. 5.36 has been adjusted to the experimental 778 keV peak and a fraction of the experimental randomly-correlated background has been added to reproduce the low-energy background, which is not present in the simulations. The simulated spectrum shows a noticeable deficiency for the 170 keV line, which is expected given the internal conversion coefficient (α_{Tot} = 3.68(6)) for an E2 transition. Besides the experimentally unobserved peak at 196 keV, there is also an excess of KX rays in the simulation. Hence, we discarded this decay scenario.

In scenario 2 displayed in fig. 5.37a, we assume that the $19/2^+$ isomer decays via a 170 keV E1 to the $11/2^-$, whose excitation energy was inferred from the properties of the α decay of ^{259}Sg (see sec. 5.3). Such an E1 decay would correspond to a K hindrance of ~700.

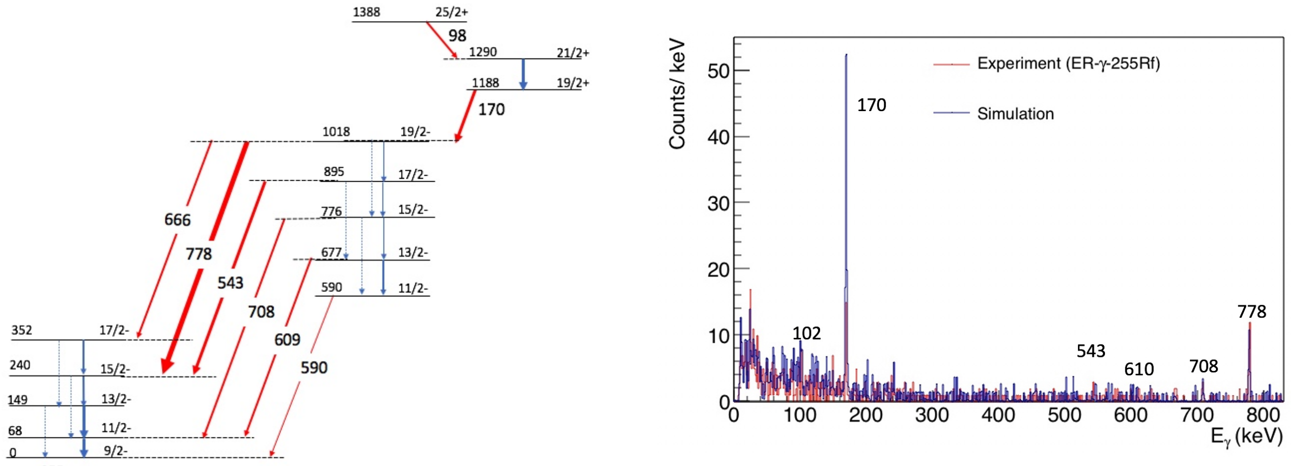

(a)

(b)

Figure 5.37: Scenario 2: a) Decay scheme b) simulated γ ray spectrum with added experimental background.

To fit the high-energy lines we adjusted the rotational energies of the members of the ground state band and placed the $11/2^-$ state at an excitation energy of 590 keV. This energy is consistent with the GSI result ~ 600 keV. Most of the flux leaves the $11/2^-$ band before the bandhead. This is possible if the $11/2^-$ band is vibrational. N. Yu. Shirikova et al. [193], have investigated the nature of states in the region around Z=100 using the quasiparticle phonon model. In ^{257}Rf, for example, the $11/2^-$ state is predicted to carry a significant one-quasiparticle⊗phonon component: $7/2[613]\otimes2^-$. Such a vibrational character of the $11/2^-$ band can also be inferred in ^{253}No. The recent identification of the $11/2^-$ state at 753 keV above the ground state in ^{253}No [K. Hauschild et al., to be published] has recently allowed to reinterpret the decay scheme of the ~ 700 μs isomer [42] as all the high-energy transitions identified in refs. [42] and [194] can easily be placed if they all deexcite the $11/2^-$ band (see fig. 5.38).

Regarding the $25/2^+$ isomer, $E_{max} \leq 200$ sets a constraint on how far the $25/2^+$ isomer can be in energy from the $19/2^+$ isomer. We assume that a low energy E2 transition deexcites the $25/2^+$ and populates the $21/2^+$ state of the $19/2^+$ band. The 25/2+ isomer cannot be lower than the $21/2^+$ because it would then have to decay via an E3 transition to the $19/2^+$ band head, and thus have a much longer lifetime. We assign the low energy E2 transition to 98 keV and the M1 transition in the band to be 102 keV, since we observe them in our experiment. However, one should point out that a 98 keV E2 transition implies a K hindrance

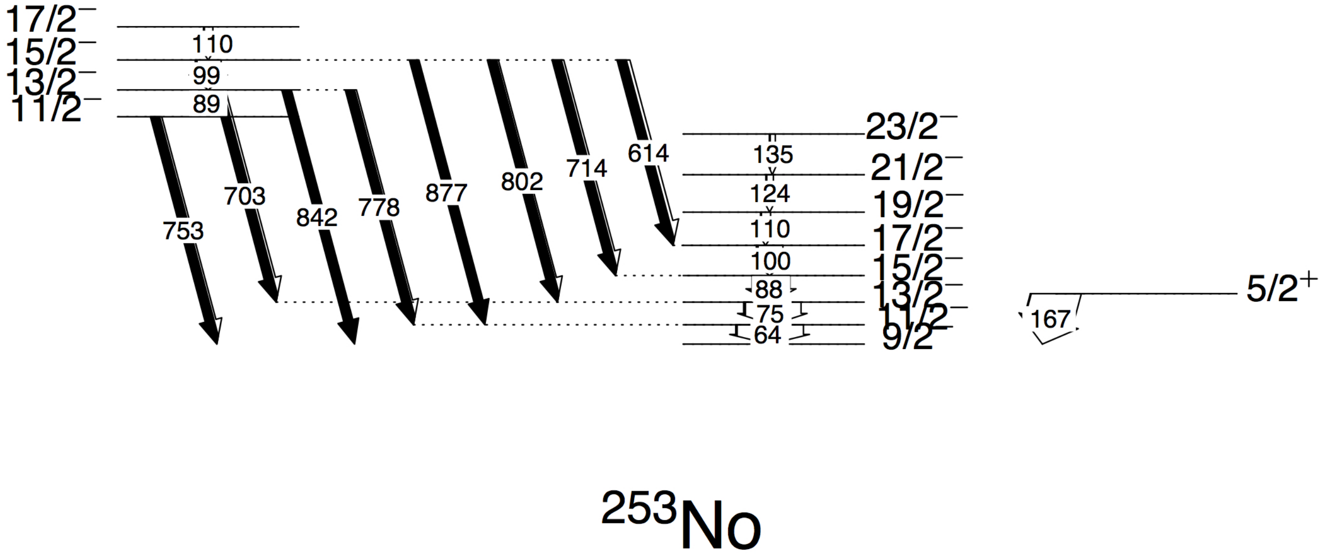

Figure 5.38: Revised partial decay scheme of ^{253}No.

of ~3000 in going from K=25/2 to K=19/2. The energy spacing of 102 keV can be reproduced by taking $\frac{\hbar^2}{2\mathcal{J}}$ = 4.9 which is acceptable for a band built on a 3 quasiparticle configuration with reduced pairing.

The spectrum of gamma rays obtained in the simulations of decay scenario 2 is shown in fig. 5.37b. Although the high-energy lines can be well accounted for in this decay scenario, there is now an excess of counts in the simulated 170 keV line. To reduce its intensity, we added an additional branch out of the isomer: a 29 keV E1 transition, that feeds the $21/2^-$ member of the $11/2^-$ band (see the decay scheme of scenario 3 in fig. 5.39a). As a test we gave 50 % gamma emission branching to each of the 2 E1 transitions. With these ingredients, a reduction of the 170 keV intensity is observed, but at the cost of extra lines, which are not visible in the experimental spectrum and which correspond to the additional M1 and E2 crossover transitions at 141 and 264 keV. Thus, this decay scenario was ruled out as well.

Since none of the above three decay schemes reproduced our experimental γ-ray spectrum, we then supposed that the $19/2^+$ isomer decays to both the ground state band and the $11/2^-$ band. This time, we changed the moment of inertia factor to be $\frac{\hbar^2}{2\mathcal{J}}$ = 5.8 for the ground sate band, resulting in a 64 keV energy spacing between the $11/2^-$ and $9/2^-$ states. This spacing is the same as the one observed in ^{253}No. The moment of inertia for the $11/2^-$ band was kept the same as the obtained rotational sequence is in line with the $11/2^-$ band observed in ^{257}Rf [168]. To fit the high-energy lines, the $11/2^-$ band has to be pushed up to 632 keV, which is slightly higher than what was inferred from α spectroscopy. The decay scheme is shown in fig. 5.40a and the comparison of the simulation result is shown in fig. 5.40b. The ingredients for simulating this decay scheme are given in table 5.23 and 5.24. We notice that we can reproduce more or less all the gamma lines except for the LX rays, which could be due to the contribution of the $5/2^+$ spin isomer neglected in this decay scheme. The confidence in this decay scenario also increases from the comparison of the E_{max} of iso2 in fig. 5.41a.

Now if we look at the simulated e- spectrum in fig. 5.41b, we see clearly a deficit of counts in the simulated spectrum around 110 keV. To make this comparison we have simply scaled the detected e- spectra from each isomeric decay by the same scaling factors used for the 778 keV and 102 keV peaks. Most contributions from both isomeric decays appear on the low-energy side of the experimental spectrum and are cut due to the threshold in the tunnel detectors. If we argue that the scaling factors applied to the γ-ray spectra do not apply to the simulated e- spectra and scale them up so as to reproduce the excess counts

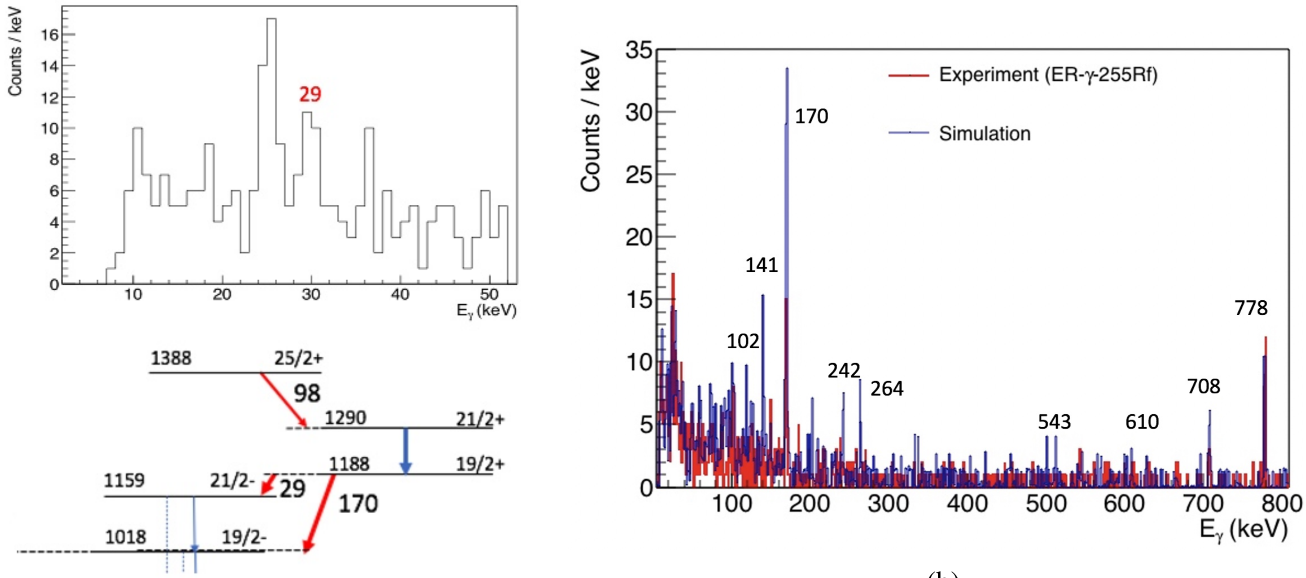

(a)

(b)

Figure 5.39: Scenario 3: a) Decay scheme (bottom) and a zoomed part of experimental γ-ray spectrum (top) b) simulated γ ray spectrum with added experimental background.

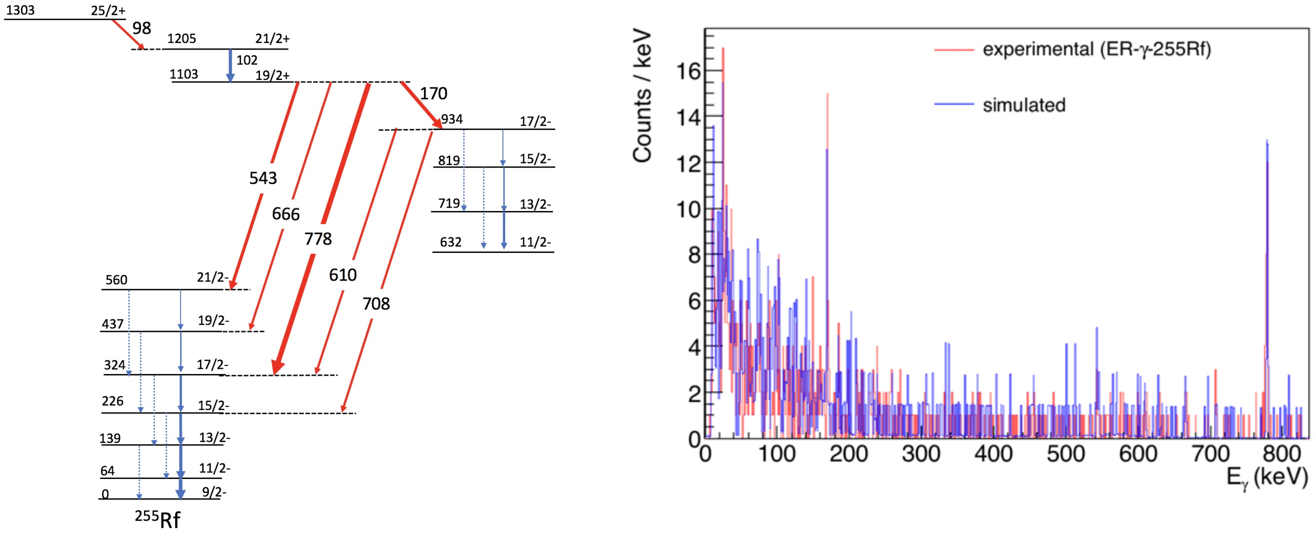

(a)

(b)

Figure 5.40: Scenario 4: a) Decay scheme (bottom) and a zoomed part of experimental γ-ray spectrum (top) b) simulated γ-ray spectrum with added experimental background.

at ~110 keV , then extra strength appears above 150 keV, which is not observed in the experiment (see fig. 5.42a). Therefore, we conclude that the excess counts in the tunnel spectrum comes from the decay of the $5/2^+$ isomer, which is expected to be populated in the fusion evaporation reaction but whose contribution could not be disentangled on the basis of lifetimes, since all 3 isomers have very similar lifetimes. The excitation energy which best fits the excess counts puts the isomer at en excitation energy of 145 keV, just below the K binding energy for Rf, which explains the lack of KX rays observed by GSI. After adding the contribution from the $5/2^+$ state, the shape and intensity of the experimental e- spectrum can be reproduced

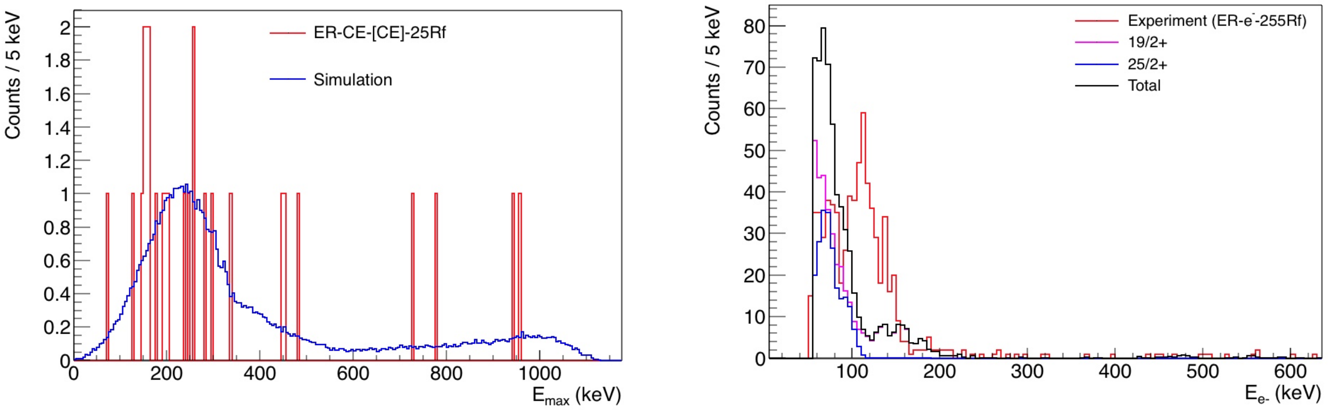

(a) (b)

Figure 5.41: a) E_max of the in the decay from 19/2$^+$ isomer b) Comparison of e- spectra, where the contribution from each of the isomeric decays are shown.

as shown in fig. 5.42b as well as the missing LX rays are recovered (see fig. 5.42c).

So far, we have used an average threshold of 80 keV and scaled the simulated γ-ray and e- spectra to fit the experimental ones. We know that the DSSD threshold is between $\sim 60-100$ keV, and depending on the chosen threshold we will have to adjust the scaling factors. This however, will not affect our conclusions.

To reproduce the CE spectrum and estimate the isomer population numbers, the correct threshold needs to be taken into account as well as the dead time associated with the implantation detector. In table 5.25 the fraction of the CE spectrum which lies below or above the two threshold extremes of 60 and 100 keV are reported for each isomer, together with the fraction of the decays, which occur during the 32 μs dead time or after it assuming $T_{1/2}(25/2^+)$= 49 $^{+13}_{-10}$ µs, $T_{1/2}(19/2^+)$ = 28.6$^{+7.5}_{-4.9}$ µs from this work and $T_{1/2}(5/2^+)$ = 50(2) µs from the GSI result.

Let us denote the number of isomers populated during the experiment by N_1, N_2 and N_3 respectively.

Spin (I)	E* (keV)	E(ΔI = 1)	E(ΔI = 2)	B(M1)/B(E2)	δ	$br_\gamma(\Delta I = 1)$	$br_\gamma(\Delta I = 2)$	α_{mixed}	$\alpha(E2)$
9/2$^-$	0	-	-	-	-	-	-	-	-
11/2$^-$	64	64	-	0.0467	0.247	100		73.2133	
13/2$^-$	139	75	139	0.066	0.244	100	18.9	43.1705	8.461
15/2$^-$	226	87	162	0.088	0.244	100	41.6	26.8149	4.393
17/2$^-$	324	98	185	0.114	0.242	100	70.16	18.4114	2.535
19/2$^-$	437	113	211	0.143	0.249	100	100	11.9013	1.503
21/2$^-$	560	123	236	0.175	0.246	68	100	9.1758	0.9823
11/2$^-$	632	-	-	-	-	-	-		
13/2$^-$	719	87	-	0.063	0.288	100	-	27.7954	
15/2$^-$	819	100	187	0.085	0.286	100	21	17.7325	2.427
17/2$^-$	934	115	215	0.109	0.29	2.2	4.9	11.4502	1.398
19/2$^+$	1103	-	-	-	-	-	-		
21/2$^+$	1205	102	-	-	-	100	-	15.2	
25/2$^+$	1303	102	-	-	-	-	-		

Table 5.23: Calculated transition energies, B(M1)/B(E2) ratios in $(\mu_n/eb)^2$, mixing ratios δ, relative gamma emission branching ratios and internal conversion coefficients for the M1 and E2 Intra band transitions from states (Spin I) having excitation energies (E* in keV). In the cases where δ is not given α_{mixed} is the internal conversion coefficient of M1 transition α_{M1}.

transition	E (keV)	σ	br_γ	α
$25/2^+ \rightarrow 21/2^+$	98	E2	100	41.43
$19/2^+ \rightarrow 17/2^-$	170	E1	27	0.1754
$19/2^+ \rightarrow 21/2^-$	543	E1	32	0.01699
$19/2^+ \rightarrow 19/2^-$	666	E1	27	0.01186
$19/2^+ \rightarrow 17/2^-$	778	E1	100	0.009068
$17/2^- \rightarrow 17/2^-$	610	M1	77	0.4192
$17/2^- \rightarrow 15/2^-$	708	M1	100	0.279
$11/2^- \rightarrow 9/2^-$	632	M1	100	0.3805

Table 5.24: Table of inter band transitions of multipole character σ with relative gamma emission branching ratios br_γ and internal conversion coefficients α.

We shall denote the fractions for each isomer given in table 5.25 by a subscript corresponding to the isomer index number. As discussed before, the detection of 2 CEs can be viewed as iso1 feeding iso2 and the CEs in both decay steps were detected. So, the number of observed (27) ER-CE-CE-^{255}Rf correlations can be

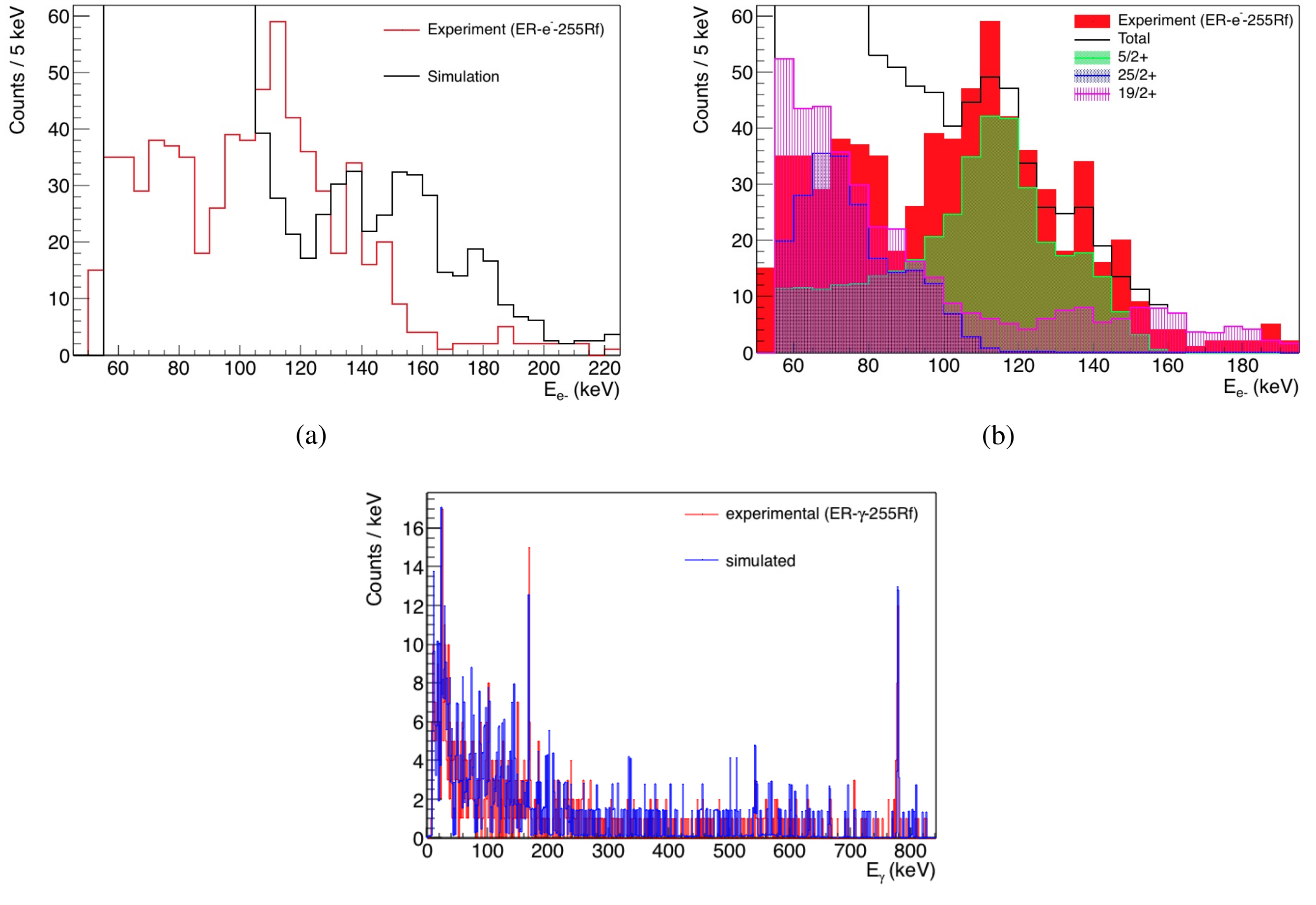

(a)

(b)

(c)

Figure 5.42: Simulated tunnel spectrum a) of iso1 + iso2 when scaled by 4, b) after including $5/2^+$ isomeric decay. c) γ-ray spectrum after adding $5/2^+$ isomer's contribution. Note that the missing LX rays in fig. 5.41b are recovered.

Isomer no.	spin parity	alive %	dead %	< 60 keV (%)	> 60 keV (%)	< 100 keV (%)	> 100 keV (%)
1	$25/2^+$	63.6	36.4	24.1	75.9	44.9	55.1
2	$19/2^+$	46	54	2.6	97.4	9.9	90.1
3	$5/2^+$	64.2	34.8	53.7	46.3	61.3	38.7

Table 5.25: Fractions of isomers that would not be detected (dead), detected (alive) because of the deadtime associated with the ADCs of the implantation DSSD. The fractions of the CE spectra below (<) and above (>) the 60 keV and 100 keV thresholds were obtained from simulations.

written as:

$$(N_1 \times (alive_1 \times aboveTH_1)) \times (alive_2 \times aboveTH_2) = 27 \tag{5.10}$$

Using the fractions given in table 5.25 we obtain $N_1 = 125(24)$ for 60 keV threshold and $N_1 = 186(36)$ for 100 keV threshold.

We can estimate the population number N_2 from the ER-CE-^{255}Rf correlations. However, when only 1 CE is detected there are multiple factors to consider as the spectrum has contribution from all 3 isomer populations. The total number (701) of ER-CE-^{255}Rf can then be expressed as:

$$\begin{aligned} N_1 \times (alive_1 \times aboveTH_1) \times (dead_2 + alive_2 \times belowTH_2) \\ +N_1 \times (dead_1 + alive_1 \times belowTH_1) \times (alive_2 \times aboveTH_2) \\ +N_2(alive_2 \times aboveTH_2) \\ +N_3 \times (alive_3 \times aboveTH_3) = 701 \end{aligned} \tag{5.11}$$

This however requires an estimation of the N_3 population of the $5/2^+$ isomer. We pointed out before that in the e- spectrum for ER-γ/e-^{255}Rf correlations there is a deficiency in the intensity without the consideration of $5/2^+$ isomer. From this deficiency we can extract a scaling factor (SF_3) that would give an estimation of N_3 from the following simple relation:

$$N_3 = SF_3 \times N_{sim} \times (dead_3 + alive_3 \times belowTH_3) \tag{5.12}$$

where N_{sim} is the number of simulations, in this case $N_{sim} = 10^5$. The scaling factor SF_i is the simple ratio of the counts (n) of e- in the energy range from 95 keV to 160 keV (where the deficiency is observed) and can be expressed as

$$SF_3 = \frac{n_{exp} - (n_{sim}(iso1) \times SF_1 + n_{sim}(iso2) \times SF_2)}{n_{sim}(iso3)} \tag{5.13}$$

where $n_{sim}(isoi)$ is the simulated total counts in the e- spectra from isomer i including deadtime and threshold effects.

The scaling factors SF_1 and SF_2 can be obtained by comparing simulated and experimental gamma ray intensities of the 778 keV peak for iso2 and the 102 keV peak for iso1 since according to our decay scheme the 102 keV peak is only due to decays of iso1. The 778 keV peak however, has two possible sources: N_1 isomeric decays when none of the CEs in the cascade are detected and N_2 isomeric decays in which case as well the CEs are not detected. With the obtained scaling factors for iso1 and iso2 we could extract $N_3 = 1171(79)$ for 60 keV threshold and $N_3 = 1265(86)$ for 100 keV threshold.

Knowing the populations N_1 and N_3 we can deduce the N_2 isomeric population from equation 5.11. The obtained values are $N_2 = 649(79)$ and 721(87) for 60 and 100 keV thresholds respectively. These numbers can in turn be translated into the following isomeric ratios: 1.9(4) % for the $25/2^+$ isomer, 8.7(1.1) % for the $19/2^+$ isomer and 15.4(1.2) % for the $5/2^+$ isomer. Although, these numbers suffer from uncertainties due to uncertainties in the deadtime and the thresholds, they are consistent with known populations of low-lying 1 quasiparticle and 3 quasiparticle states. The difference in isomeric ratios of the 2 high-K isomers may reflect the average spin populated in the reaction [195]. The comparison between the experimental and simulated CE spectra is given in fig. 5.43. The goodness of the reproduction of all the experimental spectra gives confidence in the main features of the decay scheme shown in fig. 5.44 and the proposed structure of the high-K isomers, which is in line with what is known in heavier Rf isotopes.

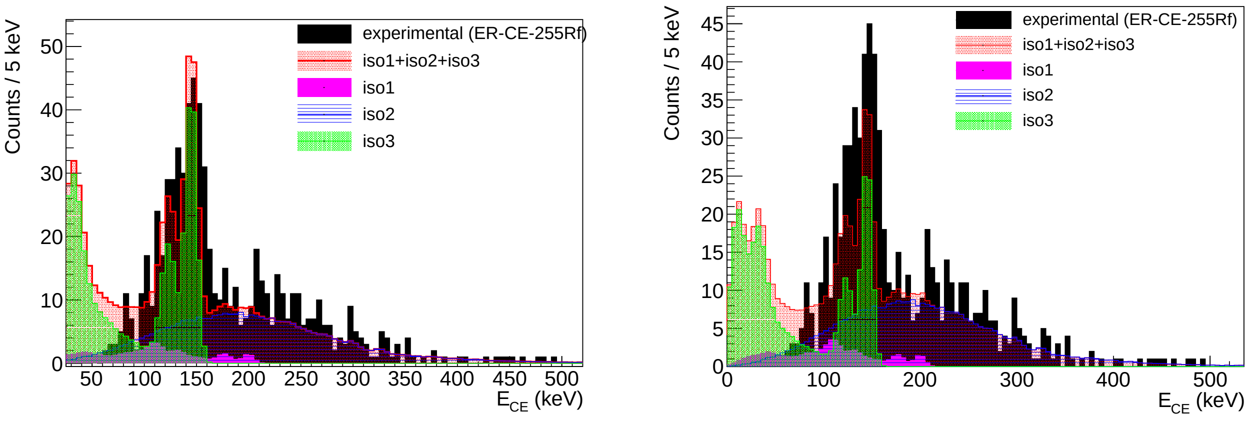

(a)

(b)

Figure 5.43: Comparison of the experimental CE spectrum with simulations showing the contributions of all 3 isomers for a) 60 keV and b) 100 keV thresholds.

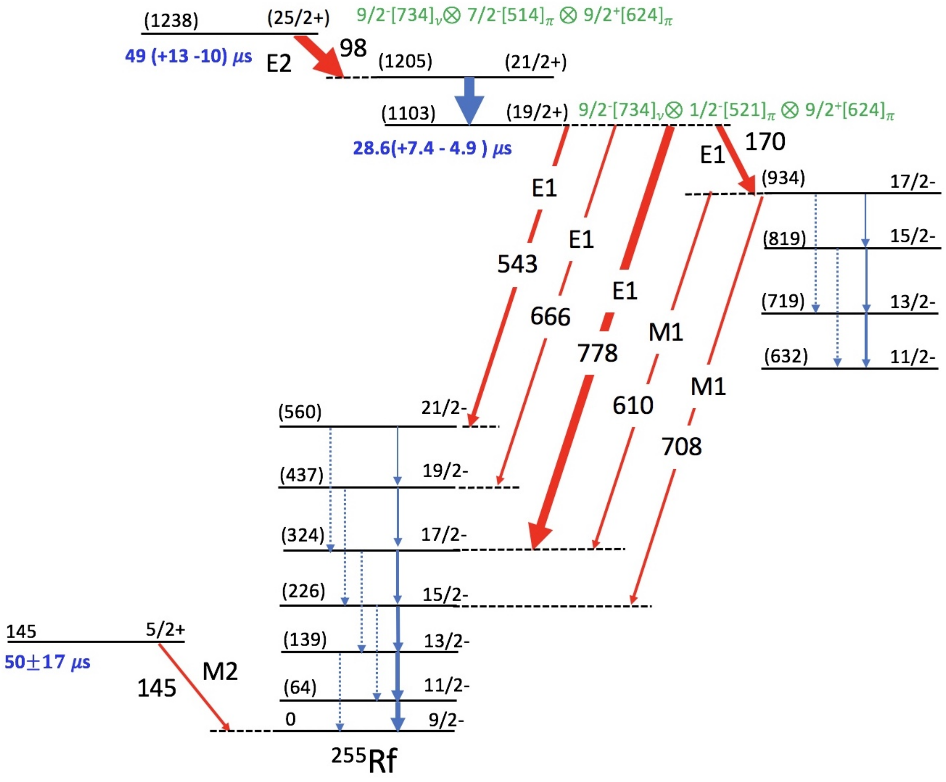

Figure 5.44: Proposed partial level scheme for ^{255}Rf.

Chapter 6

Conclusions and Perspectives

In this work, we have introduced the current configuration of the GABRIELA detection system. Using GEANT4 simulations the gamma-ray and electron detection efficiencies of this configuration have been presented. An overall increase in performance is observed compared to its previous version. We have validated the simulated efficiency curves using data from a calibration run, demonstrating that the geometry constructed in the GEANT4 code is accurate and can hence be reliably incorporated in the analysis and interpretation of experimental data. It was also demonstrated how simulations may be used to estimate the implantation depth of the evaporation residues in the implantation detector, which is crucial for determining correctly the electron detection efficiency.

It has been shown that due to summing effects, the extraction of the absolute detection efficiency is quite challenging even for cascades of only two transitions. With an increasing number of coincident transitions, as can be the case, for example, in the decay of a high K isomer or of high-energy excited states populated by alpha decay, performing a similar correction procedure may not be straightforward and can be quite cumbersome, especially since the transitions involved may not be pure or of unknown electromagnetic character. It would be erroneous to establish decay schemes based solely on the gamma-ray and conversion electron efficiency-corrected intensities. Since the internal conversion process becomes the dominating decay mode in the heavy region, more summing is expected due to atomic relaxation processes, as a result, making the study of heavy nuclei difficult. Thus, in a compact and efficient spectrometer such as GABRIELA, it is imperative to perform simulations and compare with the experimental results in order to establish decay properties of heavy nuclei. A paper based on our work on the characterization of the GABRIELA spectrometer has recently been accepted in EPJ A for publication. This characterization was essential for interpretation of the experimental results and represents a large part of this thesis work.

In this study, we have demonstrated that a proper estimation of the implantation depth profile of the evaporation residues in a detector is crucial especially for conversion electron spectroscopy and introduced a novel technique to make such an estimation. For this work, we have extended the Geant4 simulation code up to Rutherfordium. The code should be extended even further, so that it can be implemented in the studies of other superheavies. Using this simulation tool, we have interpreted fine structure in the α decay of ^{255}Rf establishing branching ratios to some known and new levels in ^{251}No. It has also allowed us to extract some measurable quantities namely, relative gamma emission branching ratios and internal conversion coefficients for transitions observed in ^{251}No. The established properties of the ground state decay of ^{255}Rf have confirmed the GSI work and show that the decay of ^{255}Rf follows the systematics of the lighter isotones i.e., there is no change in the structure of the ground state of N = 151 isotones as Z increases. The next isotone is ^{257}Sg, which could be produced with a ^{54}Cr beam on ^{204}Pb target. No spectroscopic data exists for this nucleus and the cross-section is expected to be $\sim$ 0.2 nb (a factor of 10 less than ^{255}Rf). This requires a high intensity Cr beam, which is currently being developed by the IPHC and will be used in Dubna and also at SPIRAL2 at S3 [196].

We have firmly established the existence of at least 3 isomeric states in ^{255}Rf: the expected $5/2^+[622]_\nu$ spin isomer present in the systematics of the lighter isotones and two high-K states most likely built on the $\{9/2^-\,[734]_\nu \otimes 1/2^-\,[521]_\pi \otimes 9/2^+\,[624]_\pi\}$ and the $\{9/2^-\,[734]_\nu \otimes 7/2^-\,[514]_\pi \otimes 9/2^+\,[624]_\pi\}$ configurations yielding states with K^π=19/2$^+$ and 25/2$^+$. The proposed decay scheme reproduces all of our experimental results. The fact that the 2 quasi-proton configurations explain the data suggest that the quasi-neutron states are higher in energy. This in turn implies that the N= 152 gap persists in ^{255}Rf. Although, there are some uncertainties in the energy of the E2 transition transition deexciting the 25/2$^+$ isomer (corresponding to a very large hindrance), the exact decay scheme to the 19/2$^+$ does not modify our conclusions since it is constrained by the energy E_{max} removed in the cascade. A χ^2 minimization technique, as was performed for the study of the alpha decay of the ground state of ^{255}Rf, could be performed to extract the branching ratios of the transitions from the 19/2$^+$ isomer and also to deduce the excitation energy of the 25/2$^+$ isomer. The proposed decay scheme should also be confirmed by better data. In particular, the prompt character of the high energy transitions could be ascertained by performing prompt spectroscopy at the target for ^{255}Rf. This could be attempted using JUROGAM at RITU in Jyväskylä. However, as the cross section is low and the flux is fragmented such an experiment will probably require the next-generation gamma-ray spectrometer such as AGATA [197].

Regarding the ground state decay of ^{255}Rf to the $5/2^+[622]_\nu$ state in ^{251}No, so far, we have assumed the excitation energy of the 5/2$^+$ to be above the K-shell binding energy of nobelium. This study should be revisited by placing it below the K binding. This could lower the conversion coefficient measured for the 143 keV transition and better reproduce the shape of the e- spectrum around 130 keV. This might however be a challenging task to find the correct balance between the feeding to the 5/2$^+$ and the conversion coefficients for the 143 keV transition. Artificial Intelligence methods applied to GEANT4 simulation might be the way forward.

This work has suffered from many electronics limitations such as, deadtime, high thresholds, multiplexing, cross-talk. FIFO buffers that are utilized in current experiments were not present in the experiments related to this work. Such buffering of the ADC data could have lowered the deadtime of the ADCs significantly allowing better measurements of lifetimes, especially for the short-lived isomer. By lowering the density of connectors with better grounding could reduce the cross-talk problems. Regarding the punch-through problem in the clover detector, the use of a veto detector is envisaged in future experiments.

To resolve the experimental challenges faced with the current version of GABRIELA, many upgrades will be introduced in the next version. For instance, the Ge array will consist of only clover detectors, digital electronics will be implemented in place of analog electronics. The replacement of the tunnel detectors with thicker silicon detectors instrumented with very low noise electronics is also planned in the framework of the SHEXI project. These detectors will allow high resolution LX-ray and conversion electron spectroscopy.

In superheavy studies, statistics is the biggest hurdle as the production cross-section of these nuclei is very low. Hence, it demands the development of effective data analysis and experimental techniques for identifying these rare events. To this end, particle X-ray coincidence measurements coupled with simulations can be very useful in identifying the atomic number of rarely produced superheavy nuclei. It would be also very interesting to incorporate machine learning techniques for identification of rare events in the pre-processing pulse shape analysis phase and find correlations in the events in post-processing data analysis phase. The world is becoming data-driven day by day, and machine learning will definitely change the current approach of scientific research in the future by becoming an integral tool for analyzing data and also to predict new phenomena.

Appendix A

Lifetime measurement method

If N_0 is the number of nuclei produced in a given state, the number of decays per unit is given by

$$\frac{dN(t)}{dt} = N_0 \lambda \exp(-\lambda t) \tag{A.1}$$

where λ is the decay probability per unit time. By using a change of variable $\theta = \ln t / \ln 2$ equation A.1 becomes:

$$\frac{dN(\theta)}{d\theta} = \frac{N_0}{\tau} \times \ln 2 \times 2^{\theta} \exp\left(-\frac{2^{\theta}}{\tau}\right) \tag{A.2}$$

This representation yields a peak in the time distribution at θ_{max}, which is related to the lifetime τ by $\tau = 2^{\theta_{max}}$.

In the case where 2 decays give rise to the observed time distribution, it can be fitted by the expression:

$$\frac{dN(\theta)}{d\theta} = \frac{N_0}{\tau_1} \times \ln 2 \times 2^{\theta} \exp(-2^{\theta}(\frac{1}{\tau_1} + \frac{1}{\tau_2})) + \frac{N_0}{\tau_2} \times \ln 2 \times 2^{\theta} \exp\left(-\frac{2^{\theta}}{\tau_2}\right) \tag{A.3}$$

In the event of low statistics, the K.H. Schmidt [192] approach was adopted to estimate the errors. The method is described briefly below: The arithmetic mean of the individual observed lifetimes is:

$$\bar{t_m} = \frac{1}{n} \sum_{i=1}^{n} (t_m)_i \tag{A.4}$$

For $n \geq 2$, the upper and lower limit of the lifetime τ for a given confidence level $(1 - \varepsilon)$ are:

$$\tau_{upper} \approx \frac{\bar{t_m}}{1 - z/\sqrt{n}} \tag{A.5}$$

$$\tau_{lower} \approx \frac{\bar{t_m}}{1 + z/\sqrt{n}} \tag{A.6}$$

where, the quantity z is related to the confidence level by

$$\frac{\varepsilon}{2} = \int_{z}^{\infty} \frac{1}{\sqrt{2\pi}} e^{-x^2/2} dx = \frac{1}{2} erfc(\frac{z}{\sqrt{2}}) \tag{A.7}$$

Choosing, a confidence level of $(1 - \varepsilon) = 0.68$

$$efrc^{-1}(\varepsilon) = \frac{z}{\sqrt{2}}$$

$$z = \sqrt{2} \times 0.7032 = 0.9945 \approx 1$$

Appendix B

Brief explanation of the GEANT4 data formats

B.1 Fluorescence and Auger

The fluorescence data files containing radiative transition probabilities and corresponding transition energies (obtained from the Atomic Relaxation Data, EADL) are in the ‘fluor’ directory. The naming format of these files is "fl-tr-pr-NN.dat" where NN represents the atomic number. In every file, there are three columns. A section of the Z = 100 file is in fig. B.1a as an illustration. In a file, each data set corresponding to a vacancy subshell starts with a line of its ENDL designator (see table B.1) and separated from other vacancy shell data set by a -1 line. In the intermediate lines that represent the transitions filling the vacancy, the first column gives the subshell from where the transition occurs with a probability given in the second column and the transition energy in MeV given in the third column.

For non-radiative processes, the Auger and Coster-Kronig informations are in the auger files that are named "au-tr-pr-NN.dat" and located in the ‘auger’ directory where similarly NN represents the atomic number. Each data file has four columns with every initial subshell vacancy data set starting with a vacancy subshell index line and terminating by a -1 line (see fig. B.1b). For each transition, the first column points to the electronic shell from where the relaxing electron originates that fill the current vacancy. The second column indicates the subshell from where an Auger electron gets emitted with a probability given in the 3rd column and energy value given in MeV in the 4th column.

For any initial vacancy, the sum of all the radiative and non-radiative probabilities is unity.

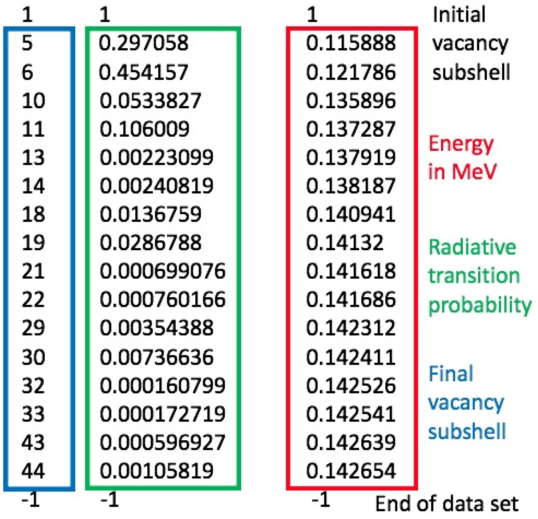

```
1     1              1
5     0.297058       0.115888
6     0.454157       0.121786
10    0.0533827      0.135896
11    0.106009       0.137287
13    0.00223099     0.137919
14    0.00240819     0.138187
18    0.0136759      0.140941
19    0.0286788      0.14132
21    0.000699076    0.141618
22    0.000760166    0.141686
29    0.00354388     0.142312
30    0.00736636     0.142411
32    0.000160799    0.142526
33    0.000172719    0.142541
43    0.000596927    0.142639
44    0.00105819     0.142654
-1    -1             -1
```

(a) Radiative transition

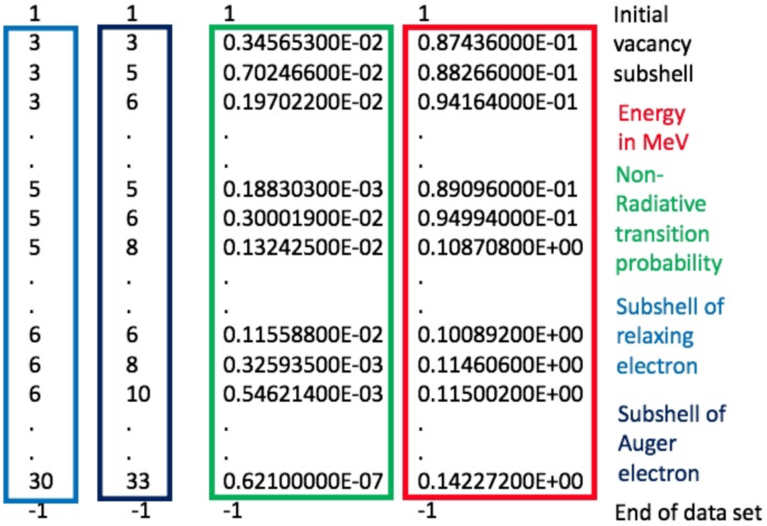

```
1     1     1                  1
3     3     0.34565300E-02     0.87436000E-01
3     5     0.70246600E-02     0.88266000E-01
3     6     0.19702200E-02     0.94164000E-01
.     .     .                  .
.     .     .                  .
5     5     0.18830300E-03     0.89096000E-01
5     6     0.30001900E-02     0.94994000E-01
5     8     0.13242500E-02     0.10870800E+00
.     .     .                  .
.     .     .                  .
6     6     0.11558800E-02     0.10089200E+00
6     8     0.32593500E-03     0.11460600E+00
6     10    0.54621400E-03     0.11500200E+00
.     .     .                  .
.     .     .                  .
30    33    0.62100000E-07     0.14227200E+00
-1    -1    -1                 -1
```

(b) Non-Radiative transition

Figure B.1: (a) Fluorescence and (b) Auger data formats in GEANT4 for Z =100.

B.2 Radioactive decay

Radioactive decays in Geant4 require two input data files to instruct Geant4 to simulate the desired decay scheme. The excitation energy defined for the primary particle in the user-defined PrimaryGeneratorAction class must be consistent with the energy level scheme of the isotope provided in the photon-evaporation file. The radioactive decay data files in the format zXX.aYYY (XX gives the atomic number and YYY, the mass number) are found in the directory "RadioactiveDecayV" with V the version number. The environment variable "G4RADIOACTIVEDATA" points to this directory. A user-defined decay data file can be supplied to Geant4, and it is this special feature of Geant4 was exploited to test different decay schemes. An example of the radioactive-decay data file is shown in the top part of fig. B.2. The lines beginning with # are comments. The headers of each decay mode from a given level are given by lines beginning with a ‘P’ indicates that the given level is a metastable state of the nucleus. The first number after P is the

Designator	Subshell	Designator	Subshell	Designator	Subshell
1	K (1s1/2)	21	N4 (4d3/2)	41	P1 (6s1/2)
2	L (2)	22	N5 (4d5/2)	42	P23 (6p)
3	L1 (2s1/2)	23	N67 (4f)	43	P2 (6p1/2)
4	L23 (2p)	24	N6 (4f5/2)	44	P3 (6p3/2)
5	L2 (2p1/2)	25	N7 (4f7/2)	45	P45 (6d)
6	L3 (2p3/2)	26	O (5)	46	P4 (6d3/2)
7	M (3)	27	O1 (5s/2)	47	P5 (6d5/2)
8	M1 (3s1/2)	28	O23 (5p)	48	P67 (6f)
9	M23 (3p)	29	O2 (5p1/2)	49	P6 (6f5/2)
10	M2 (3p1/2)	30	O3 (5p3/2)	50	P7 (6f7/2)
11	M3 (3p3/2)	31	O45 (5d)	51	P89 (6g)
12	M45 (3d)	32	O4 (5d3/2)	52	P8 (6g7/2)
13	M4 (3d3/2)	33	O5 (5d5/2)	53	P9 (6g9/2)
14	M5 (3d5/2)	34	O67 (5f)	54	P1011 (6h)
15	N (4)	35	O6 (5f5/2)	55	P10 (6h9/2)
16	N1 (4s1/2)	36	O7 (5f7/2)	56	P11 (6h11/2)
17	N23 (4p)	37	O89 (5g)	57	Q (7)
18	N2 (4p1/2)	38	O8 (5g7/2)	58	Q1 (7s1/2)
19	N3 (4p3/2)	39	O9 (5g9/2)	59	Q23 (7p)
20	N45 (4d)	40	P (6)	60	Q2 (7p1/2)
				61	Q3 (p3/2)

Table B.1: ENDL Atomic subshell designators

excitation energy in keV of the level from where the radioactive decays occur. The character following the energy represents the floating level. The "-" character indicates that the level is fixed. If the level is undetermined or floating characters such as +X, +Y, +Z, +W, +U, and +V are used. Next, the half-life of the nucleus is given in seconds. The indented lines under the 'P' lines are decay modes for that excitation. The lines with only three columns are the headers describing the total strengths of each type of decay from this level. In these lines, the first element states the decay mode, the second entry is set to always zero, the third entry is the total branching ratio of the decay mode. Therefore, for a given P line, the sum of all the elements in the third column should be 1. Following these header lines, there are lines with five or six entries (for beta decay). These lines describe how the daughter levels are populated from each decay type. In each line, the first column is the type of decay that populates the level with excitation level (keV) of the daughter specified by the second entry and its floating-level by the third entry. The branching ratio to this level is given in percentage in the fifth entry. The sixth entry is used only in the case of beta decay to describe the forbiddenness of that particular decay channel.

The instructions for the nuclear deexcitation process are provided in a photon-evaporation data file. The format of this file is illustrated in the bottom of fig. B.2 for a simple level scheme. The file for a given isotope is arranged as per the energy states in the level scheme with the possible gamma transitions emanating from each level to the lower levels. An energy level defining line contains six entries starting with an index integer number to identify the order of the state compared to the ground state whose index number is 0 by definition. The floating level of the state is identified with a string (-,+X,+Y,+Z,+U,+V,+W,+R,+S,+T,+A,+B,+C). The next entry gives the excitation energy of the level (keV) followed by the half-life in sec. For a stable ground state, the half-life is -1. Then follows the spin and parity of the level with the sign of the value corresponding to the parity sign. The final entry of the line is an integer "n" for the number of gamma transitions from the level. Below each level defining line, there is a series of n lines for n transitions. The first entry of each transition line is the order number of the state to which the gamma transition occurs. Next is the transition energy (keV), then the relative gamma emission intensity, then an integer that defines the multipolarity. For a pure transition, the integer takes value 0,1,2,3,4,5,6,7,... corresponding to an unknown multipolarity, E0, E1, M1, E2, M2, E3, M3,... respectively. For a mixed transition, the integer has the form 100×X+Y, with X and Y, representing the integers of the multipolarities involved in mixing. For example, for an M1+E2 mixed transition, the integer is 304. Following the multipolarity number is the mixing ratio. Then, the total internal conversion coefficient and the partial conversion probabilities from K-shell to N+ shells (the outer shells).

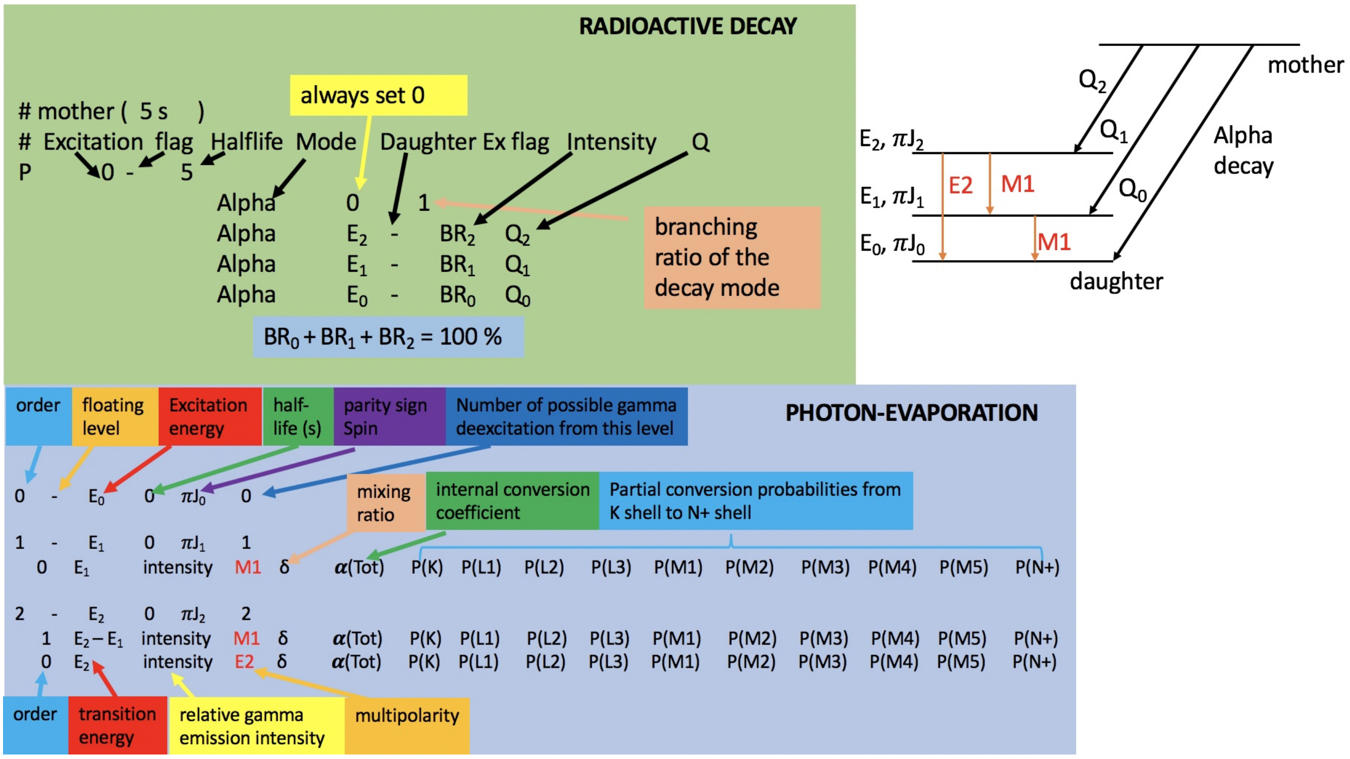

Figure B.2: Radioactive decay in GEANT4

Appendix C

GEANT4 EM Physics lists after the modifications in the source code

There are several built-in EM physics lists and models for certain physics processes that can no longer be employed in a simulation involving the primary particle to be $Z > 100$ after the modifications in the GEANT4 source code. It is because there are certain models such as G4LowEPComptonModel, G4LivermoreComptonModel that rely on data not extended for $Z > 100$. When the primary particle is an $Z > 100$ ion, the change in the Z limits in source code prompts suspension of the program because of a lack of data. Table C.1 and C.2 tabulate the built-in EM physics lists that can and cannot be used.

One can also build one's own EM class by excluding the models that do not support $Z > 100$. In the simulations of this work, the Penelope EM Physics list with some changes was used. These modifications are tabulated in table C.3. The first parameter in the SetStepFunction is $\frac{dR}{Range}$, where dR is the step size in which the energy-dependent cross-sections of interactions remain the same and the second parameter is the final range, the limit of dR. For accurate simulation, it is necessary to have smaller steps at the cost of increased computing time. The reliability of the interaction models and the tracking algorithms implemented in the PENELOPE simulation code in the energy range from a few keV up to 1 GeV was confirmed in ref. [198].

The reproduction of the Bragg peak of an alpha particle from a well-known alpha emitter is a good test for the physics list. To this end, alpha particles with 5.48 MeV energy (that of ^{241}Am alpha-particle energy) impinging into a silicon block of dimension $600 \times 600 \times 100$ µm placed perpendicular to the beam direction were simulated. The Silicon block has 400 segmented layers of equal thickness of 0.25 µm in the z-direction. The energy loss by the ionizing alpha particles during its travel through each segment gives

c1	c2
G4EmStandardPhysics_option4	G4EmStandardPhysics_option1
G4EmLivermorePhysics	G4EmStandardPhysics_option2
G4EmLowEPPhysics	G4EmStandardPhysics_option3
	G4EmStandardPhysics
	G4EmStandardPhysicsGS
	G4EmStandardPhysicsSS
	G4EmStandardPhysicsWVI
	G4EmPenelopePhysics

Table C.1: Built-in EM physics lists that can (c1) and cannot (c2) be used.

EM process	c1	c2
Photo-electric effect	G4PolarizedPEEffectModel	G4PEEffectFluoModel G4LivermorePhotoElectricModel G4LivermorePolarizedPhotoElectricModel G4PenelopePhotoElectricModel
Compton scaterring	G4LivermoreComptonModel G4LivermorePolarizedComptonModel G4LowEPComptonModel G4LivermoreComptonModelRC*	G4KleinNishinaCompton G4KleinNishinaModel G4PenelopeComptonModel G4PolarizedComptonModel
Gamma conversion	G4BetheHeitler5DModel*	G4BetheHeitlerModel G4PairProductionRelModel G4LivermoreGammaConversionModel G4BoldyshevTripletModel G4LivermoreNuclearGammaConversionModel G4LivermorePolarizedGammaConversionModel G4PolarizedGammaConversionModel
Rayleigh scattering	G4JAEAElasticScatteringModel*	G4LivermoreRayleighModel G4PenelopeRayleighModel G4LivermorePolarizedRayleighModel
e- ionization	G4PAIModel G4PAIPhotModel	G4PenelopeIonisationModel G4MollerBhabhaModel G4LivermoreIonisationModel G4PolarizedMollerBhabhaModel
μ ionisation		G4MuBetheBlochModel
ion Ionisation	G4LindhardSorensenIonModel* G4AtimaEnergyLossModel*	G4IonParametrisedLossModel G4BetheBlochModel G4BetheBlochIonGasModel G4BraggIonModel G4BraggIonGasModel
eBremsstrahlung	G4PolarizedBremsstrahlungModel*	G4PenelopeBremsstrahlungModel G4SeltzerBergerModel G4eBremsstrahlungRelModel G4LivermoreBremsstrahlungModel

Table C.2: Models that that can (c1) and cannot (c2) be used for $Z > 100$. The models indicated by '*' do not exist in the GEANT4 version used for this work.

particle	before	after
electron and positron	(0.2, 100 µm)	(0.1, 25 µm)
alpha	(0.2, 10 µm)	(0.1, 100 nm)
GenericIon	(0.2, 1µm)	(0.1, 10 nm)
proton and anti-proton	(0.2, 50µm)	(0.1, 100 nm)

Table C.3: Changes in the stepFunction Limit for ionization process made in the Penelope Physics list.

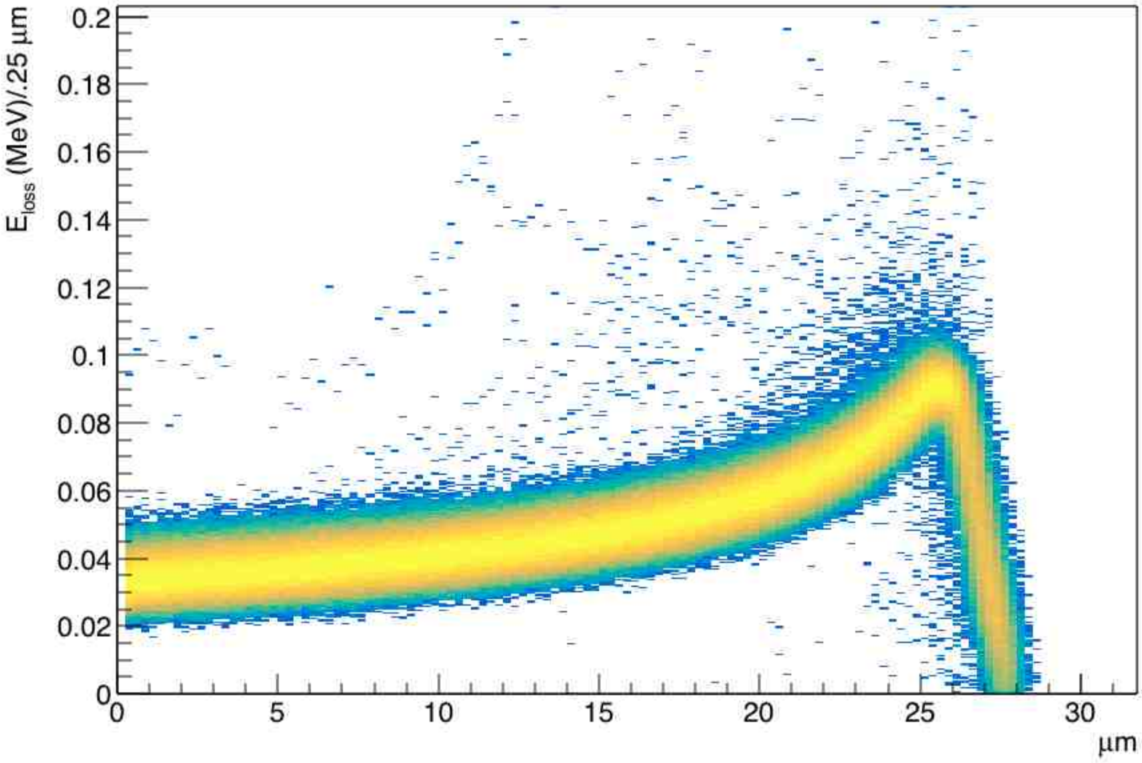

Figure C.1: Energy loss by 5.48 MeV α particles in Si as simulated in GEANT4 using modified Penelope Physics list.

the Bragg curve. Figure C.1 shows the Bragg curves of 10000 events. The mean range obtained from SRIM calculations is in agreement with the value seen in figure C.1.

Bibliography

[1] W. Greiner. Heavy into Stability. *Physics Viewpoint*, 5:115, 2012.

[2] R. Chakma et al. Gamma and conversion electron spectroscopy using GABRIELA. *The European Physical Journal A*, 56:245, 2020.

[3] E. Rutherford. LXXIX. The scattering of α and β particles by matter and the structure of the atom. *The London, Edinburgh, and Dublin Philosophical Magazine and Journal of Science*, 21(125):669–688, 1911.

[4] E. Rutherford. LVII. The structure of the atom. *The London, Edinburgh, and Dublin Philosophical Magazine and Journal of Science*, 27(159):488–498, 1914.

[5] C. Perrier and E. Segrè. Some Chemical Properties of Element 43. *The Journal of Chemical Physics*, 5(9):712, 1937.

[6] C.G. Vayenas and S.N.-A. Souentie. *Gravity, Special Relativity, and the Strong Force: A Bohr-Einstein-de Broglie Model for the Formation of Hadrons*. Springer, Boston, MA, 2012.

[7] M. Schädel and D. Shaughnessy, editors. *The Chemistry of Superheavy Elements*. Springer-Verlag, Berlin Heidelberg, 2nd edition, 2014.

[8] A.H. Wapstra. Criteria that must be statisfied for the discovery of a new chemical element to be recognized. *Pure and Applied Chemestry*, 63(6):879–886, 1991.

[9] Yu.Ts. Oganessian. Superheavy elements. *Physics World*, 19:83–95, 2004.

[10] B. Fricke and W. Greiner. The Continuation of the Periodic Table up to Z = 172. The Chemistry of Superheavy Elements. *Theoretica Chimica Acta (Berl.)*, 21:235–260, 1971.

[11] B. Fricke and G. Soff. Dirac-Forc-Slater Calculations for the ements Z = 100, Fermium ,to Z = 173. *Atomic Data and Nuclear Data Tables*, 19(1):83–95, 1977.

[12] D. Ackermann and Ch. Theisen. Nuclear structure features of very heavy and superheavy nuclei tracing quantum mechanics towards the 'island of stability' . *Physica Scripta*, 92(8):08300, 2017.

[13] R.-D. Herzberg et al. Nuclear isomers in superheavy elements as stepping stones towards the island of stability. *Nature*, 442:896–899, 2006.

[14] S. Hofmann et al. On the discovery of new elements (IUPAC/IUPAP Provisional Report). *Pure and Applied Chemistry*, 90(11):1774, 2018.

[15] A. Sobiczewski et al. Closed shells for Z > 82 and N > 126 in a diffuse potential well. *Physics Letters*, 22(4):500–502, 1966.

[16] W.D. Myers and W.J. Swiatecki. Nuclear masses and deformations. *Nuclear Physics*, 81(1):1–60, 1966.

[17] R.V. Gentry. Giant Radioactive Halos: Indicators of Unknown Radioactivity? *Science*, 169(3946):670–673, 1970.

[18] R.L. Macklin et al. Neutron multiplicity counter. *Nuclear Instruments and Methods*, 102(1):181–187, 1972.

[19] R.W. Stoughton et al. A Search for Naturally Occurring Superheavy Elements. *Nature Physical Science*, 246:26–28, 1973.

[20] R.V. Gentry et al. Evidence for primordial superheavy elements. *Physical Review Letters*, 37(1):11–15, 1976.

[21] P. Hodgson. Discovery of superheavy elements. *Nature*, 26:627, 1976.

[22] C. Stéphan et al. Search for superheavy elements in monazite ore from Madagascar. *Physical Review Letters*, 37(23):1534–1536, 1976.

[23] B.H. Ketelle et al. Search for superheavy-element decay in samples of Madagascar monazite. *Physical Review Letters*, 37(26):1734–1537, 1976.

[24] R. Middleton et al. Upper Limit for the prescence of superheavy elements in monazite from Madagascar. *Physical Review C*, 16(1):477–479, 1977.

[25] R.W. Stoughton et al. Search for superheavy elements in monazites. *Journal of Inorganic and Nuclear Chemistry*, 41:1655–1660, 1979.

[26] N.A. Jelley et al. Search for superheavy elements in monazite by Rutherford backscattering. *Nature*, 265:35–36, 1977.

[27] S.S. Kapoor et al. Search for Superheavy Elements in Monazite from Beach Sands of South India. *Pramāna*, 9(5):515–521, 1977.

[28] Yu.Ts. Oganessian and V.K. Utyonkov. Superheavy nuclei from ^{48}Ca-induced reactions. *Nuclear Physics A*, 944:62–98, 2015.

[29] Z. Patyk and A. Sobiczewski. Ground-state properties of the heaviest nuclei analyzed in an multidimensional deformation space. *Nuclear Physics A*, 533(1):132–152, 1991.

[30] W. Nazarewicz S. Ćwoik and P.H. Heenen. Structure of Odd-N Superheavy Elements. *Physical Review Letters*, 83(6):1108, 1999.

[31] M. Bender, W. Nazarewicz, and P.-G. Reinhard. Shell stabilization of super- and hyperheavy nuclei without magic gaps. *Physics Letters B*, 515(1-2):42–48, 2001.

[32] T.L. Khoo. *private comm.*

[33] Ch. Theisen et al. In-beam spectroscopy of heavy elements. *Nuclear Physics A*, 944:333–375, 2015.

[34] K.-H. Schmidt et al. Gamma-Spectroscopic investigations in the radiative fusion reaction ^{90}Zr+^{90}Zr. *Physics Letters B*, 168:39–42, 1986.

[35] E. Paul et al. In-beam γ-ray spectroscopy above ^{100}Sn using the new technique of recoil decay tagging. *Physical Review C*, 51:78–87, 1995.

[36] M. Asai et al. Nuclear structure of elements with $100 \leq Z \leq 109$ from alpha spectroscopy. *Nuclear Physics A*, 944:308–332, 2015.

[37] K. Hauschild et al. GABRIELA: A new detector array for γ-ray and conversion electron spectroscopy of transfermium elements. *Nuclear Instruments and Methods in Physics Research Section A: Accelerators, Spectrometers, Detectors and Associated Equipment*, 560:388–394, 2006.

[38] A.G. Popeko et. al. Separator for Heavy ELement Spectroscopy – velocity filter SHELS. *Nuclear Instruments and Methods in Physics Research Section B: Beam Interactions with Materials and Atoms*, 376:140–143, 2016.

[39] A. Lopez-Martens et al. Detailed spectroscopy of ^{249}Fm. *Physical Review C*, 74:044303, 2006.

[40] K. Rezynkina et al. Influence of octupole vibration on the low-lying structure of ^{251}Fm and other heavy N = 151 isotones. *Physical Review C*, 97:054332, 2018.

[41] A. Lopez-Martens et al. Isomeric states in ^{253}No. *The European Physical Journal A*, 32:245–250, 2007.

[42] A. Lopez-Martens et al. Spectroscopy of ^{253}No and its daughters. *Nuclear Physics A*, 852:15–35, 2011.

[43] K. Hauschild et al. High-K, $t_{1/2} = 1.4(1)$ ms, isomeric state in ^{255}Lr. *Physical Review C*, 78(2):021302, 2008.

[44] P. Moller et al. Nuclear ground-state masses and deformations: FRDM(2012). *Atomic Data and Nuclear Data Tables*, 109-110:1–204, 2016.

[45] J. Chadwick. The existence of a neutron. *Proceedings of the Royal Society of London A*, 132(303):692–708, 1932.

[46] G. Gamow. Mass defect curve and nuclear constitution. *Proceedings of the Royal Society of London A*, 126(803):632–644, 1930.

[47] C.F.v. Weizsäcker. Zur Theorie der Kernmassen. *Zeitschrift für Physik*, 96:431–458, 1935.

[48] P. Ring and P. Schuck. *The Nuclear Many-Body Problem.* Springer-Verlag, Berlin Heidelberg, 1980.

[49] J.M. Eisenberg and W. Greiner. *NuclearTheory: Nuclear Models.* North-Holland Publishing Company, Amsterdam London, 1970.

[50] D.L. Hill and J.A. Wheeler. Nuclear Constitution and the Interpretation of Fission Phenomena. *Physical Review*, 89(5):1102, 1953.

[51] A. Bohr. The coupling of nuclear surface oscillations to the motion of individual nucleons. *Dan. Mat. Fys. Medd.*, 26(14), 1952.

[52] A. Bohr and B.R. Mottelson. The coupling of nuclear surface oscillations to the motion of individual nucleons. *Mat Fys Medd Dan Vid Selsk*, 27(16), 1953.

[53] X. Wang. *Exotic Collective Excitations at High Spin: Triaxial Rotation and Octupole Condensation*. PhD thesis, University of Notre Dame, Notre Dame, Indiana, December 2007.

[54] A. Bohr and B.R. Mottelson. *Nuclear Structure Volume 2: Nuclear Deformations*. W. A. Benjamin, INC., Reading, Massachusetts, 1975.

[55] R.D. Woods and D.S. Saxon. Diffuse Surface Optical Model for Nucleon-Nuclei Scattering. *Physical Review*, 95(2):577–578, 1954.

[56] C.H. Townes, H. M. Foley, and W. Low. Nuclear Quadrupole Moments and Nuclear Shell Structure. *Physical Review*, 76(9):1415–1416.

[57] J. Rainwater. Nuclear Energy Level Argument for a Spheroida Nuclear Model. *Physical Review*, 79(3):432, 1950.

[58] S.G. Nilsson. Binding states of individual nucleons in strongly deformed nuclei. *Dan. Mat. Fys. Medd.*, 29, 1955.

[59] W. Loveland, D.J. Morrissey, and G.T. Seaborg. *Modern Nuclear Chemistry*. Wiley, Hoboken, New Jersey, 2006.

[60] R.R. Chasman et. al. Survay of single-particle states in the mass region Z > 228. *Review of Modern Physics*, 49(4):833, 1977.

[61] S. Ćwoik, P.H. Heenen, and W. Nazarewicz. Shape coexistence and triaxiality in the superheavy nuclei. *Nature*, 433:705–709, 2005.

[62] S. Ćwoik et al. Shell structure of the superheavy elements. *Nuclear Physics A*, 611(2-3):211–246, 1996.

[63] S. Takahara et al. The role of spin–orbit potential in nuclear prolate-shape dominance. *Physics Letters B*, 702:429, 2011.

[64] P. Stransky et al. On prolate shape predominance in nuclear deformation. *Journal of Physics: Conference series*, 322:012018, 2018.

[65] S. Raeder et al. Probing Sizes and Shapes of Nobelium Isotopes by Laser Spectroscopy. *Physical Review Letters*, 120:232503, 2018.

[66] W.-D. Schmidt-Ott, R.W. Fink, and P.V. Rao. Gamma Radiation in the Decay of ^{249}Cf. *Zeitschrift für Physik A Hadrons and nuclei volume*, 245:191–197, 1971.

[67] D.R. Inglis. Particle Derivation of Nuclear Rotation Properties Associated with a Surface Wave. *Physical Review*, 96(4):1059, 1954.

[68] S.M. Harris. Large-Spin Rotational States of Deformed Nuclei. *Physical Review Letters*, 13(22):663, 1964.

[69] S.M. Harris. Higher Order Corrections to the Cranking Model. *Physical Review*, 138(3B):509, 1965.

[70] M. Goeppert-Mayer. Nuclear configurations in the spin-orbit coupling model. I. Empirical Evidence. *Physical Review*, 78(1):16, 1950.

[71] M. Goeppert-Mayer. Nuclear configurations in the spin-orbit coupling model. II. Theoretical considerations. *Physical Review*, 78(1):22, 1950.

[72] K.L.G. Heyde. *The Nuclear Shell Model*. Springer-Verlag, Berlin Heidelberg, 2nd edition, 1994.

[73] A. Bohr and B.R. Mottelson. The coupling of nuclear surface oscillations to the motion of individual nucleons. *Mat Fys Medd Dan Vid Selsk*, 26(14), 1952.

[74] A. Bohr and B.R. Mottelson. Collective and individual-partice aspects of nuclear structure. *Mat Fys Medd Dan Vid Selsk*, 27(16), 1953.

[75] G.D. Dracoulis, P.M. Walker, and F.G. Kondev. Review of Metastable States in Heavy Nuclei. *Reports on Progress in Physics*, 79(7):076301, 2016.

[76] J.A. Becker et. al. Level spin for superdeformed nuclei near A = 194. *Physical Review C*, 46(3):889, 1992.

[77] V.M. Strutinsky. Shell effects in nuclear masses and deformation energies. *Nuclear Physics A*, 95(2):420–442, 1967.

[78] International Network of Nuclear Structure and Decay Data Evaluators. Evaluated Nuclear Structure Data File.

[79] A.H. Becquerel. Sur les radiations émises par phosphorescence. *Comptes-rendus de l'Académie des science*, 122:420–421, 1896.

[80] A.H. Becquerel. Sur les radiations invisibles émises par les corps phosphorescents. *Comptes-rendus de l'Académie des science*, 122:501–503, 1896.

[81] P. Radvanyi and J. Villian. The discovery of radioactivity. *Comptes Rendus Physique*, 18(9-10):544–550, 2017.

[82] E. Rutherford. VIII. Uranium Radiation and the Electrical Conduction Produced by It. *The London, Edinburgh, and Dublin Philosophical Magazine and Journal of Science*, 47(284):109–163, 1899.

[83] E. Rutherford and T. Royds. XXI. The nature of the α particle from radioactive substances. *The London, Edinburgh, and Dublin Philosophical Magazine and Journal of Science*, 17(98):281–286, 1909.

[84] G. Gamow. Quantum Theory of the Atomic Nucleus. *Zeitschrift für Physik*, 51:204–212, 1928.

[85] R.W. Gurney and E.U. Condon. Wave Mechanics and Radioactive Disintegration. *Nature*, 122:439, 1928.

[86] V.E. Viola and G.T. Seaborg. Nuclear systematics of the heavy elements—II Lifetimes for alpha, beta and spontaneous fission decay. *Journal of Inorganic and Nuclear Chemistry*, 28(3):741 – 761, 1966.

[87] J.O. Rusmussen. Alpha decay. *in Alpha-, beta- and gamma-ray spectroscopy*, pages 701–743, 1965.

[88] G. Royer. Analytic expressions for alpha-decay half-lives and potential barriers. *Nuclear Physics A*, 848:279–291, 2010.

[89] H. Hatsukawa, H. Nakahara, and D.C. Hoffman. Systematics of Alpha Decay Half-lives. *Physical Review C*, 42(2):674, 1990.

[90] B.A. Brown. Simple Relation for Alpha Decay Half-lives. *Physical Review C*, 46(2):811, 1992.

[91] A. Parkhomenko and A. Sobiczewski. Phenomenological Formula for α-Decay Half-lives of Heaviest Nuclei. *Acta Physica Polonica B*, 36(10):3095, 2005.

[92] C.J. Gallagher Jr. and J.O. Rasmussen. Alpha-Decay Hindrance-Factor Calculations. *Journal of Inorganic and Nuclear Chemistry*, 3:333–344, 1957.

[93] M.A. Preston. The Theory of Alpha-Radioactivity. *Physical Review*, 71(12):865–877, 1947.

[94] H.J. Mang. Calculation of α-Transition Probabilities. *Physical Review*, 119(3):1069, 1960.

[95] G. Igo. Optical Model Potential at the Nuclear Surface for the Elastic Scattering of Alpha Particles. *Physical Review Letters*, 1(2):72, 1958.

[96] J.O. Rasmussen. Alpha-Decay Barrier Penetrabilities with an Exponential Nuclear Potential: Even-Even Nuclei. *Physical Review*, 113(6):1593–1598, 1959.

[97] J.O. Rasmussen. Alpha-Decay Barrier Penetrabilities with an Exponential Nuclear Potential: Odd-Mass Nuclei. *Physical Review*, 115(6):1675–1679, 1959.

[98] I. Perlman and J.O. Rasmussen. *Alpha Radioactivity in Kernreaktionen III / Nuclear Reactions III*, pages 109–204. Springer, Berlin, Heidelberg, 1957.

[99] R. Blendowske and H. Walliser. Systematics of Cluster-Radioactivity-Decay Constatnts as suggested by Microscopic Calculations. *Physical Review Letters*, 61(17):1930, 1988.

[100] O. Hahn and F. Strassmann. Über die Entstehung von Radiumisotopen aus Uran durch Bestrahlen mit schnellen und verlangsamten Neutronen. *Naturwissenschaften*, 26:755–756, 1938.

[101] O. Hahn and F. Strassmann. Über den Nachweis und das Verhalten der bei der Bestrahlung des Urans mittels Neutronen entstehenden Erdalkalimetalle. *Naturwissenschaften*, 27:11–15, 1939.

[102] L. Meitner and O.R. Frisch. Disintegration of Uranium by neutrons: a new type of nuclear reaction. *Nature*, 143:239, 1939.

[103] O.R. Frisch. Physical Evidence for the Division of Heavy Nuclei under Neutron Bombardment. *Nature*, 143:276, 1939.

[104] N. Bohr and J.A. Wheeler. The Mechanism of Nuclear Fission. *Physical Review*, 56:426, 1939.

[105] G.N. Flerov and K.A. Petrzhak. *Journal of Physics U.S.S.R.*, 3:275, 1940.

[106] G.N. Flerov and K.A. Petrzhak. Spontaneous Fission of Uranium. *Physical Review*, 58:89–89, 1940.

[107] K.A. Petrzhak and G.N. Flerov. Spontaneous Fission of Nuclei. *Soviet Physics Uspekhi*, 4(2):305, 1961.

[108] V.E. Viola et al. Systematics of fission fragment total kinetic energy release. *Physical Review C*, 31(4):1550–1552, 1985.

[109] F.P. Heßberger. Spontaneous fission properties of superheavy elements. *The European Physical Journal A*, 53:75, 2017.

[110] J. Suhonen. *From Nucleons to Nucleus: Concepts of Microscopic Nuclear Theory*. Springer, Berlin, Heidelberg, New York, 2007.

[111] C.J. Gallagher Jr. and S.A. Moszkowski. Coupling of Angular Momenta in Odd-Odd Nuclei. *Physical Review*, 111(5):1282–1290, 1958.

[112] C.J. Gallagher Jr. and S.A. Moszkowski. Coupling of Angular Momenta in Two-Particle States in Deformed Even-Even Nuclei. *Physical Review*, 126(4):1525–1531, 1962.

[113] G. Alaga, K. Alder, A. Bohr, and B.R. Mottelson. Intensity rules for beta and gamma transitions to nucleat rotational states. *Dan. Mat. Fys. Medd.*, 29(9), 1955.

[114] F.G. Kondev et al. Configurations and hindered decays of K isomers in deformed nuclei with $A > 100$. *Atomic Data and Nuclear Data Tables*, 103-104:50–105, 2015.

[115] K. S. Krane. *Introductory Nuclear Physics*. Wiley, New York, NY, 3rd edition, 1987.

[116] T. Kibédi et al. Evaluation of theoretical conversion coefficients using BrIcc. *Nuclear Instruments and Methods in Physics Research Section A: Accelerators, Spectrometers, Detectors and Associated Equipment*, 589(2):202–229, 2008.

[117] Ch. Theisen et. al. Internal conversion and summing effects in heavy nuclei spectroscopy. *Nuclear Instruments and Methods in Physics Research Section A: Accelerators, Spectrometers, Detectors and Associated Equipment*, 589(2):230–242, 2008.

[118] F. Soddy. The stability of Lead isotopes from Thorium. *Nature*, 99:244, 1917.

[119] G. Gamow. Isomeric Nuclei? *Nature*, 133:833, 1934.

[120] G. Gamow. Negative protons and nuclear structure. *Physical Review*, 45:728–729, 1934.

[121] O. Hahn. Über ein neues radioaktives Zerfallsprodukt im Uran. *Naturwissenschaften*, 9:84, 1921.

[122] C.F.v. Weizsäcker. Metastabile Zustände der Atomkerne. *Naturwissenschaften*, 24:813, 1936.

[123] D.E. Alburger. *Nuclear Isomerism in Kernreaktionen III / Nuclear Reactions III*, pages 1–108. Springer, Berlin, Heidelberg, 1957.

[124] P. Walker and G. Dracoulis. Energy traps in atomic nuclei. *Nature*, 399:35, 1999.

[125] K.E.G. Lobner. Systematics of absolute transition probabilities of K-Forbidden gamma-ray transitions. *Physics Letters B*, 26(6):369–370, 1986.

[126] S. Eeckhaudt. *Spectroscopy in the transfermium region: probing rotational, non-yrast and isomeric structures in* ^{253,254}No. PhD thesis, University of Jyväskylä, Jyväskylä, Finland, June 2006.

[127] F. Bernthal et. al. Connection between backbending and high-spin isomer decay in ^{179}W. *Physics Letters B*, 74(3):211–214, 1978.

[128] P.M. Walker et. al. K-forbidden transitions from multi-quasiparticle states. *Physics Letters B*, 408(1-4):42–46, 1997.

[129] B. Sulignano et al. Identification of K isomer in ^{252}No. *The European Physical Journal A*, 33:327, 2007.

[130] S.K. Tandel et al. K isomer in ^{254}No: Probing Single-Particle Energies and Pairing Strengths in the Heaviest Nuclei. *Physical Review Letters*, 97(8):082502, 2006.

[131] H.M. David et al. Decay and fission hindrance of two- and four-quasiparticle K isomers in ^{254}Rf. *Physical Review Letters*, 115(13):132502, 2015.

[132] A.P. Robinson et al. Search for a 2-quasiparticle high-K isomer in ^{256}Rf. *Physical Review C*, 83(6):064311, 2011.

[133] H.B. Jeppesen et al. Multi-quasiparticle states in ^{256}Rf. *Physical Review C*, 79(3):031303(R), 2009.

[134] K. Hauschild *et al.* Isomeric states in ^{256}Rf. *to be published.*

[135] E. Rutherford. LIV. Collision of α particles with light atoms. IV. An anomalous effect in nitrogen. *The London, Edinburgh, and Dublin Philosophical Magazine and Journal of Science*, 37(222):581–587, 1919.

[136] W. Loveland. *Nuclear Chemistry in Encyclopedia of Physical Science and Thechnology*. Academic Press, 3rd edition, 2003.

[137] C.E. Düllmann. Production and study of chemical properties of superheavy elements: Selected results from the last 10 years. *Radiochimica Acta*, 107(7):587–602, 2019.

[138] Yu.Ts. Oganessian et. al. Experiments on the synthesis of neutron-deficient kurchatovium isotopes in reactions induced by ^{50}Ti Ions. *Nuclear Physics A*, 239(1):157–171, 1975.

[139] J.F. Ziegler, M.D. Ziegler, and J.P. Biersack. SRIM – The stopping and range of ions in matter (2010). *Nuclear Instruments and Methods in Physics Research Section B: Beam Interactions with Materials and Atoms*, 268(11-12):1818–1823, 2010.

[140] W.J. Huang et al. The AME2016 atomic mass evaluation (II). Tables, graphs and references. *Chinese Physics C*, 41(3):030003, 2017.

[141] J.H. Hamilton, S. Hofmann, and Yu.Ts. Oganessian. Search for Superheay Nuclei. *Annual Review of Nuclear and Particle Science*, 63(1):383–405, 2013.

[142] S. Hofmann. Super-heavy nuclei. *Journal of Physics G: Nuclear and Particle Physics*, 42(11):114001, 2015.

[143] A.V. Yeremin et al. The Vassilissa facility for electrostatic separation and study of complete fusion reaction products. *Nuclear Instruments and Methods in Physics Research Section A: Accelerators, Spectrometers, Detectors and Associated Equipment*, 274(3):528 – 532, 1989.

[144] A.V. Yeremin et al. The kinematic separator VASSILISSA performance and experimental results. *Nuclear Instruments and Methods in Physics Research Section A: Accelerators, Spectrometers, Detectors and Associated Equipment*, 350(3):608–617, 1994.

[145] A.V. Yeremin et al. The electrostatic separator VASSILISSA Performance and experimental results. *Nuclear Instruments and Methods in Physics Research Section B: Beam Interactions with Materials and Atoms*, 126(1-4):329–333, 1997.

[146] A.V. Yeremin et. al. Velocity filter SHELS: Performance and experimental results. *Nuclear Instruments and Methods in Physics Research Section B: Beam Interactions with Materials and Atoms*, 463:219–220, 2020.

[147] A.V. Yeremin et. al. Experimental tests of the modernized VASSILISSA separator (SHELS) with the use of accelerated ^{50}Ti ions. *Physics of Particles and Nuclei Letters*, 12:43–47, 2015.

[148] K. Rezynkina et. al. First Experimental Tests of SHELS: a New Heavy Ion Separator at the JINR. *Acta Physica Polonica B*, 46:623–626, 2015.

[149] G. Duchêne et al. The Clover: a new generation of composite Ge detectors. *Nuclear Instruments and Methods in Physics Research Section A: Accelerators, Spectrometers, Detectors and Associated Equipment*, 432(1):90–110, 1999.

[150] G. Knoll. *Radiation Detection and Measurement*. Wiley, New York, NY, 4th edition, 2010.

[151] W.R. Leo. *Techniques for Nuclear and Particle Physics Experiments: A How-to Approach*. Spinger-Verlag, Berlin Heidelberg, 2nd edition, 1994.

[152] K. Rezynkina. *Structure of the heaviest nuclei: spectroscopy of* ^{251}Fm *and digital signal processing development*. PhD thesis, Université Paris-Saclay, Orsay, France, Septembre 2016.

[153] A.V. Isaev et al. Application of a double-sided stripped Si detector in the focal plane of the VASILISSA separator. *Instruments and Experimental Techniques*, 54(1):37–42, 2011.

[154] D. Radford. RadWare.

[155] W.J. Huang and G. Audi. Corrections of alpha- and proton-decay energies in implantation experiments. *EJP Web Conferences*, 146:10007, 2017.

[156] Geant4 Collaboration. *Book For Applicarion Developers, Release 10.5*. 2018.

[157] Geant4 Collaboration. *Physics Reference Manual, Release 10.5*. 2018.

[158] Geant4 Collaboration. *Guide for Physics Lists, Release 10.5*. 2018.

[159] S. Agostinelli et al. GEANT4- a simulation toolkit. *Nuclear Instruments and Methods in Physics Research Section A: Accelerators, Spectrometers, Detectors and Associated Equipment*, 506(1):250–303, 2003.

[160] S. Hauf et al. Radioactive Decays in GEANT4. *IEEE Transactions on Nuclear Science*, 60(4):2966–2983, 2013.

[161] LG. Sarniento et al. A GEANT4 simulation package for the TASISpec experimental detector setup. *Nuclear Instruments and Methods in Physics Research Section A: Accelerators, Spectrometers, Detectors and Associated Equipment*, 667(1):26–31, 2012.

[162] LG. Sarniento. Nuclear spectroscopy with GEANT4: The superheavy challenge. *EPJ Web of Conference*, 131:05004, 2016.

[163] R.B. Firestone et. al. *Table of Isotopes*. John Wiley and Sons, New York, 8th edition, 1996.

[164] K. Hauschild et al. Half-life and excitation energy of the $I^{\pi} = 13/2^{+}$ isomer in ^{209}Ra. *Physical Review C*, 77(4):047305, 2008.

[165] J F C Cocks and JUROSPHERE Collaboration. γ-ray spectroscopy of neutron-deficient Ra isotopes. *Journal of Physics G: Nuclear and Particle Physics*, 25(4):839, 1999.

[166] J.B. Moulton et al. A new method for calibrating the pulse-height defect in solid state detectors. *Nuclear Instruments and Methods*, 157(2):325–331, 1978.

[167] I. Rezanka et al. New $i_{\frac{13}{2}}$ isomer $^{207}\mathrm{Rn}^{m}$. *Physical Review C*, 10(2):766–768, 1974.

[168] J. Rissanen et. al. Decay of the high-K isomeric state to a rotational band in ^{257}Rf. *Phys. Rev. C*, 88(4):044313, 2013.

[169] G.N. Flerov et al. Synthesis and physical identification of the isotope of element 104 with mass number 260. *Physics Letters*, 13(1):73–75, 1964.

[170] G.T. Seaborg. Transuranium Elements: A Half Century. *ACS Symposium*, 1990.

[171] K. Hyde et al. A History and Analysis of the Discovery of Elements 104 and 105. *Radiochimica Acta*, 42(2):57–102, 1987.

[172] A. Ghiorso et al. Positive Identification of Two Alpha-Particle-Emitting Isotopes of Element 104. *Physical Review Letters*, 22(24):1317–1320, 1969.

[173] C.E. Bemis et al. X-Ray Identification of Element 104. *Physical Review Letters*, 31(10):647–650, 1973.

[174] P.R. Fields et. al. Production of the New Element 102. *Physical Review*, 107(5):1460, 1957.

[175] J. Milsted. The New Element Nobelium: The Preparation of Nobelium. *Nature*, 180:1012, 1957.

[176] H.A.C. McKay. The New Element Nobelium: Preparation of Trans-Uranium Elements. *Nature*, 180:1010, 1957.

[177] A. Ghiorso et. al. Attempts to Confirm the Existence of the 10-Minute Isotope of 102. *Physical Review Letters*, 1(1):17, 1958.

[178] A. Ghiorso et. al. Element No. 102. *Physical Review Letters*, 1(1):18, 1958.

[179] B.F. Thornton and S.C. Burdette. Nobelium non-believers. *Nature Chemistry*, 6:652, 2014.

[180] G.N. Flerov et. al. A History and Analysis of the Discovery of Element 102. *Radiochemica Acta*, 56:111–124, 1992.

[181] H. Kragh. *From Transuranic to Superheavy Elements: A story of Disputes and Creation*. Springer International Publishing, 2018.

[182] F.P. Heßberger et. al. Study of Evaporation Residues Produced in Reactions of ^{207,208}Pb with ^{50}Ti. *Zeitschrift für Physik A: Atomic Nuclei*, 321:317–327, 1985.

[183] F.P. Heßberger et. al. Spontaneous fission and alpha-decay properties of neutron deficient isotopes $^{257-253}$104 and ^{258}106. *Zeitschrift für Physik A: Atomic Nuclei*, 359:415–425, 1997.

[184] F.P. Heßberger et. al. Decay properties of neutron-deficient isotopes ^{256,257}Db, ^{255}Rf, ^{252,253}Lr. *The European Physical Journal A*, 12:57–67, 2001.

[185] F.P. Heßberger et. al. Alpha-gamma decay studies of ^{255}Rf, ^{251}No and ^{247}Fm. *The European Physical Journal A*, 30:561–569, 2006.

[186] S. Antalic et. al. Nuclear isomers in ^{259}Sg and ^{255}Rf. *The European Physical Journal A*, 51:41, 2015.

[187] J. Khuyagbaatar et. al. The identification and confirmation of isomeric states in ^{254}Rf and ^{255}Rf through conversion electron detection. *Nuclear Physics A*, 994:121662, 2020.

[188] P. Mosat et. al. K isomerism in ^{255}Rf and total kinetic energy measurements for spontaneous fission of ^{255,256,258}Rf. *Physical Review C*, 101(3):034310, 2020.

[189] I. Ahmad et al. Alpha Decay of ^{251}Fm. *Physical Review C*, 8(2):737–744, 1973.

[190] F.B. Heßberger et. al. Alpha-gamma decay studies of ^{253}No and its daughter products ^{253}Md , ^{249}Fm. *The European Physical Journal A*, 48:75, 2012.

[191] A.P. Lashko et. al. Anomalous internal conversion of the K-forbidden 55 keV E1-transition in ^{177}Hf. *The European Physical Journal A*, 49:21, 2013.

[192] K.-H. Schmidt. Some Remarks on the Error Analysis in the Case of Poor Statistics. *Zeitschrift für Physik A- Atoms and Nuclei*, 316:19–26, 1984.

[193] N.Yu. Shirikova et al. Structure of the low-lying states of the odd-neutron nuclei with $Z \approx 100$. *The European Physical Journal A*, 51:21, 2015.

[194] S. Antalic et al. Isomeric states in ^{253}No and ^{253}Fm. *The European Physical Journal A*, 47:62, 2011.

[195] G. Henning et al. Fission Barrier of Superheavy Nuclei and Persistence of Shell Effects at High Spin: Cases of ^{254}No and ^{220}Th. *Physical Review Letters*, 113(26):262505, 2014.

[196] F. Déchery et al. The Super Separator Spectrometer S^3 and the associated detection systems: SIRIUS & LEB – REGLIS$_3$. *Nuclear Instruments and Methods in Physics Research Section B: Beam Interactions with Materials and Atoms*, 376:125–130, 2016.

[197] S. Akkoyun et al. AGATA- Advanced GAmma Tracking Array. *Nuclear Instruments and Methods in Physics Research Section A: Accelerators, Spectrometers, Detectors and Associated Equipment*, 668:26–58, 2012.

[198] J. Sempau et al. Experimental benchmarks of the Monte Carlo code PENELOPE. *Nuclear Instruments and Methods in Physics Research Section B: Beam Interactions with Materials and Atoms*, 207(2):107–123, 2003.

université
PARIS-SACLAY

ÉCOLE DOCTORALE
Particules, hadrons, énergie et noyau :
instrumentation, imagerie, cosmos
et simulation (PHENIICS)

Titre: Caractérisation du multi-détecteur GABRIELA et spectroscopie de décroissance des noyaux ^{255}Rf et ^{251}No

Mots clés: Noyaux super lourds, structure nucléaire, spectroscopie γ, e^- et α, caractérisation des détecteurs, simulation GEANT4

Résumé: Une question sans réponse qui se trouve au carrefour de la physique et de la chimie est: quelle est la limite du tableau périodique. Les théories nucléaires suggèrent l'existence de ce qu'on appelle "l'îlôt de stabilité", habitée par des éléments super-lourds à longue durée de vie. Ces éléments ne doivent leur existence qu'à d'importants effets quantiques. Ainsi, les éléments super-lourds forment un laboratoire unique pour l'étude de la structure et de la dynamique nucléaires sous l'influence d'une très forte répulsion Coulombienne entre les nombreux protons du noyau. Cependant, un défi théorique réside dans la prédiction de la position exacte de cet îlôt, car différents modèles prédisent la position des prochaines fermetures de couches au delà de Z = 82 et N=126 à Z = 114, 120 ou 126, et N = 172, 184 de façon plutôt inharmonieuse. Pour mieux comprendre le comportement de la matière nucléaire dans des conditions extrêmes du nombre de protons et de neutrons et contraindre les modèles nucléaires, il est donc nécessaire d'étudier la nature et la séquence d'états dans des noyaux transactinides plus légers et plus accessibles par des études spectroscopiques. Dans ce travail, des états de ^{255}Rf ont été peuplés par la réaction de fusion-évaporation ^{50}Ti(^{207}Pb,2n)^{255}Rf en utilisant un faisceau intense de ^{50}Ti fourni par le cyclotron U400 du FLNR à Dubna. Les résidus d'évaporation ont été séparés du faisceau et du fond d'autres produits de réaction à l'aide du séparateur de noyaux de recul SHELS et implantés dans le détecteur d'implantation du dispositif GABRIELA. Le multidétecteur GABRIELA permet d'effectuer des corrélations de temps et en position entre les noyaux implantés et leurs désintégrations ultérieures et est sensible à l'émission de rayonnemments gamma, d'électrons de conversion interne, de particules alpha et de produits de fission. Pour interpréter les spectres de désintégration expérimentaux, le multidétecteur GABRIELA a été caractérisé à l'aide de simulations GEANT4, qui ont été validées avec des données d'étalonnage. En particulier, l'impact des effets de sommation sur l'efficacité de la détection des rayons gamma et des électrons a été étudié et a montré que les simulations sont essentielles pour interpréter des résultats expérimentaux obtenus grâce à des dispositifs compactes et efficaces comme GABRIELA. Une nouvelle méthode pour estimer le profil de profondeur d'implantation des résidus d'évaporation a été mise au point, ce qui est essentiel notamment pour la spectroscopie des électrons de conversion interne. Afin de pouvoir utiliser GEANT4 pour des éléments plus lourds que Fm (Z = 100), le code source a été modifié et les données de fluorescence et d'émission Auger ont été extrapolées pour permettre des simulations précises de décroissances radioactives jusqu'à l'élément Rf. En utilisant les données expérimentales obtenues sur le noyau ^{257}Rf étudié à Dubna et le schéma de désintégration connu de l'isomère $\frac{21}{2}^+$ de haut K, la fonctionnalité du code GEANT4 modifié a été validée. Les simulations ont ensuite été utilisées pour étudier la structure fine de décroissance alpha du ^{255}Rf et dériver les rapports d'embranchements vers les états du ^{251}No. Les rapports d'embranchements de décroissance gamma et les coefficients de conversion interne de transitions du ^{251}No ont également été extraits. Dans le ^{255}Rf, deux nouveaux états isomériques de haut K ont été identifiés et l'existence à basse énergie d'excitation d'un isomère de spin a été confirmée. Les comparaisons quantitatives et qualitatives des spectres expérimentaux aux simulations ont permis d'établir les schémas de désexcitation les plus probables et d'assigner les configurations quasi-particules possibles pour les 3 isomères.

Title: Characterization of the multi-detector GABRIELA and decay spectroscopy of ^{255}Rf and ^{251}No

Keywords: Superheavy nuclei, nuclear structure, γ-ray, e^- and α spectroscopy, detector characterization,GEANT4 simulations

Abstract: One unanswered question that lies at the crossroad of physics and chemistry is: what is the limit of the periodic table. Nuclear theories suggest the existence of the so-called "island of stability", inhabited by long-lived superheavy elements. These elements can materialize only because of strong quantum shell stabilizing effects. Thus, superheavy elements form a unique laboratory for studying nuclear structure and dynamics under the influence of very large Coulomb forces between the numerous protons in the nucleus. However, a theoretical challenge lies in the prediction the exact position of this island as different models predict the position of the next shell closures at Z = 114, 120, or 126, and N = 172, 184 beyond the closed spherical shells at Z = 82 and N = 126 rather inharmoniously. To better understand the behavior of nuclear matter for extreme values of proton and neutron numbers and constrain nuclear models it is, therefore, necessary to investigate the nature and sequence of states in lighter, more accessible, transactinide nuclei through spectroscopic studies. In this work, states of ^{255}Rf were populated through the fusion-evaporation reaction ^{50}Ti(^{207}Pb,2n)^{255}Rf using an intense ^{50}Ti beam provided by the U400 cyclotron of FLNR in Dubna. The evaporation residues were separated from the beam and background of other reaction products using the recoil separator SHELS and implanted into the implantation detector of the GABRIELA setup. The GABRIELA multidetector array allows to perform time and position correlations between the implanted nuclei and their subsequent decays and is sensitive to the emission of gamma rays, internal conversion electrons, alpha particles and fission products. To interpret the experimental decay spectra, the GABRIELA multidetector was characterized using GEANT4 simulations, which were validated with calibration data. In particular, the impact of summing on the gamma-ray- and electron-detection efficiencies was investigated and showed that simulations are vital for interpreting experimental results obtained using compact and efficient setups like GABRIELA. A novel method to estimate the implantation depth profile of the evaporation residues was devised, which is essential especially for internal-conversion-electron spectroscopy. To be able to use GEANT4 for elements heavier than Fm (Z = 100), the source code was modified and the Fluorescence and the Auger emission data were extrapolated to allow accurate radioactive decay simulations up to the element Rf. Using ^{257}Rf experimental data obtained in Dubna and the known decay scheme of the $\frac{21}{2}^+$ high-K isomer, the functionality of the modified GEANT4 code was validated. Simulations were then used to study the fine structure alpha decay of ^{255}Rf and derive branching ratios to states in ^{251}No. The gamma-decay branching ratios and internal conversion coefficients for transitions in ^{251}No were also extracted. In ^{255}Rf, two new high-K isomeric states were identified and the existence of a low-lying spin isomer was confirmed. Quantitative and qualitative comparisons of the experimental spectra to simulations have allowed to establish the likely decay schemes and assign possible quasiparticle configurations for all 3 isomers.

Université Paris-Saclay
Espace Technologique / Immeuble Discovery
Route de l'Orme aux Merisiers RD 128 / 91190 Saint-Aubin, France